

Validation of MEG source imaging of neuronal oscillations and connectivity with intracranial EEG

Jawata Afnan

Doctor of Philosophy

Integrated Program in Neuroscience



McGill University

August 2024

A thesis submitted to McGill University in partial fulfillment of the requirements of
the degree of Doctor of Philosophy

©Jawata Afnan, 2024

I dedicate my thesis to my parents, MD. Zahirul Haq (Abba) and Surya Haq (Amma). Their dream, struggle, and inspiration have brought me to where I stand today.

Contents

Abstract	x
Résumé.....	xii
Acknowledgments	xiv
Contribution to original knowledge	xvi
Contribution of authors	xix
List of Figures.....	xxiii
List of Tables	xxxv
1 Introduction.....	1
2 Fundamentals of epilepsy and pre-surgical investigation.....	6
2.1 Definition of epilepsy.....	6
2.2 Classification of seizures and epilepsies	7
2.3 Treatment of epilepsy	9
2.4 Presurgical investigation of epilepsy	9
2.4.1 Interictal epileptiform discharges	13
2.5 Conclusion	15
3 EEG/MEG source imaging.....	16
3.1 History of EEG/MEG.....	16
3.1.1 History of EEG	16
3.1.2 History of MEG.....	17
3.2 Cellular origin of EEG/MEG signals	18
3.3 Differences and complementary strengths of EEG and MEG	22
3.4 EEG and MEG instrumentation	23
3.5 Estimating the neuronal sources from EEG/MEG measurement.....	27
3.6 EEG/MEG forward problem.....	28
3.6.1 Quasi-static approximation of Maxwell's equations	28
3.6.2 Source model	31
3.6.3 Head model	31
3.6.4 Tissue conductivities	32

3.6.5	Coregistration of EEG/MEG sensors with anatomy	33
3.7	EEG/MEG inverse problem.....	33
3.7.1	Dipole fitting approach	34
3.7.2	Dipole scanning approach	35
3.7.3	Distributed source imaging models	38
3.7.4	Other inverse methods	45
3.8	Challenges and limitations of EEG/MEG source imaging	45
3.8.1	Ill-posed nature of inverse problem	46
3.8.2	Localizing deep brain activity	46
3.9	Conclusion	49
4	EEG/MEG in resting state oscillations and connectivity	53
4.1	Introduction	53
4.2	Resting-state oscillations	53
4.2.1	Canonical frequency bands.....	53
4.2.2	Brain regions associated with different frequencies	54
4.2.3	Decomposition of power spectrum into periodic and aperiodic components	58
4.3	Resting-state connectome.....	60
4.4	EEG/MEG based functional connectome.....	62
4.5	Connectivity metrics used in connectome study and challenges	63
4.5.1	Phase-based metrics	63
4.5.2	Amplitude-based Metrics	64
4.6	Resting state EEG/MEG connectome studies	66
4.6.1	Which connectivity metrics are suitable for EEG/MEG resting state analysis	67
4.6.2	Comparison of EEG/MEG connectome with other modalities.....	68
4.6.3	Connectome studies with intracerebral EEG	71
4.7	Conclusion	73
5	Validation of EEG/MEG source imaging	74
5.1	Necessity of validation	74
5.2	Methods of validation.....	74

5.2.1	Numeric simulation studies	74
5.2.2	Intracranial EEG.....	77
5.3	Integration of SIEEG with EEG/MEG.....	79
5.4	Challenges integrating simultaneous EEG/MEG and SIEEG	80
5.4.1	Technical challenges	81
5.4.2	Quantitative comparison between EEG/MEG and SIEEG	83
5.4.3	Limited spatial coverage and lack of normal resting state iEEG	87
5.5	iEEG atlas of normal resting state activity	87
5.6	Conclusion	89
6	Manuscript 1: Validating MEG source imaging of resting state oscillatory patterns with an intracranial EEG atlas	90
6.1	Preface.....	90
6.2	Abstract:	91
6.3	Introduction	92
6.4	Material and methods	94
6.4.1	Experimental design.....	94
6.4.2	Ground truth: MNI iEEG atlas	95
6.4.3	Subject selection criteria for MEG.....	96
6.4.4	MEG data acquisition	96
6.4.5	Anatomical MRI, MEG-MRI co-registration and forward model estimation	96
6.4.6	MEG data preprocessing	97
6.4.7	MEG source imaging using wavelet Maximum Entropy on the Mean (wMEM)	97
6.4.8	Estimation of virtual iEEG (ViEEG) data from the MEG source map.....	99
6.4.9	Frequency specific brain maps of relative power	100
6.4.10	Analysis of spectral oscillatory components	101
6.4.11	Comparison of ViEEG spectra with iEEG.....	101
6.4.12	Comparison of ViEEG with iEEG in terms of peak frequency	102
6.4.13	Comparison with minimum norm estimate (MNE) and LCMV beamformer ...	103
6.5	Results.....	104
6.5.1	Frequency specific brain maps of relative power	104

6.5.2	Analysis of spectral oscillatory components	105
6.5.3	Comparison of ViEEG spectra with iEEG.....	106
6.5.4	Comparison of ViEEG with iEEG in terms of oscillatory peaks	110
6.5.5	iEEG and ViEEG amplitude	112
6.5.6	Comparison with minimum norm estimate (MNE) and LCMV beamformer ...	114
6.6	Discussion.....	115
6.6.1	Removing the aperiodic component improves the spectral comparison between ViEEG and iEEG.....	116
6.6.2	MEG spectra were better estimated in lateral regions than in medial regions ...	117
6.6.3	Dominance of alpha oscillations in MEG.....	118
6.6.4	Differences in signal relative power.....	119
6.6.5	wMEM for resting state localization and comparison with MNE and beamformer 120	
6.6.6	Limitations	121
6.7	Conclusion	122
6.8	Acknowledgment.....	122
7	Manuscript 2 EEG/MEG source imaging of deep brain activity within the Maximum Entropy on the Mean framework: simulations and validation in epilepsy.....	123
7.1	Preface.....	123
7.2	Abstract	124
7.3	Introduction	125
7.4	Materials and methods.....	128
7.4.1	Experimental design.....	128
7.4.2	Maximum entropy on the mean method and depth weighting	128
7.4.3	MEG and HD-EEG realistic simulations	130
7.4.4	Resting-state data acquisition for simulation	132
7.4.5	Data preprocessing.....	133
7.4.6	IEDs from patients with focal epilepsy.....	133
7.4.7	Source space and forward model estimation.....	134
7.4.8	Validation metrics	135

7.5	Results	136
7.5.1	Simulation of single epileptic source: MEG	136
7.5.2	Simulation of mixed sources in the hippocampus and the neocortex in MEG ..	141
7.5.3	Simulation of single epileptic source: HD-EEG	144
7.5.4	Evaluation on clinical MEG/HD-EEG data from patients with focal epilepsy ..	147
7.5.5	Depth-weighted wMEM	151
7.6	Discussion	151
7.6.1	Including hippocampus in the source model.....	152
7.6.2	Depth-weighted cMEM improved localization for deep sources	152
7.6.3	Complex simulations involving mesial and neocortical sources.....	155
7.6.4	Sensitivity of EEG/MEG sensors to deep activity	156
7.6.5	Depth-weighted wMEM	156
7.6.6	Limitations	157
7.7	Conclusion	157
7.8	Acknowledgment.....	158
8	Manuscript 3: Validating MEG estimated resting state connectome with intracranial EEG	159
8.1	Preface.....	159
8.2	Abstract	160
8.3	Introduction	160
8.4	Materials and methods.....	162
8.4.1	Experimental design.....	162
8.4.2	Ground truth: iEEG atlas.....	163
8.4.3	MEG	164
8.4.4	Cross-modal correlation.....	168
8.4.5	Estimation of connectivity metrics.....	169
8.5	Results.....	171
8.5.1	Connectivity estimated by MEG versus iEEG	171
8.5.2	Cross-modal spatial correlation: AEC and OAEC	172
8.5.3	Cross-modal spatial correlation: <i>PLV</i> and <i>wPLI</i> *	175

8.5.4	Cross-modal spatial correlation for superficial versus deep sources	177
8.5.5	Connectivity as a function of distance between two ROIs	178
8.5.6	Cross-modal spatial correlation and the number of subjects averaged in ROI pairs 179	
8.6	Discussion	181
8.6.1	Moderate correlations between MEG and iEEG connectome	182
8.6.2	Compromise between removing spurious connectivity and genuine zero-lag connectivity	185
8.6.3	Cross-modal correlations for deep versus superficial ROIs	187
8.6.4	Limitations	188
8.7	Conclusions	190
8.8	Acknowledgment.....	190
9	Manuscript 4: Validating MEG source imaging of oscillations and connectivity using simultaneous MEG-intracerebral EEG	191
9.1	Preface.....	191
9.2	Abstract	192
9.3	Introduction	193
9.4	Materials and methods.....	195
9.4.1	Experimental design.....	195
9.4.2	Simultaneous SEEG-MEG data	196
9.4.3	SEEG contact localization.....	198
9.4.4	MEG Source space and forward model estimation	198
9.4.5	MEG and SEEG data preprocessing.....	199
9.4.6	MEG source imaging using wavelet Maximum Entropy on the Mean (wMEM) 199	
9.4.7	Estimation of virtual SEEG data from the MEG source map.....	200
9.4.8	Frequency specific relative power.....	200
9.4.9	Connectivity metrics	201
9.4.10	Cross-modal spatial correlation between MEG and SEEG results.....	201
9.5	Results.....	201

9.5.1	Relative power spectral density	202
9.5.2	Connectivity	205
9.6	Discussion	207
9.6.1	Deep source localization	208
9.6.2	Compromise between removing spurious connectivity and genuine zero-lag connectivity	209
9.6.3	Moderate to low correlations between MEG and SEEG connectome	211
9.6.4	Limitations	212
9.7	Conclusions	212
10	Overall discussion and conclusions	214
10.1	Main methodological contributions and limitations	214
10.2	Future directions.....	222
Appendix A for manuscript 1 in Chapter 6.....		228
Spatial prior model:.....		228
Initialization of the parcels:		229
Selection of baseline for resting state localization:		230
Appendix B for manuscript 2 in Chapter 7.....		231
Coherent Maximum Entropy on the mean (cMEM).....		231
Depth-weighted cMEM (cMEM _ω)		233
Wavelet Maximum Entropy on the mean (wMEM)		234
Depth-weighted wMEM (wMEM _ω)		235
References.....		236

Abstract

Due to the ill-posed nature of the Electro/Magneto- EncephaloGraphy (EEG/MEG) source imaging problem, its ability to localize brain activity, particularly from deep brain generators and during the resting state, requires validation. Intracerebral EEG, an invasive method used for the presurgical evaluation of some drug-resistant epileptic patients, is considered the gold standard for validating non-invasive EEG/MEG source localization. This thesis aimed to validate MEG source localization of resting state oscillations and MEG-derived connectivity. This was done first at a group level for healthy participants using the intracranial EEG (iEEG) atlas of normal brain activity, and then at a single-subject level using simultaneous MEG and intracerebral EEG acquired from patients with epilepsy. The EEG/MEG inverse problem was solved using the Maximum Entropy on the Mean (MEM), a method capable of accurately localizing superficial cortical generators and their spatial extent. The thesis is organized into four manuscript-based studies.

In Study 1, we adapted the MEM method to localize EEG/MEG resting-state brain activity and validated its ability to localize resting-state oscillations from a group of healthy participants using the iEEG atlas as the ground truth. The atlas of physiological normal iEEG had been developed by pooling data from 110 patients with refractory epilepsy; the atlas included only the electrodes implanted in healthy brain regions. We demonstrated that MEG-estimated oscillations were more accurately estimated in superficial regions compared to deep regions. We also observed widespread leakage of alpha oscillations in MEG in the frontal and deep brain regions, likely due to spatial leakage associated with MEG source imaging.

In Study 2, we proposed a depth-weighted adaptation of the MEM method for EEG/MEG source imaging and evaluated it using realistic high-density EEG/MEG simulations and high-density EEG/MEG recordings from patients with focal epilepsy. The depth-weighted method significantly improved the localization of deep brain activity, particularly from the hippocampus in patients with mesial temporal lobe epilepsy.

In Study 3, we conducted a group-level validation of MEG-derived resting-state connectome using the same dataset as in Study 1. Using four widely used connectivity metrics, Amplitude Envelope Correlation (AEC), orthogonalized AEC (OAEC), Phase Locking Value (PLV), and weighted-phase lag index (wPLI), we found that the correlations between MEG and iEEG connectomes were

moderate to low, indicating that MEG connectivity results should be interpreted with caution. We also found that metrics corrected for zero-lag connectivity to address source leakage issues had a lower correlation with iEEG than metrics that were not corrected.

In Study 4, using simultaneous MEG and intracerebral EEG acquired from patients with epilepsy, we validated the group-level findings from Studies 1 and 3 at a single-subject level. We found that MEG retrieved oscillatory and connectivity patterns with moderate to low correlations when compared to intracerebral EEG. We found that MEG-estimated power was more accurately estimated in superficial channels compared to deep channels. The group-level findings in Study 3 were reflected at the single-subject level: connectivity metrics that correct for zero-lag connectivity showed low correlations between MEG and intracerebral EEG. This highlighted the trade-off; while EEG/MEG may capture more connectivity due to source leakage, removing zero-lag connectivity can eliminate true connections.

These four studies identified brain regions, frequencies, and connectivity metrics for which non-invasive EEG/MEG source imaging is likely to be reliable, particularly noting the influence of generator depth. The proposed methodological framework and findings can also be applied to analyze, understand, and interpret EEG/MEG source imaging in neurodegenerative diseases.

Résumé

Le problème inverse de localisation de sources électro/magnéto-encéphalographiques (EEG/MEG) étant mal posé, il est nécessaire de valider sa capacité à localiser l'activité cérébrale, en particulier les générateurs cérébraux profonds et pendant l'état de repos. L'EEG intracérébral (iEEG), une méthode invasive utilisée lors de l'évaluation préchirurgicale de certains patients épileptiques réfractaires, est considéré comme la méthode de référence pour valider la localisation de sources EEG/MEG. Cette thèse a pour but de valider la précision des localisations MEG, pour reconstruire les oscillations et profils de connectivité pendant l'état de repos. Pour ce faire, nous avons adapté une méthode maximisant l'entropie sur la moyenne (MEM), afin de localiser les générateurs corticaux et leur étendue spatiale. Nous proposons une validation du MEM: (i) en comparant des données MEG d'un groupe de participants sains avec un atlas iEEG de l'activité cérébrale normale, (ii) au niveau individuel à partir d'enregistrements simultanés MEG/iEEG chez des patients épileptiques.

Dans l'étude 1, nous avons adapté le MEM pour localiser les oscillations de l'activité cérébrale au repos, en comparant les localisations MEG d'un groupe de participants sains avec l'atlas iEEG. L'atlas iEEG combine les données de 110 patients afin de caractériser l'activité intracérébrale physiologique et ce en n'incluant que les électrodes implantées dans des régions saines. Nous avons démontré que les oscillations localisées en MEG étaient plus exactes dans les régions superficielles que profondes. Par ailleurs, les localisations MEG d'oscillations alpha étaient faussement localisées de manière étendue dans les régions frontales et profondes, probablement en raison de problèmes de conduction volumique.

Dans l'étude 2, nous avons implémenté une pondération en profondeur de la méthode MEM, puis évalué la localisation de sources EEG haute densité et MEG à l'aide de simulations réalistes et de données acquises chez des patients épileptiques. Le MEM pondéré en profondeur a amélioré de manière significative la localisation de l'activité cérébrale profonde, en particulier au niveau de l'hippocampe.

Dans l'étude 3, nous avons validé au niveau de groupe, les profils de connectivité fonctionnelle mesurés à l'état de repos en MEG, en utilisant les mêmes données que dans l'étude 1. À l'aide de 4 mesures de connectivité fréquemment utilisées, nous avons constaté que les corrélations spatiales

entre connectomes MEG et iEEG étaient modérées, suggérant d'interpréter avec prudence les connectomes MEG. En utilisant des mesures de connectivité qui corrigent l'influence des corrélations synchrones (phase nulle) pour réduire les effets de conduction volumique, nous avons obtenu une corrélation spatiale avec l'iEEG plus faible qu'en utilisant des mesures non corrigées.

Dans l'étude 4, nous avons validé au niveau individuel les résultats de groupe des études 1 et 3 en utilisant des données MEG et iEEG acquises simultanément chez des patients épileptiques. La localisation MEG a permis de reconstruire des oscillations et profils de connectivité présentant des corrélations spatiales modérées en comparaison aux mesures iEEG. La localisation des oscillations était plus précise pour les régions superficielles que profondes. Comme pour l'étude 3, nous avons obtenu une corrélation spatiale plus faible entre connectomes MEG et iEEG en considérant des mesures de connectivité qui corrigent l'influence des corrélations synchrones, suggérant un compromis entre corriger l'effet des conductions volumiques synchrones et le risque d'éliminer de vraies connexions.

Ces études ont identifié les régions du cerveau, les bandes de fréquences et les mesures de connectivité pour lesquelles la localisation EEG/MEG est probablement fiable. Le cadre méthodologique et nos résultats peuvent être appliqués pour analyser, comprendre et interpréter les localisations EEG/MEG dans le cadre des maladies neurodégénératives.

Acknowledgments

I would like to express my immense gratitude to my supervisors, Dr. Christophe Grova and Dr. Jean Gotman, for their support, encouragement, guidance, patience, and kindness throughout my PhD journey. I am deeply grateful for their time and ideas, their insightful feedback, and their emotional support. I am also incredibly fortunate to be the last PhD student of Dr. Jean Gotman.

I extend my gratitude to the members of my dissertation committee, Dr. Birgit Frauscher and Dr. Boris Bernhardt, as well as my academic mentor, Dr. Sylvain Baillet, and my candidacy examiner, Dr. Karim Jerbi. Their valuable comments, critiques, and advice have greatly improved my projects. My sincere thanks go to Dr. Jean-Marc Lina for his continuous guidance on the methodological aspects of my work. I am also grateful to our collaborators, Dr. Christian B  nar, Dr. Birgit Frauscher, Dr. Eliane Kobayashi, Dr. Jean Michel Badier, Dr. Francesca Bonini, and Dr. Giovanni Pellegrino, for sharing data and for their support in the design and writing of my articles.

I would like to thank the funding agencies that supported me throughout my PhD: the Canadian Open Neuroscience Platform (CONP) Scholarship, the Irma Bauer Fellowship (McGill University), the Fonds de Recherche du Qu  bec - Sant   (FRQS) Doctoral Scholarship, and the Graduate Mobility Award (McGill University). I would also like to express my gratitude to all the patients and healthy participants whose data contributed to this research.

Special thanks go to Dr. Zhengchen Cai and Dr. Nicol  s von Ellenrieder for their advice, guidance, and assistance throughout my PhD. I have learned so much from Zhengchen and Nicol  s - not only academically but also about the importance of kindness and compassion toward colleagues, as well as how to grow into a better human being. I am also thankful to Dr. Tanguy Hedrich and Dr. Chifaou Abdallah, from whom I learned a great deal, and who provided significant help with my projects. Thanks to Dr. Zhengchen Cai and Edouard Delaire for their efforts in correcting my thesis. I am grateful to Dr. Oba   Bin Ka  b Ali, Dr. Umit Aydin, and Dr. Makoto Uji for their support and advice during my PhD.

I am fortunate to have worked with amazing people who supported me along the way. I am grateful to my friends and colleagues from the Multifunkim Laboratory and Gotman Lab: Tamir Avigdor, Edouard Delaire, Yimeng Wang, Dr. Aura Gonzalez Ramirez, Dr. Victoria Ros, Dr. Abdullah Azeem, Dr. Andreas Koupparis, Natalja Zazubovits, Dr. Fatemeh Razavipour, Amanda Spilkin,

Dr. Thaera Arafat, Dr. John Thomas, Dr. Katharina Schiller, Shahla Bakian Dogaheh, Arielle Dascal, Mahdi Mobarak-Abadi, Helia Mirabi, Dr. Hassan Khajehpour, Lydia Stoutah, Dr. Alice Ballabeni, Ilian Azzouz, Dr. Mathilde Reyt, Dr. Niels de Joode, Dr. Maëva Laquittaine, Dr. Mustafa Aykut Kural, and Riwa Itani. My gratitude extends to Aude Jegou for her support and encouragement. I am thankful to Toula Papadopoulos and Sylvain Milot for their assistance during my PhD. Thanks to Dr. Marc Lalancette, who assisted me and my colleagues with the recording of EEG and MEG. I also want to thank my colleagues and friends from the ANPHY Lab: Dr. Sana Hannan, Erica Minato, Alyssa Ho, Laetitia Wang, Winnie Wei, and Kassem Jaber. I am grateful to Jessica Royer for her valuable suggestions. My gratitude also goes to my friends and colleagues at the Dynamap Lab, Aix-Marseille University, who welcomed me warmly: Maria Fratello, Dr. Damián Dellavale, Samuel Medina Villalon, Victor Lopez-Madrone, Dr. Flavius Bratu, Aurore Semeux-Bernier, Bruno Colombet, Maëva Daoud, Christian Ferreyra, Elodie Garnier, Nicolas Hemmer, Khoubeib Kanzari, Lisa Soncin, Sara Simula, and others. I would like to thank my friends Nusrat Koley Apu, Muna, Heme, Jamy, Sunam, Naznin, Naba, and Rumpa for being an invaluable part of my life.

Finally, my heartfelt thanks to my parents, MD Zahirul Haq (Abba) and Surya Haq (Amma), who endured countless struggles to help me reach where I am today; my brothers, Enamul Haq (Bhaijan) and Shajadul Haq (Chhotobhai); my sisters-in-law, Jannatul Ferdous and Nurjahan Bilkish; my sister, Farjana Ferdous; my partner, Dhritiman Bhattacharya; and my nieces (Nushba and Anahita) and nephews (Zahiyan and Nameer) for their love and support.

Contribution to original knowledge

This PhD thesis was based on the realization of four original studies, each consisting of a research manuscript. Here are the statements of originality corresponding with each of those four studies.

Study 1: Validating MEG source imaging of resting state oscillatory patterns with an intracranial EEG atlas.

This study is the first group-level validation of MEG non-invasive localization of resting-state oscillations in the whole brain in a healthy population, using an intracranial EEG atlas of normal brain activity as the ground truth. We adapted the wavelet MEM source imaging method to localize specifically resting-state oscillations of low signal-to-noise ratio data and provided a brain atlas identifying regions that can be accurately estimated by MEG in terms of resting-state oscillations. For quantitative comparison purposes, we converted MEG sources estimated using wMEM along the cortical surface into virtual intracranial EEG data, after applying an intracranial EEG forward model to MEG sources. This approach was applied to each intracranial EEG contact of the atlas, and we proposed new quantitative metrics to compare the oscillatory patterns in both datasets (virtual and real intracranial EEG data). Our wMEM method adapted for resting state localization is available on the open-source platform Brainstorm (<https://neuroimage.usc.edu/brainstorm/Tutorials/TutBEst/>).

Afnan, J., von Ellenrieder, N., Lina, J.M., Pellegrino, G., Arcara, G., Cai, Z., Hedrich, T., Abdallah, C., Khajepour, H., Frauscher, B., Gotman, J., Grova, C., 2023. Validating MEG source imaging of resting state oscillatory patterns with an intracranial EEG atlas. *NeuroImage*, 274,p.120158. <https://doi.org/10.1016/j.neuroimage.2023.120158>

Study 2: EEG/MEG source imaging of deep brain activity within the Maximum Entropy on the Mean framework: simulations and validation in epilepsy.

We proposed and implemented depth weighting in MEM-based source imaging methods to improve the usually poor localization of deep brain activity from EEG and MEG recordings. We also included an accurate surface segmentation of bilateral hippocampi in our source space, to more realistically recover these deep generators. Through extensive simulations using high-density EEG and MEG, we demonstrated that the proposed method improves source localization in deep

regions. The method showed significant improvement when compared to our previous MEM implementation and to standard depth-weighted minimum norm estimate methods in localizing deep sources. When applied to real MEG and high-density EEG data from patients with epilepsy, we demonstrated that our new implementation significantly improves localization accuracy, especially for patients with mesial temporal lobe epilepsy. Our implementation of depth-weighted MEM is available for both cMEM and wMEM versions on the open-source platform Brainstorm (<https://neuroimage.usc.edu/brainstorm/Tutorials/TutBEst/>).

Afnan, J; Cai, Z; Lina, J.M.; Abdallah, C; Delaire, E.; Avigdor, T.; Ros, V.; Hedrich, T.; von Ellenrieder, N.; Kobayashi, E.; Frauscher, B; Gotman, J., and Grova, C., 2024. EEG/MEG source imaging of deep brain activity within the Maximum Entropy on the Mean framework: simulations and validation in epilepsy. *Human Brain Mapping*. 2024 Jul 15;45(10):e26720. doi: <https://doi.org/10.1002/hbm.26720>

Study 3: Validating MEG estimated resting state connectome with intracranial EEG

Using the depth-weighted wMEM method proposed in Study 2, we validated the MEG-derived connectome for a group of healthy individuals against the intracranial EEG atlas of normal brain activity as the ground truth. We evaluated the effectiveness of four widely used connectivity metrics, identifying the specific frequency bands and metrics where the MEG-derived connectome was accurately estimated and where it was weakly estimated. To do so, we applied the same methodology proposed in Study 1, converting MEG sources into virtual intracranial EEG data. We then proposed an original resampling methodology to take into account the limited spatial sampling of the MNI intracranial EEG atlas when assessing functional connectivity (since only paired electrodes from the same subjects could be considered), proposing for the first time spatial correlations between functional connectomes estimated from MEG sources and intracranial EEG data at the group level. To the best of our knowledge, this is the first group-level validation of an MEG-derived connectome using intracranial EEG.

Afnan, J., Cai, Z., Lina, J. M., Abdallah, C., Pellegrino, G., Arcara, G., Khajehpour, H., Afnan, J., Cai, Z., Lina, J. M., Abdallah, C., Pellegrino, G., Arcara, G., Khajehpour, H., Frauscher, B., Gotman, J., & Grova, C. (in press). Validating MEG estimated resting state connectome with intracranial EEG. *Network Neuroscience*.

Study 4: Validating MEG source imaging of oscillations and connectivity using simultaneous MEG-intracranial EEG

Using simultaneous recordings of MEG and intracerebral EEG data in five patients with epilepsy, we validated resting-state power and connectivity patterns at the single-subject level. To do so, we benefitted from challenging simultaneous MEG/intracerebral EEG data recorded by our collaborators at Aix-Marseille University (France, under the direction of Dr. Christian-G. Bénar). By applying the original quantification methods proposed in Studies 1 and 3 to individual subject recordings, we demonstrated that our main group-level findings from these studies are also applicable at the individual level. In our assessment of connectivity metrics, we found that amplitude-based metrics were more accurate for estimating the MEG connectome compared to phase-based metrics, particularly when these metrics were corrected to remove zero-lag connectivity to address the issue of source leakage.

Afnan, J; Fratello, M.; Bonini, F.; Medina, S.; Cai, Z.; Badier, J.M.; Bartolomei, F.; Gotman, J.; Benar, C.; Grova, C., “Validating MEG source imaging of oscillations and connectivity patterns using simultaneous MEG-intracranial EEG” in preparation.

Contribution of authors

All the work presented in this thesis was authored by myself, in collaboration with my supervisors **Christophe Grova, PhD** and **Jean Gotman, PhD**. We together designed the studies, developed and performed the analyses, interpreted the results and wrote the manuscripts. This thesis consists in four studies as follows. The contributions of each co-author other than myself and my supervisors are summarized below.

Study 1: Validating MEG source imaging of resting state oscillatory patterns with an intracranial EEG atlas.

Authors: Jawata Afnan, Nicolás von Ellenrieder, Jean-Marc Lina, Giovanni Pellegrino, Giorgio Arcara, Zhengchen Cai, Tanguy Hedrich, Chifaou Abdallah, Hassan Khajehpour, Birgit Frauscher, Jean Gotman, Christophe Grova (Published in *NeuroImage*, 274,p.120158.

<https://doi.org/10.1016/j.neuroimage.2023.120158>)

- Dr. Nicolás von Ellenrieder was involved with the design of the study, assisted with intracranial EEG data processing, the interpretation of the results and writing and reviewing the manuscript.
- Dr. Jean-Marc Lina assisted with the adaptation and implementation of resting state wMEM, the interpretation of the results and writing and reviewing the manuscript.
- Dr. Giovanni Pellegrino was involved in the MEG data acquisition, data curation, revision of manuscript
- Dr. Giorgio Arcara was involved in the MEG data acquisition, data curation, revision of manuscript
- Dr. Zhengchen Cai assisted with the design of the analysis and revised the manuscript
- Dr. Tanguy Hedrich assisted with MEG data processing and revised the manuscript
- Dr. Chifaou Abdallah assisted with MEG data preprocessing (sleep scoring), the interpretation of the data, and revised the manuscript.
- Dr. Hassan Khajehpour was involved in the interpretation of the results and revision of the manuscript.
- Dr. Birgit Frauscher provided useful advice in the design of the study. She also revised the manuscript.

Study 2: EEG/MEG source imaging of deep brain activity within the Maximum Entropy on the Mean framework: simulations and validation in epilepsy.

Jawata Afnan, Zhengchen Cai, Jean-Marc Lina, Chifaou Abdallah, Edouard Delaire, Tamir Avigdor, Victoria Ros, Tanguy Hedrich, Nicolas von Ellenrieder, Eliane Kobayashi, Birgit Frauscher, Jean Gotman, and Christophe Grova (Published in *Human Brain Mapping* (2024) Jul 15;45(10):e26720. doi: <https://doi.org/10.1002/hbm.26720>)

- Dr. Zhengchen Cai assisted with the adaptation and implementation of depth weighted MEM, the interpretation of the results and writing and reviewing the manuscript.
- Dr. Jean-Marc Lina assisted with the development and implementation of depth weighted MEM, the interpretation of the results and writing and reviewing the manuscript.
- Dr. Chifaou Abdallah visually identified the EEG and MEG interictal spikes, assisted with the delineation of the gold standard irritative zone from clinical data, interpretation of the data and helped in the recollection of the patients' history, and revised the manuscript.
- Edouard Delaire worked on the implementation of depth weighted MEM from the standalone version to the Open-source platform (Brainstorm).
- Tamir Avigdor assisted with high density EEG data processing and coregistration.
- Dr. Victoria Ros helped in gathering clinical data and information, delineation of the gold standard irritative zone from clinical data, contributed to the interpretation of the results and revision of the manuscript.
- Dr. Tanguy Hedrich assisted with MEG and EEG simulations and revision of the manuscript
- Dr. Nicolas von Ellenrieder was involved in the interpretation of the results and revision of the manuscript.
- Dr. Eliane Kobayashi helped gathering clinical data and information on MEG, and revision of manuscript
- Dr. Birgit Frauscher helped gathering clinical data and information on high density EEG, interpretation of the data and revision of manuscript.

Study 3: Validating MEG estimated resting state connectome with intracranial EEG

Jawata Afnan, Zhengchen Cai, Jean-Marc Lina, Chifaou Abdallah, Giovanni Pellegrino, Giorgio Arcara, Hassan Khajehpour, Birgit Frauscher, Jean Gotman, and Christophe Grova (in press, *Network Neuroscience*).

- Dr. Zhengchen Cai assisted with the design and analysis, interpretation and reviewing the manuscript.
- Dr. Jean-Marc Lina was involved in data analysis, interpretation and revision of the manuscript
- Dr. Chifaou Abdallah was involved in the interpretation of the results and revision of the manuscript.
- Dr. Giovanni Pellegrino was involved in the MEG data acquisition, data curation, revision of manuscript
- Dr. Giorgio Arcara was involved in the MEG data acquisition, data curation, revision of manuscript
- Dr. Hassan Khajehpour assisted with data analysis, and revision of the manuscript
- Dr. Birgit Frauscher was involved in the interpretation of the results and revision of the manuscript.

Study 4: Validating MEG source imaging of oscillations and connectivity using simultaneous MEG-intracranial EEG

Maria Fratello (co-first author), Francesca Bonini, Samuel Medina Villalon, Zhengchen Cai, Jean-Michel Badier, Fabrice Bartolomei, Jean Gotman, Christian-G Bénar, Christophe Grova

Manuscript in preparation.

- Maria Fratello (co-first author) assisted with intracerebral EEG data processing, processing of MRI for coregistration, and localization of intracerebral EEG channels.
- Dr. Francesca Bonini visually identified MEG resting state oscillations and assisted with interpretation of results.
- Samuel Medina Villalon was involved with intracerebral EEG data processing, processing of MRI for coregistration, and localization of intracerebral EEG channels.
- Dr. Zhengchen Cai assisted with data analysis and preparation of the manuscript.

- Dr. Jean-Michel Badier assisted with the simultaneous MEG and intracerebral EEG data acquisition and processing, the design of the study and analysis, the interpretation of the results and the preparation of the manuscript.
- Dr. Fabrice Bartolomei assisted with patient recruitment, the design of the study and analysis, the interpretation of the results, and the preparation of the manuscript.
- Dr. Christian-G Bénar assisted with the simultaneous MEG and intracerebral EEG data acquisition and processing, with the design of the study and analysis, the interpretation of the results, and the preparation of the manuscript.

List of Figures

- Figure 2-1 : Framework for classification of the epilepsies. *Denotes onset of seizure. Reprinted from ILAE classification of the epilepsies: Position paper of the ILAE Commission for Classification and Terminology by Scheffer et al. (2017).8
- Figure 2-2 ILAE 2017 classification of seizure types. Reprinted from Operational classification of seizure types by the International League Against Epilepsy: Position Paper of the ILAE Commission for Classification and Terminology by Fisher et al. (2017) Reprinted with permission from John Wiley and Sons.9
- Figure 2-3 Criteria of interictal epileptiform discharges according to the International Federation of Clinical Neurophysiology, as described in Kane et al. (2017) and illustrated by Kural et al. (2020). Reprinted from Criteria for defining interictal epileptiform discharges in EEG: A clinical validation study by Kural et al. (2020). Reprinted with permission from Wolters Kluwer Health, Inc..... 14
- Figure 3-1 The first recorded EEG in human brain by Berger from his young son (top) in 1925. The bottom line is a 10 Hz sine wave used as a time marker (Brazier 1961) <https://psycnet.apa.org/record/1962-05971-000>. 16
- Figure 3-2 MEG recording by Cohen 1972 using SQUID sensors. Simultaneous EEG and MEG traces of alpha activity from normal human brain during eyes open and eyes closed conditions. The magnetometer was located at the left occipital region, as were the bipolar set of EEG leads. Figure reprinted from Magnetoencephalography: Detection of the Brain's Electrical Activity with a Superconducting Magnetometer by Cohen (1972). Reprinted with permission from the American Association for the Advancement of Science. 17
- Figure 3-3 (A) The major divisions of the brain (medial view). (B) Simplified drawing of the cerebral cortex of human brain consisting of four lobes: frontal, parietal, temporal, and occipital. Figures are reprinted from Principles of Neural Science (Fifth Edition) edited by Eric R. Kandel (Kandel et al., 2021). Reprinted with permission from the University of Chicago.Press. 19
- Figure 3-4 Left: Excitatory postsynaptic potentials (EPSPs) are generated at the apical dendritic tree of a cortical pyramidal cell and trigger the generation of a current that flows through the volume conductor from the non-excited membrane of the soma and basal dendrites to the apical dendritic tree sustaining the EPSPs. Some of the current takes the shortest route between the source and the sink by travelling within the dendritic trunk (primary current in blue), while conservation of electric charges imposes that the current loop be closed with extracellular currents flowing through the volume conductor, including distant parts (secondary currents in red). Right: Large cortical pyramidal nerve cells are organized in macro-assemblies with their dendrites normally oriented to the local cortical surface. This spatial arrangement and the simultaneous activation of a large population of these cells contribute to the spatio-temporal superposition of the elemental activity of every cell,

resulting in a current flow that generates detectable EEG and MEG signals. Figure retrieved from <i>Electromagnetic brain mapping</i> by Baillet et al. (2001) © 2001 IEEE.	21
Figure 3-5 When considering a spherical head geometry, MEG is only sensitive to tangential current dipoles for which the magnetic fields (in blue) extend outside the head, those dipoles are mainly located along the sulci of the cortical surface. For purely radial sources, mainly located on the gyri, the magnetic field does not extend beyond the head and is invisible to MEG sensors. For EEG, both radial and tangential dipoles will generate electric fields (in red) and measurable electrical potentials, whereas EEG will be more sensitive to dipolar current sources located along the gyri, since they will be closer to the sensors, when compared to tangential sources along the sulci.....	23
Figure 3-6 (top) The electrode layout of the 10-20 system (left) and corresponding brain regions (right). (Bottom) EEG layout with 10-10 system (Figure from https://info.tmsi.com/blog/the-10-20-system-for-eeeg). A = Ear lobe, C = central, P = parietal, F = frontal, O = occipital, Fp = frontal polar, FT = frontal temporal, AF - intermediate between Fp and F, FT - between F and T, TP - between T and P, CP - between C and P, PO - between P and O.....	24
Figure 3-7 Schematics of MEG instrumentation. A single-channel axial gradiometer and associated SQUID inside a dewar filled with liquid helium. The bottom depicts the sensor array of a 306-channel MEG helmet. Illustration taken from IFCN-endorsed practical guidelines for clinical magnetoencephalography (MEG) by Hari et al. (2018).	25
Figure 3-8 Common pick-up coil geometries. (A) magnetometer, (B) planar gradiometer, (C) axial gradiometer. Modified from <i>Magnetoencephalography---theory, instrumentation, and applications to noninvasive studies of the working human brain</i> Hämäläinen et al. (1993). Reprinted with permission from the American Physical Society.	26
Figure 3-9 Schematic representation of the whole head coverage with 275 MEG sensors in a CTF system. Each sensor is named with 5 digits and the first is M for MEG. The small figure on the upper right corner shows the second and the third characters and the bigger figure shows the last three digits of the sensor name. Taken from Brainstorm tutorial:	27
Figure 3-10 Key parts of estimating the neuronal sources from EEG/MEG measurement. The inverse problem attempts to locate the sources from recorded measurements, whereas the forward problem assumes a source definition to calculate a potential distribution map. Illustration taken from <i>EEG/MEG Source Imaging: Methods, Challenges, and Open Issues</i> by Wendel et al. (2009), https://doi.org/10.1155/2009/656092	28
Figure 3-11 In the dipole fitting approach, a dipole is modeled to represent a patch of activated cortex. From Scherg (1984).....	35
Figure 3-12 (a) MEM uses a reference distribution v and solves the inverse problem by maximizing the relative entropy (minimizing the Kullback-Leibler divergence) between the source distribution and the reference distribution under the constraint of explaining the data. (b) Definition of the reference distribution: the brain activity is considered to be organized into K cortical parcels. Each cortical parcel k is then characterized by an activation hidden state variable S_k , describing if the parcel is active or not. Figure reprinted from Concordance	

between distributed EEG source localization and simultaneous EEG-fMRI studies of epileptic spikes Grova et al. (2008). Reprinted with permission from Elsevier.	42
Figure 3-13 Schematic view of different source configurations and their reflection on MEG. (a) Only deep sources are active (hippocampus and amygdala). As activation is of a “closed field” type, no visible signal is recorded from the surface. (b) Activity from hippocampus propagates to nearby neocortex, which has a structured source geometry (open field) and can be seen as a signal at the surface (small because of the depth). (c) Only subparts of hippocampus and amygdala are active, producing an open field and small signal at the surface. (d) The activity from deep structures is overshadowed by activity from the superficial neocortex that has a higher amplitude because of shorter distance to the sensors. Illustration taken from Detection and localization of deep sources in magnetoencephalography: A review Benar et al. (2021). Reprinted with permission from Elsevier.	48
Figure 4-1 Group average of relative power maps for all frequency bands (delta (2–4 Hz), theta (4–8 Hz), alpha (8–12 Hz), beta (15–30 Hz), gamma1 (30–80 Hz), and gamma2 (80–150 Hz)). (A) Top View. (B) Left view. Values range between 0 and 1, indicating the power of cortical signals relatively to the total signal power across the frequency spectrum. Illustration taken from Brainstorm Pipeline Analysis of Resting-State Data From the Open MEG Archive by Niso et al. (2019).	55
Figure 4-2 Brain map of natural frequencies during resting state MEG. Distribution of natural oscillations at the single-voxel level exhibiting both a medial-to-lateral and a posterior-to-anterior gradient of increasing frequency. Canonical frequency band ranges are color-coded to facilitate interpretation. Illustration taken from The natural frequencies of the resting human brain: An MEG-based atlas by Capilla et al. (2022).	56
Figure 4-3 Histogram of all detected spectral peaks (across ROIs and participants) delineates the classical frequency bands used in the EEG and MEG literature (theta 3.5–7.5 Hz, alpha 8.5–13 Hz, low-beta 15–25 Hz and high-beta 27.5–34). Illustration taken from The frequency gradient of human resting-state brain oscillations follows cortical hierarchies by Mahjoory et al. (2020).	57
Figure 4-4 Histogram of Spectral Power Density peaks of whitened data found across all electrodes and participants. Note that Hertz is scaled logarithmically (applied whitening to dampen the 1/f effect). Illustration taken from Dominant frequencies of resting human brain activity as measured by the electrocorticogram by Groppe et al. (2013). Reprinted with permission from Elsevier.	58
Figure 4-5 Periodic and aperiodic components of the spectra in log-log space shown for an (A) Example of a linear 1/f trend and (B) 1/f with a bend called knee. The periodic component is described with a peak frequency, power of the peak over the aperiodic component and the bandwidth, or the width of the peak. The aperiodic component is characterized by the offset, (overall up/down translation of the whole spectrum), the exponent, and the knee.	
Figure from https://fooof-tools.github.io/fooof/auto_tutorials/plot_01-	

ModelDescription.html#sphx-glr-auto-tutorials-plot-01-modeldescription-py (Donoghue et al., 2020), <https://doi.org/10.1038/s41593-020-00744-x>. 59

Figure 4-6: The presence of an intrinsic whole-brain connectivity organization in electrophysiological data. A) Sensory and motor ICNs as observed with seed-based connectivity in source-space MEG amplitude coupling. The spectral plot (right) indicates a strong contribution from alpha and beta band oscillations to these intrinsic networks (adapted from Hipp et al., 2012). B) Temporal ICA of band-specific oscillation amplitudes in MEG yields numerous ICNs (four are shown as examples), including sensory/motor as well as higher-order networks. Alpha and especially beta bands captured ICN organization well. A direct comparison between the MEG-derived (bottom row) and the fMRI-derived (top-row) independent component maps demonstrates high spatial similarity (adapted from Brookes et al., 2011). C) Connection-wise connectivity strength is spatially associated between fMRI and intracranial electrophysiology (ECoG amplitude coupling, pooled over patients). The strength of this correlation is around ~ 0.35 for all frequency bands (adapted from Betzel et al., 2019). D) A similar spatial association of connection-wise connectivity strength is observed between fMRI and concurrently recorded scalp EEG (phase coupling). The left scatterplot shows an example for the beta band, where each data point is from one connection (region pair) of the connectome averaged across subjects (adapted from Wirsich et al., 2017). This relationship is reproducible at similar effect size across various MRI field strengths (1.5–7T) and EEG densities (64–256 channels) (adapted from Wirsich et al., 2021). Illustration taken from Connectomics of human electrophysiology by Sadaghiani et al. (2022), <https://doi.org/10.1016/j.neuroimage.2021.118788>. 71

Figure 4-7 Schematic overview showing the process by which connectivity is calculated in electrophysiological data. Figure taken from Connectomics of human electrophysiology by Sadaghiani et al. (2022), <https://doi.org/10.1016/j.neuroimage.2021.118788>. 73

Figure 5-1 Schematic of electrocorticography (ECoG) and stereotaxic EEG (SEEG) adapted from Miller and Fine (2022). (A) Grids of brain surface ECoG electrodes are placed through large openings in the skull (craniotomies), and SEEG electrodes are placed through bolts embedded in the skull. (B) ECoG electrodes sample the exposed brain surface covering the targeted neocortical regions. (C) SEEG electrodes are implanted irregularly and sparsely, although they can be targeted precisely. (D) SEEG can precisely sample surface/deep grey matter and subcortical structures. Figure reprinted from Decision-making in stereotactic epilepsy surgery by Miller and Fine (2022). Reprinted with permission from John Wiley and Sons. 78

Figure 5-2. Use of depth electrodes as ground truth for validating EEG and ECoG source localization for superficial and deep sources. Deep and superficial sources are at locations (1) and (2), respectively. The color bars indicate the measurement strength of the source activity when measured at the origin of the source (maximum strength) and with ECoG or EEG electrodes. Light blue and dark blue represent the measured strength for deep and superficial sources, respectively. The measurements of deep and superficial sources are attenuated at subdural and scalp levels but to a different extent. From a perspective of the scalp (EEG),

attenuation is likely so strong that the SNR for deep and superficial sources do not differ as much as they do from a subdural perspective (ECoG). Taken from Localization of deep brain activity with scalp and subdural EEG by Hnazaee et al. (2020), https://doi.org/10.1016/j.neuroimage.2020.117344	80
Figure 5-3 (A) Simultaneous high density-EEG and SEEG (adapted from ((De Stefano et al., 2022), (Mikulan et al., 2020))). (B) Simultaneous MEG and SEEG (adapted from (Velmurugan et al., 2022))) (Figure from Simultaneous invasive and non-invasive recordings in humans: A novel Rosetta stone for deciphering brain activity by Pigorini et al. (2024)).	81
Figure 5-4 Comparison of the depth electrode holding screws for the two patients. Reconstructions were obtained from post-implantation CT scans. (a) Rear view of the reconstruction for the patient 1 (with long screws). (b) and (c) Reconstruction for short screws on profile and rear view respectively for patient 2. Figure from Technical solutions for simultaneous MEG and SEEG recordings: towards routine clinical use Badier et al. (2017). Reprinted with permission from IOP Publishing.	82
Figure 5-5 Experimental setup within the shielded room of the MEG. (A) Depth electrode connectors. (B) Cable extensions. (C) Head boxes. (D) Battery operated amplifiers. (E) Optical fiber for the transmission of the data outside the shielded room. Figure from Technical solutions for simultaneous MEG and SEEG recordings: towards routine clinical use Badier et al. (2017). Reprinted with permission from IOP Publishing.....	83
Figure 5-6 (i) Virtual sensors (VS) reconstructed at brain locations that matched the iEEG implantation. (ii) For each virtual sensor, computation of its mean source activation across time acquired from data recorded by the High Density-EEG (HD-EEG) and MEG sensors to reconstruct virtual sensor time series for HD-EEG (HD-EEG-VSs) and MEG (MEG-VSs), respectively. Figure retrieved from Non-invasive mapping of epileptogenic networks predicts surgical outcome by Corona et al. (2023). Reprinted with permission from Oxford University Press.....	85
Figure 5-7 The virtual iEEG potential estimated from MEG using cMEM source localization (left) shows good correspondence with recorded iEEG potentials (right) for a patient exhibiting right orbito-frontal spikes. Figure reprinted from Intracranial EEG potentials estimated from MEG sources: A new approach to correlate MEG and iEEG data in epilepsy by Grova et al. (2016). Reprinted with permission from John Wiley and Sons.	86
Figure 5-8 Localization of the 1785 EEG channels with normal physiological activity analyzed for this study. The 1520 channels from stereo-EEG electrodes are visualized in blue, and the 265 channels from cortical grids and strips are in yellow. Note that for the ‘inflated’ brain display at the bottom, the electrodes are projected on the cortical surface. Figure from Atlas of the normal intracranial electroencephalogram: neurophysiological awake activity in different cortical areas by Frauscher et al. (2018). Reprinted with permission from Oxford University Press.	88
Figure 6-1 : Analysis pipeline to compare the spectral properties estimated by MEG with the MNI iEEG atlas, as ground truth. Ground truth MNI iEEG atlas (Frauscher et al., 2018) consists of	

2300 channels collected from 110 subjects with epilepsy, retaining only the healthy brain regions. For each iEEG channel, 60 seconds of resting state data during wakefulness were used. MEG pipeline: MEG data were collected from 45 healthy participants, each having 60 seconds of resting state data during wakefulness (only 10 seconds of data are shown in this figure). We applied wavelet-MEM (wMEM) to solve the MEG inverse problem. For each source map, we estimated virtual iEEG (ViEEG) data at each position of 2300 channels (positions obtained from the MNI iEEG atlas). We compared the spectral characteristics (spectra and oscillatory peaks) between iEEG and ViEEG for 38 ROIs (MICCAI atlas). To consider only the oscillatory components, the aperiodic components were removed from the spectra using the FOOOF toolbox (Donoghue et al., 2020)..... 95

Figure 6-2: Group average of relative PSD values across each frequency band and over all the available channels in each ROI of the iEEG atlas, the ground truth, the MEG-estimated ViEEG using wavelet-MEM (wMEM) method. The number of channels in each ROI (N_{ROI}) in iEEG varies. For each ROI, ViEEG was estimated for $45 \times N_{ROI}$ channels, where the total number of subjects is 45. The relative PSD for each channel is calculated as the ratio of the power of the signal in each frequency bin relative to the total power of the signal. Relative PSD value for a channel range between 0 and 1. The color bar ranges from minimum to maximum value among iEEG and ViEEG in each frequency band, such that the scale is the same for both modalities in a given band. The corresponding t_{map} is shown in (B). We showed with color the ROIs which were statistically different (Welch's unequal variances t-test, $p < 0.05$, Bonferroni corrected for 38 ROIs and 5 frequency bands, positive t corresponding to larger PSD in iEEG when compared to ViEEG). 105

Figure 6-3: Decomposition of spectra into periodic and aperiodic components shown in a few example ROIs for iEEG and ViEEG. For both iEEG and ViEEG, the top panel shows the relative PSD before and after removing the aperiodic component and the bottom panel shows the probability histogram of identified peaks in δ (0.5-4Hz), θ (4-8Hz), α (8-13Hz), β (13-30Hz) and γ (30-80Hz). The aperiodic fits and oscillatory peaks are identified using the FOOOF toolbox (Donoghue et al., 2020)..... 106

Figure 6-4: Comparison of periodic components of MEG-estimated spectra with ground truth iEEG, with aperiodic components (A) and without aperiodic components (B) shown for a few selected ROIs. For each spectrum, we are reporting the median value (black, blue and orange straight lines) together with corresponding standard deviation (shaded area) over all channels. Average overlaps between ViEEG and iEEG spectra across each spectral band are shown in (C). The value of overlap is calculated at each frequency bin and ranges from 0 to 1. For a ROI, if the median of PSD_{ViEEG} perfectly coincides with the median of PSD_{iEEG} at all frequency bins within a specific frequency band, the average overlap is 1. In A and B frequency bins are marked as red dots when iEEG and ViEEG are statistically different (Mann Whitney U Test, $p < 0.05$, Bonferroni corrected for 38 ROIs and 160 frequency bins). ... 108

- Figure 6-5: Average overlap between ViEEG and iEEG spectra across each spectral band for each of the 38 ROIs, (A) with and (B) without aperiodic components. The value of overlap is calculated at each frequency bin and ranges from 0 to 1. For a ROI, if the median of PSD_{ViEEG} perfectly coincides with the median of PSD_{iEEG} at all frequency bins within a specific frequency band, the average overlap is 1. 110
- Figure 6-6: (A) Probability histogram of all identified peaks in all ROIs for iEEG and ViEEG using the FOOOF toolbox. (B) Probability histogram for all identified peaks in hippocampus for iEEG and ViEEG for one subject. We also show the percentage difference of the number of channels exhibiting spectral peaks in ViEEG compared to iEEG in each spectral band, as a proportion of the total number of channels in the ROI. The value of ***Peak_estimatedSUBi*** ranges from -100% to 100%. The peaks are well estimated by ViEEG in comparison with iEEG, for a specific frequency band, if ***Peak_estimatedSUBi*** is close to zero. 111
- Figure 6-7: Median values of ***Peak_estimatedSUBi*** over 45 subjects are plotted for 38 ROIs. ***Peak_estimatedSUBi*** measures the percentage difference of the number of channels exhibiting spectral peaks in ViEEG compared to iEEG, as a proportion of the total number of channels in each ROI, for each spectral band and ROI, calculated for each subject i . The value of the median ***Peak_estimatedSUBi*** over all subjects ranged from -100% to 100%. Median (***Peak_estimatedSUBi***) = +100% indicates that all the channels from ViEEG in a ROI (N_{ROI}) showed a peak in that frequency band, whereas no peak was identified in any of the iEEG channels in that ROI. We called it a 100% overestimation of oscillatory peaks by MEG-estimated ViEEG in this ROI. On the contrary, a -100% estimation is obtained when all the iEEG channels in a ROI exhibit peaks, but no peak was identified in ViEEG in that ROI, resulting in a 100% underestimation. The peaks were better estimated by ViEEG for the ROIs if the median (***Peak_estimatedSUBi***) was close to zero. The values in the color bar are ranging from underestimation (-100%, negative values, cooler color) to overestimation (+100%, positive values, warmer color) of channels exhibiting peak by MEG-estimated ViEEG. 112
- Figure 6-8: Average amplitude across the channels in each ROI, normalized by the average amplitude across all ROIs. The bar plot shows the absolute difference of normalized amplitude between iEEG and ViEEG. The right panel shows the difference of normalized amplitude between iEEG and ViEEG on the inflated cortical surface (lateral and medial views) (top) and the corresponding t_{map} (bottom). For t_{map} , we showed the ROIs which were statistically different (Welch's unequal variances t-test, $p < 0.05$, Bonferroni corrected for 38 ROIs, positive t corresponding to larger amplitude in iEEG when compared to ViEEG). 113
- Figure 7-1 Analysis pipeline to evaluate depth-weighted cMEM compared to standard cMEM and depth-weighted MNE using MEG and HD-EEG simulations of epileptic discharges, as well as actual interictal epileptic discharges from MEG and HD-EEG in patients with focal epilepsy..... 128

Figure 7-2: (A) AUC, (B) SD, and (C) D_{\min} for three source imaging methods are shown on the cortical surface at the locations of 300 simulated sources in MEG. The average eccentricity values for those 300 generators are shown in (D). Each parcel is one simulated source with the color representing the metric value associated with it. Regions where no sources were generated are shown as grey. When there was overlap between sources, a line was superimposed on the new color to illustrate the overlap from the previous source. Increases in AUC and decreases in SD and D_{\min} by $cMEM_{\omega}$ were observed mostly for the medial regions, whereas $cMEM_{\omega}$ and $cMEM$ presented similar performances for superficial sources. Brain maps are shown for 6 views: right lateral, left lateral, right medial, left medial, hippocampi top and hippocampi bottom. 138

Figure 7-3: The differences in AUC, SD, and D_{\min} between $cMEM_{\omega}$ and $cMEM$ ($cMEM_{\omega} - cMEM$) are shown on the cortical surface at the locations of 300 simulated sources in MEG. Increases in AUC and decreases in SD and D_{\min} (warmer color) were observed mostly for the deeper regions. Regions where no sources were generated are shown as grey. When there was overlap between sources, a line was superimposed on the new color to illustrate the overlap from the previous source. Brain maps are shown for 6 views: right lateral, left lateral, right medial, left medial, hippocampi top and hippocampi bottom. 139

Figure 7-4: For 300 MEG simulations at $SE=3$ and $SNR=2$, the plot of AUC (A1), SD (A2), and D_{\min} (A3) as a function of eccentricity for $cMEM$, $cMEM_{\omega}$ and MNE_{ω} . The comparison of the three methods is summarized for AUC (B1), SD (B2), and D_{\min} (B3) for 99 (out of 300) sources with an eccentricity of less than 60 mm. On each boxplot, the central mark indicates the median, and the bottom and top edges of the box indicate the 25th and 75th percentiles, respectively. If the groups are statistically different after post-hoc analysis, the significance levels are shown as: '***' for $p < 0.001$, '**' for $p < 0.01$, and '*' for $p < 0.05$ 140

Figure 7-5: Example of two simulated generators first in the hippocampus (A) and then in the lateral neocortex after 15 ms delay (B). Three source imaging methods were applied to the averaged interictal epileptic discharges. The surface of the hippocampus is included in the source model (and presented in the figure as separate structures). The metrics AUC, SD, and D_{\min} were calculated at 358 ms (peak of the source in the hippocampus) and at 373 ms (peak of the neocortical source). The scale is different for the 3 methods but source maps have been interpreted relatively for each method. 142

Figure 7-6: Source imaging for 100 simulations of mixed generators in the hippocampus and the ipsilateral neocortex after 15 ms delay. AUC, SD and D_{\min} are calculated separately for each generator at the peak of the spike (358 ms for hippocampal generator and 373 ms for neocortical generator). On each boxplot, the central mark indicates the median, and the bottom and top edges of the box indicate the 25th and 75th percentiles, respectively. If the groups are statistically different after post-hoc analysis, the significance levels are shown as: '***' for $p < 0.001$, '**' for $p < 0.01$, and '*' for $p < 0.05$ 144

Figure 7-7: The differences in AUC, SD, and D_{\min} between $cMEM_{\omega}$ and $cMEM$ ($cMEM_{\omega} - cMEM$) are shown on the cortical surface at the locations of 300 simulated sources in HD-EEG.

Increases in AUC and decreases in SD and D_{\min} (presented warmer color) were observed mostly for the deeper regions. Regions where no sources were generated are shown as grey. When there was overlap between sources, a line was superimposed on the new color to illustrate the overlap from the previous source. Brain maps are shown for 6 views: right lateral, left lateral, right medial, left medial, hippocampi top and hippocampi bottom..... 145

Figure 7-8: For 300 HD-EEG simulations at $SE=3$ and $SNR=2$, the plot of AUC (A1), SD (A2), and D_{\min} (A3) as a function of eccentricity for three source imaging methods. The comparison of the three methods is summarized for AUC (B1), SD (B2), and D_{\min} (B3) for 56 (out of 300) deep sources with an eccentricity less than 45 mm. For each boxplot, the central mark indicates the median, and the bottom and top edges of the box indicate the 25th and 75th percentiles, respectively. If the groups are statistically different after posthoc analysis, the significance levels are shown as: ‘****’ for $p < 0.001$, ‘**’ for $p < 0.01$, and ‘*’ for $p < 0.05$ 146

Figure 7-9: (A) Example of a MEG patient with mesial temporal lobe epilepsy. The source imaging methods were applied to the average of 16 selected interictal epileptic discharges. The surface of the hippocampus is included in the source model (shown as separate structures). The metrics AUC, SD, and D_{\min} were calculated at the midpoint of the rising phase of the spike (-10ms). The scale is different for the 3 methods, but source maps are interpreted relatively for each method. (B) Comparison of the MEG source imaging methods in terms of the validation metrics AUC, SD and D_{\min} for 8 patients with mesial temporal lobe epilepsy. Each boxplot represents metrics from one source imaging method. On each boxplot, the central mark indicates the median, and the bottom and top edges of the box indicate the 25th and 75th percentiles, respectively. If the groups are statistically different after post-hoc analysis, the significance levels are shown as: ‘****’ for $p < 0.001$, ‘**’ for $p < 0.01$, and ‘*’ for $p < 0.05$ 148

Figure 7-10: (A) Example localization of HD-EEG source imaging methods for a patient with mesial temporal lobe epilepsy. The source imaging methods were applied to an average of 28 interictal epileptic discharges. The surface of the hippocampus is included in the source model (shown as separate structures). The metrics AUC, SD, and D_{\min} were calculated at the midpoint of the rising phase of the spike (-10ms). The scale is different for the 3 methods but source maps are interpreted in a relative manner for each method. (B) Comparison of the EEG source imaging methods in terms of the validation metrics AUC, SD and D_{\min} for 9 patients with mesial temporal lobe epilepsy. Each boxplot represents metrics from one source imaging method. On each boxplot, the central mark indicates the median, and the bottom and top edges of the box indicate the 25th and 75th percentiles, respectively. If the groups are statistically different after posthoc analysis, the significance levels are shown as: ‘****’ for $p < 0.001$, ‘**’ for $p < 0.01$, and ‘*’ for $p < 0.05$ 151

Figure 8-1: The iEEG connectome consists of connectivity metrics between pairs of channels, obtained from a total of 110 patients. In each of 45 MEG connectomes, all connections originated from a single subject. To generate a new MEG connectome comparable to the

original iEEG connectome, MEG subjects were randomly chosen to contribute connections between ROIs while preserving spatial information. This process was repeated for all ROI pairs, resulting in a bootstrap resampled MEG connectome, mimicking the same subjects group distribution as our original iEEG connectome. The spatial Pearson correlation between the original iEEG connectome and the bootstrap resampled MEG connectome was computed.

This overall process was iterated 5000 times, yielding 5000 correlation values..... 168

Figure 8-2: Connectivity averaged across frequency bands estimated by MEG and iEEG calculated using (A) **AEC**, (B) **OAEC**, (C) **PLV**, and (D) **wPLI** *. For iEEG, we considered all 1278 iEEG ROI pairs available from all patients of the iEEG atlas and showed the averaged connectivity across six frequency bands. For MEG we considered 1278 virtual iEEG ROI pairs from each of the 45 subjects and showed the averaged connectivity across 45 subjects and six frequency bands. The median value of each distribution is displayed. 172

Figure 8-3: (A) Distribution of cross-modal correlations as well as the null distribution (red) between MEG and iEEG for six frequency bands calculated for AEC (blue) and OAEC (green). (B) The medians of the distribution of cross-modal correlations are shown in the bar plot. The correlation was considered significant if its overlap with the null range was less than 2.5% (equivalent to a 5% two-tailed threshold, with 2.5% in each tail). The frequency bands that showed significantly higher correlations than the null distribution are marked with an asterisk (*). 174

Figure 8-4: The median of the distribution of cross-modal correlations is depicted, considering all connections, intra-hemispheric connections, and inter-hemispheric connections for (A) AEC and (B) OAEC. The correlation was considered significant if its overlap with the null range was less than 2.5% (equivalent to a 5% two-tailed threshold, with 2.5% in each tail). Frequency bands with significantly higher correlations than the null distribution are marked with an asterisk (*). 174

Figure 8-5: Distribution of cross-modal correlations as well as the null distribution (red) between MEG and iEEG for six frequency bands calculated for **PLV** (blue) and **wPLI** * (green) (A). The medians of the distribution of cross-modal correlations were shown as a bar plot (B). The correlation was considered significant if its overlap with the null range was less than 2.5% (equivalent to a 5% two-tailed threshold, with 2.5% in each tail). The frequency bands that showed significantly higher correlations than the null distribution were marked with an asterisk (*). 176

Figure 8-6: (A) Eccentricity of iEEG channels shown on the brain cortex with 80% transparency to ensure all deep iEEG channels are visible. (B) Distribution of the distances between ROI pairs for all pairs exhibiting either an eccentricity > 85 mm (top) or < 85 mm (bottom). The cross-modal correlation between MEG and iEEG for two groups (both eccentricity values > 85 mm in blue and both eccentricity values < 85 mm in red) for **AEC** (C), **OAEC** (D), **PLV** (E), and **wPLI** * (F). The correlation was considered significant if its overlap with the null range was less than 2.5% (equivalent to a 5% two-tailed threshold, with 2.5% in each tail).

The frequency bands that showed significantly higher correlations than the null distribution were shown with a *	178
Figure 8-7: (A) AEC and OAEC as a function of distance between two ROIs plotted for iEEG and MEG in the beta band. (B) The distribution of differences between OAEC and AEC (OAEC minus AEC) for MEG and iEEG.	179
Figure 8-8: Distribution of cross-modal spatial correlations between MEG and iEEG connectomes in the beta band obtained using AEC and OAEC (obtained from 5000 bootstrap MEG samples), as we increase the minimum number of subjects from 1 to 5 in each ROI pair. Increasing the minimum number of subjects in each ROI pair (as shown on the left) decreases the available coverage of the iEEG connectome from 44% to 3% (as shown on the right). For example, the bottom row displays histograms of the correlations between MEG and iEEG connectomes when the iEEG connectome was created with ROI pairs that include at least 1 patient, covering 44% of the connectome.	180
Figure 9-1 Analysis pipeline to compare the spectral and connectivity patterns estimated by MEG with the simultaneously acquired SEEG, as ground truth. MEG: 60 s of resting state data during wakefulness were marked in MEG in a dominant frequency band. Using the marking from MEG, 60 s data were obtained from the simultaneously acquired SEEG, which is considered the ground truth. Virtual SEEG: The MEG source map, obtained with wMEM, was converted to virtual SEEG potentials for each SEEG channel. Comparison between virtual SEEG and SEEG: The virtual SEEG estimated from MEG were quantitatively compared with SEEG in terms of power spectral density and connectivity. For each SEEG and virtual SEEG channel, the relative power spectral density was computed and averaged across all the frequency bins within the dominant canonical frequency band. The spatial correlation between the SEEG and virtual SEEG relative power was computed. The spatial correlation between the SEEG and virtual SEEG connectomes was computed.	197
Figure 9-2 (A) Relative power spectral density averaged for all frequency bins within the frequency band of interest (Beta: 13-30Hz) for each channel of SEEG and MEG for patient #1 (two views). A threshold of 50% of the maximum activity is used for display. (B) MEG average relative power as a function of SEEG average relative power plotted for all channels in the beta band. The spatial correlation between MEG and SEEG average power was 0.54. (C) The observed spatial MEG/SEEG correlation of 0.54 is shown as a blue dot compared to the null distribution. (D) Distribution of eccentricity, which is a measure of the distance between the center of the head and the location of the SEEG channel. Low eccentricity and high eccentricity are associated with deep channels and superficial channels, respectively. (E) Using an eccentricity threshold of 60 mm, the correlations between MEG and SEEG relative power for channels > 60 mm and < 60 mm are shown. The spatial correlation between MEG and SEEG for superficial channels was higher than for deep channels.	203
Figure 9-3(A-D) For patients #2-5, (top) The spatial correlation between MEG and SEEG relative power spectral density is shown as a blue dot compared to the null distribution. (Bottom) Using an eccentricity threshold of 60 mm, the correlations between MEG and SEEG relative	

power for channels > 60 mm and channels < 60 mm are shown. For Patients #2 and #3, the analysis was done in the alpha band (8-13Hz). For Patients #4 and #5, the analysis was done in the theta band (4-8Hz). 204

Figure 9-4 (A) Connectivity between all 4560 channel pairs estimated by MEG (orange) and SEEG (green) in Patient #1 calculated using **AEC**, **OAEC**, **PLV**, and **wPLI** * in the Beta band (for a total of 96 channels in bipolar reference montage). In addition to every channel pair connectivity values (every point on the graph), the underlying distribution of connectivity values is also presenting using a boxplot representation and the median value of every distribution is indicated. (B) The spatial cross-modal correlations between MEG and SEEG for **AEC**, **OAEC**, **PLV**, and **wPLI** * in the Beta band is presented as a blue cross, whereas the connectivity null distribution estimated using surrogate data for each metric is shown in red..... 205

Figure 9-5 Spatial cross modal correlation between MEG and SEEG connectome for **AEC**, **OAEC**, **PLV**, and **wPLI** * for patients #2 to #5. For Patients #2 and #3, the analysis was done in the alpha band (8-13Hz). For Patients #4 and #5, the analysis was done in the theta band (4-8Hz). The null distribution of connectivity values estimated from surrogate data for each metric is shown in red. 206

Figure 10-1: (A) A patient with intracerebral EEG (stereotaxic EEG or SEEG) implanted in left and right hippocampus. (B) Example SEEG electrode shown that has some contacts in deep hippocampus and some contacts in the superficial regions. (C) Example of an interictal epileptic discharge in SEEG. The same IED was marked in simultaneous MEG and reconstructed using (D) standard cMEM (no depth weighting) and (E) depth weighted cMEM (cMEM_w). The MEG source maps were finally converted to SEEG space for (F) cMEM and (G) depth weighted cMEM (cMEM_w). Compared to SEEG IED in C, cMEM could not localize the spike within deep contacts but depth weighted cMEM provided more accurate localization in deep hippocampus contacts..... 223

Figure 10-2 Interictal epileptic discharge (IED) for all electrodes (color shows activity thresholded at 50% of the maximum) for (A) stereotaxic EEG or SEEG, (B) MEG estimated using cMEM and converted to the SEEG space and (C) MEG estimated using depth weighted cMEM (cMEM_w) and converted to the SEEG space. cMEM failed to localize activity in the hippocampus, whereas the depth-weighted cMEM successfully localized it, consistent with the SEEG ground truth. However, depth-weighted cMEM also produced some ghost localizations on the lateral cortex. 224

List of Tables

Table 2-1 Summary of the strengths and limitations of each modality	11
Table 3-1 Assumptions, advantages and limitations of different source imaging methods.....	49
Table 4-1 Connectivity characteristics of imaging modalities adapted from Adding dynamics to the Human Connectome Project with MEG by Larson-Prior et al. (2013). Reprinted with permission from Elsevier.	61
Table 4-2 Mathematical techniques to characterize connectivity between electrical signals derived from separate brain regions. Table from Sadaghiani et al. (2022) https://doi.org/10.1016/j.neuroimage.2021.118788	65
Table 9-1: Summary of spatial cross-modal correlations between MEG and SEEG for average relative power (correlations that were significantly higher than the null distribution are reported using bold font).....	204
Table 9-2 Summary of spatial cross-modal correlations between MEG and SEEG for connectome (correlations that were significantly larger than the null distribution are reported using bold font))	207

1 Introduction

Epilepsy is a neurological disorder that affects approximately 1% of the global population and is characterized by spontaneous seizures. Proper diagnosis and medication can prevent seizures in about 70% of those affected. However, for the remaining 30% who are drug-resistant, surgery becomes an effective treatment option (Guekht et al., 2021) if the epilepsy is focal and presurgical evaluation can identify the specific region responsible for seizure generation. In addition to seizures, patients with epilepsy also exhibit interictal epileptic discharges (IEDs), which are abnormal neuronal discharges typically originating from regions (called the irritative zone) that overlap with the seizure generators but occur without any clinical manifestation (Hauf et al., 2012).

Electroencephalography (EEG) and Magnetoencephalography (MEG) are widely used non-invasive techniques to detect IEDs and delineate the irritative zone and help define the seizure onset zone (Rosenow & Lüders, 2001). EEG and MEG record brain activity with high temporal resolution, allowing for the study of brain dynamics during abnormal events such as seizures and IEDs, as well as during the resting state, a state when the brain is not engaged in specific activity. Resting-state EEG/MEG has been extensively employed in both healthy (Brookes et al., 2011; Giraud & Poeppel, 2012; Schnitzler & Gross, 2005b) and diseased brains (Aydin et al., 2020; Hirano & Uhlhaas, 2021) to study oscillations and connectivity patterns (Sadaghiani et al., 2022).

Estimating the neuronal generators from scalp measurements recorded on EEG/MEG sensors requires solving an ill-posed inverse problem (Darvas et al., 2004), where no unique solution exists unless prior assumptions are made to guide the selection of the solution. Many source imaging methods have been developed over the years to address this challenge, yet two main limitations persist: (1) the challenge of localizing deep brain activity using EEG/MEG, which remains debated (Barkley & Baumgartner, 2003) despite evidence suggesting that deep activity can be recorded by surface sensors (Pizzo et al., 2019; Seeber et al., 2019); and (2) the difficulty of localizing and analyzing resting-state brain activity, which is often characterized by a low signal-to-noise ratio. Importantly, EEG/MEG estimated sources are susceptible to source leakage, which is defined as the influence of a source on the estimation of the generators within its neighborhood (Brookes et al., 2012; Hedrich et al., 2017). Source leakage affects the spatial accuracy of EEG/MEG estimated

sources and introduces spurious false positives in connectivity measures (Palva et al., 2018; Palva & Palva, 2012). As more studies use EEG/MEG source localization to detect deep brain activity and analyze resting-state oscillations and connectivity, it is crucial to validate the accuracy of these methods in such conditions.

The only gold standard for validating EEG/MEG source imaging is intracerebral EEG, an invasive technique used in some epilepsy patients during presurgical evaluation. Based on clinical hypotheses, intracerebral EEG electrodes are implanted directly into brain tissue, including deep structures such as the hippocampus (Jayakar et al., 2016). Unlike EEG/MEG, the acquisition of intracerebral EEG data is invasive and is only used in drug-resistant cases of epilepsy during presurgical investigation. Intracerebral EEG records brain activity with high temporal and spatial resolution as it is in close proximity to the neuronal generators, making it the best available method to validate non-invasive EEG/MEG results, but because of the invasiveness of the implantation procedure, spatial sampling remains limited to few regions of interest which are specific to the epilepsy of every patient. Ideally, simultaneous recordings of EEG/MEG and intracerebral EEG offer the best opportunity for such validation (De Stefano et al., 2022; Pigorini et al., 2024; Pizzo et al., 2019). However, this type of simultaneous acquisition is technically challenging (Badier et al., 2017; Dubarry et al., 2014) and not feasible for many research groups due to resource constraints. Several groups have developed atlases of intracranial EEG by merging data from the healthy brain regions from many patients (Bernabei et al., 2022; Frauscher et al., 2018; Taylor et al., 2022). These atlases provide a valuable resource for studying brain activity at a group level.

The main motivation of this thesis is to determine the limitations of non-invasive MEG source imaging in accurately identifying intracerebral sources and connectivity. We first aimed to validate MEG source imaging of resting-state activity at the group level in a healthy population. As ground truth, we exploited the intracranial EEG atlas of normal brain activity developed by Frauscher et al. (2018), which compiled data from 110 patients who underwent intracranial EEG implantation during presurgical evaluation, only keeping the data from the electrodes implanted in healthy brain regions. Next, we aimed to validate the group-level findings at the single-subject level using simultaneous MEG and intracerebral EEG data from patients with epilepsy, which were acquired by our collaborators at Aix-Marseille University (France, under the direction of Dr. Christian-G. Bénar). *We hypothesized that MEG source imaging could recover the spectral and connectivity*

patterns observed in intracerebral EEG more accurately in some regions than in others, and we aimed to define regions of high and low accuracy.

To solve the EEG/MEG inverse problem, we used the Maximum Entropy on the Mean (MEM) method (Amblard et al., 2004; Chowdhury et al., 2013), developed by our group. This method has been shown to recover the spatial extent of neural generators more accurately than conventional distributed source imaging techniques (Abdallah et al., 2022; Chowdhury et al., 2013; Heers et al., 2016a; Pellegrino et al., 2018; Pellegrino, Hedrich, et al., 2020). MEM has two variants: the coherent MEM (cMEM), which assumes a stable organization of the brain along parcels as prior information and is suitable for localizing event-related brain activity including spontaneous interictal epileptic discharges (IEDs) (Chowdhury et al., 2013; Heers et al., 2016a), and wavelet MEM (wMEM), designed for localizing transient oscillations (Avigdor et al., 2021; Lina et al., 2012; Pellegrino et al., 2016; von Ellenrieder et al., 2016). While MEM methods have been successful in accurately localizing superficial cortical generators (Chowdhury et al., 2015; Grova et al., 2006), their effectiveness in localizing deep brain activity has been limited. In this thesis, we propose and validate two adaptations of MEM. First, we adapted the wMEM method to enhance the localization of resting-state oscillations. Second, we introduced a depth-weighted adaptation for both cMEM and wMEM to improve the localization of deep brain activity without compromising the accuracy of superficial source localization.

This thesis is organized as follows: Chapters 2 to 5 provide the necessary background information for this thesis. In Chapter 2, we briefly introduce epilepsy and different diagnostic tools (including but not limited to EEG/MEG and intracerebral EEG) used during the presurgical investigation for patients for whom drug therapy is not effective and who are considered for brain surgery. Chapter 3 covers the history of EEG and MEG, the cellular origins of the signals detected by these modalities, and the theory associated with the challenging estimation of neuronal sources from surface measurements. It provides a brief overview of various inverse methods, highlighting their strengths and limitations, and emphasizes the importance of the validation of source imaging methods, particularly for deep source localization. In Chapter 4, we discuss the utility and challenges of EEG/MEG in studying resting state brain activity, with a focus on resting state oscillations and connectomics research. Chapter 5 provides an overview of intracerebral EEG, discussing its role as a ground truth for validating EEG/MEG source localization, the challenges

of integrating intracerebral EEG with non-invasive EEG/MEG modalities, and how normative atlases enable validation of EEG/MEG localization at a group level.

The core content of this PhD thesis is then presented in four manuscripts in Chapters 6 to 9. Chapter 6 presents our first published manuscript (Afnan et al., 2023): *Validating MEG source imaging of resting state oscillatory patterns with an intracranial EEG atlas*. We validated MEG source imaging of resting-state oscillations in a group of healthy participants with intracranial EEG of normal brain activity using the Montreal Neurological Institute (MNI) intracranial EEG atlas (Frauscher et al., 2018) (<https://mni-open-ieegatlas.research.mcgill.ca/>). We proposed and adapted wMEM for resting state localization, i.e. when dealing with the localization of ongoing background activity characterized by small signal-to-noise ratio data. wMEM results were compared with two widely used source imaging methods: the minimum norm estimate (Hämäläinen & Ilmoniemi, 1994) and beamformer (Van Veen et al., 1997).

Chapter 7 presents our second published manuscript (Afnan et al., 2024): *EEG/MEG source imaging of deep brain activity within the maximum entropy on the mean framework: Simulations and validation in epilepsy*. We proposed a depth-weighted adaptation of MEM to improve the localization of deep brain activity and added a detailed segmentation of the surface bilateral hippocampi in our source space for source imaging. We evaluated this method using extensive high-density EEG and MEG realistic simulations of IEDs as well as real IEDs recorded from patients with focal epilepsy. The aim of this study was to improve EEG/MEG source localization of deep brain activity by MEM, while preserving its capability to localize superficial generators.

Chapter 8 presents our third manuscript (Afnan et al., in press): *Validating MEG estimated resting state connectome with intracranial EEG*. This study used the same dataset as Chapter 6, i.e. MEG resting state source imaging from healthy controls and the MNI intracranial EEG atlas of normal brain activity. We validated the MEG-derived connectomes with intracranial EEG connectomes for four widely used connectivity metrics (Amplitude Envelope Correlation (AEC), orthogonalized AEC (OAEC), Phase Locking Value (PLV), and weighted-phase lag index (wPLI)). For those four metrics, the issue of source leakage associated with MEG-derived connectivity was investigated.

Chapter 9 presents our fourth manuscript ((Afnan et al., 2024), in preparation): *Validating MEG source imaging of oscillations and connectivity using simultaneous MEG-intracerebral EEG*. In this final study, we validated the group-level findings from studies 1 and 3 at a single-subject level in patients with epilepsy using simultaneous MEG and intracerebral EEG data. For this study, we applied our original adaptation of MEM methods developed in Chapters 6 and 7 to simultaneous MEG and intracerebral EEG data acquired by our collaborators at Aix-Marseille University (France, under the direction of Dr. Christian-G. Bénar). We applied at the single subject level, our specific evaluation metrics proposed in Chapters 6 and 8, to assess MEG accuracy in recovery oscillatory and connectivity patterns from resting state data. Finally, Chapter 10 concludes this PhD thesis by discussing the key findings and contributions, addressing potential limitations, and exploring future directions for the proposed research.

2 Fundamentals of epilepsy and pre-surgical investigation

This chapter will provide a brief overview of epilepsy, classification of seizures and epilepsy, and treatment options, especially for patients for whom drug therapy is not effective and who are considered for brain surgery. It will also briefly cover different diagnostic tools used during presurgical investigation, including but not limited to electrophysiological techniques such as electroencephalography (EEG) and magnetoencephalography (MEG).

2.1 Definition of epilepsy

Epilepsy is one of the most common neurological diseases. Currently, epilepsy affects approximately 65 million people around the world (Milligan, 2021). Epilepsy has been recognized since ancient times. The word ‘epilepsy’ is derived from the Greek word ‘epilambanein’ which means ‘to seize, possess, or afflict’ (Blair, 2012). An early description of an epileptic seizure was found in a 2000 B.C. text in the Akkadian language, where epilepsy was considered to be a form of demonic possession. It was described as: *“His neck turns left, his hands and feet are tense and his eyes wide open, and from his mouth froth is flowing without his having any consciousness.”* The exorcist named this condition *antasubbû*, which translates as “the hand of sin” (Labat, 1951; Magiorkinis et al., 2010). In the fifth century BC, Hippocrates, who is regarded as the father of medicine, disputed the divine origin of epilepsy and formally described it as a disease. He attempted a scientific approach to study epilepsy in his book *On the Sacred Disease* (Magiorkinis et al., 2010). In the 19th and 20th centuries, significant advancements were made in the field of epilepsy. These advancements were brought about by progress in neurosurgery, the development of antiepileptic drugs, a better understanding of disease mechanisms, and the invention of electroencephalography (EEG) (Magiorkinis et al., 2014).

Epilepsy is primarily manifested by unprovoked or spontaneous seizures. A seizure is an abnormal and hyper-synchronized neuronal firing in a part of the brain or across the whole brain. The International League against Epilepsy (ILAE) and the International Bureau for Epilepsy defined epilepsy as *“a disorder of the brain characterized by an enduring predisposition to generate epileptic seizures, and by the neurobiological, cognitive, psychological, and social consequences of this condition. The definition of epilepsy requires the occurrence of at least one epileptic seizure”* (Fisher et al., 2005). More recently ILAE updated and codified the definition of epilepsy for

clinical diagnosis as follows: “*Epilepsy is a disease of the brain defined by any of the following conditions: 1) At least two unprovoked (or reflex) seizures occurring >24h apart; 2) One unprovoked (or reflex) seizure and a probability of further seizures similar to the general recurrence risk (at least 60%) after two unprovoked seizures, occurring over the next 10 years; 3) Diagnosis of an epilepsy syndrome*” (Fisher et al., 2014). The term ‘epilepsy syndrome’ will be described in the next section.

2.2 Classification of seizures and epilepsies

The types of epileptic seizures can vary widely from patient to patient, and many classification systems have been used over the years. Accurate classification of seizures and epilepsy is necessary for determining the etiology (causes), proper treatment management, and prognosis. According to the 2017 ILAE classification system (Fisher et al., 2017), three levels of classification are used: 1) Seizure classification, 2) Epilepsy classification, and 3) Epilepsy syndrome classification (Figure 2-1).

Seizure classification: Based on seizure onset, seizures are classified as focal, generalized, or unknown. Focal seizures (previously called partial seizures) begin in one focus (focal brain region in one hemisphere). In contrast, generalized seizures involve both hemispheres at onset. If it is not possible to categorize the seizure as focal or generalized, it is classified as ‘unknown onset’.

Once the seizure onset is determined, further distinctions are made based on whether consciousness is impaired: aware or impaired awareness seizures. This classification is specific to focal seizures (focal aware or focal impaired awareness seizures). Generalized seizures typically impair consciousness. Based on the involvement of motor activity during seizures, focal and generalized seizures are also classified as motor onset and non-motor onset seizures. For generalized and unknown onset seizures with motor involvement, they are further classified as ‘tonic-clonic’ or ‘other motor.’ If focal seizures spread to involve both hemispheres, they are described as ‘focal to bilateral tonic-clonic’ (previously known as secondary generalized) (Figure 2-2) (Fisher et al., 2017).

Epilepsy classification: After determining the seizure type for an individual, the next level is diagnosing the type of epilepsy (Figure 2-1). The categories are focal epilepsy (characterized by focal onset seizures), generalized epilepsy (characterized by seizures with generalized onset),

combined generalized and focal epilepsy (patients presenting both generalized and focal seizures), and unknown type epilepsy (not possible to determine whether the epilepsy type is focal or generalized) (Fisher et al., 2017).

Epilepsy syndrome classification: The third level of classification involves making a specific syndromic diagnosis. Epilepsy syndrome is different from epilepsy type. Epilepsy syndromes are described as combinations of features including seizure types, EEG findings, imaging results, genetic factors, and age-dependent characteristics. The diagnosis of epilepsy syndrome allows for a broader classification than just identifying the seizure type (Scheffer et al., 2017).

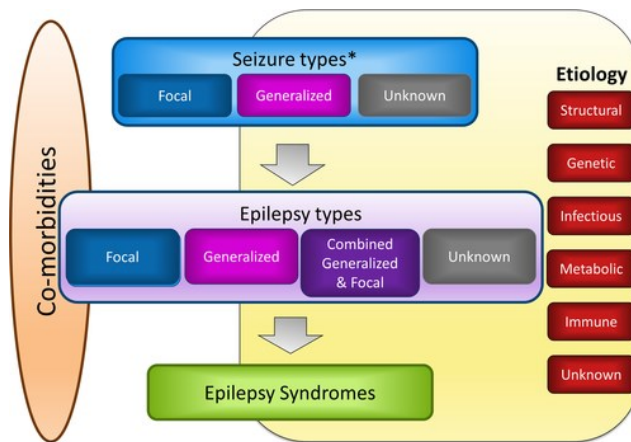


Figure 2-1 : Framework for classification of the epilepsies. *Denotes onset of seizure. Reprinted from *ILAE classification of the epilepsies: Position paper of the ILAE Commission for Classification and Terminology* by Scheffer et al. (2017).

ILAE 2017 Classification of Seizure Types Basic Version

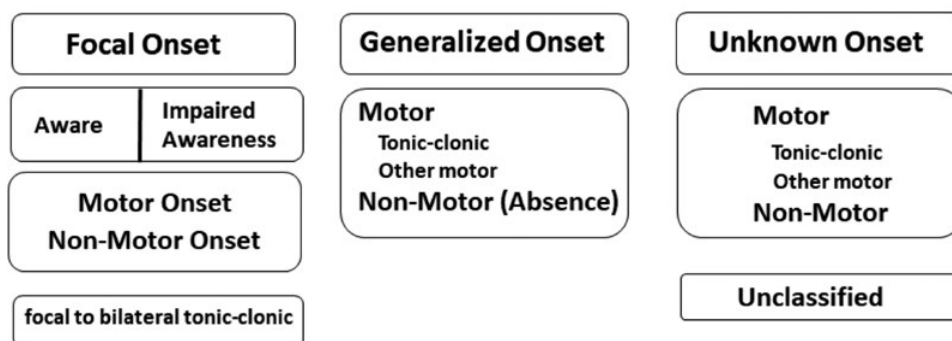


Figure 2-2 ILAE 2017 classification of seizure types. Reprinted from *Operational classification of seizure types by the International League Against Epilepsy: Position Paper of the ILAE Commission for Classification and Terminology* by Fisher et al. (2017) Reprinted with permission from John Wiley and Sons.

For each level of classification, etiology (causes) is also determined by considering six subgroups: structural, genetic, infectious, metabolic, immune, and unknown (Scheffer et al., 2017). The etiology of epileptic seizures varies widely across age groups. In children, genetic factors or malformations of cortical development are the most common causes. In adults, common causes include brain injuries, brain tumors, and neurodegenerative disorders (especially in elderly patients) (Falco-Walter, 2020). Additionally, the etiology of seizures is unknown in approximately 50% of cases (Tanaka et al., 2013).

2.3 Treatment of epilepsy

Epilepsy is a serious chronic neurological disease in which mortality is threefold higher than in the general population (Levira et al., 2017). The treatment of epilepsy does not cure epilepsy but aims to control the frequency and severity of the seizures. The primary treatment for epilepsy is the use of antiepileptic drugs to prevent seizures. Approximately 70% of people can achieve seizure freedom with proper diagnosis and medication. For the remaining 30% who are resistant to drug therapy and have a focal epilepsy, surgical treatment is the most effective way to control seizures (Guekht et al., 2021). Surgery targets the focal brain region that generates epileptic seizures. The goal is to achieve seizure freedom while preserving essential brain functions. The location and the volume (or size) of the brain region targeted for surgical treatment are assessed through extensive presurgical investigations which will be discussed in the next section.

2.4 Presurgical investigation of epilepsy

The aim of the presurgical investigation is first to delineate the epileptogenic zone (the brain region that needs to be removed to prevent a patient's seizures), assess whether resection of the epileptogenic zone is likely to achieve seizure freedom, and minimize the risk of inducing postoperative cognitive or neurological deficits (Ryvlin et al., 2014). According to Rosenow and Lüders (2001), the cortical zones that are indicative of the location and extent of the epileptogenic zones and are important to identify during the presurgical investigation are: the symptomatogenic

zone, the irritative zone, the seizure onset zone, the epileptogenic lesion, the epileptogenic zone, and the functional deficit zone. The definitions of these cortical zones are as follows:

Epileptogenic zone: This is the area of the cortex indispensable for generating seizures. This zone is a theoretical concept and cannot be directly estimated with current diagnostic methods but is inferred from identifying other zones that are defined below.

Symptomatogenic zone: The area of the cortex that generates ictal (seizure) symptoms when activated/stimulated by epileptic discharges. This region is detected through careful analysis of the seizure history or long-term ictal video recordings. This zone may or may not overlap with the epileptogenic zone.

Irritative zone: The area of the cortex that generates interictal epileptiform discharges (IEDs), which are abnormal neuronal discharges that occur spontaneously between seizures and are observed in the EEG. IEDs are more frequent than seizures. They occur without apparent clinical manifestation and the irritative zone often overlaps with regions responsible for seizure generation (Alarcon et al., 1997).

Seizure onset zone: The area of the brain where clinical seizures are generated.

Epileptogenic lesion: A radiographic lesion involved in seizure generation. Not all lesions are epileptogenic and many epileptogenic zones do not include visible lesions.

Functional deficit zone: Brain regions that are functionally abnormal either due to the lesion itself or abnormal neuronal activity caused by the epilepsy. These regions can be close to or distant from the epileptogenic tissue.

Identifying these cortical zones is necessary to delineate the possible epileptogenic zone. To define the location and volume of these regions, a variety of diagnostic tools are used, including short duration scalp EEG, prolonged video-EEG monitoring, magnetoencephalography (MEG), magnetic resonance imaging (MRI), positron emission tomography (PET), single photon emission computed tomography (SPECT), functional MRI (fMRI), neuropsychological tests, and intracranial EEG (Rosenow & Lüders, 2001). MRI is a structural neuroimaging technique used to identify the location of an epileptogenic lesion such as scar tissue or malformations of cortical development, called focal cortical dysplasia (FCD) (Urbach et al., 2022). This is routinely used

during presurgical evaluation. EEG and MEG are non-invasive electrophysiological techniques that can record neuronal activity related to ictal and interictal epileptiform discharges. EEG and MEG provide high temporal resolution of few milliseconds but have relatively poor spatial resolution, particularly for deep sources (these issues will be discussed in detail in later part of the thesis). They notably require the resolution of an ill-posed inverse problem of EEG/MEG source imaging (Baillet et al., 2001). Another non-invasive technique utilized during presurgical investigation is fMRI, which indirectly estimates the location of active brain tissue at a high spatial resolution by measuring changes in blood oxygen levels resulting from neuronal activity. Combining the complementary strengths of fMRI (high spatial resolution) and EEG (high temporal resolution, specificity for epilepsy) using simultaneous EEG-fMRI allows for accurate identification of the local hemodynamic changes elicited by the occurrence of interictal discharges, independently of the depth of the source (Gotman & Pittau, 2011; Ikemoto et al., 2022). PET and SPECT are two non-invasive neuroimaging techniques that involve injecting a radioactive tracer. PET could be used to measure baseline glucose metabolism in the brain, localizing regions exhibiting low metabolism, while SPECT measures cerebral blood flow changes (Kim & Mountz, 2011). When the radioactive tracer is injected at the time of a seizure, ictal SPECT allows capturing, within the whole brain, cerebral blood flow at the time of seizures (O'Brien et al., 1999). Whereas most of these non-invasive investigations are considered during phase 1 of presurgical mapping, an invasive electrophysiological technique called intracranial EEG is regularly used during the so-called phase 2 of presurgical evaluation of epilepsy, especially when other non-invasive techniques do not provide converging results about the underlying epileptogenic zone. Intracranial EEG involves placing electrodes directly on or within the brain tissue to record electrical activity, thus providing high spatial and temporal resolution. These diagnostic techniques collectively provide complementary information about the epileptogenic zone and the other cortical zones defined above. The table below summarizes the basic definitions, strengths, limitations, and uses of each modality in epilepsy diagnosis (Rosenow & Lüders, 2001).

Table 2-1 Summary of the strengths and limitations of each modality

Modality	Basics	Use in Epilepsy Diagnosis	Strengths	Limitations
Structural MRI	Utilizes magnetic fields to create	Identifies structural abnormalities such as epileptogenic lesions, tumors,	High spatial resolution, non-invasive.	Does not provide functional information.

	images of brain anatomy.	or cortical malformations associated with epilepsy.		
EEG (25 channels)	Measures electrical activity of the brain using electrodes placed on the scalp.	Useful in localizing the irritative zone (interictal epileptic spikes) and the seizure onset zone	High temporal resolution, widely available, non-invasive. Allows long-term monitoring and seizure recording	Low spatial resolution for standard EEG (25 channels), limited in detecting deep brain activity.
MEG (200-300 channels)	Measures magnetic fields produced by neuronal activity in the brain.	Useful in localizing the irritative zone (interictal epileptic spikes) and occasionally the seizure onset zone. Complementary to EEG.	High temporal resolution, non-invasive. After applying source imaging, relatively high spatial resolution for superficial sources, more limited for deep generators	Expensive, limited availability, limited recording duration, limited in detecting deep brain activity
PET	Involves injecting a positron-emitting tracer to visualize metabolic processes as for instance baseline glucose metabolism.	Identifies areas of hypo- or hypermetabolism related to functional deficit zone and epileptogenic zones	Provides metabolic information, useful for localizing seizure focus in non-lesional epilepsy.	Expensive, radiation exposure, limited spatial resolution compared to MRI.
SPECT	Uses gamma rays to create 3D images by detecting a radioactive tracer injected into the bloodstream.	Useful in localizing changes in blood flow the seizure onset zone and the functional deficit zone.	Can capture ictal changes in blood flow, useful for localizing seizure onset zones.	Lower spatial resolution than MRI, and radiation exposure. Requires accurate injection of radioactive tracer at the time of seizure.
EEG-fMRI	Measures brain activity by detecting changes	Useful in identifying irritative zones (interictal epileptic spikes).	High spatial resolution, non-invasive, provides	Poor temporal resolution, indirect

	in blood flow and metabolism.		functional information.	measure of neural activity
Intracranial EEG	Involves placing electrodes directly on or within the brain tissue.	Provides precise localization of the seizure onset and irritative zones, used when non-invasive methods are insufficient.	High spatial and temporal resolution, direct measurement of neuronal activity.	Invasive, risk of infection, bleeding, and other complications. Poor spatial sampling (covers a small fraction of brain).

The presurgical investigation of epilepsy is usually conducted in two phases. Phase 1 includes high-resolution MRI, long-term video scalp EEG, and neuropsychological assessment. If the results are ambiguous regarding the location of the possible epileptogenic zone, additional phase 1 investigations are conducted. These may include high-density EEG, MEG, interictal EEG and MEG source imaging (source imaging will be discussed in Chapter 3), simultaneous EEG-fMRI to localize the irritative zone, PET to localize the functional deficit zone and ictal SPECT. The routine investigation may vary across centers and depending on neuroimaging techniques/equipment available. If the results from different phase 1 investigations are still inconclusive, intracranial EEG is considered for a phase 2 evaluation (Baumgartner et al., 2019).

2.4.1 Interictal epileptiform discharges

Although it is possible to record seizures using long-term video EEG, it may be rare to capture seizures using EEG and MEG when recorded for short periods (~1 hour). In contrast, interictal epileptiform discharges (IEDs) are spontaneous, abnormal paroxysmal (i.e. sudden and uncontrolled) events that occur more frequently than seizures and are easily recorded by EEG/MEG; they are not accompanied by overt behavioral manifestations and are not perceived by the patient. The brain regions that generate IEDs, called the irritative zones, are often closely related to epileptogenic zones (Alarcon et al., 1997). Investigating IEDs and identifying the irritative zones are important aspects of the presurgical evaluation of patients.

Detection of IEDs requires the expertise of a trained epileptologist (Zijlmans et al., 2002). IEDs can include EEG/MEG patterns with different characteristics such as spikes, sharp waves, or polyspikes. Spikes or sharp waves are transient events whose amplitude is distinguishable from

the physiological EEG background. Polyspikes are described as a fast series of spikes. According to the International Federation of Clinical Neurophysiology, as described in Kane et al. (2017) and nicely illustrated by Kural et al. (2020) used in Figure 2-3, IEDs have to fulfill at least 4 of the following 6 criteria in EEG: “(1) di- or tri-phasic waves with sharp or spiky morphology (i.e., pointed peak); (2) different wave duration than the ongoing background activity: either shorter or longer; (3) asymmetry of the waveform: a sharply rising ascending phase and a more slowly decaying descending phase, or vice versa; (4) the transient is followed by an associated slow after-wave; (5) the background activity surrounding IEDs is disrupted by the presence of the IEDs; and (6) distribution of the negative and positive potentials on the scalp suggests a source of the signal in the brain, corresponding to a radial, oblique, or tangential orientation of the source”.

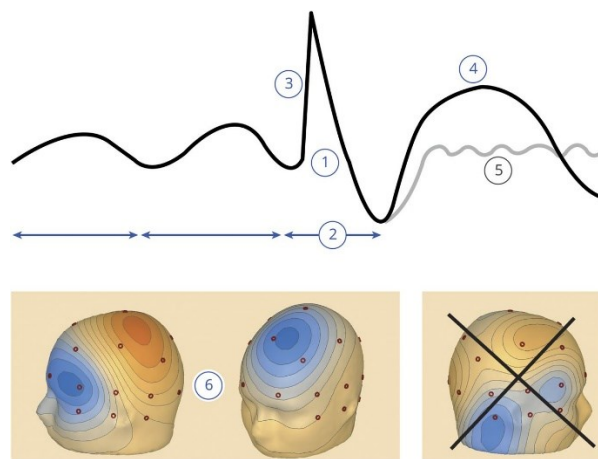


Figure 2-3 Criteria of interictal epileptiform discharges according to the International Federation of Clinical Neurophysiology, as described in Kane et al. (2017) and illustrated by Kural et al. (2020). Reprinted from *Criteria for defining interictal epileptiform discharges in EEG: A clinical validation study* by Kural et al. (2020). Reprinted with permission from Wolters Kluwer Health, Inc.

The detection criteria for IEDs are formally described for EEG but not for MEG. In practice, epileptologists follow a similar approach when marking IEDs in MEG. If simultaneous EEG is available, EEG information is also considered for marking IEDs in MEG. More details on IEDs detected using scalp EEG/MEG and intracranial EEG, the complementary nature of EEG versus MEG in detecting IEDs, and the strengths and limitations of these methods will be discussed in Chapters 3.

2.5 Conclusion

Accurate localization of the epileptogenic zone is important for patients with drug-resistant epilepsy to assess their eligibility for surgery and to identify the brain regions that need to be resected to become seizure-free. Among the various structural and functional neuroimaging techniques, non-invasive EEG and MEG are useful diagnostic tools for localizing seizure onset zones and irritative zones during presurgical investigation. Intracranial EEG is an invasive technique used during presurgical investigation if the results from non-invasive techniques are inconclusive. In this thesis, I will focus on EEG/MEG and intracranial EEG. More details about these techniques will be discussed in the subsequent chapters.

3 EEG/MEG source imaging

3.1 History of EEG/MEG

3.1.1 History of EEG

The Electroencephalogram (EEG) records the electrical fields of the brain (Berger, 1929). The concept of electricity in living organisms was first discovered in the 1780s by Dr. Luigi Galvani, an Italian professor, who identified "animal electricity" through his experiments with frogs (Catacuzzeno et al., 2024). The earliest understanding of brain function through electrical stimulation was derived from animal studies, notably by Dr. Fritsch and Dr. Hitzig in Germany in 1870. Dr. Richard Caton from Liverpool first recorded electrical activity from the exposed brains of rabbits and monkeys using a galvanometer in 1875. He is considered the first electroencephalographer and discoverer of EEG (Collura, 1993). The first human EEG was recorded and discovered by Dr. Hans Berger, a German neuropsychiatrist. He published his first report of human EEG in 1929 (Berger, 1929). Figure 3-1 shows a trace of EEG recorded by Dr. Berger from his son. He also discovered the dominant 10 Hz waves in human EEG in eyes closed condition and coined the term "alpha wave".

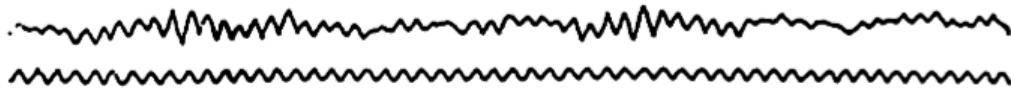


Figure 3-1 The first recorded EEG in human brain by Berger from his young son (top) in 1925. The bottom line is a 10 Hz sine wave used as a time marker (Brazier 1961) <https://psycnet.apa.org/record/1962-05971-000>.

Berger also recorded human EEG during sleep, brain injury, and epilepsy (Sutter & Kaplan, 2017). Berger's work was initially met with widespread disbelief but ultimately set a milestone in the history of clinical EEG, particularly after his findings were replicated by Adrian and Matthews (1934) in Cambridge and Hallowell Davis at Harvard in Boston. The use of EEG in North America flourished through the work of Frederic Gibbs and Erna Gibbs in the field of epilepsy, Alfred Loomis in sleep studies, and psychophysiolgist Herbert Jasper and neurosurgeon Wilder Penfield (who worked in Montreal, Canada) in the field of focal epilepsy. By the 1950s, EEG had become a widely used tool in universities and hospitals for both research and diagnosis (Coenen, 2024).

3.1.2 History of MEG

Unlike EEG, the history of MEG is more recent. MEG records the magnetic fields generated by the electrical activity of the brain. Recording the magnetic fields of the brain is challenging because typical scalp magnetic fields are on the order of 10 billionth of the earth's magnetic field. To capture these minute magnetic fields, sophisticated sensors are required, and thus MEG systems are housed inside magnetically shielded rooms. The first MEG recording was performed in the late 1960s by David Cohen, a physicist at the University of Illinois, using a copper induction coil (Cohen, 1968). The detection of the brain magnetic field improved (Cohen, 1972) (Figure 3-2) after the invention of Superconducting QUantum Interference Device (SQUIDS) by Silver and Zimmerman (1965). SQUIDS are extremely sensitive magnetometers that can measure very small changes in magnetic fields in a superconducting environment. Figure 3-2 shows the alpha rhythm detected by simultaneous MEG and EEG, placing the detectors at the left occipital region (Cohen, 1972).

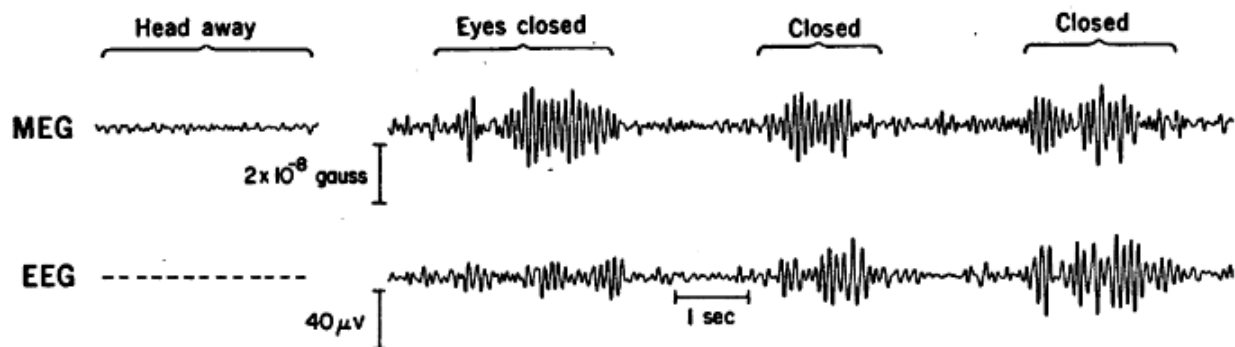


Figure 3-2 MEG recording by Cohen 1972 using SQUID sensors. Simultaneous EEG and MEG traces of alpha activity from normal human brain during eyes open and eyes closed conditions. The magnetometer was located at the left occipital region, as were the bipolar set of EEG leads. Figure reprinted from *Magnetoencephalography: Detection of the Brain's Electrical Activity with a Superconducting Magnetometer* by Cohen (1972). Reprinted with permission from the American Association for the Advancement of Science.

Using SQUID sensors, the first whole-head MEG system with 122 sensors became available in 1992 (Ahonen et al., 1993), followed by a system with 306 sensors in 1998. MEG is much less commonly used than EEG due to the significant difference in the cost of purchasing and maintaining MEG equipment. The primary reason for the high cost is the need for a cryogenic

system to cool the SQUID sensors, which requires liquid helium. In recent years, new magnetic field-sensing technology has been developed using quantum sensors, known as optically pumped magnetometers (OPMs). OPM sensors do not require complex maintenance, such as cooling and liquid helium (Brookes et al., 2022). Currently more than 200 whole head MEG systems are operational around the world (Matsubara et al., 2024).

3.2 Cellular origin of EEG/MEG signals

Before describing the cellular origin of EEG and MEG signals, a simplified drawing of the cerebrum of the human brain is shown in Figure 3-3. The brain is composed of six regions: the medulla, pons, midbrain, cerebellum, diencephalon, and cerebrum or telencephalon (Figure 3-3A) (Kandel et al., 2000). The cerebrum consists of two cerebral hemispheres. Each hemisphere contains the cerebral cortex (i.e., the wrinkled outer layer, also called gray matter), the underlying white matter (featuring fiber tracts connecting different regions) and three deep structures: the hippocampus, amygdala, and basal ganglia (not shown). Another major deep structure is the thalamus (not shown), which is part of the diencephalon. The thalamus connects the basal ganglia and cerebellum to the cerebral cortex and plays an important role in the transmission of information. The two hemispheres are connected by the corpus callosum, a large bundle of axons (axon is defined in the next paragraph) that links similar regions between the left and right hemispheres. Each cerebral cortex can be further described in four lobes: the frontal, parietal, temporal, and occipital lobes (Kandel et al., 2000). The cortex is a thin sheet of tissue approximately 2-4 mm in thickness with many folds. The folds are called gyri, and the grooves between the folds are called sulci or fissures. The fundamental unit of brain and nervous system is the neuron, which is a specialized brain cell with intrinsic electrical properties.

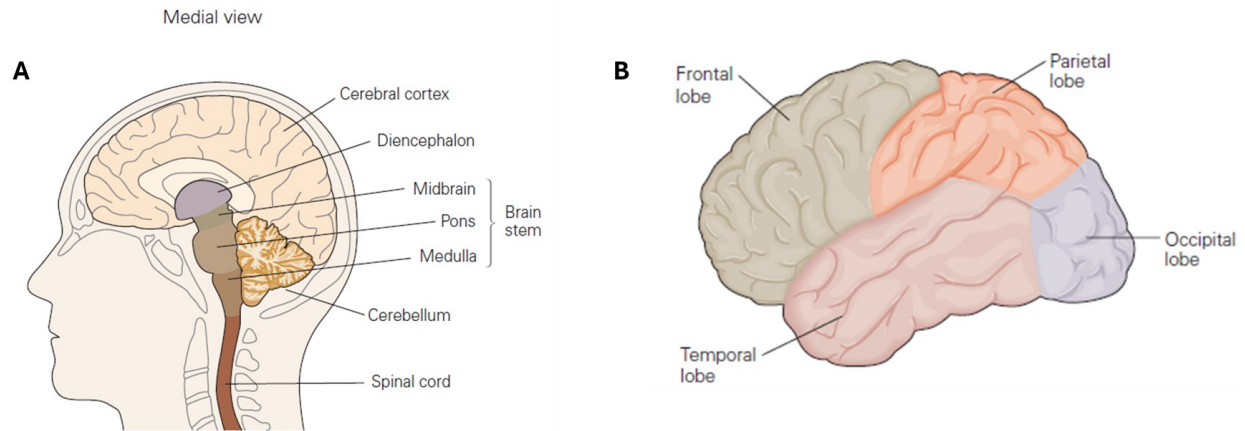


Figure 3-3 (A) The major divisions of the brain (medial view). (B) Simplified drawing of the cerebral cortex of human brain consisting of four lobes: frontal, parietal, temporal, and occipital. Figures are reprinted from *Principles of Neural Science* (Fifth Edition) edited by Eric R. Kandel (Kandel et al., 2021). Reprinted with permission from the University of Chicago Press.

EEG and MEG signals are generated by the summed electrical activities of populations of neurons (Lopes da Silva, 2023). There are approximately 10^{11} neurons in the human brain. Neurons communicate with each other to transfer information. Neurons are composed of three main parts: the soma or the cell body, the dendrites, and the axons. The cell body, which contains the nucleus, is the main part. Dendrites are branch-like extensions around the cell body that receive incoming signals. Dendrites that grow from the apex of the soma are called apical dendrites, and the dendrites that grow from the base of the soma are called basal dendrites (Mihaljević et al., 2020). Axons provide a pathway to transfer signals from the cell body to other parts of the nervous system. The dendrites and soma of neurons are located in the gray matter of the cortical sheet, where EEG/MEG signals originate through synchronization. Communication and connectivity between populations of neurons are facilitated by axons in the white matter fibers, which enable both local and long-distance connections. Neurons transmit information from one cell to another using specialized contacts called synapses (Stevens, 1979). The neuron that sends information is called the presynaptic neuron, and the neuron that receives information is called the postsynaptic neuron. The transmission is mediated by chemical messengers called the neurotransmitters located in the presynaptic terminal (axon of the presynaptic neuron). The postsynaptic terminal is the location of the neuron receiving those neurotransmitters.

The main contributors to EEG/MEG signals are specific types of neurons called pyramidal neurons, located within a few millimeters' depth of the cortical surface, as well as in deeper

structures such as notably the hippocampus and the amygdala. When a sufficient number of these pyramidal neurons are aligned in a spatially organized manner and activated in a coordinated way, the resulting magnetic fields or electric potentials will add up so that they give rise to EEG and MEG signals that can be recorded at a distance from the generators (Lopes da Silva, 2013).

When activated, neurons generate electrical current at the level of the cellular membrane. Two types of neuronal activations are possible: fast action potentials and slower postsynaptic potentials. Whereas the resting intracellular potential is -70mV , an action potential is generated when this intracellular membrane potential reaches a threshold around $-50/-55\text{ mV}$. The action potentials consist in a rapid jump of the intracellular membrane potential (lasting only 1 or 2 ms, like an impulse) from negative to positive, before returning to resting membrane potential. The action potential is mediated by sodium and potassium voltage-dependent ionic conductance and propagates rapidly along the axon, therefore allowing communication between neurons. In contrast, the slower membrane potential is due to synaptic activation mediated by neurotransmitters. EEG/MEG signals are believed to be generated mainly from slower postsynaptic potential. Postsynaptic potentials are slower (around 10ms) so they are easier to synchronize in space and time when compared to action potentials (around 1ms). Two main kinds of postsynaptic potentials are the excitatory postsynaptic potentials (EPSPs) and the inhibitory postsynaptic potentials (IPSPs). In an EPSP, the membrane potential moves closer to the threshold (depolarization), increasing the likelihood of generating an action potential. In contrast, in an IPSP, the membrane potential moves further away from the threshold (hyperpolarization), reducing the likelihood of generating an action potential. At the level of the synapse, when there is a net positive inward current in the neuron (at the apical dendrite), it is called an EPSP. Extracellularly, a current sink is created at the apical dendrite by the EPSP. In contrast, for an IPSP, a net outward current occurs from the neuron, so extracellularly an active current source is created by the IPSP (Lopes da Silva, 2004). In the case of EPSP, the apical dendritic membrane becomes transiently depolarized (less negative than the soma and basal dendrites). For this potential difference, the distant basal dendrites become a passive source and current flows from the source to the sink at the apical dendrites (Gloor, 1985). In this way, a current dipole configuration is created. Generally, the apical dendrites of pyramidal cells point towards the cortical surface.

Some current will flow directly from the source to the sink. The current loop must be closed, and therefore some extracellular current will flow. The intracellular flow of current is called the primary current, and the extracellular current is called the secondary or volume conduction current (Figure 3-4) (Baillet et al., 2001). These primary and secondary postsynaptic currents are believed to be the source of electric potentials and magnetic fields. EEG is driven by extracellular currents, while MEG is generated by both primary and secondary currents, with a greater contribution from primary currents.

However, signal generated by one single neuron is not enough to generate a measurable scalp EEG or MEG field. To generate electric and magnetic fields on a macroscopic level, spatial and temporal integration is required. This is the main reason EEG and MEG are mainly generated by pyramidal neurons since their dendrites are spatially aligned parallel to each other and oriented perpendicular to the cortical surface (Nunez & Silberstein, 2000), so that their resulting electrical or magnetic fields can sum up, if the postsynaptic potentials of the neurons occur synchronously (Lopes da Silva, 2004).

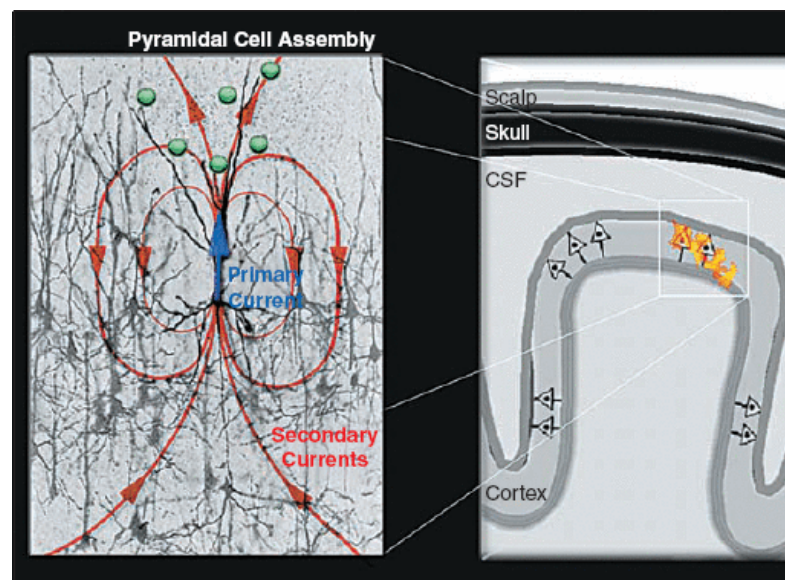


Figure 3-4 Left: Excitatory postsynaptic potentials (EPSPs) are generated at the apical dendritic tree of a cortical pyramidal cell and trigger the generation of a current that flows through the volume conductor from the non-excited membrane of the soma and basal dendrites to the apical dendritic tree sustaining the EPSPs. Some of the current takes the shortest route between the source and the sink by travelling within the dendritic trunk (primary current in blue), while conservation of electric charges imposes that the current

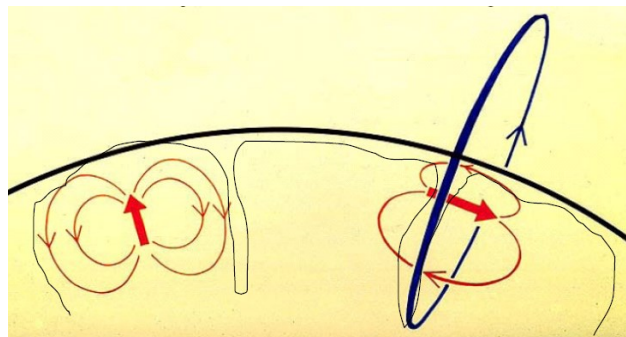
loop be closed with extracellular currents flowing through the volume conductor, including distant parts (secondary currents in red). Right: Large cortical pyramidal nerve cells are organized in macro-assemblies with their dendrites normally oriented to the local cortical surface. This spatial arrangement and the simultaneous activation of a large population of these cells contribute to the spatio-temporal superposition of the elemental activity of every cell, resulting in a current flow that generates detectable EEG and MEG signals. Figure retrieved from *Electromagnetic brain mapping* by Baillet et al. (2001) © 2001 IEEE.

The concept of open field versus closed field is also important to mention. In synaptic activation, the current flow consists of longitudinal and transverse components. The longitudinal component is parallel to the main axis of the neuron and will add up if many neurons are aligned parallel to each other. This case is called an open field, allowing all electric or magnetic fields to sum up efficiently in space, to give rise to EEG/MEG signals. The pyramidal neurons are aligned with their apical dendrites perpendicular to the cortical surface and this results in open field. In contrast, if the neurons are not aligned, i.e. have a random geometric organization, the components tend to cancel each other out and the resulting net field is decreased or zero; this is called a closed field (Lorente De Nó, 1947). This topic will be discussed more in section 3.8.

3.3 Differences and complementary strengths of EEG and MEG

EEG and MEG are generated by the same populations of neurons during synaptic activity but measure different aspects of neural activity. The main source of EEG signals is extracellular volume conduction currents, whereas MEG signals primarily arise from intracellular primary currents with a smaller contribution from the volume conduction currents. EEG signals are mainly contributed by volume currents that travel through the scalp, skull, and cerebrospinal fluid to reach the scalp, which reduces signal strength and makes them more sensitive to noise. An electrical contact on the skin is required to record an EEG signal. In contrast, MEG signals are less affected by the scalp, skull, and cerebrospinal fluid, resulting in less attenuation and distortion by these tissues (Nunez & Srinivasan, 2006). This is why, to produce a detectable signal or relatively large signal-to-noise ratio, for instance, an interictal epileptic spike, EEG requires the activation of spatially extended generators covering at least 4 to 8 cm² along the cortical surface (Tao et al., 2007; von Ellenrieder et al., 2014). On the other hand, MEG requires a generator covering of 3 to 4 cm² along the cortical surface to produce IEDs with enough signal-to-noise ratio to be detected above background data (Oishi et al., 2002).

Another important difference between MEG and EEG is that they are sensitive to different orientations of sources. When considering the head as a spherical model, MEG measures the magnetic field generated mainly by primary currents, which are strongest when the current flow is tangential to the head surface. The resulting magnetic fields need to extend outside the head to be detected by MEG sensors, which are placed around the head. On the other hand, within this spherical head geometry, radial dipoles do not generate magnetic fields outside the head (Figure 3-5). Consequently, within actual head geometry, MEG becomes mainly sensitive to tangential current dipoles, which are overall localized along the sulci of the cortical surface, and poorly sensitive to radial current dipoles, which are mainly localized along the gyri of the cortical surface. On the other hand, EEG is sensitive to both radial (along the gyri) and tangential (within the sulci) current dipoles sources, but since electrical potentials are decreasing as one over the square of the distance, EEG becomes more sensitive to radial current sources on the gyri (Baillet et al., 2001).



David Cohen NMH/MIT

Figure 3-5 When considering a spherical head geometry, MEG is only sensitive to tangential current dipoles for which the magnetic fields (in blue) extend outside the head, those dipoles are mainly located along the sulci of the cortical surface. For purely radial sources, mainly located on the gyri, the magnetic field does not extend beyond the head and is invisible to MEG sensors. For EEG, both radial and tangential dipoles will generate electric fields (in red) and measurable electrical potentials, whereas EEG will be more sensitive to dipolar current sources located along the gyri, since they will be closer to the sensors, when compared to tangential sources along the sulci.

3.4 EEG and MEG instrumentation

EEG: To record EEG, sensors or electrodes are either glued directly onto the scalp or placed on the head using a cap. It is essential to ensure good electrical conductivity between the skin and the electrodes. This can be achieved by cleaning the skin with an abrasive gel and applying a good

conductive medium. The electrodes record small bioelectrical potentials, which are then amplified and converted into digital signals by a device called an amplifier. The amplified signals are subsequently stored on a computer. In some systems, amplification and analog-to-digital conversion occur directly at the electrode level, on the participant's head. These 'active electrodes' have the benefit of minimizing noise caused by the wires (Xu et al., 2017). The number of electrodes may range from a few electrodes to up to 512 electrodes. The positions of the electrodes are usually based on a specific configuration known as a montage. In 1958, Dr. Jasper at the Montreal Neurological Institute introduced the 10-20 system, consisting of 19 electrodes, reflecting a standardized configuration (Figure 3-6). Other montages with a greater number of electrodes, such as the 10-10 system (81 electrodes) proposed by Chatrian et al. (1985), and the 10-5 system (329 electrodes) proposed by Jurcak et al. (2007), have also been developed. Figure 3-6 illustrates the 10-20 system proposed by Dr. Jasper and the 10-10 system (Nuwer et al., 1998).

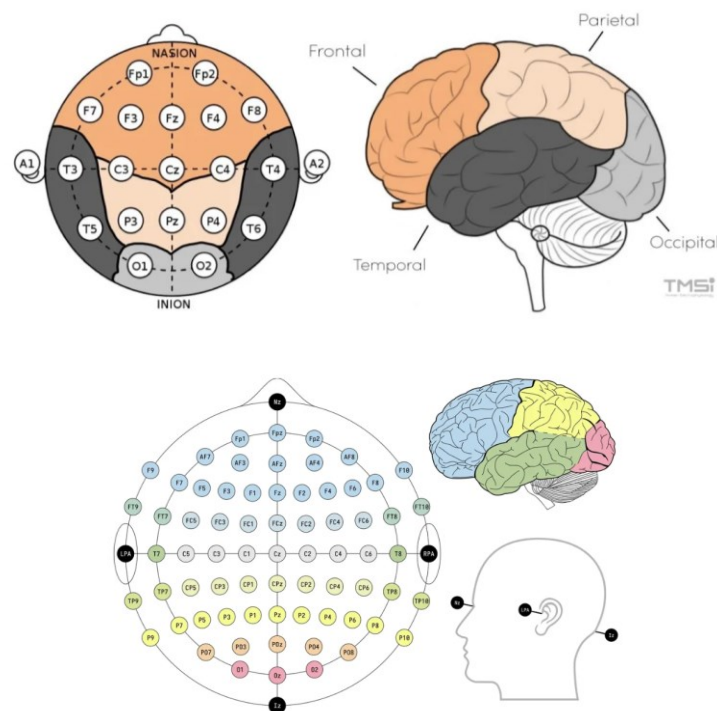


Figure 3-6 (top) The electrode layout of the 10-20 system (left) and corresponding brain regions (right). (Bottom) EEG layout with 10-10 system (Figure from <https://info.tmsi.com/blog/the-10-20-system-for-eeeg>). A = Ear lobe, C = central, P = parietal, F = frontal, O = occipital, Fp = frontal polar, FT = frontal temporal, AF - intermediate between Fp and F, FT - between F and T, TP - between T and P, CP - between C and P, PO - between P and O.

MEG: In contrast to EEG, traditional SQUID MEG sensors are usually placed inside a helmet. A SQUID is an ultrasensitive detector consisting of two superconductors separated by thin insulating layers that can convert quanta of magnetic flux into electrical voltage (Josephson, 1962). Therefore, using SQUID technology requires working in a superconducting state, which necessitates cooling the device at a very low temperature within a cryogenic dewar filled with liquid helium (Figure 3-7). Importantly, since magnetic fields generated by neuronal activity are tiny (order of femto- to picoTesla), one needs to reduce significantly environmental magnetic noise. To do so, MEG systems are located inside a magnetically shielded room, gradiometers instead of magnetometers as well as additional reference sensors might be considered to reduce the influence of magnetic background noise.

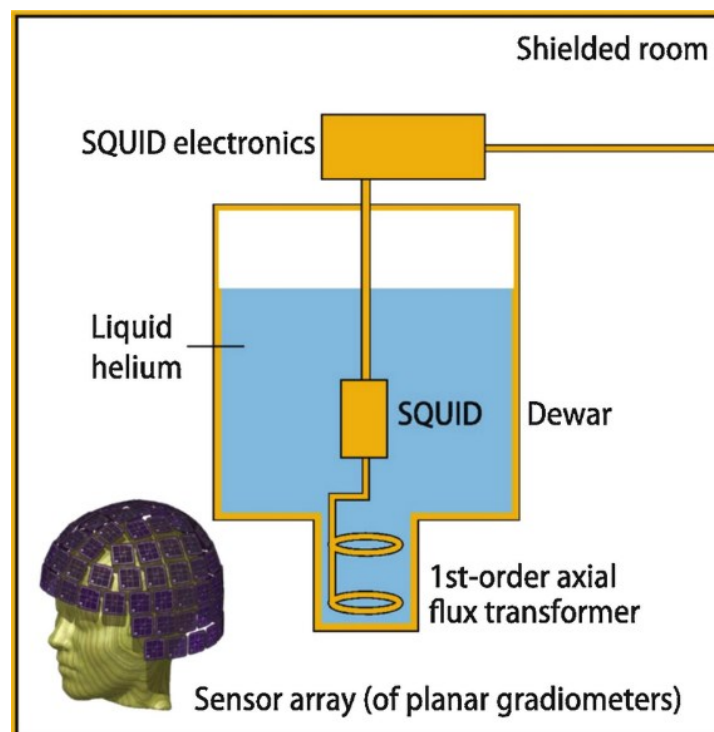


Figure 3-7 Schematics of MEG instrumentation. A single-channel axial gradiometer and associated SQUID inside a dewar filled with liquid helium. The bottom depicts the sensor array of a 306-channel MEG helmet. Illustration taken from *IFCN-endorsed practical guidelines for clinical magnetoencephalography (MEG)* by Hari et al. (2018).

The simplest type of magnetic field detector is called a magnetometer, which consists of a single coil placed close to the head (Figure 3-8). This configuration is highly sensitive to brain magnetic flux but also sensitive to environmental noise. Another type of coil configuration is the

gradiometer, which consists of two oppositely wound coils. When they are next to each other, tangential to the head, it is called a planar gradiometer. When the coils are one above the other, radial to the head, it is called an axial gradiometer. Gradiometers therefore measure the gradient of magnetic flux. This configuration helps cancel out environmental noise that is common to both coils. However, due to this configuration, gradiometers are also less sensitive to deep brain activity, an issue that will be discussed in section 3.8.

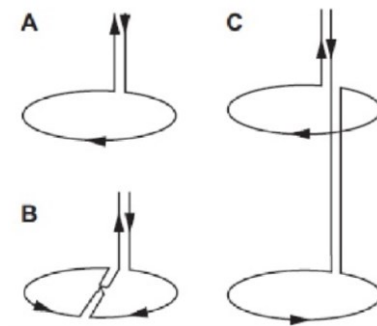


Figure 3-8 Common pick-up coil geometries. (A) magnetometer, (B) planar gradiometer, (C) axial gradiometer. Modified from *Magnetoencephalography---theory, instrumentation, and applications to noninvasive studies of the working human brain* Hämäläinen et al. (1993). Reprinted with permission from the American Physical Society.

Most of the current whole-head MEG systems can contain more than 300 SQUIDS connected to sensor coils. The MEG system used for this thesis is the CTF system with 275 SQUID sensors connected to axial gradiometers (Figure 3-9).

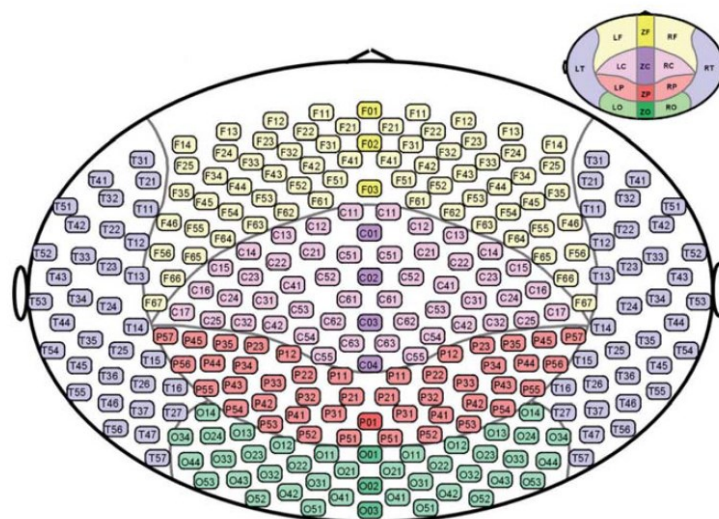


Figure 3-9 Schematic representation of the whole head coverage with 275 MEG sensors in a CTF system. Each sensor is named with 5 digits and the first is M for MEG. The small figure on the upper right corner shows the second and the third characters and the bigger figure shows the last three digits of the sensor name. Taken from Brainstorm tutorial:

https://neuroimage.usc.edu/brainstorm/Tutorials/ChannelFile#Display_the_sensors.

3.5 Estimating the neuronal sources from EEG/MEG measurement

Since we have now presented and discussed the underlying neuronal generators that give rise to electrical and magnetic fields detectable at the scalp level (or a few centimeters away from the scalp in the case of MEG), EEG and MEG sensors can measure these signals, which can be interpreted at the sensor level to provide important information, for instance, the posterior alpha rhythm in physiological condition or, in the case of epilepsy, which sensors could detect abnormal epileptic spikes or seizures. This interpretation is made by assuming that the generator region is located below the sensors and associated with a large amplitude signal. To move beyond sensor-level analysis and localization, estimating more accurately the location of the neuronal sources that generate a specific distribution of EEG and MEG recorded at the scalp is known as the inverse problem of EEG/MEG. Actually, this inverse problem is mathematically ill-posed since it does not have a unique solution. There are indeed an infinite number of possible source combinations that can give rise to the same EEG/MEG signals (von Helmholtz, 2004). Therefore, specific assumptions are needed to obtain a single estimate of the EEG/MEG sources. Before solving the inverse problem, one needs to first solve the so-called forward problem (Figure 3-10). The objective of the forward model is to model the EEG/MEG response at the electrodes for a known configuration of sources, considering and modeling brain structures such as the scalp, brain, and other layers through which the electrical or magnetic fields propagate. Unlike the inverse problem, the forward problem is a well-posed problem and admits a unique solution, however underlying head modeling may be challenging.

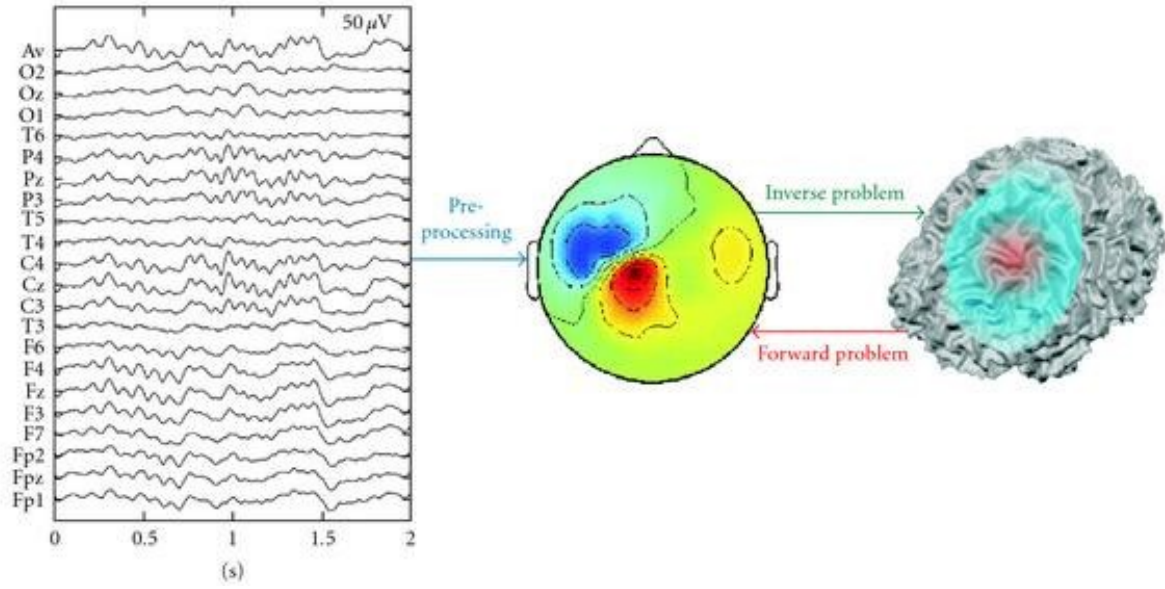


Figure 3-10 Key parts of estimating the neuronal sources from EEG/MEG measurement. The inverse problem attempts to locate the sources from recorded measurements, whereas the forward problem assumes a source definition to calculate a potential distribution map. Illustration taken from *EEG/MEG Source Imaging: Methods, Challenges, and Open Issues* by Wendel et al. (2009), <https://doi.org/10.1155/2009/656092>.

3.6 EEG/MEG forward problem

3.6.1 Quasi-static approximation of Maxwell's equations

The forward model is solved using Maxwell's equations of electrical and magnetic fields. The following four differential equations are used to calculate the electric field \mathbf{E} , the magnetic field \mathbf{B} when the charge density is ρ , current density is \mathbf{J} , ϵ_0 and μ_0 are the electrical permittivity and the magnetic permeability of free space, t is time. The nabla operator ∇ is the vector differential operator ($\nabla \mathbf{E}$ refers to the gradient of the vector \mathbf{E} , $\nabla \cdot \mathbf{E}$ refers to the divergence of the vector \mathbf{E} and $\nabla \times \mathbf{E}$ refers to the curl of the vector \mathbf{E}).

$$\begin{cases} \nabla \cdot \mathbf{E} = \frac{\rho}{\epsilon_0} \\ \nabla \cdot \mathbf{B} = 0 \\ \nabla \times \mathbf{E} = -\frac{\partial \mathbf{B}}{\partial t} \\ \nabla \times \mathbf{B} = \mu_0 \left(\mathbf{J} + \epsilon_0 \frac{\partial \mathbf{E}}{\partial t} \right) \end{cases} \quad (1)$$

To calculate the electric and magnetic fields, a ‘quasistatic’ approximation is usually considered. The term ‘quasistatic’ means a condition where the propagation, conductance, and inductive effects can be ignored in a constant conductor (Plonsey & Heppner, 1967). The frequencies of interest for EEG and MEG are typically less than 100 Hz in most applications, which is much slower compared to the propagation of electromagnetic waves that travel at the speed of light. Moreover, the magnetic permeability of biological tissue is approximately similar to that of free space. Considering this quasi-static approximation, the time derivatives terms of in Maxwell equations can be neglected, resulting in the following:

$$\begin{cases} \nabla \cdot \mathbf{E} = \frac{\rho}{\epsilon_0} \\ \nabla \cdot \mathbf{B} = 0 \\ \nabla \times \mathbf{E} \approx 0 \\ \nabla \times \mathbf{B} \approx \mu_0 \mathbf{J} \end{cases} \quad (2)$$

$\nabla \cdot \mathbf{E} = \frac{\rho}{\epsilon_0}$ is actually Gauss law, stating that the presence of a static charge density will create an electric field, whereas $\nabla \cdot \mathbf{B} = 0$ Gauss law for magnetism states that there is “no magnetic charge” creating \mathbf{B} , all magnetic field lines that enter a closed surface should also exit the surface. $\nabla \times \mathbf{B} \approx \mu_0 \mathbf{J}$ is Ampère law mentioning that the presence of a current density, i.e. electric charges in motion, will create a magnetic field. Finally, exploiting the fact that $\nabla \times \mathbf{E} \approx 0$, the electrical field \mathbf{E} is conservative and could be written as a negative gradient of the electric potential.

$$\mathbf{E} = -\nabla V \quad (3)$$

As mentioned before, the current in the brain can be divided into primary and volume conduction currents as follows:

$$\mathbf{J} = \mathbf{J}^p + \mathbf{J}^v \quad (4)$$

This equation can be written as:

$$\mathbf{J} = \mathbf{J}^p + \sigma \mathbf{E} = \mathbf{J}^p - \sigma \nabla V \quad (5)$$

Where σ is the conductivity of the medium (which is related to the local electrical permittivity ϵ of the medium)

As the divergence of a curl is zero, $\nabla \cdot \nabla \times \mathbf{B} = 0$ and consequently $\nabla \cdot \mathbf{J} = 0$, which also means conservation of current density (every current density entering a closed surface should also exit the surface).

Combining $\nabla \cdot \mathbf{J} = 0$ with equation (5), we obtain the following differential equation:

$$\nabla \cdot (\sigma \nabla V) = \nabla \cdot \mathbf{J}^p \quad (6)$$

This is the fundamental differential equation to be solved for the EEG/MEG forward problem. It will consist in placing a unit current density source \mathbf{J}^p somewhere in the brain before computing the electric potential V on all EEG electrodes and the corresponding magnetic field \mathbf{B} on all MEG channels. The process is repeated placing \mathbf{J}^p for every possible position in the source space (e.g. along a 3D grid inside the brain, along the cortical surface fixing the orientation of the source perpendicular to the cortical surface).

In free space, one can actually directly calculate the magnetic field \mathbf{B} at location \mathbf{r} , for a corresponding primary source \mathbf{J}^p placed in \mathbf{r}' , using the Biot-Savart law,

$$\mathbf{B}(\mathbf{r}) = \frac{\mu_0}{4\pi} \mathbf{J}^p(\mathbf{r}') \times \frac{\mathbf{r} - \mathbf{r}'}{\|\mathbf{r} - \mathbf{r}'\|^3} \quad (7)$$

Similarly, one can calculate the electric potential V in \mathbf{r} , for a corresponding primary source \mathbf{J}^p placed in \mathbf{r}' ,

$$V(\mathbf{r}) = \frac{1}{4\pi \epsilon_0} \mathbf{J}^p(\mathbf{r}') \cdot \frac{\mathbf{r} - \mathbf{r}'}{\|\mathbf{r} - \mathbf{r}'\|^3} \quad (8)$$

The solution to the forward problem of EEG and MEG can be obtained using equations 6 , 7 and 8. In practice, solving the forward problem consists in estimating V first before estimating corresponding magnetic position \mathbf{B} , using $\nabla \times \mathbf{B} = \mu_0 \mathbf{J} = \mu_0 (\mathbf{J}^p - \sigma \nabla V)$, for each specific position of a unit current source \mathbf{J}^p . The main difficulty is that one should consider that within the head the conductivity values (σ in equation (6)) vary from one tissue to the other and therefore head geometry should be accurately modeled. When not in free space, ϵ_0 in Equation (2) should be replaced by ϵ , which is the electric permittivity of the specific medium (which depends on σ). The magnetic permeability of different biological tissues is similar to that of free space (μ_0). Therefore, the geometry of the head model and the electrical conductivities of the different layers are the main factors that govern the forward model (Darvas et al., 2004). Detailed reviews on

forward solutions with mathematical emphasis can be found in the following papers (Gramfort et al., 2011; Hämäläinen et al., 1993; Kybic et al., 2005; Pürits et al., 1993).

3.6.2 Source model

The source model describes the organization of the current sources at a macro-scale level that generates the EEG and MEG signals (Lecaignard & Mattout, 2015). The most commonly used model to describe the current source is the equivalent current dipole (ECD) model. There are two main approaches to the ECD model: (i) The dipolar approach: This approach considers that brain activity could be modeled considering a small number of ECDs at fixed positions, mimicking the activity of small patches of cortex. (ii) The distributed sources or imaging approach: This approach considers a few thousand ECDs to model the entire source space. The ECDs can be distributed either on a 3D grid covering the whole brain volume with unconstrained orientation or along the cortical surface with normal orientation to represent the orientation of pyramidal cells.

3.6.3 Head model

After defining the source space model, the head model is another important part of the forward model which is computed based on certain assumptions on the geometry of the head and the conductivity to allow solving the main differential equation (8).

Spherical models: The simplest form of the head model assumes that the head can be represented using one or more homogenous concentric spheres each representing the layers of head tissue such as the scalp, the skull, and the brain. This simple geometry allows finding analytic expressions for the electric potentials and the magnetic field on the surface (De Munck et al., 1988; Rush & Driscoll, 1968). The *3-shell* model proposed in De Munck et al. (1988) used three layers for the scalp, skull and brain with isotropic conductivities. Because of the important influence of skull conductivity on EEG, which results in spatial smearing of volume conduction currents, spherical models are not appropriate for EEG modeling. Spherical models could be more suitable for MEG because the magnetic permeabilities of different biological tissues are similar to that of free space. Another model usually considered for MEG is called the *overlapping spheres*, for which a best-fit spherical model of the brain is estimated iteratively for each sensor (Huang et al., 1999).

Realistic models: realistic head models consist in numerical models developed to better represent the head tissue properties and their corresponding conductivity values when solving the forward

model for either EEG or MEG. Main realistic head models consist of either Boundary element models (BEM) (Hamalainen & Sarvas, 1989) or Finite element models (FEM) (Marino et al., 1993). BEM: The BEM models use surface meshes extracted from anatomical MRI segmentation and assume homogeneous and isotropic conductivity for each of the three layers: brain, skull, and scalp. BEM models are computationally heavy compared to spherical models but provide a more realistic model of electrical and magnetic field generations (Mosher et al., 1999). The BEM model also might have numerical instabilities if the surfaces are not properly closed and non-overlapping especially for patients who have holes in their skulls (Von Ellenrieder et al., 2014). This OpenMEEG BEM solver (Gramfort et al., 2010; Kybic et al., 2005) has been proposed specifically to ensure robustness to numerical instabilities and is the model we have used in this thesis. BEM does not handle the anisotropic or heterogeneous conductivity value within head tissues.

FEM: FEM, on the other hand, uses 3D meshes within the head volume where each mesh element can have different conductivity (isotropic or anisotropic), allowing to account for tissue non-homogeneity. When compared to BEM, FEM can provide a more realistic solution to the forward model but is also computationally intensive. FEM models can include various tissues such as blood vessels, fat, soft and hard bone, anisotropic white matter, and eyes, but obtaining such detailed information from standard MRI is challenging (Medani et al., 2023).

3.6.4 Tissue conductivities

The conductivity values of the different head tissues are critical, especially for EEG. In this thesis, we have used the BEM model with the inner skull, outer skull, and the scalp surfaces and used the corresponding conductivity values of 0.33:0.0165:0.33 S/m respectively (Ferree et al., 2000; Hoekema et al., 2003; Lai et al., 2005). We used the OpenMEEG BEM implementation (Gramfort et al., 2010) available in the Brainstorm software (Tadel et al., 2011) to solve the forward model. Estimating tissue electrical conductivity might be challenging, especially when considering advanced realistic FEM models, for which we also might need to estimate conductivity anisotropy tensors (von Ellenrieder et al., 2012). In conclusion, solving the forward model for EEG and MEG is a well-posed problem that admits a unique solution. However, when considering more and more realistic head models, identification of the parameters of the model (tissue conductivity values) is becoming challenging, while numeric estimations are becoming computationally intensive.

3.6.5 Coregistration of EEG/MEG sensors with anatomy

Coregistration of EEG/MEG sensors with individual anatomical MRI is essential for accurate source localization. This process involves determining the positions of EEG/MEG sensors relative to three fiducial points (nasion, left, and right peri-auricular) using a digitization or tracking device during the acquisition. These same fiducial points are also marked on the MRI images. An initial registration between sensors and MRI is done based on the three fiducial points. However, this initial registration is approximate and can be sensitive to errors in identifying the fiducial points. To improve accuracy, the shape of the head is sampled using the digitization device and subsequently used to coregister with the MRI, resulting in a more precise coregistration.

In this thesis, to improve coregistration accuracy, the exact positions of the localization coils and the shape of the subject's head were digitized using a 3D Polhemus localizer for subsequent coregistration with the anatomical MRI. The coregistration was performed using the skin surface segmented from a T1-weighted MRI. The iterative closest point algorithm (Besl & McKay, 1992) was used to ensure accurate coregistration between the MRI-segmented skin mesh and the head shape digitized with the 3D Polhemus localizer. For high density EEG (Chapter 7), same coregistration approach was applied, with high density EEG sensor positions estimated using the Geodesic Photogrammetry System (GPS, Electrical Geodesics Inc., Eugene, OR) (Hedrich et al., 2017).

3.7 EEG/MEG inverse problem

Once the EEG/MEG forward model is estimated, solving the inverse problem of EEG/MEG source localization consists in estimating the cortical current that generates the EEG and MEG data recorded at the sensor level. Therefore, detection of the cortical generators from EEG/MEG data measured at the scalp or outside the head requires solving the following equation:

$$\mathbf{m}(t) = \mathbf{G}\mathbf{j}(t) + \mathbf{e}(t) \quad (9)$$

Where $\mathbf{m}(t)$ is the q -dimensional measurement vector for EEG or MEG signal at time t where q denotes the number of EEG/MEG sensors, $\mathbf{j}(t)$ is the r -dimensional vector denoting the current density of r dipolar sources at time t and \mathbf{G} is the lead field matrix with a dimension of $q \times r$, i.e. the resolution of the forward model estimating the contribution of each of the r dipolar sources of unit 1 on the q sensors. $\mathbf{e}(t)$ models an additive measurement noise at time t . The objective is

then to estimate the current density $\mathbf{j}(t)$ from the measured data $\mathbf{m}(t)$ and the estimated lead field matrix \mathbf{G} , considering the noise $\mathbf{e}(t)$.

The inverse problem is fundamentally ill-posed, a fact recognized long before the advent of EEG and MEG (Helmholtz, 1853), especially because we are looking for a 3D distribution of currents given rise to EEG or MEG signal on the scalp surface. No unique solution exists for a specific set of EEG/MEG sensor-level data; thus, assumptions/constraints must be made about the underlying current sources, based on the existing knowledge about the anatomical and neurophysiological basis of the brain signals, to formulate a so-called restricted inverse problem (Fender, 1987). Therefore, any source localization method depends on these prior assumptions. Three main strategies have been proposed for solving the inverse problem: i) dipole fitting approach ii) dipole scanning approach and iii) distributed imaging approach.

3.7.1 Dipole fitting approach

The dipole fitting approach assumes that neuronal activity can be modeled using one or a few equivalent current dipoles (ECDs). This was the first and still a widely used source model in EEG and MEG (Ebersole, 1997; Scherg & Von Cramon, 1986; Wendel et al., 2009) mainly popularized by the first available commercialized software package (Besa software package developed by the team of Dr Scherg notably). A dipole is modeled to represent a small patch of activated cortex, i.e., the center of activity of a geometrically restricted collection of synchronously activated neurons (Figure 3-11). The dipoles can be modeled as moving dipoles with unknown position, orientation, and amplitude; rotating dipoles with fixed position and unknown orientation and amplitude; or fixed dipoles with fixed position and orientation and unknown amplitude. Once the position of a dipole is known, the problem becomes linear and the orientation and amplitude of this dipole can be estimated using a least squares fitting approach. On the other hand, especially since the influence of an ECD on EEG or MEG sensors is decreasing as one over the square of the distance, estimating the location of a dipole requires solving a non-linear problem (Mosher et al., 1992). An important model is the time-varying current dipole model proposed by Scherg (1984), for which the position and orientation of a few ECDs are estimated first within a specific time window of the signal of interest. In the second step, the positions of the localized ECDs remain fixed and the time course of their magnitude over the whole temporal window is estimated using a least square fitting.

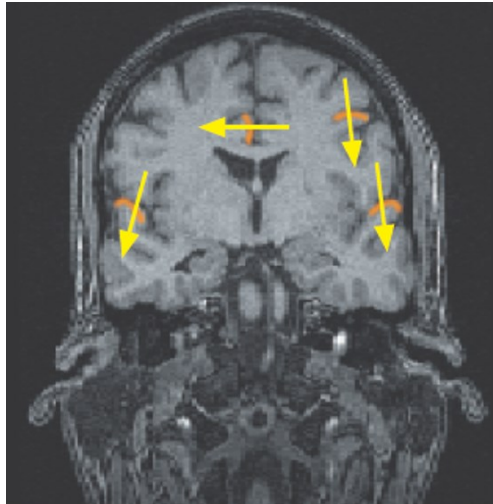


Figure 3-11 In the dipole fitting approach, a dipole is modeled to represent a patch of activated cortex. From Scherg (1984).

Localization using ECD is a well-established method that can provide very accurate localization of focal generators if sufficient knowledge of the cortical generator is available to guide the location of the ECDs. One such example is the localization of evoked potentials in EEG or evoked fields in MEG, for instance in the somatosensory or auditory cortex (Salmelin, 2010) or during epileptic spikes (Merlet & Gotman, 1999; Pellegrino et al., 2018).

In low SNR conditions, dipole fitting approaches could be inaccurate (Hara et al., 2007; Shiraishi et al., 2005). Knowing the underlying number of sources or how many ECDs to fit is indeed a tedious task. Importantly, this approach cannot determine the spatial extent of the underlying generator. When activation involves spatially extended cortical regions, as is often the case with interictal epileptic spikes, it can lead to spurious localization of deep ECD sources (Kobayashi et al., 2005).

3.7.2 Dipole scanning approach

The dipole scanning approach is an extension of the single dipole fitting approach. One limitation of the dipole fitting approach is indeed the unknown number of ECDs to fit. The dipole scanning approach considers a 3D grid within the source space and then tests the relevance of fitting a dipolar source sequentially on each grid point. Consequently, it provides a 3D map where the local maxima are considered as the most relevant dipoles. Some widely used dipole scanning approaches are beamforming approaches such as the linearly constrained minimum variance (LCMV) method

(Van Veen et al., 1997) and Multiple Signal Classification approach (MUSIC) (Mosher et al., 1992).

3.7.2.1 Multiple signal classification approach (MUSIC)

Mosher et al. (1992) proposed a dipole scanning approach that is based on an eigenvalue decomposition of data aiming to isolate the signal of interest (called signal subspace) from noise (noise subspace) (the signal subspace and noise subspace being orthogonal to each other). The number of sources is assumed to be less than the number of sensors. The whole brain volume is scanned to find the source locations that contribute to the signal space. The local maxima of the 3D MUSIC map will provide the best possible dipole locations for which the time course can be estimated using a least square fitting approach once dipole locations are known. Other variants of MUSIC such as Recursive-MUSIC, RAP-MUSIC (Mosher & Leahy, 1998) have been proposed; they involve an iterative approach of MUSIC to identify the best dipole sources as well as the underlying number of ECDs to fit. The main limitation of the MUSIC approach is a lack of an objective separation between the signal space and the noise space.

3.7.2.2 Beamforming (Van Veen et al., 1997)

Beamforming techniques apply a linear spatial filter at a specific position of the 3D grid to isolate the contribution of that particular source while minimizing the activity or interference from all other locations on the grid. Similar to MUSIC, beamforming scans all possible locations of the grid sequentially. For each position \mathbf{r} , Beamforming consists in estimating an optimal spatial filter \mathbf{W}_r that is applied to the data as:

$$\mathbf{S}(\mathbf{r}) = \mathbf{W}_r^t \mathbf{m}(t) \quad (10)$$

Where $\mathbf{S}(\mathbf{r})$ is the amount of the contribution at the source location \mathbf{r} . This model also assumes a focal generator at each grid point that can be modeled using one ECD model. The main idea of Beamforming technique is to estimate for every source location \mathbf{r} , a spatial filter that will extract the signal coming from this source location while reducing / cancelling the signal originating from other location within but also outside the head. A widely used beamforming approach is called the linearly constrained minimum variance (LCMV) method (Van Veen et al., 1997) which estimates the spatial filter \mathbf{W}_r by minimizing the source variance Σ .

$$\Sigma(\mathbf{r}) = E[\mathbf{S}(\mathbf{r})\mathbf{S}(\mathbf{r})^t] = \mathbf{W}_r^t \Sigma_m \mathbf{W}_r \quad (11)$$

Where Σ_m is the data covariance matrix: $\Sigma_m = E[\mathbf{m}(t)\mathbf{m}(t)^t]$

The solution of the minimum variance beamformer filter for a dipolar source at the source location \mathbf{r} is then given by:

$$\mathbf{W}_{LCMV,r}^t = (\mathbf{G}_r^t \Sigma_m^{-1} \mathbf{G}_r)^{-1} \mathbf{G}_r^t \Sigma_m^{-1} \quad (12)$$

Where \mathbf{G}_r is the gain matrix at location \mathbf{r} considering three orthogonal orientations (i.e. solution of the forward model for the location \mathbf{r}).

The resulting beamformer output signal $\mathbf{S}^*(\mathbf{r}) = \mathbf{W}_{LCMV,r}^t \mathbf{m}(t)$ estimated in position \mathbf{r} is usually referred to as a virtual sensor placed at the location \mathbf{r} .

Beamformer techniques are easy to implement. Key components in LCMV beamformer estimation (equation (12)) are modeling of the forward model at the location \mathbf{r} and an accurate estimation of the data covariance matrix, which is usually obtained from a single trial (non-averaged data) and requires some numerical regularization. However, this technique is not appropriate when correlated sources are involved, since the spatial filter aims to focus on the activity of one source while removing the influence of the others (Sekihara et al., 2002). Also, the spatial filter is computed from the gain matrix and data covariance matrix. This method is sensitive to errors in the forward model (Wax & Anu, 1996). Thus, beamforming is particularly useful for MEG (as opposed to EEG), because obtaining an accurate forward model \mathbf{G} is easier in MEG. Importantly, for a stable estimation of the data covariance matrix, long stationary data is ideally required (Cheyne et al., 2006; Oswal et al., 2014).

Limitations of the dipole scanning approach: It is worth mentioning that the dipole scanning approach uses a dipole fitting approach and thus has the same limitations while fitting an ECD for each position of the grid. Consequently, in theory, these methods remain ideal to localize focal generators. To localize spatially extended generators, several attempts were made such as beamforming using cortical patches (Hillebrand & Barnes, 2011; Limpiti et al., 2006) or the 2q-ExSo-MUSIC (2q-th order extended source MUSIC) algorithm (Birot et al., 2011). These methods are computationally more demanding and are still facing challenges when localizing correlated sources or spatio temporal propagation (Chowdhury et al., 2016).

3.7.3 Distributed source imaging models

Distributed source imaging techniques assume that brain activity is generated by a large number of small dipolar sources which are distributed over the source domain (cortical surface or 3D volume grid) covering the whole brain (Dale & Sereno, 1993). The position of the dipoles in the source space is fixed thus the localization problem becomes linear since only amplitude (and orientations) needs to be estimated from the data. The orientation of the dipoles may be constrained, typically normal to the cortical surface or free. The solution of the inverse problem provides a 3D image of source intensities for each dipole. This is why distributed source models are called the imaging approach.

Unlike the dipole fitting or scanning approach, the number of dipoles in distributed source imaging models in the source space is large (typically a few thousand). Thus, although the problem is linear, it is still highly underdetermined (the number of sensors being much less than the number of sources, a few hundred versus a few thousand). Therefore, solving this underdetermined linear problem necessitates additional assumptions to identify the ‘most likely’ solution (Michel et al., 2004). Different distributed source imaging methods have been proposed using different assumptions.

Two main complementary approaches to handle the underdetermined problem are the regularization and probabilistic approaches. The distributed methods often can be described within both frameworks and equivalences could be considered to switch from one framework to the other.

3.7.3.1 Regularization techniques

The regularization techniques solve the inverse problem $\mathbf{m}(t) = \mathbf{G}\mathbf{j}(t) + \mathbf{e}(t)$ by tuning a trade-off between the data fit (i.e. finding a solution that explains well the data) and a regularization function. Regularization is important to account for the noise in data, otherwise, the estimated solution would explain 100% variance of the measured data, which would be similar to overfitting. The regularization step adds stability to the solution so that adding a small variance in the data would not result in a large variation in source estimation (Michel et al., 2004). A commonly used regularization technique is Tikhonov regularization, which solves inverse problems by minimizing the following cost function:

$$\hat{\mathbf{j}}(t) = \underset{\mathbf{j}}{\operatorname{argmin}} \{ ((\mathbf{m}(t) - \mathbf{G}\mathbf{j}(t))^T \mathbf{L}_m (\mathbf{m}(t) - \mathbf{G}\mathbf{j}(t)))^p + \lambda (\mathbf{j}(t)^T \mathbf{L}_j \mathbf{j}(t))^p \} \quad (13)$$

Here $((\mathbf{m}(t) - \mathbf{G}\mathbf{j}(t))^T \mathbf{L}_m (\mathbf{m}(t) - \mathbf{G}\mathbf{j}(t)))^p$ is the data fit term and $\lambda(\mathbf{j}(t)^T \mathbf{L}_j \mathbf{j}(t))^p$ is the regularizing term, defined by a p -norm where $p = 1$ or 2 would correspond to L-1 norm and L-2 norm. λ is a hyperparameter that controls the trade-off between the data fit and the constraint. \mathbf{L}_m and \mathbf{L}_j are weighting matrices for the data and the regularizing term respectively. Based on the choice of these weighting matrices, different variants of distributed source imaging methods have been proposed. Some of the widely used inverse solutions based on the Tikhonov regularization principle are:

Minimum norm estimates (MNE)

The minimum norm solution was the earliest solution to the inverse problem for distributed source models (Hämäläinen & Ilmoniemi, 1994). It assumes that the estimated current distribution should have minimum overall intensity. This means this method will choose a unique source configuration with the minimum overall energy (intensity) among all possible source configurations that equally fit the data. It is obtained by choosing a L-2 norm ($p = 2$) and using weighting matrices defined as $\mathbf{L}_m = \mathbf{\Sigma}_e$, representing the inverse of the noise covariance matrix and $\mathbf{L}_j = \mathbf{\Sigma}_s$ modeling inverse of the source covariance matrix.

$$\hat{\mathbf{j}}_{MNE}(t) = \underset{\mathbf{j}}{\operatorname{argmin}} \{ \|\mathbf{m}(t) - \mathbf{G}\mathbf{j}(t)\|_{\mathbf{\Sigma}_e}^2 + \lambda \|\mathbf{j}(t)\|_{\mathbf{\Sigma}_s}^2 \} = (\mathbf{G}\mathbf{\Sigma}_e\mathbf{G}^T + \lambda\mathbf{\Sigma}_s)^{-1} \mathbf{G}^T \mathbf{\Sigma}_e \mathbf{m}(t) = \mathbf{W}_{MNE} \mathbf{m}(t) \quad (14)$$

Here \mathbf{W}_{MNE} is the resulting MNE linear operator (or kernel). For MNE solution, $\mathbf{\Sigma}_s$ is usually considered as the identity matrix.

Since MNE aims at minimizing the energy of the solution, the standard MNE solution tends to bias the estimation toward more superficial sources, since to produce similar amplitude scalp data, deep generators would need to exhibit larger source amplitudes. To address this issue, a *depth-weighted MNE* version was proposed by (Lin et al., 2006). To do so, the inverse source covariance model $\mathbf{\Sigma}_s$ is weighted for each source covariance using a factor that enhances the contribution from deep sources and penalizes the contribution from superficial sources. Lin et al (2006) proposed to add a weighting coefficient defined as $(\mathbf{G}_r^T \mathbf{G}_r)^{-\omega}$, i.e. the inverse of the energy corresponding lead field for a source r at a specific power ω . This topic will be discussed in more detail in Chapter 7. Two other variants of MNE have been proposed for which the contribution

from deep sources is enhanced, by using a noise-normalization approach: dynamic statistical parametric mapping (dSPM) (Dale et al., 2000) and Standardized low-resolution electromagnetic tomography (sLORETA) (Pascual-Marqui, 2002).

Dynamic statistical parametric mapping (dSPM) is a variant of MNE method obtained by normalizing the MNE solution at each source point by the noise estimate of that location. The noise estimation is obtained by applying the MNE operator \mathbf{W}_{MNE} to the noise covariance matrix Σ_e as: $diag(\mathbf{W}_{MNE}\Sigma_e\mathbf{W}_{MNE}^T)$. The dSPM solution is obtained by:

$$\hat{\mathbf{j}}_{dSPM}(t) = \frac{\hat{\mathbf{j}}_{MNE}(t)}{\sqrt{diag(\mathbf{W}_{MNE}\Sigma_e\mathbf{W}_{MNE}^T)}} \quad (15)$$

Standard low-resolution electromagnetic tomography (sLORETA) is another variant of MNE solution using a noise-normalized approach. Here, the MNE solution is normalized by the total variance of the estimated source, not just the noise variance used in dSPM. The estimated total variance is given by $diag(\mathbf{W}_{MNE}(\mathbf{G}\Sigma_s\mathbf{G}^T + \lambda\Sigma_e)\mathbf{W}_{MNE}^T)$. The sLORETA solution can be obtained by:

$$\hat{\mathbf{j}}_{sLORETA}(t) = \frac{\hat{\mathbf{j}}_{MNE}(t)}{\sqrt{diag(\mathbf{W}_{MNE}(\mathbf{G}\Sigma_s\mathbf{G}^T + \lambda\Sigma_e)\mathbf{W}_{MNE}^T)}} \quad (16)$$

In noise-free condition, this method has been shown to produce zero localization error (Pascual-Marqui, 2002).

LORETA

Low-resolution electromagnetic tomography (LORETA) was proposed by Pascual-Marqui et al. (1994). This approach combines the depth weighting MNE with a spatial Laplacian operator to introduce a spatial smoothness constraint between sources. Thus, LORETA will select a solution exhibiting maximum spatial smoothness. LORETA was originally proposed for a 3D volume grid as the source model. When applied on a cortical surface (Wagner et al., 1996), the method was called cortical LORETA (cLORETA). The basis of the assumption is that neuronal activities in neighboring regions are spatially correlated. This concept has been criticized because this assumption could be unreasonable for some cases such as the medial part of two hemispheres, which are anatomically very close along a 3D grid but functionally distinct. Consequently,

LORETA may provide over-smoothed solutions blurring the medial regions of two hemispheres (Fuchs et al., 1999; Michel et al., 2004; Trujillo-Barreto et al., 2004).

3.7.3.2 Probabilistic approaches

Another interesting methodological framework to solve the underdetermined inverse problem of distributed source imaging is using a probabilistic approach using Bayesian inference. I will briefly describe the formulation of the inverse problem within a Bayesian framework. This methodological framework is fully complementary to the regularization-based approaches that have been described in the previous section, and most methods can be expressed within both frameworks.

When considering a probabilistic approach, any form of uncertainty is formulated in terms of probability distribution and therefore variables, such as signals, sources and noise are modeled as random variables. Within this probabilistic framework, Bayes rules are formulated as follows:

$$p(\mathbf{j}|\mathbf{m}) = \frac{p(\mathbf{m}|\mathbf{j})p(\mathbf{j})}{p(\mathbf{m})} \quad (17)$$

Where $p(\mathbf{j}|\mathbf{m})$ is the conditional probability distribution of the sources \mathbf{j} knowing the measured data \mathbf{m} . $p(\mathbf{m})$ is the distribution of data (also called model evidence). $p(\mathbf{j})$ is the probability distribution of the sources, describing our *a priori* knowledge on the sources, $p(\mathbf{m}|\mathbf{j})$ is the data likelihood, i.e. the conditional probability distribution of observing the data \mathbf{m} , when the underlying sources \mathbf{j} are known, therefore the data likelihood depends on the forward model and the noise model.

Finally, $p(\mathbf{j}|\mathbf{m})$ is called the a posteriori distribution of the sources knowing the measured data \mathbf{m} . This is the distribution of interest we would like to assess when solving the inverse problem. Actually a typical solution to the inverse problem is to choose the Maximum a posteriori (MAP) estimate, by choosing the estimation of \mathbf{j} that maximizes the posterior distribution of \mathbf{j} for a given measurement \mathbf{m} (Chowdhury, 2017).

$$\hat{\mathbf{j}}_{MAP} = \underset{\mathbf{j}}{\operatorname{argmax}} p(\mathbf{j}|\mathbf{m}) \quad (18)$$

The assumption or constraint can be modeled by choosing a specific source prior $p(\mathbf{j})$. It is worth mentioning that the methods described above based on regularization techniques such as minimum

norm estimate or beamformer can also be formulated within this Bayesian framework (Baillet et al., 2001; Hedrich, 2020; Kaipio & Somersalo, 2006).

For EEG/MEG source imaging, several Bayesian methods have been proposed (Henson et al., 2010; Trujillo-Barreto et al., 2004; Wipf et al., 2010). Within this probabilistic framework, another method entitled the Maximum Entropy on the Mean (MEM), has been proposed in the context of EEG and MEG source imaging by our group in collaboration with Dr. Jean-Marc Lina (Ecole de Technologie Supérieure, Montreal). MEM-based methods have been largely investigated for EEG/MEG source imaging in this thesis. In the next section, MEM methods will be briefly described.

3.7.3.3 Maximum entropy on the mean (MEM)

The inverse problem of the distributed source imaging can be solved within the Maximum Entropy on the Mean (MEM) framework (Amblard et al., 2004), which uses a Bayesian probabilistic approach.

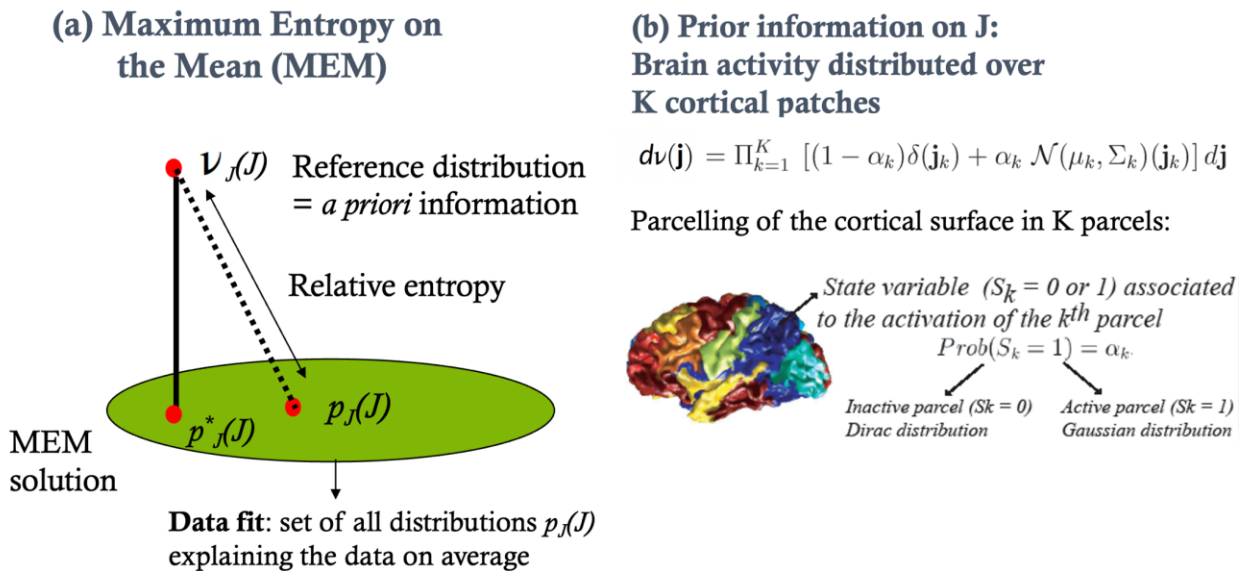


Figure 3-12 (a) MEM uses a reference distribution ν and solves the inverse problem by maximizing the relative entropy (minimizing the Kullback-Leibler divergence) between the source distribution and the reference distribution under the constraint of explaining the data. (b) Definition of the reference distribution: the brain activity is considered to be organized into K cortical parcels. Each cortical parcel k is then characterized by an activation hidden state variable S_k , describing if the parcel is active or not. Figure

reprinted from Concordance between distributed EEG source localization and simultaneous EEG-fMRI studies of epileptic spikes Grova et al. (2008). Reprinted with permission from Elsevier.

The key feature of the MEM method when applied to EEG/MEG source imaging is that it relies on a flexible spatial prior, assuming that brain activity is organized in K cortical parcels (K being usually within the order of magnitude of number of sensors). The activity of every parcel is scaled by the probability of activation of every parcel α_k , which is tuned through a hidden state variable S_k . When the parcel is active, a Gaussian distribution is used as the prior of the activity within the parcel. When the parcel is inactive, a Dirac distribution is considered that allows to shut down the activity from this parcel (Figure 3-12). Starting from such a prior “reference” v distribution (Figure 3-12b), the model is fitted to data by maximizing the relative entropy (i.e. minimizing the Kullback-Leibler divergence) between a solution explaining the data $p(j)$ and the prior reference v (Figure 3-12a). In other words, the MEM principle aims to estimate the distribution that provides “maximum uncertainty about missing information carried by the data (Jaynes, 1957)” with respect to the prior reference distribution. As a result, MEM can either switch off or switch on the parcels during the localization process, while still allowing local contrast on the cortical surface within the active parcels. Our team proposed and validated two main versions of MEM source localization: **the coherent MEM (cMEM)** originally proposed in Chowdhury et al (2013), is our standard variant of MEM and assumes a stable parcellation of the brain along time (Abdallah et al., 2022; Chowdhury et al., 2016; Chowdhury et al., 2013; Grova et al., 2016), as well as the wavelet-based extension of the MEM, wMEM (Lina et al., 2012; Pellegrino et al., 2016; von Ellenrieder et al., 2016). For coherent MEM (cMEM), the term “coherent” refers to the fact that we are using a coherent spatial prior, i.e. a data-driven parcellation which is fixed along time (Abdallah et al., 2022; Chowdhury et al., 2016; Chowdhury et al., 2013; Grova et al., 2016). wMEM consists in applying first a discrete wavelet transformation (Daubechies wavelets) to characterize the oscillatory patterns in the data before considering the MEM solver to solve the EMSI problem (Lina et al., 2012).

Coherent MEM

As mentioned before, detection of the cortical generators from EEG/MEG data measured at scalp or outside the head requires solving equation 8: $\mathbf{m}(t) = \mathbf{G}\mathbf{j}(t) + \mathbf{e}(t)$

Within the MEM framework (Amblard et al., 2004), \mathbf{j} denoting the intensities of r dipolar sources is considered as a random variable described by the probability distribution $dp(\mathbf{j}) = p(\mathbf{j})d\mathbf{j}$. To regularize the inverse problem, we incorporate prior information on \mathbf{j} in the form of a reference distribution $d\nu(\mathbf{j})$. The Kullback Leibler divergence or v-entropy is then defined as:

$$S_v(dp) = - \int_{\mathbf{j}} \log \left(\frac{dp(\mathbf{j})}{d\nu(\mathbf{j})} \right) dp(\mathbf{j}) = - \int_{\mathbf{j}} f(\mathbf{j}) \log (f(\mathbf{j})) d\nu(\mathbf{j}) \quad (19)$$

Where f is a ν -density of dp defined as $dp(\mathbf{j}) = f(\mathbf{j})d\nu(\mathbf{j})$. The ν -entropy $S_v(dp)$ measures the amount of information brought by the data with respect to the prior $d\nu$. We introduce a data fit constraint as the set of probability distributions on \mathbf{j} that explains the data on average.

$$\mathbf{m} - [\mathbf{G}|\mathbf{I}_q] \left[\frac{E_{dp}[\mathbf{j}]}{e} \right] = 0, \quad dp \in C_M \quad (20)$$

Where C_M is the set of probability distributions on \mathbf{j} that explains the data on average, $E_{dp}[\mathbf{j}] = \int_{\mathbb{R}} \mathbf{j} dp(\mathbf{j})$ denotes the mathematical expectation of \mathbf{j} with respect to the probability distribution dp and \mathbf{I}_q is a $q \times q$ identity matrix. Among all the possible distributions of $dp(\mathbf{j})$ that explain the data \mathbf{m} on average, MEM solution is derived from maximizing the ν -entropy (i.e. minimizing the Kullback-Leibler divergence between a solution explaining the data $p(\mathbf{j})$ and the prior reference ν) (Amblard et al., 2004; Grova et al., 2006). More details on MEM formulations are described in Chowdhury et al. (2016). More details including specific additional MEM developments proposed in this thesis as well as initialization of the reference distribution ν will be described in detail in Appendices of Chapters 6 and 7 which are reported at the very end of this thesis.

Wavelet MEM

wMEM is another version of MEM specifically designed to localize brain oscillatory patterns. wMEM applies a discrete wavelet transformation (Daubechies wavelets) to characterize the oscillatory patterns in the data before applying the MEM solver (Lina et al., 2012). In wMEM, the time expansion of data is substituted with a time-scale representation. In terms of wavelet expansion, equation 8 can be written as:

$$\mathbf{d}_{s,n} = \mathbf{G}\mathbf{w}_{s,n} + \mathbf{w}^\epsilon_{s,n} \quad (21)$$

Where $\mathbf{d}_{s,n}$, $\mathbf{w}_{s,n}$ and $\mathbf{w}^{\epsilon}_{s,n}$ are the wavelet coefficients for the data, the sources, and the measurement noise, respectively, for a particular discrete time index n and scale s ($s=1,2,3\dots$ with $s = 0$ being the sampling scale).

cMEM/wMEM for EEG/MEG source imaging have a preference toward superficial solutions (Chowdhury, 2017; Grova et al., 2006), since so far, we have not considered any depth-weighted strategy for both methods. On the other hand, depth weighted strategy is commonly considered for MNE (Hämäläinen & Ilmoniemi, 1994) and Beamformer (Van Veen et al., 1997). This is a core topic of this thesis and will be discussed in Chapter 7 (see methodological details in the Appendix of Chapter 7, which is reported at the very end of this thesis).

3.7.4 Other inverse methods

In the previous section, we have described some of the widely used inverse methods. Our list was not exhaustive, and many other inverse methods have been proposed within this framework such as FOCUSS (FOCal Underdetermined System Solution) (Gorodnitsky et al., 1995) and LAURA (Local Auto-Regressive Averages) (Rolando Grave de Peralta Menendez et al., 2001). Some methods assume that brain activity is sparse. Some methods that use sparsity-induced penalties to find the optimal solution are minimum current estimate (Uutela et al., 1999), and mixed-norm method (MxNE) (Gramfort et al., 2012). Iteratively reweighted edge sparsity minimization (IRES) proposed by (Sohrabpour et al., 2016) is another method based on sparsity on the solution and is suggested to be accurate in estimating focally extended sources. Several methods based on deep learning have also been proposed (Adler & Öktem, 2017).

3.8 Challenges and limitations of EEG/MEG source imaging

The accuracy of the solution to the inverse problem depends on many factors, such as the choice of the inverse method, the underlying assumptions associated with the inverse method (regularization approach, prior model), the accuracy of the forward model, the sensitivity of the sensors (EEG versus MEG or MEG magnetometer versus MEG gradiometer), the sensitivity to superficial versus deep brain activity. Some of the factors described in this section include the ill-posed nature of the inverse problem, challenges of localizing deep brain activity, the sensitivity of EEG versus MEG sensors, and the differences between magnetometer and gradiometer sensors.

The difficulty of localizing low SNR signals, especially in resting-state activity will be described in Chapter 4.

3.8.1 Ill-posed nature of inverse problem

The EEG/MEG inverse problem is inherently ill-posed, meaning that a specific EEG or MEG measurement can be generated by an infinite number of source configurations. Different source imaging methods, as described in the previous section, select a solution based on specific assumptions. It is therefore impossible to find a solution with 100% certainty. The solution can be called the most probable solution based on certain assumptions. This inherent uncertainty cannot be completely overcome, and the results of source imaging should always be interpreted with the understanding that they represent the most probable solution given certain assumptions.

3.8.2 Localizing deep brain activity

Localization of deep brain activity is a major challenge for EEG/MEG source imaging. Signals generated by deep sources quickly decrease in strength, becoming weaker by the time they reach the scalp, especially since signals issuing from deep regions will be hidden by stronger signals generated in cortical superficial regions. Two main factors that are important to consider in this context: the underlying structure of deep brain generators and the differing sensitivities of EEG and MEG sensors.

Closed structure of subcortical regions

In Section 3.2, I briefly mentioned that the main contributors to EEG/MEG signals are pyramidal neurons located in the cortical surface and subcortical structures such as the hippocampus and the amygdala. The concept of open and closed fields was also briefly introduced. The population of pyramidal neurons in the cortical layers features dendrites that are oriented in parallel (within one specific neuron and over population of neurons as well), the overall orientation being perpendicular to the circumvolute cortical surface. When a population of pyramidal cells is activated synchronously (i.e. synchronous post-synaptic potentials), the current components add up to create an open field. On the other hand, the interneurons which are mainly controlling inhibition levels around the pyramidal cell do not feature such spatial organization. The stellate interneuron cells indeed feature a closed-loop structure, and they do not contribute to EEG/MEG signals. Unlike pyramidal cells along the cortical surface, the subcortical structures are considered

generators of closed fields, which means the alignment of the pyramidal neurons is such that the current components cancel each other out. This is nicely depicted in Figure 3-13 (Benar et al., 2021), which shows that the field generated within the subcortical structures can completely cancel out, resulting in no detectable signal at the surface.

Another scenario is that the activity from the subcortical structure propagates to the nearby neocortex, creating an open field that is detectable on the surface (Alarcon et al., 1994). However, since it is generated very deep in the brain and the signal strength decreases with distance, only a very weak signal reaches the surface. It is also possible that not the whole structure of the subcortical region is activated. If only part of the subcortical structure is activated and able to create an open field, some signal could be detected at the surface, though it would be weak due to the depth of generation. Another possibility is that with the activated subcortical structure, a simultaneous neocortical source could be activated, generating a larger signal on the surface. Thus, the signal detected by the EEG/MEG sensors would be contributed by both cortical and subcortical generators.

While it is generally accepted that detecting activity from deep structures using EEG/MEG recordings is challenging, several studies using simultaneous intracerebral EEG and EEG/MEG have provided evidence that activity from deep structures can indeed be detected on the surface. For instance, Seeber et al. (2019) demonstrated with simultaneous high-density EEG and deep brain stimulation electrodes that scalp EEG could detect deep activity from subcortical structures, such as the thalamus. Similar findings were reported by Pizzo et al. (2019) using simultaneous intracerebral EEG and MEG. This topic will be discussed in more detail in Chapter 5.

To study deep brain activity, an interesting anatomical and electrophysiological model was proposed by Attal et al. (2009). Depending on the types of neural generators (open and closed field cells) and their preferred orientation, subcortical structures were modeled as volume grids or surface meshes. The thalamus, striatum, and amygdala were modeled by placing current dipoles on the volume grid with random orientation; the hippocampus was modeled as a surface mesh placing the current dipoles orthogonally to the surface. In this thesis (Chapter 7), we will use the model proposed by Attal et al. (2009) to add the hippocampal structure in our source model to study EEG/MEG source localization of deep activity.

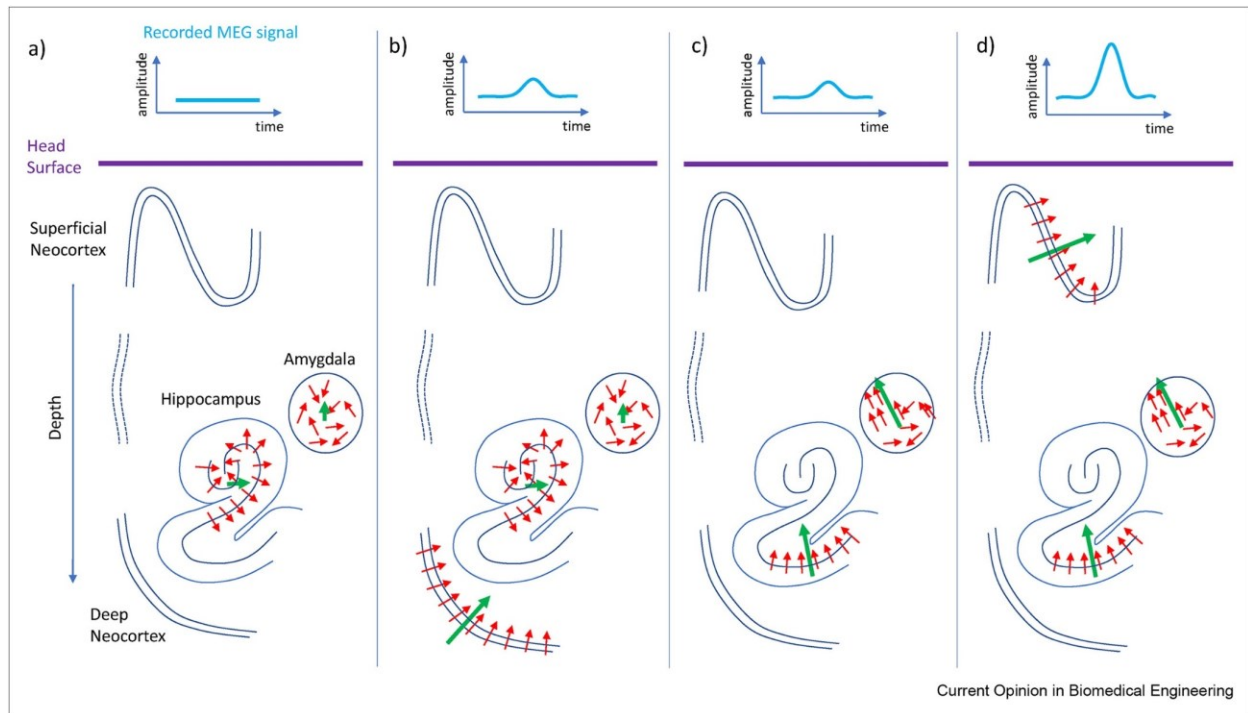


Figure 3-13 Schematic view of different source configurations and their reflection on MEG. (a) Only deep sources are active (hippocampus and amygdala). As activation is of a “closed field” type, no visible signal is recorded from the surface. (b) Activity from hippocampus propagates to nearby neocortex, which has a structured source geometry (open field) and can be seen as a signal at the surface (small because of the depth). (c) Only subparts of hippocampus and amygdala are active, producing an open field and small signal at the surface. (d) The activity from deep structures is overshadowed by activity from the superficial neocortex that has a higher amplitude because of shorter distance to the sensors. Illustration taken from *Detection and localization of deep sources in magnetoencephalography: A review* Benar et al. (2021). Reprinted with permission from Elsevier.

Sensitivity of sensors

As mentioned above, the signals from deep brain structures are weak and not easy to detect by surface measurements. The ability of EEG/MEG to detect deep brain activity is thus debated, especially for MEG (Barkley & Baumgartner, 2003; Kaiboriboon et al., 2010; Leijten et al., 2003; Rampp & Stefan, 2007; Shigeto et al., 2002). Both EEG and MEG magnetometers measure signals that decrease as 1 over the square of the distance. There are differences between the sensitivity of EEG versus MEG sensors; EEG sensors are directly placed on the scalp, whereas traditional MEG SQUID sensors are placed inside a helmet around the scalp (not directly touching the scalp). EEG is more sensitive to radial and deep sources whereas MEG using gradiometers is more sensitive to

tangential and superficial sources (Goldenholz et al., 2009; Kakisaka et al., 2013). Using median nerve stimulation, Fuchs et al. (1998) suggested that deep sources mainly contribute to EEG data while superficial and tangential sources contribute mainly to MEG data.

For MEG, the detectability of cortical generators also depends on the coil configurations. Magnetometers consist of a single superconducting coil that directly measures magnetic fields. Gradiometers, in contrast, consist of two oppositely wound coils that measure the spatial gradient of the magnetic fields. In the configuration of gradient coils, environmental noise gets canceled out because the noise is assumed to have the same effect on both coils. Magnetometers can pick up that noise. Thus, gradiometers are superior in noise cancellation. However, signals coming from deep sources are noisy and usually have a low signal-to-noise ratio. Magnetometers can pick up that signal, but gradiometers may consider it noise and cancel it out. This is why gradiometers are less sensitive to deep source activity (Dash et al., 2021; Hämäläinen et al., 1993). The new generation optically pumped magnetometers (OPMs) (which do not require cooling using liquid helium) are placed directly on the scalp and thus improve the SNR of the signal by reducing the distance between sources and sensors. They also seem to have a better ability to measure signals from deep sources such as the hippocampus (Tierney et al., 2021).

3.9 Conclusion

In this chapter, I briefly described the history of EEG and MEG, the cellular origin of the signals detected by EEG and MEG, and the estimation of neuronal sources from surface measurements. Different inverse methods have been briefly described with their strengths and limitations. The objective of this chapter was to introduce the readers to the challenges and limitations of EEG/MEG source imaging. Table 3-1 summarizes the assumptions, advantages, and limitations of the source imaging methods described in this chapter.

Table 3-1 Assumptions, advantages and limitations of different source imaging methods

	Method	Assumption	Advantages	Limitations
Dipole fitting approach	Equivalent current dipole (ECD) fitting (Scherg & Von Cramon, 1986)	<p>The measurement is generated by a single focal source</p> <p>The source activity can be properly modeled as a single dipole or a few dipoles</p> <p>The number of dipoles is known</p>	Valid for spatially focal sources such as evoked sensory motor sources	<p>Assumption of focal sources is not always valid</p> <p>Knowing the number of dipoles a priori is not feasible in many applications</p>
	MUSIC (Mosher et al., 1992)	<p>Source space can be divided into signal subspace and noise subspace.</p> <p>Number of sources is assumed to be less than the number of sensors</p>	<p>Knowing the number of dipoles a priori is not required</p> <p>More accurate localization compared to ECD fitting</p>	<p>Lack of an objective definition of separating the signal space from the noise space</p> <p>Limited performance if the sources to be localized are correlated</p>
Dipole scanning approach	Beamformer (Van Veen et al., 1997)	Spatial filters to isolate the signals from specific locations in the brain while suppressing noise and	Useful for MEG because obtaining an estimating the forward model is usually more accurate	<p>Spatially separate but temporally correlated sources can be suppressed (Brookes et al., 2007)</p> <p>sensitive to errors in the forward model</p>

		Method	Assumption	Advantages	Limitations
			interference from other sources.		long stationary data is ideally required for an accurate estimation of the data covariance structure
Distributed source imaging		Minimum norm solution (Hämäläinen & Ilmoniemi, 1994)	Estimated current distribution should have minimum overall intensity	Linear, easy to implement and provides good initial results in terms of current estimation.	Resulting solutions tend to be overly smooth, not sensitive to spatial extent Fails to address the issue of deep source localization which is address in depth weighted MNE
		Depth weighted MNE (Lin et al., 2006)	Variant of MNE with a depth weighting parameter to enhance contribution from deep sources	Sensitive to deep sources Better spatial accuracy than MNE	Not sensitive to spatial extent of the source
		sLORETA (Pascual-Marqui, 2002)	Noise normalized variant of MNE	Sensitive to deep sources Better spatial accuracy than MNE	Resulting solutions tend to be overly smooth, not sensitive to spatial extent Numerical instabilities in deep structures when the estimated source variance is closed to zero

Method	Assumption	Advantages	Limitations
dSPM (Dale et al., 2000)	Noise normalized variant of MNE	Sensitive to deep sources Better spatial accuracy than MNE	Resulting solutions tend to be overly smooth, not sensitive to spatial extent Numerical instabilities in deep structures when the estimated source variance is closed to zero
LORETA (Pascual-Marqui et al., 1994)	Assumes spatial smoothness	Sensitive to deep sources (Asadzadeh et al., 2020) Slightly sensitive to extended sources (Grova et al., 2006)	May provide over-smoothed solutions increased blurring over 3D grid Numerical instabilities when applied on a tessellated cortical surface (because of the computation of the Laplacian), regularization is required
cMEM (Chowdhury et al., 2013)	Flexible spatial prior, assuming that brain activity is organized in cortical parcels	Sensitive to spatial extent of the source	Poorly sensitive to deep sources, no depth weighted strategy applied
wMEM (Lina et al., 2012)	Flexible spatial prior, assuming that brain activity is organized in cortical parcels	Suitable for the localization of transient oscillations (seizure onset, high frequency oscillation) or ongoing resting state activity	Poorly sensitive to deep sources, no depth weighted strategy applied

4 EEG/MEG in resting state oscillations and connectivity

4.1 Introduction

This chapter will discuss the utility and challenges of EEG/MEG in studying spontaneous brain activity. Resting-state refers to the state of the brain when the subject is awake but not engaged in any specific task or exposed to any external stimuli (Niso et al., 2019). Understanding resting brain activity has gained increasing interest. EEG and MEG are widely used to study resting brain activity due to their high temporal resolution and non-invasive nature. Analyzing resting-state activity in healthy brains provides a baseline for studying alterations associated with diseases such as schizophrenia (Hirano & Uhlhaas, 2021), Alzheimer's disease (Montez et al., 2009), Parkinson's disease (Bosboom et al., 2006), and epilepsy (Aydin et al., 2020). The resting-state analysis will be discussed in two sub-categories: resting-state oscillations and connectomics analysis.

4.2 Resting-state oscillations

One of the most studied types of resting-state brain activity is brain oscillations, a concept as old as the history of EEG. Berger identified a large amplitude rhythm of approximately 10 Hz, induced by eye closure during wakefulness, and named it the alpha rhythm (Berger, 1929). He also named the faster, smaller amplitude wave beta, which appears when the eyes are open. Brain oscillations have been associated with different brain states (wakefulness or sleep, eyes closed or open), health, and disease. This chapter only focuses on wakefulness resting state activity.

4.2.1 Canonical frequency bands

EEG/MEG oscillations are classified into canonical frequency bands such as delta (1–4 Hz), theta (4–8 Hz), alpha/mu (8–13 Hz), beta (13–30 Hz), and gamma (30–80 Hz), although the limits of these bands vary slightly in the literature. According to Lopes da Silva (2013), the bands are classified as infra low (<0.2 Hz), delta (0.2-3.5 Hz), theta (4-7.5 Hz), alpha and mu (8-13 Hz), beta (14-30 Hz), gamma (30-90 Hz), and high-frequency oscillations (HFO; >90 Hz). Slower frequencies are generally generated by large spatial regions, whereas higher frequencies are generated by more local regions.

The terms ‘brain rhythms’ and ‘oscillations’ are often used interchangeably. ‘Oscillation’ is also used to limit analysis to a frequency band of interest. As described by Lopes da Silva (2013), *“EEG/MEG activity within a given frequency range does not imply that a well-defined oscillation exists; to identify an EEG/MEG oscillation, one has to show a spectral peak within the frequency band of interest. The oscillation is then defined by the peak frequency, bandwidth, and power (or amplitude)”*. Studies of brain oscillation are conducted in terms of peak frequency (also called spectral peak), power spectral density (PSD), and average band power or amplitude.

4.2.2 Brain regions associated with different frequencies

Alpha is the best studied oscillation as it is easily detectable from the occipital lobe when a person is at rest with their eyes closed. Alpha oscillation is also found in the parietal and temporal lobes. Alpha activity decreases with attention, when performing a task, or visual input (Nunez et al., 2001). Beta oscillations are mostly found in the pre- and post-central gyri and are associated with the motor system (Jensen et al., 2019). Theta oscillations are prominent over frontal midline regions (Mitchell et al., 2008). Whereas they constitute a hallmark of sleep rhythms, delta oscillations are broadly distributed and prominent in pathological states during wakefulness. Gamma oscillations are not always localized in the same regions (Groppe et al., 2013).

Figure 4-1 shows the group average of brain maps computed from MEG-estimated resting state power in source space for five healthy participants reported by Niso et al. (2019) after applying dynamic statistical parametric mapping (dSPM). Power was calculated in delta (2–4 Hz), theta (4–8 Hz), alpha (8–12 Hz), beta (15–30 Hz), gamma1 (30–80 Hz), and gamma2 (80–150 Hz) bands. They found strong delta power over fronto-orbital regions and anterior temporal poles, distributed theta power bilaterally over the frontal lobe, alpha power over the parieto-occipital regions, strong beta power over the pre- and post-central lobules, and low and high gamma power dominant over the prefrontal and occipital areas.

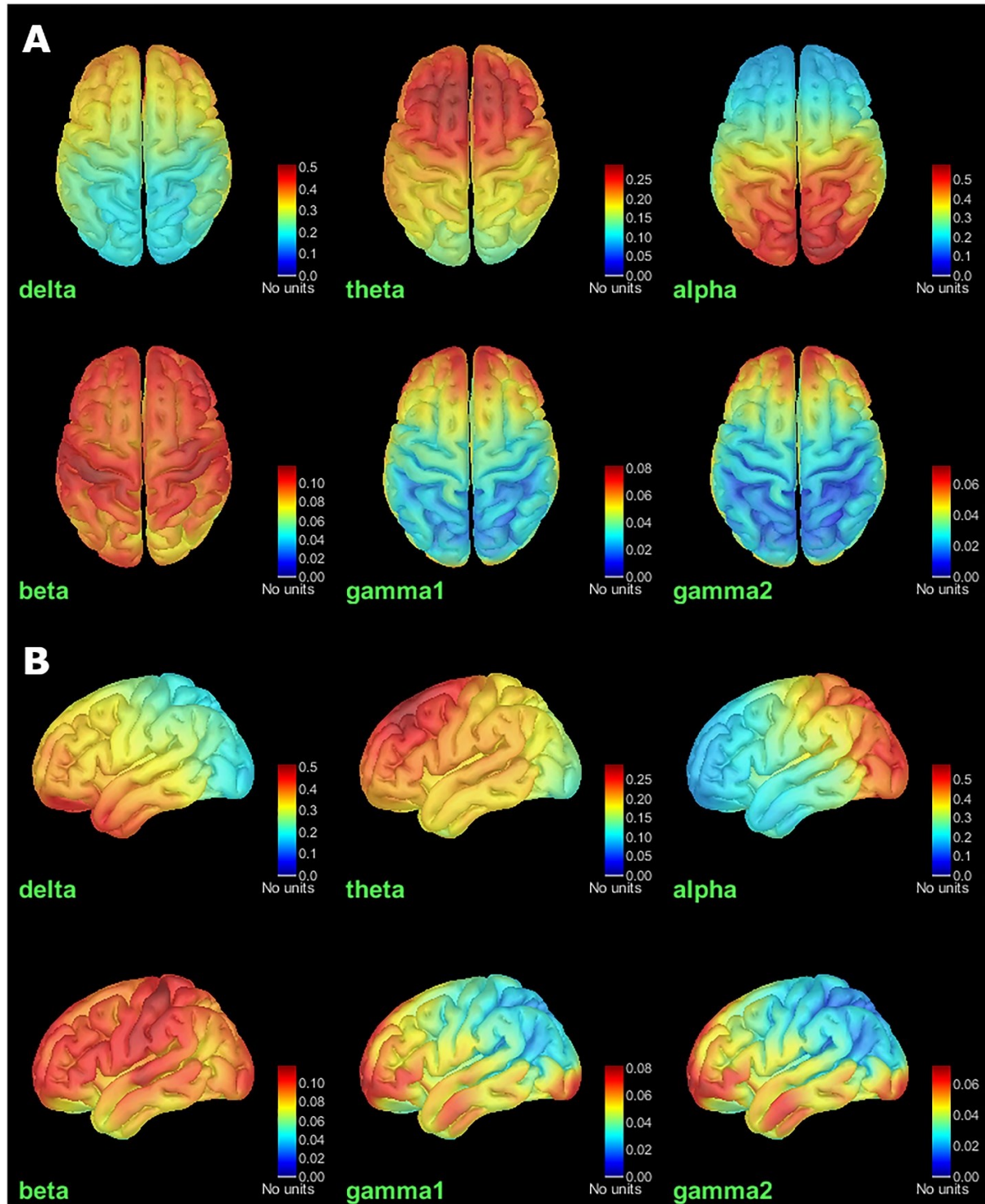


Figure 4-1 Group average of relative power maps for all frequency bands (delta (2–4 Hz), theta (4–8 Hz), alpha (8–12 Hz), beta (15–30 Hz), gamma1 (30–80 Hz), and gamma2 (80–150 Hz)). (A) Top View. (B) Left view. Values range between 0 and 1, indicating the power of cortical signals relatively to the total

signal power across the frequency spectrum. Illustration taken from *Brainstorm Pipeline Analysis of Resting-State Data From the Open MEG Archive* by Niso et al. (2019).

Using resting-state MEG data from 128 healthy participants, Capilla et al. (2022) provided a brain map of natural frequency, using linearly constrained minimum variance (LCMV) beamforming (Van Veen et al., 1997) to localize resting state MEG data along the cortical surface. Natural frequency was defined as “*the peak frequency of the most characteristic spectral pattern of a brain region in comparison with others.*” They found delta and theta band peaks in the medial frontal and temporal regions, alpha peaks in posterior occipital-temporal regions, beta peaks in the motor and lateral prefrontal cortex, and high alpha and low beta peaks in the parietal region (Figure 4-2). This study did not use predefined canonical frequency bands. Using a data-driven approach, they showed that the frequencies associated with each brain region were organized in a manner resembling the canonical frequency bands. The most dominant frequency band was alpha (8-13 Hz). Similarly, using ~200 MEG resting-state data from healthy individuals localized using the LCMV beamformer, Mahjoory et al. (2020) reported that MEG spectral peaks were indeed organized in canonical frequency bands: 4–7.5 Hz (theta), 8.5–13 Hz (alpha), 15–25 Hz (low beta), and 27.5–34 Hz (high beta) (Figure 4-3).

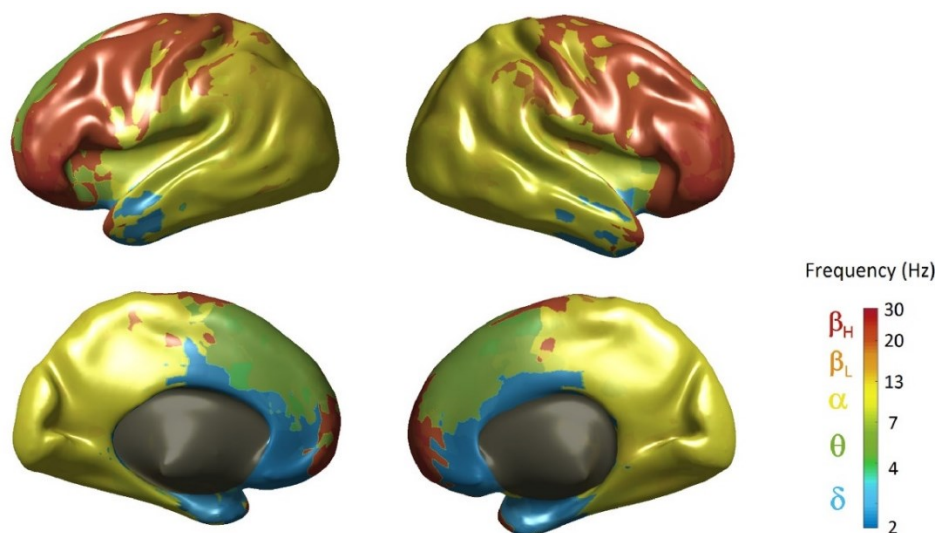


Figure 4-2 Brain map of natural frequencies during resting state MEG. Distribution of natural oscillations at the single-voxel level exhibiting both a medial-to-lateral and a posterior-to-anterior gradient of increasing frequency. Canonical frequency band ranges are color-coded to facilitate interpretation. Illustration taken from *The natural frequencies of the resting human brain: An MEG-based atlas* by Capilla et al. (2022).

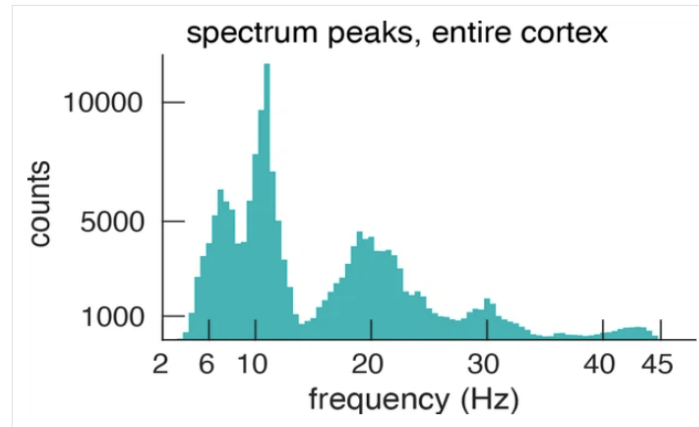


Figure 4-3 Histogram of all detected spectral peaks (across ROIs and participants) delineates the classical frequency bands used in the EEG and MEG literature (theta 3.5–7.5 Hz, alpha 8.5–13 Hz, low-beta 15–25 Hz and high-beta 27.5–34). Illustration taken from *The frequency gradient of human resting-state brain oscillations follows cortical hierarchies* by Mahjoory et al. (2020).

In contrast, when using intracranial ECoG data from 15 individuals with epilepsy, Groppe et al. (2013) reported that the dominant awake resting state frequency was around theta (~7 Hz), unlike the ~10 Hz alpha activity reported by EEG/MEG studies. The histogram of spectral peaks showed peaks mostly around 7 Hz and also around 3, 9, 15, 22, and 35 Hz respectively (Figure 4-4). However, they noted that careful investigation is needed to confirm these differences because the data were not representative of normal brain activity.

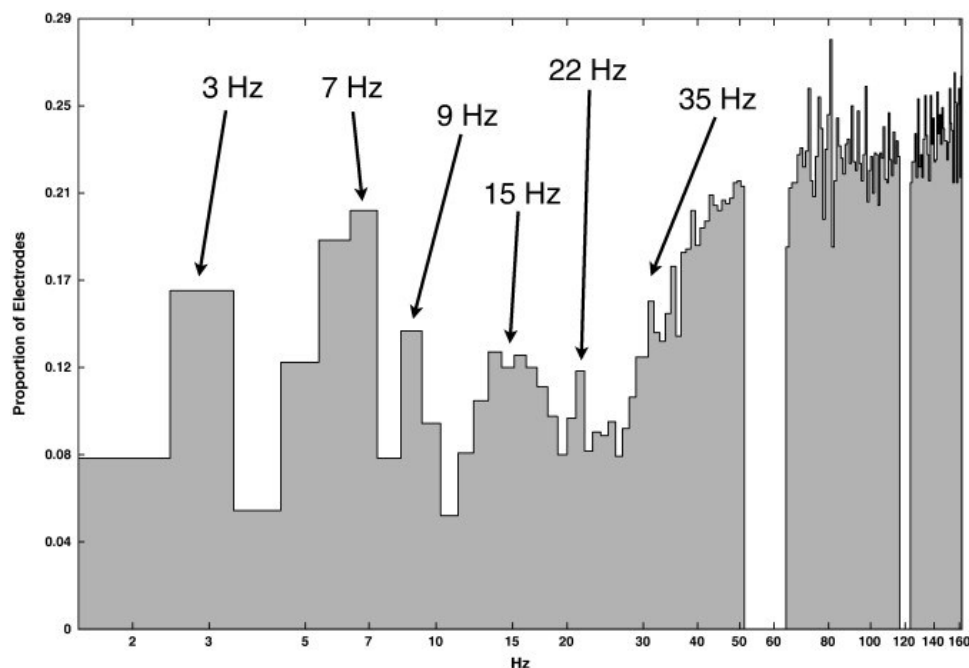


Figure 4-4 Histogram of Spectral Power Density peaks of whitened data found across all electrodes and participants. Note that Hertz is scaled logarithmically (applied whitening to dampen the $1/f$ effect). Illustration taken from *Dominant frequencies of resting human brain activity as measured by the electrocorticogram* by Groppe et al. (2013). Reprinted with permission from Elsevier.

In summary, while specific brain regions have been robustly associated with particular frequency bands in both EEG and MEG studies, it is crucial to validate the localization and spatial extent of resting-state oscillations carefully. This is because EEG and MEG require solving the inverse problem and reconstructing signals from deep sources is more uncertain than from superficial regions. ECoG studies, which are typically restricted to superficial regions, have reported some differences in dominant frequency bands and spectral peaks. However, to compare EEG/MEG resting state oscillations in healthy brain, intracranial EEG studies should be carefully conducted to include electrodes from healthy brain regions, following the methodology proposed by Frauscher et al. (2018) when developing the first atlas of physiological intracranial EEG data. We will carefully consider this atlas for our validation studies in Chapters 6 and 8.

4.2.3 Decomposition of power spectrum into periodic and aperiodic components

Importantly, before assessing oscillatory peaks from electrophysiology signals it is important to consider that the power spectrum of electrophysiological signals typically follows a power law distribution, i.e., power decreases exponentially with increasing frequency. Actually, when plotting the logarithm of power spectrum energy as a function of the logarithm of the frequency, this power law ($1/f$ trend) will result in a linear negative slope within this log-log representation. This trend, known as the aperiodic component, or $1\text{-over-}f$ ($1/f$) component (also known as the arrhythmic or scale free component of electrophysiological signals), was previously regarded as background noise of little interest in the spectra (Bush et al., 2024). Traditionally, most studies did not separate this aperiodic component when evaluating power spectra. However, recent research has suggested that separating periodic and aperiodic components provides a more accurate estimation of the periodic component, especially when analyzing electrophysiological power spectra targeting neuronal oscillations (Donoghue et al., 2021; Wen & Liu, 2016). This shift in approach has been facilitated by the development of specific methods designed to extract this $1/f$ component, such as irregular-resampling auto-spectral analysis (IRASA) (Wen & Liu, 2016) and ‘Fitting Oscillations & One Over F’ (FOOOF or specparam) (Donoghue et al., 2020). FOOOF has become a widely

used method (Donoghue et al., 2020) (Huang et al., 2021; Mahjoory et al., 2020; Ramsay et al., 2021; Senoussi et al., 2022; Wiesman et al., 2022) for separating the periodic components from the aperiodic components of the spectra by parameterizing the power spectra as a combination of these two elements. The FOOOF algorithm employs an iterative fit-refit process to model the power spectral density, where the aperiodic component is represented by an exponential function, and each periodic component is modeled as a Gaussian function. The central frequency identified in each Gaussian fit is then considered as an ‘oscillatory peak’ (Figure 4-5).

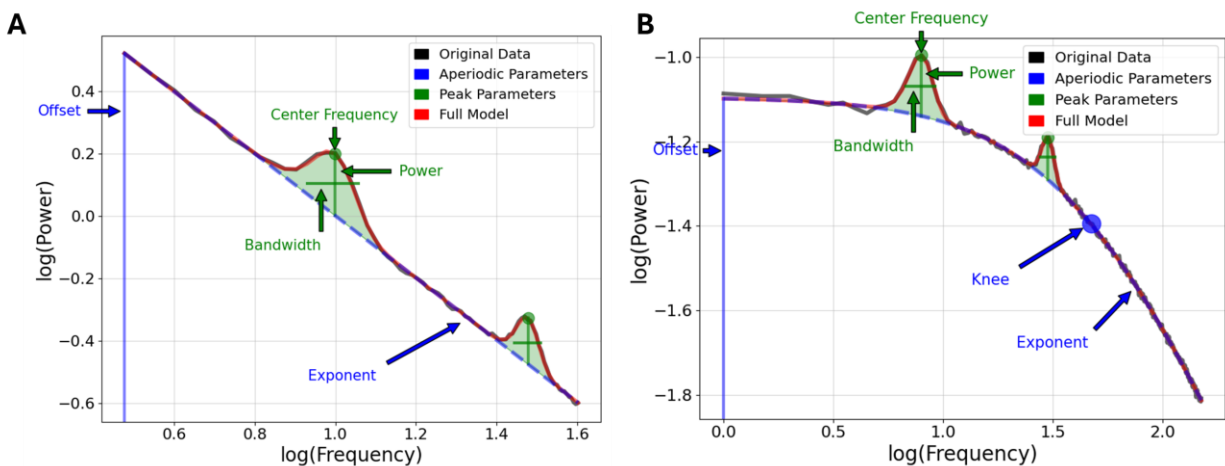


Figure 4-5 Periodic and aperiodic components of the spectra in log-log space shown for an (A) Example of a linear $1/f$ trend and (B) $1/f$ with a bend called knee. The periodic component is described with a peak frequency, power of the peak over the aperiodic component and the bandwidth, or the width of the peak. The aperiodic component is characterized by the offset, (overall up/down translation of the whole spectrum), the exponent, and the knee. Figure from https://fooof-tools.github.io/fooof/auto_tutorials/plot_01-ModelDescription.html#sphx-glr-auto-tutorials-plot-01-modeldescription-py (Donoghue et al., 2020), <https://doi.org/10.1038/s41593-020-00744-x>.

The aperiodic component is typically characterized by its slope (also called the $1/f$ exponent) and the offset of the broadband power of the signal (Figure 4-5) (He, 2014; Pani et al., 2022). When plotted in log-log space, the aperiodic component appears as a straight line across frequencies. However, depending on the electrophysiological data and frequency range, this component may not form a pure line in the log-log plot and could instead display a bend or knee. The knee frequency is the point where the slope of the spectrum changes. For instance, knee frequencies have been identified at around 20 Hz in resting-state EEG (Colombo et al., 2019) and 15 Hz in

resting-state MEG (Chaoul & Siegel, 2021). Using ECoG data from patients with Parkinson's disease and intracerebral EEG from patients with epilepsy, Bush et al. (2024) found that cortical structures exhibited a knee frequency around 17 Hz, while subcortical structures did not show a knee.

Importantly, the aperiodic components have recently garnered significant interest (Bódizs et al., 2021; da Silva Castanheira et al., 2024; He, 2014; Ostlund et al., 2021; Ouyang et al., 2020; Schaworonkow & Voytek, 2021; Wilkinson & Nelson, 2021). The slope of the $1/f$ component has been associated with factors such as aging (Voytek et al., 2015), different states of consciousness (Huang et al., 2020), sleep stages (Miskovic et al., 2019) and disruption of excitation/inhibition balance in diseases such as epilepsy, autism, and Alzheimer's (Martínez-Cañada et al., 2023; Salvatore et al., 2024). Given the recent advancements in understanding these aperiodic components, it has become necessary to validate both the periodic and aperiodic components estimated by EEG/MEG source imaging and to assess whether these components are influenced by source imaging methods and their parameters, modalities and sensor types, and source localization from deep brain generators. In this thesis, we primarily focused on the periodic component of oscillations, and therefore, the $1/f$ component was first carefully removed for spectral analysis.

4.3 Resting-state connectome

Brain connectomics is a field of neuroscience that focuses on the study of the brain's connectome, a concept introduced by Sporns et al. (2005). Sporns et al. (2005) defined the connectome as "*the connection matrix of the human brain.*" Marc et al. (2013) further described the connectome as "*a complete graph of a neural network...a comprehensive list of every connection in a defined neural region.*" The scale of the connectome ranges from the micro-scale of individual synaptic connections between neurons to the macro-scale of brain regions and interregional pathways.

Initially, the study of the human brain connectome focused primarily on MRI-based imaging modalities (Glasser et al., 2016). Structural connectomes were computed using diffusion-weighted MRI (dMRI), providing a static map of anatomical connections (Sporns, 2011). Initiated with the seminal work of Biswal et al. (1997), functional connectivity was mainly investigated using resting state fMRI, which offers an indirect measure of neural activity by monitoring the whole brain slow

hemodynamic fluctuations (Larson-Prior et al., 2013). The great majority of resting state fMRI studies in healthy and pathological conditions investigate static correlations between very slow hemodynamic fluctuations (< 0.1 Hz) (Fox & Raichle, 2007), whereas dynamic fMRI connectivity analysis has recently emerged (Preti et al., 2017). In the neuroimaging field, the term "functional connectivity" was first defined by Karl Friston as "the temporal correlations between spatially remote neurophysiological events" (Friston et al., 1993).

In recent years, to better understand dynamic brain activity by leveraging the high temporal resolution of electrophysiological methods, EEG and MEG have become popular in functional connectome studies. However, these methods have limited spatial resolution. While anatomical connectomes can achieve submillimeter precision and fMRI provides approximately 2 mm voxel resolution (Uğurbil et al., 2013), the spatial resolution of EEG and MEG remains around 10 mm, even after applying source imaging techniques (Lin et al., 2006). See Table 4-1 from (Larson-Prior et al., 2013)) summarizing the anatomical connectivity, and functional connectivity by fMRI and EEG/MEG.

Table 4-1 Connectivity characteristics of imaging modalities adapted from *Adding dynamics to the Human Connectome Project with MEG* by Larson-Prior et al. (2013). Reprinted with permission from Elsevier.

	Dynamic structure	Imaging basis	Imaging characteristics	Variety of connectivity metrics
Anatomical connectivity	Static	Anisotropic diffusion of water	Recoverable with diffusion tensor imaging (DTI) technique, diffusion spectrum imaging (DSI) (~ 1 mm resolution)	One

	Dynamic structure	Imaging basis	Imaging characteristics	Variety of connectivity metrics
fMRI connectivity	frequency range nominally < 0.1 Hz	Indirect measure of neural population activity (hemodynamic response to synchronized neural population activity, BOLD)	Recoverable with fMRI (~ 3 mm resolution)	A few, but mainly correlation between BOLD signals
Electrophysiological connectivity	Strongly nonstationary, frequency range from DC to ~ 1000 Hz	Direct measure of synchronized neural population activity (magnetic/electric fields generated by synchronized synaptic current)	Model dependent (~ 4 mm precision for sparse cortical activations, ~ 10 mm spatial resolution) Requires solving the EEG/MEG source imaging inverse problem	Many

In the following sections, the use of EEG/MEG in connectomics studies, their strengths, and their challenges will be discussed.

4.4 EEG/MEG based functional connectome

The use of non-invasive electrophysiological methods such as EEG and MEG in connectomics studies offers several advantages. These methods allow for the study of the human brain in both

healthy individuals and patient groups. When compared to fMRI studies, they offer high temporal resolution for examining brain dynamics and therefore a plethora of possible connectivity metrics, where most fMRI connectomes are built using a correlation between fMRI BOLD signals. Importantly, EEG/MEG also enables the study of connectomes across different frequency bands. However, there are two main challenges: (i) challenges associated with EEG/MEG source imaging such as low SNR signal, particularly from deep generators and resting-state activity, and (ii) the issue of volume conduction in EEG, and the field spread in MEG, which introduces source leakage issues after source reconstruction.

4.5 Connectivity metrics used in connectome study and challenges

Connectivity studies in electrophysiological connectomics can be categorized into within-frequency band and between-frequency band analyses. The connectivity metrics used in within-frequency band studies can be classified into amplitude-based and phase-based metrics. The same metrics can also be considered to study the between-frequency band analyses (will not be discussed). In this section, we will first review the different connectivity metrics proposed when estimating EEG/MEG connectomes.

4.5.1 Phase-based metrics

A common metric to compute functional connectivity between two different brain regions is coherence. Coherence measures the linear synchrony between two signals in a specific frequency band. Srinivasan et al. (2007) defined coherence as “*a measure of synchronization between two signals based mainly on phase consistency; that is, two signals may have different phases, but high coherence occurs when this phase difference tends to remain constant.*” The main limitation of the coherence metric is its inability to analyze non-linear and non-stationary signals. Coherence is a measure of spectral covariance and does not separate the effects of amplitude and phase (Zhang et al., 2014).

Another widely used phase-based metric appropriate for studying interactions between nonstationary data is the Phase Locking Value (PLV) (Lachaux et al., 1999), also known as mean phase coherence (MPC) (Mormann et al., 2000). Bruña et al. (2018) defined PLV as: “*PLV evaluates the spread of the distribution of phase differences, and the connectivity estimation is linked to this spread. The narrower the distribution of the phase difference, the higher the PLV*”

value, which ranges between zero (no phase dependence) and one (complete phase dependence)". PLV is similar to coherence but not affected by the signal amplitude. PLV does not require stationarity of data.

However, both PLV and coherence are sensitive to volume conduction (or field spread in MEG) and source leakage issue, which introduces spurious connectivity with zero phase difference (Bruña et al., 2018). To address this, metrics that discard zero-lag connectivity have been proposed, such as the imaginary part of coherency (Nolte et al., 2004), imaginary PLV (iPLV), and corrected imaginary PLV (ciPLV) (Bruña et al., 2018). However, it is acknowledged that metrics correcting for zero-lag connectivity may also remove genuine zero-lag interactions, resulting in false negatives (see our detailed analysis and discussion in Chapters 8 and 9).

Another phase-based metric is the phase lag index (PLI) (Stam et al., 2007), which measures the consistency of phase lags between two signals. Kim and Davis (2021) defined PLI as: "*The PLI is a mathematical calculation between two signals where nonzero phase lag between two signals are calculated and summarized as an index value where 1 represents maximal phase synchrony and 0 represents no synchrony*". PLI and its variations, such as the weighted phase lag index (wPLI) (Vinck et al., 2011) and directed phase lag index (dPLI) (Stam & van Straaten, 2012), are by definition corrected for zero-lag connectivity as they consider only nonzero phase lags.

The phase and amplitude (also called envelope) estimates of the signals can be computed using the Hilbert transform or by using wavelets (Le Van Quyen et al., 2001; Schnitzler & Gross, 2005a). While it is technically feasible to apply this transform and obtain phase and amplitude estimates on broadband time series data, it is recommended to apply it on narrowband signals to obtain meaningful and interpretable estimates (Cohen, 2014).

4.5.2 Amplitude-based Metrics

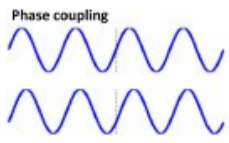
A popular metric for computing functional connectivity is amplitude envelope correlation (AEC). Bruns et al. (2000) defined AEC as: "*Amplitude envelope correlation involves the calculation of the spectral amplitude envelope from a time series using a Fourier transform, and then the correlation between the two envelopes is calculated within a given time window.*" Bandpass filtering of data in canonical frequency bands using the Hilbert transform to extract the signal envelope in a specific frequency band (Brookes et al., 2011) has been commonly used in later

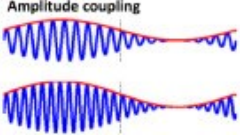
studies. AEC is also affected by source leakage, which can be mitigated by a process called orthogonalization (Brookes et al., 2012). To address this issue, a pairwise orthogonalization process is applied before computing the correlation between the envelopes. Orthogonalization between two signals involves removing the signal components that share the same phase between the two signals (Brookes et al., 2011; Colclough et al., 2016; Hipp et al., 2012).

Sadaghiani et al. (2022) summarizes these metrics in Table 4-2. They recommended leakage correction for EEG/MEG connectivity analysis while also acknowledging that this process also removes true zero-lag connectivity.

Table 4-2 Mathematical techniques to characterize connectivity between electrical signals derived from separate brain regions. Table from Sadaghiani et al. (2022)

<https://doi.org/10.1016/j.neuroimage.2021.118788>

Measurement	Mechanism	Considerations	Methods of application
	<p>We seek a fixed phase relationship between band limited signals, from spatially separated brain regions.</p>	<p>Should always be applied in source space to mitigate problems with volume conduction (EEG) or field spread (MEG) Signal ‘leakage’ between regions can lead to artificially high phase coupling metrics. Consequently leakage correction is required.</p>	<p>Coherence; phase locking value (PLV); phase difference derivative – all assess fixed phase relationships but are affected by signal leakage)</p> <p>Imaginary Coherence; phase lag index (PLI); weighted phase lag index (wPLI) - inherently correct for leakage by removing zero phase lag interactions.</p>

Measurement	Mechanism	Considerations	Methods of application
	<p>The amplitude (or power) envelope of band limited oscillations is computed and we seek to find correlations in the amplitude envelope between regions</p>	<p>Should always be applied in source space. As with phase interactions, ‘leakage’ between regions can lead to artificially high correlation and so leakage correction is required.</p>	<p>Amplitude coupling is typically measured via Pearson correlation between envelope signals. Prior to this, to mitigate source leakage, signal orthogonalization should be applied using either pairwise or symmetric methods.</p>

The list of connectivity metrics was not exhaustive and many other metrics exist such as mutual information-based metric (Ioannides et al., 2000), metrics based on Granger causality (Granger, 1969) such as directed transfer function (DTF) (Kaminski & Liang, 2005) and or the partial directed coherence (Baccalá & Sameshima, 2001). We refer the readers to the review paper (Schoffelen & Gross, 2009) for more details on these metrics.

4.6 Resting state EEG/MEG connectome studies

In task-based (stimulus/response) connectivity studies, trials are typically repeated many times and averaged. These trials are often compared relative to a baseline period considered as the reference. The baseline is usually taken from a pre-stimulus ongoing background. In most task-based studies, resting-state activity during the task is normalized with the baseline to identify a contrast. These studies also often focus on a few sensors of interest or brain regions of interest instead of whole-brain coverage (Sadaghiani et al., 2022). However, when studying resting-state activity, the data are by definition low SNR. Additionally, resting state EEG/MEG connectome studies usually consider the whole brain. Therefore, since we are dealing with whole brain characterization of the connectomes using low SNR resting state data, the choice of source imaging method connectivity metrics requires careful consideration and caution. Several studies investigated the reliability of

the connectivity metrics focusing notably on the source leakage issue. In the next section, a few of these studies will be briefly mentioned in this context.

4.6.1 Which connectivity metrics are suitable for EEG/MEG resting state analysis

Validation of connectome estimated from EEG/MEG source imaging applied to resting state data remains challenging and is the main topic of this thesis. Due to the lack of a definitive ground truth, many studies propose to use numeric simulations (Haufe et al., 2013; Vallarino et al., 2023), which are still lacking realism to mimic real resting state data. Another approach, which is not per se a proper validation, is to assess consistency or reproducibility, comparing correlations between connectivity networks estimated using specific metrics across different sessions or subjects (Colclough et al., 2016). Such an approach has been largely considered when assessing the consistency of fMRI-based connectomes (Bellec et al., 2010). Additionally, correlations between connectomes estimated across different modalities have been also considered (Rizkallah et al., 2020; Wirsich et al., 2020; Wirsich et al., 2021). The Intraclass Correlation Coefficient (ICC) is commonly used to evaluate the consistency of connectivity metrics across various conditions or sessions. High ICC values suggest that a metric is consistent and reproducible, while low ICC values indicate variability or inconsistency. Various terms such as consistency, reproducibility, and reliability have been used across studies to describe these important aspects.

Using resting-state MEG data, Colclough et al. (2016) reported that metrics that are not corrected for zero-lag connectivity (uncorrected) showed higher reproducibility and consistency when compared to the metrics that remove zero-lag connectivity (corrected). Among the corrected metrics, the most consistent metric was orthogonalized AEC. They reported, “*the most consistent connectivity measure to employ for resting-state studies is the correlation between orthogonalised, band-limited, power envelopes*”. Using resting state MEG, Garcés et al. (2016) reported high reliability for uncorrected metrics (PLV and AEC) compared to zero-lag-corrected metrics (orthogonalized AEC and PLI). Similar results were reported after localizing EEG resting state data by Nagy et al. (2024) and Duan et al. (2021). Using high-density EEG and MEG resting state data localized, Rizkallah et al. (2020) compared high-density EEG and MEG connectomes with fMRI-derived connectomes, finding significant but low correlations for uncorrected metrics (AEC and PLV). Metrics that removed zero-lag connectivity did not exhibit significant spatial cross-modal correlations. These studies suggested that volume conduction or source leakage might

contribute to the high reliability observed for uncorrected metrics and that corrected metrics might also eliminate genuine neural synchrony driven by underlying anatomical structures. Generally, zero-lag corrected metrics are recommended despite their lower consistency.

To summarize, uncorrected metrics generally exhibit higher reproducibility and consistency across sessions and subjects and stronger correlations with fMRI-derived connectomes. However, they are largely influenced by volume conduction and signal leakage. In contrast, corrected metrics aim to reduce the effects of volume conduction and signal leakage, and underlying “true” connectivity values are more likely an order of magnitude smaller when compared to metrics biased by volume conduction and signal leakage. However, removing zero-lag connectivity values may also eliminate true neural synchrony, resulting in reduced reproducibility and weaker correlations with other modalities.

Palva et al. (2018) considered MEG simulations to investigate the issue of source leakage. They defined two types of false positives associated with EEG/MEG-derived connectivity: artificial coupling due to signal spread in source reconstruction and spurious coupling from ghost interactions. They defined ‘ghost interactions’ as “false-positive interactions that reflect true interactions with misestimated locations.” Their study demonstrated that metrics corrected for zero-lag connectivity could address the issue of artificial coupling but remained prone to spurious coupling. They concluded that it is challenging to completely eliminate false coupling, even with corrected metrics.

These studies highlight the complexity of assessing connectivity metrics in EEG/MEG research and emphasize the importance of careful interpretation of results, especially in the context of resting-state data. A major limitation of these studies is the absence of a definitive ground truth or reliance on simplistic simulations as ground truth.

4.6.2 Comparison of EEG/MEG connectome with other modalities

Several MEG studies that considered amplitude envelope correlation-based metrics have provided evidence of the presence of intrinsic connectivity networks (ICNs), similar to the one previously established using resting state fMRI studies. For example, using beamformer source imaging and AEC metric, Hipp et al. (2012) showed that MEG-derived resting state source space connectivity could reflect several typical ICNs such as somatomotor, visual, and auditory networks (Figure

4-6A). They reported that typical ICNs were mostly reflected in the alpha and beta bands. Using an independent component analysis on connectivity obtained using amplitude envelope correlation on MEG resting state data (after beamformer source imaging), Brookes et al. (2011) found that several ICNs could be identified and that they were similar to fMRI-derived ICNs with high spatial similarity (Figure 4-6B).

Several studies (Hipp & Siegel, 2015; Wirsich et al., 2020; Wirsich et al., 2021) investigated connection-wise spatial similarity between connectomes derived from two types of modalities (EEG/MEG and fMRI). Wirsich et al. (2017) reported significant but small cross-modal correlations between the two modalities at the individual level using simultaneous fMRI and EEG using phase-based and amplitude-based connectivity metrics (after applying minimum-norm source imaging). A larger effect size was found when they correlated the group average of EEG and fMRI-derived connectomes. This cross-modal correlation with a similar effect size was reproduced using simultaneous EEG-fMRI for different EEG montages (from 64 channels to 256 channels) and MRI field strengths (1.5 to 7T) (Wirsich et al., 2021) (Figure 4-6D).

Similar cross-modal correlations were found when fMRI-derived connectivity was compared with intracranial ECoG (Figure 4-6C) (Betz et al., 2019). These results were summarized in Figure 4-6 by Sadaghiani et al. (2022). Although these studies have found consistent cross-modal connectivity patterns, fMRI is an indirect measure of neuronal activity that measures the changes in blood oxygenation using blood-oxygen-level-dependent (BOLD) contrast. Thus, direct comparison between fMRI and EEG/MEG connectomes is not optimal and one-to-one correspondence is therefore not expected, since these modalities and proposed metric are sensitive to different components of the underlying functional connectome.

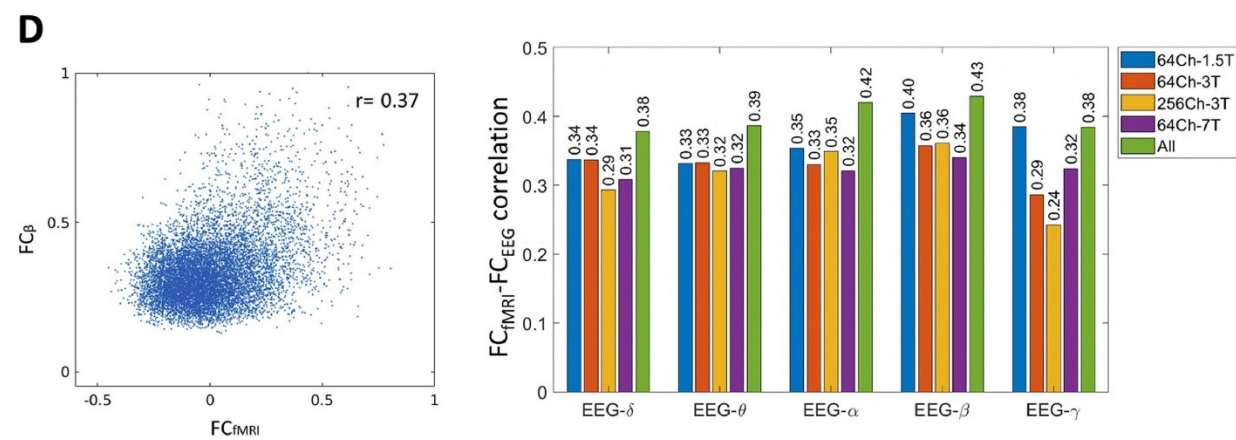
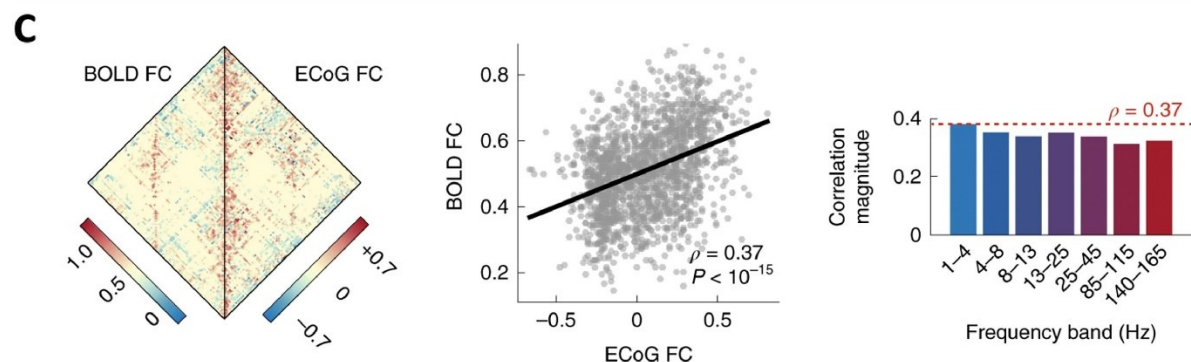
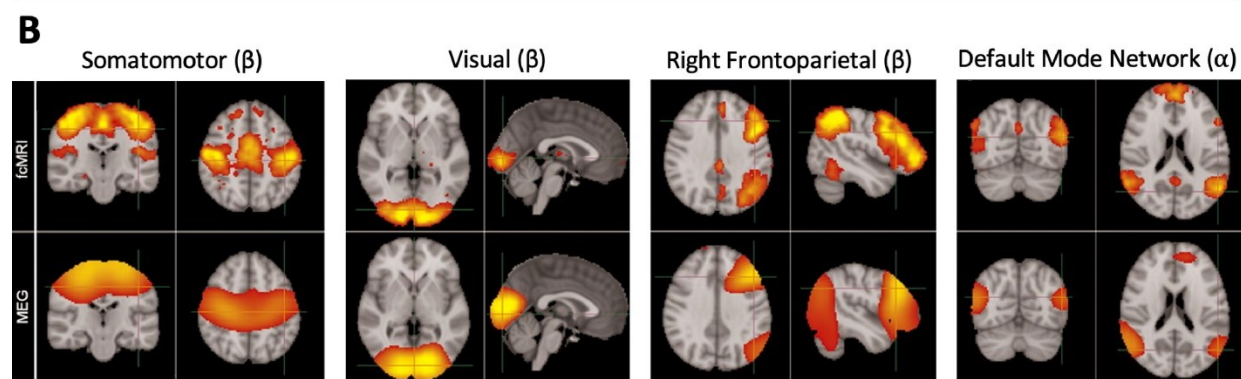
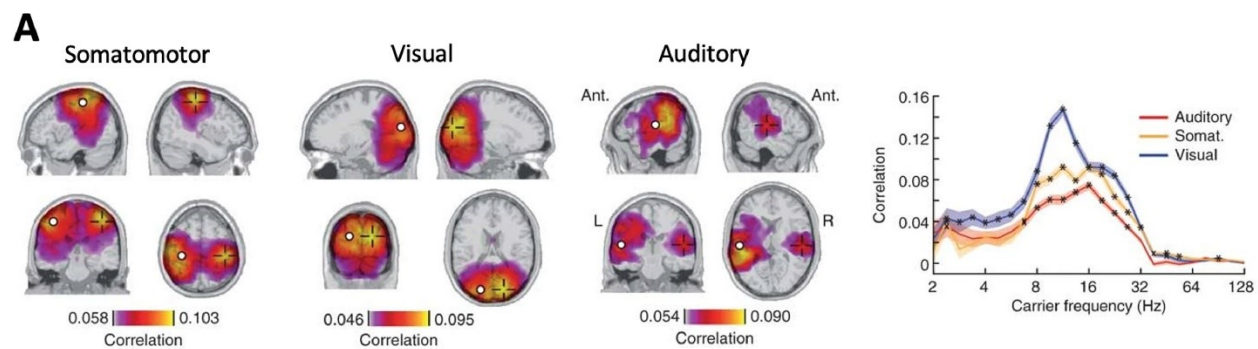


Figure 4-6: The presence of an intrinsic whole-brain connectivity organization in electrophysiological data. A) Sensory and motor ICNs as observed with seed-based connectivity in source-space MEG amplitude coupling. The spectral plot (right) indicates a strong contribution from alpha and beta band oscillations to these intrinsic networks (adapted from Hipp et al., 2012). B) Temporal ICA of band-specific oscillation amplitudes in MEG yields numerous ICNs (four are shown as examples), including sensory/motor as well as higher-order networks. Alpha and especially beta bands captured ICN organization well. A direct comparison between the MEG-derived (bottom row) and the fMRI-derived (top-row) independent component maps demonstrates high spatial similarity (adapted from Brookes et al., 2011). C) Connection-wise connectivity strength is spatially associated between fMRI and intracranial electrophysiology (ECoG amplitude coupling, pooled over patients). The strength of this correlation is around ~ 0.35 for all frequency bands (adapted from Betzel et al., 2019). D) A similar spatial association of connection-wise connectivity strength is observed between fMRI and concurrently recorded scalp EEG (phase coupling). The left scatterplot shows an example for the beta band, where each data point is from one connection (region pair) of the connectome averaged across subjects (adapted from Wirsich et al., 2017). This relationship is reproducible at similar effect size across various MRI field strengths (1.5–7T) and EEG densities (64–256 channels) (adapted from Wirsich et al., 2021). Illustration taken from *Connectomics of human electrophysiology* by Sadaghiani et al. (2022), <https://doi.org/10.1016/j.neuroimage.2021.118788>.

4.6.3 Connectome studies with intracerebral EEG

Connectivity studies reported using in-situ intracerebral EEG data provide highly accurate estimations of connectivity due to the high SNR signals (unlike EEG/MEG) and the ability to investigate deep brain structures (unlike ECoG). These techniques do not depend on the resolution of an ill-posed source localization problem, but on the other hand, intracranial EEG suffers from limited spatial sampling and they do not cover the whole brain, at the single-patient level. Using a large cohort of intracerebral EEG, Williams et al. (2023) examined group-level resting-state connectomes using PLV. Using the Louvain community detection algorithm (Blondel et al., 2008), they identified different modules of networks from the connectome and found that these modules consisted of anatomically contiguous regions. Unlike resting-state fMRI, intracerebral EEG-derived connectomes did not show a distributed pattern, indicating that intracerebral EEG connectivity using PLV was more local. They also found that these modules were highly similar across canonical frequency bands. One limitation of this study is the data used in this study were

not from normal brains (i.e. they also included electrodes in pathological regions). In this thesis, we used a normative intracranial EEG atlas to validate MEG-derived connectomes (Frauscher et al., 2018), assuming both modalities represent normal brain activity. We also validated the connectome at a single-subject level using simultaneously acquired MEG and intracerebral EEG data, despite the limited spatial coverage at single subject level.

The overall pipeline for computing connectomes from EEG/MEG is nicely summarized by Sadaghiani et al. (2022), as shown in Figure 4-7. The general steps to compute EEG/MEG connectome are: (i) select clean segments of resting state data (with no motion artifacts, eyes closed or eyes open fixating a cross), (ii) Select the frequency bands of interest, (ii) Use brain parcellation for a macroscale connectome analysis, this will reduce the dimensionality of the problem by assessing the time course of specific brain regions, defined using an ad-hoc parcellation of the whole brain or cortical surface (iii) Apply a source imaging method, (iv) Compute within-frequency or between-frequency connectivity between two regions using leakage-corrected metrics to assess the connectome at the spatial scale defined by the chosen parcellation. The properties of the estimated connectome could also be characterized using metrics derived from graph theory. Although, most studies including Sadaghiani et al. (2022) recommended to apply leakage-corrected metrics to compute EEG/MEG connectivity, proper validation is necessary to confirm this approach. This will be a core focus of this thesis.

Importantly, they also outlined the pipeline for computing connectomes from intracranial EEG (iEEG). The iEEG pipeline is similar to the above steps, except that a few can be skipped, such as brain parcellation (although in our intracranial EEG studies at the group level, we also consider brain parcellation, described in Chapters 6 and 8), source localization, and leakage correction. This figure provides a clear summary demonstrating that iEEG (particularly SIEG), can serve as a ground truth because it records brain activity with high SNR directly from the brain tissue, including deep structures. Therefore, it does not require source localization and is minimally affected by source leakage, eliminating the need for leakage correction.

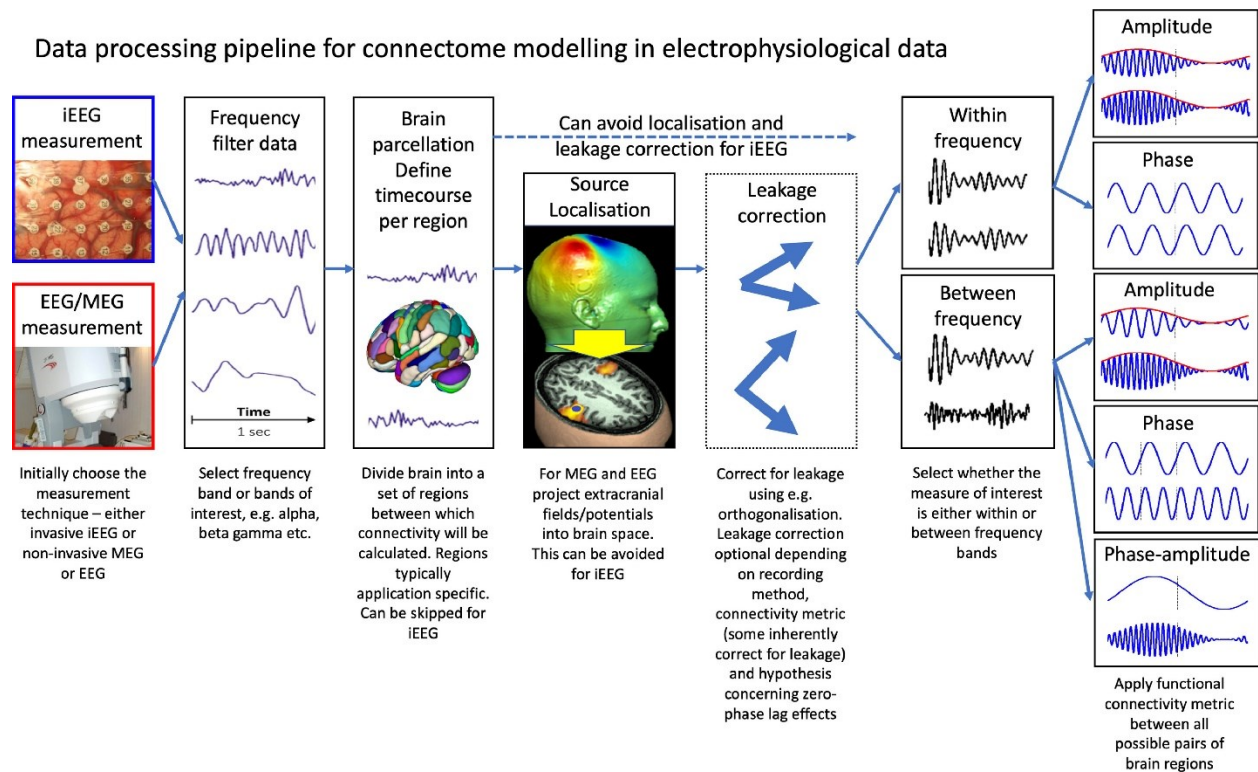


Figure 4-7 Schematic overview showing the process by which connectivity is calculated in electrophysiological data. Figure taken from *Connectomics of human electrophysiology* by Sadaghiani et al. (2022), <https://doi.org/10.1016/j.neuroimage.2021.118788>.

4.7 Conclusion

This chapter described the challenges of EEG/MEG source localization of resting state activity in terms of oscillations and connectivity. We also briefly mentioned how intracranial EEG can be used as ground truth to validate EEG/MEG resting state characteristics. In Chapter 5, more details of intracranial EEG will be described.

5 Validation of EEG/MEG source imaging

5.1 Necessity of validation

Why do we need to validate EEG/MEG source imaging? EEG/MEG source imaging involves solving an ill-posed inverse problem. Therefore EEG/MEG source solutions depend on certain assumptions associated with the choice of a particular source imaging method, and the underlying neuronal generators of the EEG/MEG can never be found with 100% certainty. Source imaging results should be interpreted considering these underlying methodological assumptions. EEG/MEG source localization accuracy also depends on the quality of the detected signal. A high signal-to-noise ratio (SNR) signal is necessary to ensure good and accurate localization. Sources generated from deep brain structures are associated with low SNR scalp signals, making them more difficult to detect and localize from surface measurements. Localizing low SNR resting state or background activity is more difficult than localizing high SNR evoked responses from controlled tasks or spontaneous high SNR abnormal activity, such as epileptic discharges. Localizing a single evoked response or a spontaneous epileptic event is difficult due to low SNR signals, but averaging increases the SNR, thereby improving localization accuracy. However, averaging is not meaningful when analyzing ongoing resting state activity. Thus, EEG/MEG source localization needs to be validated, especially when localizing resting state activity and deep brain activity, which are low SNR signals, but also with high SNR signals because the assumptions made in solving the inverse problem are not necessarily correct.

5.2 Methods of validation

Validation of EEG/MEG source imaging is difficult due to the lack of ground truth. Two main approaches have been considered to validate EEG/MEG source localization: (i) numeric simulations involving different levels of realism and (ii) comparison with intracranial EEG data.

5.2.1 Numeric simulation studies

Simulation models allow us to quantitatively compare the accuracy of EEG/MEG source imaging with a simulated perfectly controlled ground truth. Simulations provide a simplistic configuration of the generators of brain activity and several levels of simulation realism have been proposed. In this section, we are reporting the main trends considered when validating source localization

results using simulations, whereas it would be impossible to provide an exhaustive description given the very large number of publications considering numeric simulation to validate EEG/MEG source localization algorithms. For instance, simulations using a single dipole to represent a brain generator have been largely used (Fuchs et al., 1998; Pascual-Marqui, 2002). Recently, Sohrabpour et al. (2015) simulated single dipoles at different locations with added white Gaussian noise to investigate the relationship between EEG source localization and the number of electrodes. Using those approaches, the underlying simulated dipolar sources are too simplistic and can at best mimic a few early primary sensory responses (e.g. auditory evoked response, electrical median nerve stimulation). Moreover, adding white noise to those simulations is also too simplistic, since real EEG/MEG noise or background is known to be correlated in space and time. In epilepsy, the expected generators of epileptic discharges are often spatially extended over a few square centimeters of the cortex (Tao et al., 2007; von Ellenrieder et al., 2014) and therefore considering a single dipole may not be appropriate to simulate generators of epileptic discharges. To address specially this issue, simulations of an extended patch of uniform activity along the cortical surface have been proposed (Chowdhury et al., 2013; Grova et al., 2006; Liu et al., 2002; Trujillo-Barreto et al., 2004). To be realistic, real EEG/MEG background activity can be added as noise to the activity of the simulated patch, therefore reproducing also a realistic noise structure mimicking real data. This approach provides a way to validate the results of different source imaging methods and their ability to recover the spatial extent of the sources. This model can be extended to two or more patches of simulations to mimic the propagation of epileptic spikes (Chowdhury et al., 2016; Grova et al., 2006). Whereas a large number of source localization techniques were validated considering one or several point-like dipolar sources (correlated or not), the main question addressed by those techniques was the localization error and the ability to localize superficial versus deep focal sources (Fuchs et al., 1999; Pascual-Marqui, 2002; Pascual-Marqui et al., 2002; Stephen et al., 2003). Using our proposed realistic simulation framework and the new validation metrics based on the area under the ROC curve to assess the sensitivity of source localization methods to the spatial extent of the sources (Grova et al., 2006), the MEM-based technique cMEM was found to be more accurate in estimating the spatial extent of the simulated generators located in superficial regions (Chowdhury et al., 2016; Chowdhury et al., 2013; Chowdhury et al., 2015) compared to other distributed source imaging methods such as minimum norm estimate (MNE). Whereas our studies demonstrated that linear distributed source imaging techniques are poorly

sensitive to the spatial extent of underlying sources (Chowdhury et al., 2013; Hedrich et al., 2017; Pellegrino, Hedrich, et al., 2020), other non-linear methods complementary to our MEM approach have also been proposed to assess the spatial extent of epileptic sources (Biro et al., 2011; Chowdhury et al., 2016; Sohrabpour et al., 2020; Sohrabpour & He, 2021). Our previous studies also reported the limitation of cMEM in localizing deep sources, whereas only the fusion of EEG and MEG gradiometers slightly improved the accuracy of cMEM localization for deep generators (Chowdhury et al., 2015). Localizing accurately spatially extended generators located in deep seated regions is a core part of this thesis. It will be discussed further in Chapter 7, where we propose a depth weighting approach in MEM methods and validate it using a realistic simulation environment as well as real EEG/MEG data from patients with focal epilepsy.

Neuronal computational models based on combined biophysical/physiological generative models have been also considered to realistically model simulations of brain activity. Neural mass models based on excitatory and inhibitory interactions of the neuronal population within a macrocolumn of cortex have been proposed to generate realistic physiological and pathological (epileptic) signals (Cosandier-Rim    et al., 2007; Lopes da Silva et al., 1976; Wendling, 2005; Wendling et al., 2000; Wilson & Cowan, 1972). Combining these models over different regions, connecting these models locally or at a distance have been used to model spatially extended generators of epileptic discharges (Cosandier-Rim    et al., 2008). These simulation models allow varying the geometry of the sources while generating a realistic temporal activity that resembles the sensor level activity shown by intracerebral electrodes (Cosandier-Rim    et al., 2007) or MEG sensors (Badier et al., 2007). These models are useful to validate the ability of source imaging methods to reconstruct the time course of the sources (Chowdhury et al., 2016). Hassan et al. (2017) proposed an extensive neural mass model to simulate an extended epileptic network involved during the generation and propagation of epileptic spikes measured in EEG, which resulted in an interesting realistic simulation framework to validate the accuracy of source imaging techniques and connectivity metrics during spike propagation.

While simulations are often useful, it is important to keep in mind that actual brain activity is complex, and modeling brain activity realistically is difficult. Providing realistic simulations of resting-state brain activity featuring long-distance connectivity patterns is even more difficult than simulating focal or focally extended sources, as usually considered in epilepsy. Moreover, even if

it is always possible to simulate connectivity patterns between brain regions (Palva et al., 2018; Vallarino et al., 2023), adding realistic noise or background becomes challenging. One could not add real background EEG/MEG, as for realistic simulations of epileptic discharges (Chowdhury et al., 2013), since such real background will feature unknown connectivity patterns. On the other hand, when considering unstructured white noise in those simulations, underlying simulated connectivity patterns could be retrieved too easily. Neural mass models have been recently proposed to simulate resting state networks (Allouch et al., 2023; Allouch et al., 2022; Bensaid et al., 2019) to evaluate source localization and connectivity analyses. However, they often lack realism when compared to actual resting state brain activity. This leads to our next section, which discusses the use of intracranial EEG as ground truth to validate source imaging techniques. Intracranial EEG records brain activity with high temporal and spatial resolution and provides the best way to validate non-invasive source imaging results for both event-related brain activity, such as epileptic discharges, and resting state activity.

5.2.2 Intracranial EEG

When EEG recordings are obtained with electrodes implanted directly inside the skull/brain, they are called intracranial EEG (iEEG). iEEG electrodes are mostly implanted in patients with epilepsy during presurgical evaluation (Parvizi & Kastner, 2018). The selection of brain sites is based on clinical grounds. iEEG can be either in the form of electrocorticography (ECoG), which uses strips or grids of electrodes located in the subdural space, or stereotaxic EEG (SEEG), which involves bundles of electrodes implanted inside the brain to reach deep sources (Figure 5-1). SEEG is also called depth electrodes.

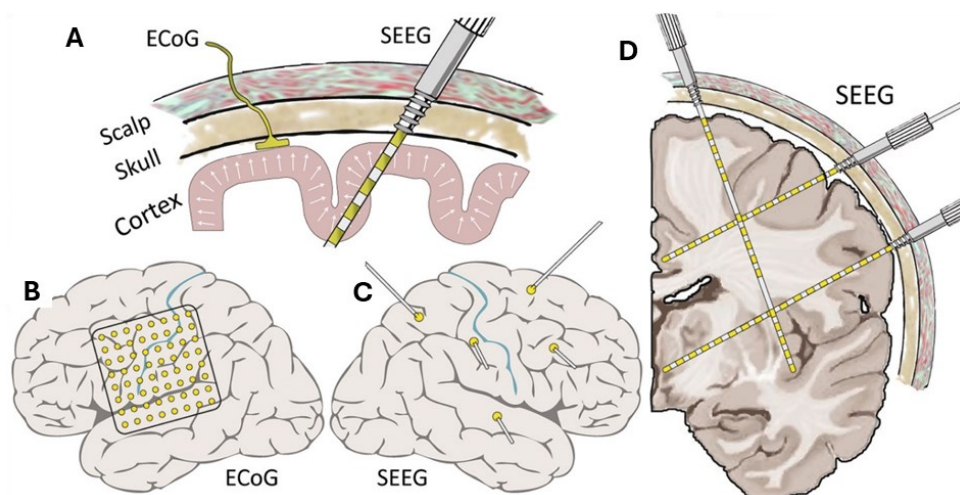


Figure 5-1 Schematic of electrocorticography (ECoG) and stereotaxic EEG (SEEG) adapted from Miller and Fine (2022). (A) Grids of brain surface ECoG electrodes are placed through large openings in the skull (craniotomies), and SEEG electrodes are placed through bolts embedded in the skull. (B) ECoG electrodes sample the exposed brain surface covering the targeted neocortical regions. (C) SEEG electrodes are implanted irregularly and sparsely, although they can be targeted precisely. (D) SEEG can precisely sample surface/deep grey matter and subcortical structures. Figure reprinted from *Decision-making in stereotactic epilepsy surgery* by Miller and Fine (2022). Reprinted with permission from John Wiley and Sons.

ECoG and SEEG were introduced for the treatment of patients with drug-resistant epilepsy, parkinsonism, and some other diseases (brain tumors) in the late 1940s and early 1950s (Crandall et al., 1963; Li & Van Buren, 1972; Penfield & Jasper, 1954; Talairach et al., 1962). SEEG is used for investigating deep structures, and ECoG is used for investigating neocortical regions (Reif et al., 2016). SEEG is less invasive than ECoG. The placement of ECoG electrodes requires a craniotomy (surgical removal of part of the bone from the skull to expose the brain). SEEG electrodes are implanted using stereotactic surgery (often robot-guided insertion using individual patient MRI) (Parvizi & Kastner, 2018). Each patient is often implanted with 5-15 depth electrodes, each consisting of 10-14 contacts (Miller et al., 2009). Both types of electrodes are placed under anesthesia and the patients are then transferred to the hospital room where they are recorded continuously for days up to two or three weeks. During the continuous recording, seizures and interictal epileptic activity are captured, and electrical stimulation procedures and sometimes focal thermocoagulation of epileptogenic zones are also performed (Taussig et al., 2015). They are time-consuming and expensive procedures.

iEEG records local field potentials (postsynaptic potentials) generated by a large population of neurons (~500,000 cells around the electrode (Miller et al., 2009)). As electrodes are placed directly into the brain tissue, iEEG can record local in situ signals at millimeter resolution. iEEG electrodes are mainly sensitive to local brain activity, depending on the underlying geometry of the electrode contacts and space between contacts (von Ellenrieder et al., 2021). The temporal resolution of iEEG is at the millisecond level, similar to scalp EEG and MEG.

However, iEEG is an invasive technique and is only available in a few hospitals, thus having limited accessibility. Because there is some risk attached to each implanted electrode, their number is limited to what is required clinically and this results in a small fraction of the brain being

explored (each electrode contact is only sensitive to generators in a radius of about 5 mm). Most focal epilepsy cases are temporal or frontal lobe epilepsy, and thus parietal, occipital, and inter-hemispheric areas are much less frequently implanted (Parvizi & Kastner, 2018).

5.3 Integration of SEEG with EEG/MEG

The motivation for simultaneous recordings of SEEG and scalp EEG/MEG is usually to leverage the complementary advantages of the two modalities: EEG/MEG provides a global view of the brain but with low spatial specificity and requires solving the source imaging inverse problem, while SEEG can detect brain activity with high spatial specificity, even from deep sources, but has limited spatial coverage. Additionally, SEEG integration of SEEG with non-invasive techniques is an interesting approach to overcome the limited spatial sampling of SEEG (Gavaret et al., 2016). Gavaret et al. (2016) showed a patient in whom epileptic spikes were not visible in scalp EEG/MEG. However, spikes identified in MEG using markings from SEEG were detectable when averaged. Source localization of MEG data triggered by SEEG data identified a generator that was actually missed by SEEG implantation, illustrating the complementarity of both approaches

However, in this thesis, we did not use iEEG and EEG/MEG as complementary modalities. Instead, we used iEEG as the ground truth for validating EEG/MEG source localization results. The neuronal generators for both scalp EEG/MEG and iEEG are believed to originate from postsynaptic potentials from a large population of neurons. The extent to which signals are detected by EEG/MEG or iEEG depends on the proximity of the electrode to the source, as well as the location and orientation of the neuronal sources (deep/superficial, gyrus/sulcus). Simultaneous recording of EEG/MEG and iEEG provides the best way to validate EEG/MEG source imaging. The schematic representation proposed by Hnazaee et al. (2020) (Figure 5-2) is a simplistic illustration of this concept. Hnazaee et al. (2020) reported the first study with simultaneous EEG/ECoG/SEEG resting state data to quantitatively compare the localization accuracy for EEG and ECoG source localization from deep sources, using SEEG recording as the ground truth. For two sources, one deep (light blue) and one superficial (dark blue), the ground truth depth electrode can detect both sources with high spatial and temporal resolution. The color bar shows the strength of the signals detected by each modality (full color from red to green means maximum signal strength detected by depth electrodes, whereas only one red bar detected by scalp EEG for deep source means the signal is highly attenuated). ECoG can detect the superficial source well but not

the deep source (signal attenuated). The signal is attenuated for both the superficial and deep sources in scalp EEG. This is a nice illustration of how depth electrodes can be used as ground truth for the localization of surface measurements.

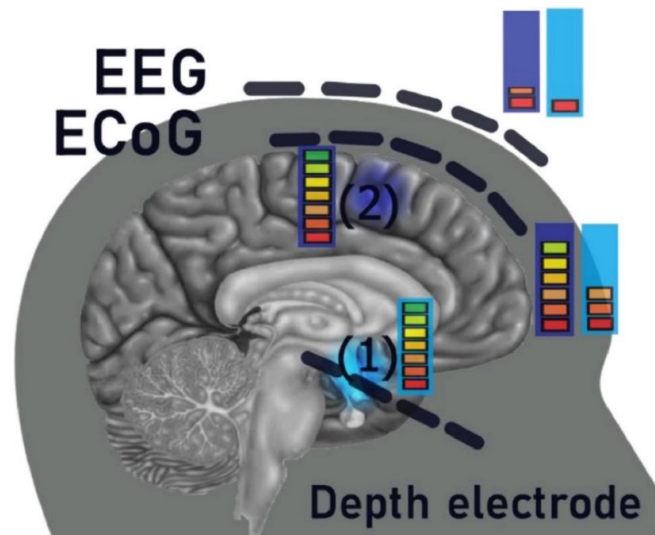


Figure 5-2. Use of depth electrodes as ground truth for validating EEG and ECoG source localization for superficial and deep sources. Deep and superficial sources are at locations (1) and (2), respectively. The color bars indicate the measurement strength of the source activity when measured at the origin of the source (maximum strength) and with ECoG or EEG electrodes. Light blue and dark blue represent the measured strength for deep and superficial sources, respectively. The measurements of deep and superficial sources are attenuated at subdural and scalp levels but to a different extent. From a perspective of the scalp (EEG), attenuation is likely so strong that the SNR for deep and superficial sources do not differ as much as they do from a subdural perspective (ECoG). Taken from *Localization of deep brain activity with scalp and subdural EEG* by Hnazaee et al. (2020), <https://doi.org/10.1016/j.neuroimage.2020.117344>.

5.4 Challenges integrating simultaneous EEG/MEG and SEEG

Several groups have implemented simultaneous recordings of MEG-SEEG or EEG-SEEG to study epilepsy (De Stefano et al., 2022; Kakisaka et al., 2012; Mikulan et al., 2020; Pacia & Ebersole, 1997; Santiuste et al., 2008) (Figure 5-3) or cognition (Dalal et al., 2009) or to show evidence of deep brain activity detected by EEG/MEG sensors (Pizzo et al., 2019; Seeber et al., 2019). Integrating EEG/MEG with SEEG has an advantage over ECoG because SEEG is less invasive. Since ECoG requires a craniotomy, this procedure distorts the scalp signals (von Ellenrieder et al., 2014). However, combining these invasive and non-invasive modalities presents numerous

challenges that must be addressed during the acquisition setup and the data processing steps (Pigorini et al., 2024).

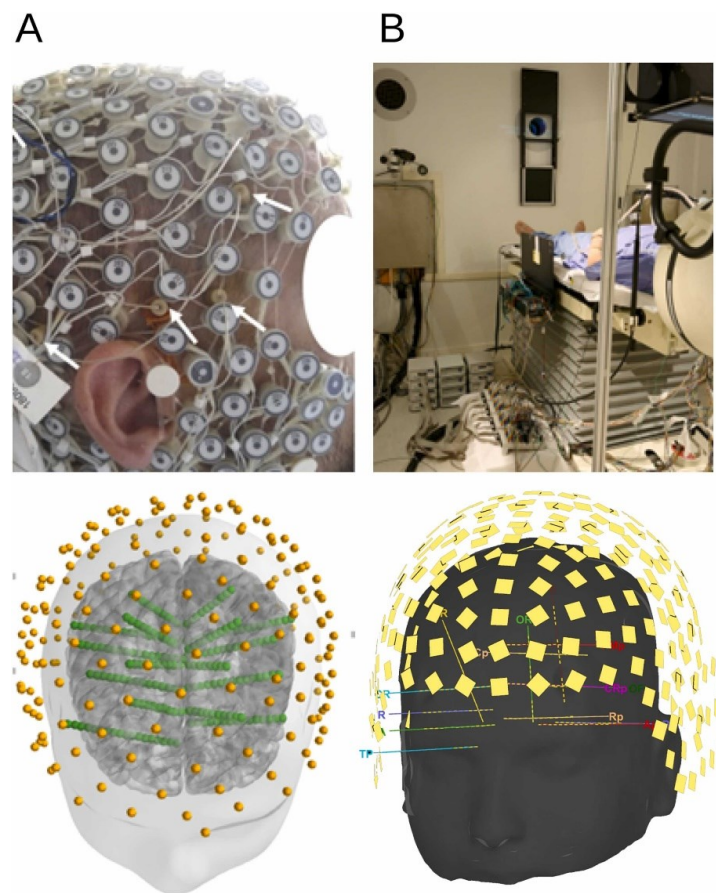


Figure 5-3 (A) Simultaneous high density-EEG and SEEG (adapted from ((De Stefano et al., 2022), (Mikulan et al., 2020))). (B) Simultaneous MEG and SEEG (adapted from (Velmurugan et al., 2022))) (Figure from Simultaneous invasive and non-invasive recordings in humans: A novel Rosetta stone for deciphering brain activity by Pigorini et al. (2024))

5.4.1 Technical challenges

The first report of simultaneous MEG and SEEG recording was published by Santiuste et al. (2008) using only one electrode. The first trimodal simultaneous EEG-MEG-SEEG recording was published by Dubarry et al. (2014) by our collaborators from Aix-Marseille University (PI of the project Dr. C. Bénar). In this study, they reported the challenges of simultaneous recording setup, such as the influence of SEEG amplifiers on MEG signal quality. One other challenge of simultaneous MEG-SEEG is that patients are implanted with SEEG electrodes which are attached

using insertion screws (Figure 5-4a). Finally, the patient's head is wrapped with post-operative bandages to limit infection risks. The placement of scalp EEG electrodes or the MEG helmet needs to be optimized to avoid the risk of infection that could arise from friction between the iEEG electrodes and the scalp electrodes. For MEG, it can be difficult to fit the patient's head inside the MEG helmet. For high-density EEG, the bandage needs to be removed to fit the EEG cap on the patient's head, increasing the risk of infection due to the contact between the EEG electrodes and the iEEG electrodes (Pigorini et al., 2024). In MEG, positioning the patient's head inside the MEG helmet might be compromised by the size of the MEG helmet and the size of insertion screws. In Badier et al. (2017), they addressed this issue using dedicated small insertion screws (Fig 4-4b,c). In addition, using optically insulated amplifiers (Figure 5-5) to reduce the effects of SEEG amplifiers on MEG data, Badier et al. (2017) recorded up to 256 SEEG channels without compromising signal quality for both MEG and SEEG. For integrating high-density EEG with SEEG, (Mikulan et al., 2020) adopted some safety measures such as sterilizing the EEG cap and disinfecting the skin before and after using the EEG cap.

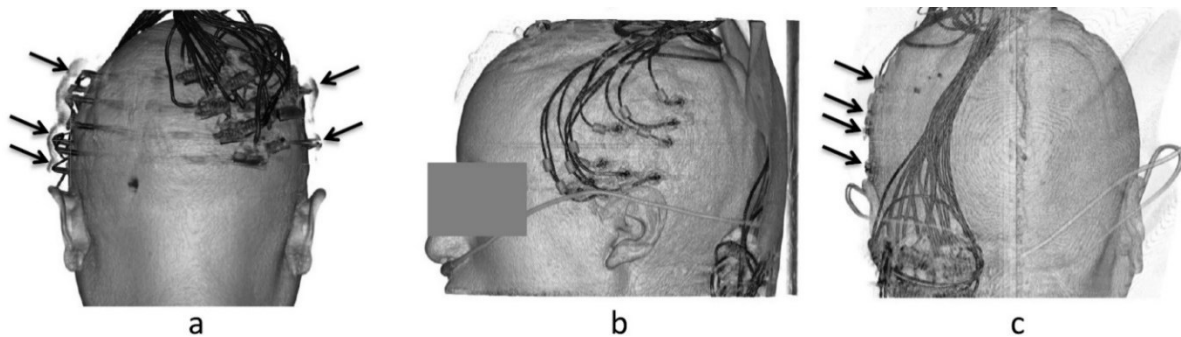


Figure 5-4 Comparison of the depth electrode holding screws for the two patients. Reconstructions were obtained from post-implantation CT scans. (a) Rear view of the reconstruction for the patient 1 (with long screws). (b) and (c) Reconstruction for short screws on profile and rear view respectively for patient 2. Figure from *Technical solutions for simultaneous MEG and SEEG recordings: towards routine clinical use* Badier et al. (2017). Reprinted with permission from IOP Publishing.

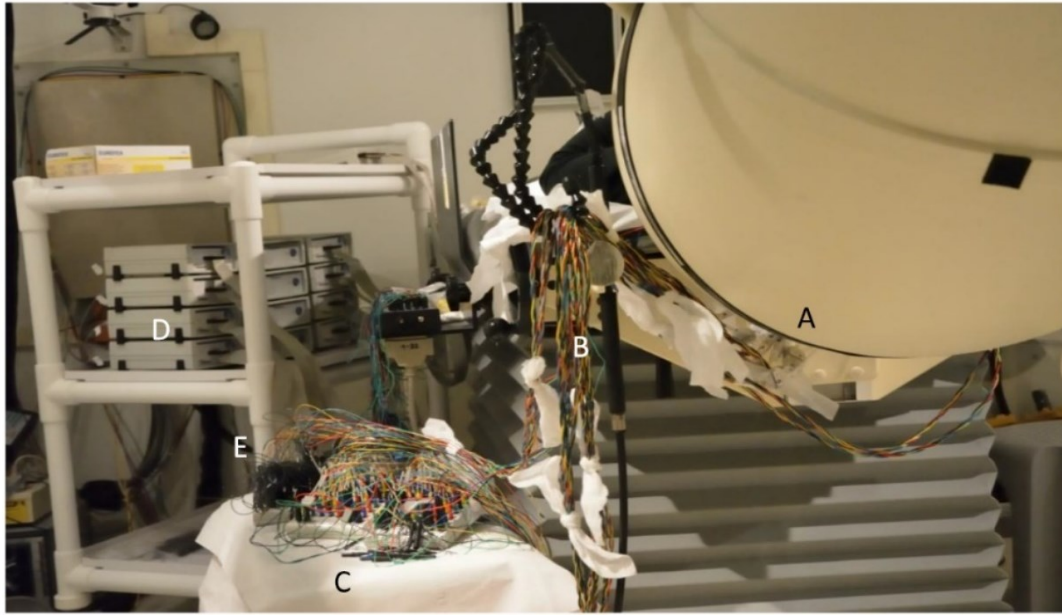


Figure 5-5 Experimental setup within the shielded room of the MEG. (A) Depth electrode connectors. (B) Cable extensions. (C) Head boxes. (D) Battery operated amplifiers. (E) Optical fiber for the transmission of the data outside the shielded room. Figure from *Technical solutions for simultaneous MEG and SEEG recordings: towards routine clinical use* Badier et al. (2017). Reprinted with permission from IOP Publishing.

In addition, temporal alignment between the invasive and non-invasive recordings should be carefully ensured, either by using the same amplifier (Barborica et al., 2021) or accurate external triggers (De Stefano et al., 2022). The spatial alignment is equally important when comparing both modalities. Therefore, the exact location of the iEEG contacts should be obtained by the co-registration of preimplantation anatomical MRI and post-implantation CT/MRI (Pigorini et al., 2024; Villalon et al., 2018; Zelmann et al., 2023), whereas standard head localization and coregistration approaches to localize the position of EEG electrodes /MEG sensors with the MRI anatomical model (section 3.6.5). For more details, we refer the readers to this recent review article describing the technical challenges of these simultaneous recordings (Pigorini et al., 2024).

5.4.2 Quantitative comparison between EEG/MEG and SEEG

Most clinical studies comparing EEG/MEG sources imaging with iEEG results are actually done qualitatively, usually at a sub-lobar level (Abdallah et al., 2017; Heers et al., 2016b). Studies that compare EEG/MEG source imaging with intracranial EEG quantitatively, either for simultaneous

or non-simultaneous data, face the challenge of using a common space for both modalities. EEG/MEG source imaging is estimated either along a cortical surface or within a 3D grid whereas SEEG results consists in discrete sparse measurements located in the intracranial space directly in the grey or white matter where electrodes are implanted. To address this comparison issue, a few approaches have been proposed.

Virtual sensor using beamformer: Corona et al. (2023) and Tamilya et al. (2021) used beamforming source imaging for EEG/MEG to reconstruct virtual sensors at the positions of the intracranial EEG electrodes. For beamforming, they initially used the entire brain volume as the source space. The output of the beamformer was then used to reconstruct activity at the virtual sensor locations, which were placed at the same locations as the iEEG contacts. To compute the virtual time series at each SEEG contact position, they considered all the beamformer grid points within a volume around each iEEG contact (within 5 mm for SEEG electrodes and 10 mm for subdural electrodes) before averaging these virtual beamformer signals to obtain a single time series for every iEEG contact (Figure 5-6). However, it is worth mentioning that Beamformer localization still assumes a dipolar model for every point on the grid, limiting the beamformer ability to reconstruct large extended generators, as this is the case in epilepsy.

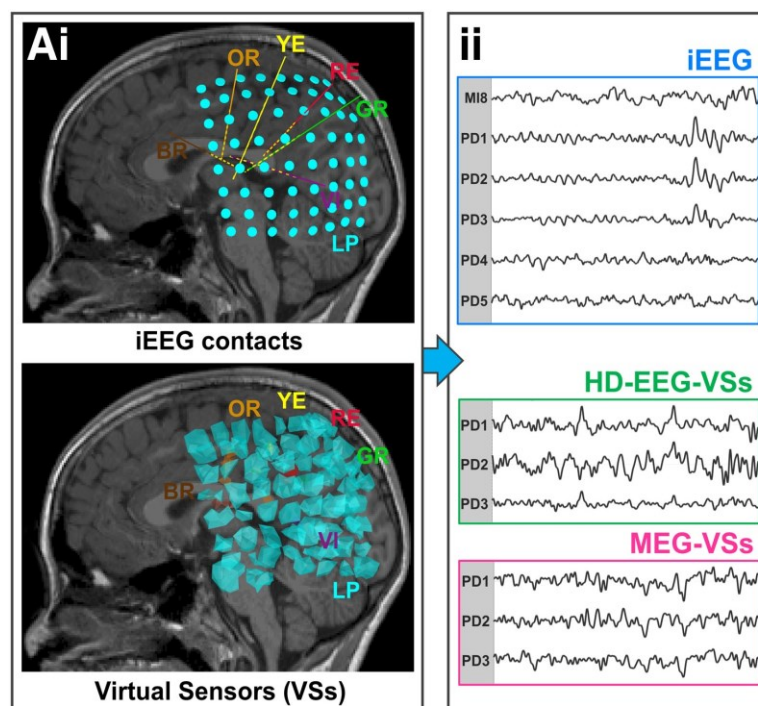


Figure 5-6 (i) Virtual sensors (VS) reconstructed at brain locations that matched the iEEG implantation. (ii) For each virtual sensor, computation of its mean source activation across time acquired from data recorded by the High Density-EEG (HD-EEG) and MEG sensors to reconstruct virtual sensor time series for HD-EEG (HD-EEG-VSs) and MEG (MEG-VSs), respectively. Figure retrieved from *Non-invasive mapping of epileptogenic networks predicts surgical outcome* by Corona et al. (2023). Reprinted with permission from Oxford University Press.

Virtual iEEG potential: Grova et al (2016) proposed an original method to estimate the electrical potential at iEEG electrode locations from EEG/MEG reconstructed source map that allows quantitative comparison between EEG/MEG sources and iEEG recordings. Three steps are required to obtain virtual iEEG potentials from EEG/MEG source imaging are: (i) obtain EEG/MEG source reconstructed maps using any distributed source imaging method that uses a cortical surface as a source model, (ii) calculate the iEEG forward model that estimates the influence of each dipolar source along the cortical surface to each iEEG channel position; and (iii) apply the iEEG forward model to the EEG/MEG reconstructed source map to estimate virtual iEEG potentials on each iEEG electrode channel (the methodological considerations are described in Grova et al. (2016)). To do so, our proposed SEEG forward model G_{SEEG} assumes an infinite volume conductor characterized by a conductivity σ of 0.25 S.m^{-1} (Cosandier-Rim    et al., 2008). To avoid numerical instabilities, when the sources on the cortical surface were too close to the SEEG contacts (cortical source / SEEG contact distance $< 3 \text{ mm}$), the distance was set to 3 mm instead, keeping the orientation of the dipolar source. This method was evaluated on five clinical cases to localize epileptic discharges and reported that the source localization method cMEM provided quite accurate results in recovering the location and spatial extent of the underlying generators compared to iEEG (as shown in Figure 5-7) (Grova et al 2016). In this study, we also demonstrated that when using source localization technique not or less sensitive to the spatial extent generators (MNE, LORETA), the spatio-temporal concordance between MEG estimated virtual iEEG potentials and real iEEG potentials significantly decreased.

In Abdallah et al. (2022), this method was used to quantitatively assess the spatial overlap between EEG/MEG source imaging with EEG/fMRI in localizing the primary irritative zone, and the seizure onset zone defined by iEEG, on a dataset of 17 patients. This approach allows for a direct comparison between iEEG potentials and EEG/MEG-estimated virtual iEEG potentials. This is the main method we considered to compare MEG source imaging with iEEG data, either from an

iEEG atlas at a group level (Chapters 6 and 8) or when considering simultaneous MEG/SEEG recordings (Chapter 9).

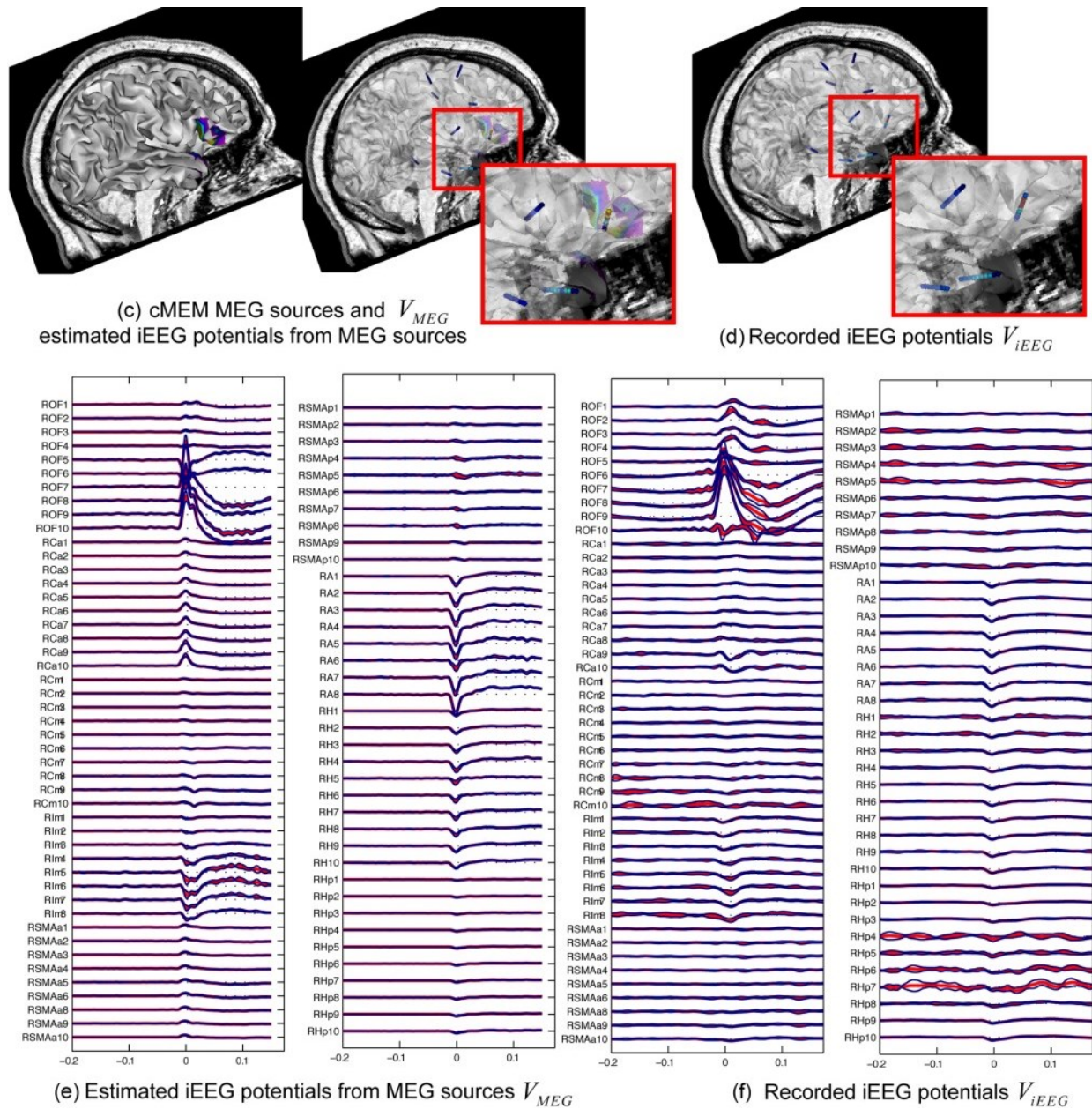


Figure 5-7 The virtual iEEG potential estimated from MEG using cMEM source localization (left) shows good correspondence with recorded iEEG potentials (right) for a patient exhibiting right orbito-frontal spikes. Figure reprinted from *Intracranial EEG potentials estimated from MEG sources: A new approach*

to correlate MEG and iEEG data in epilepsy by Grova et al. (2016). Reprinted with permission from John Wiley and Sons.

5.4.3 Limited spatial coverage and lack of normal resting state iEEG

Finally, another challenge in validating EEG/MEG source imaging with iEEG is that iEEG is only implanted in patients who are candidates for surgical procedures such as epileptic surgery or deep brain stimulation. Moreover, for a single patient, iEEG provides limited spatial coverage when compared to EEG/MEG covering the whole head surface. Additionally, as intracranial electrodes are usually implanted in presumably affected brain regions, there is a lack of intracranial recordings from normal healthy brain activity. To address these issues, Frauscher et al. (2018) published an atlas of iEEG data by pooling iEEG data from many patients but only including channels from presumably healthy brain regions (i.e. SEEG contacts that did not exhibit any epileptic discharges). This iEEG atlas is described in the next section.

5.5 iEEG atlas of normal resting state activity

The atlas of normal intracranial EEG developed by Frauscher et al. (2018) included both SEEG and subdural grids/strips from a large number of subjects but only including the electrodes that are implanted in presumably healthy brain regions. The inclusion criteria were (quoting from (Frauscher et al., 2018)):

- (i) *presence of at least one channel with normal activity. Such channels are not common (on average 11% of channels per patient as shown in one of our previous studies)(Frauscher et al., 2015). A channel with normal activity is defined as a channel localized in normal tissue as assessed by MRI, is located outside the seizure onset zone, does not show at any time of the circadian cycle interictal epileptic discharges (according to the clinical report of the complete implantation and to a careful investigation of one night of sleep by a board-certified electrophysiologist), and shows the absence of overt slow-wave anomaly;*
- (ii) *presence of peri-implantation imaging (CT or MRI) for exact localization of individual electrode contacts (contacts located in the white matter were excluded);*
- (iii) *availability of a controlled intracranial EEG recording obtained after a minimum of 72 h after insertion of stereo-EEG electrodes or 1 week after placement of subdural grids or strips (medications are usually not yet lowered), and at least 12 h after a generalized tonic-*

clonic seizure, 6 h in case of focal clinical seizures, or 2 h in case of purely electrographic seizures, and not after electrical stimulation, as done in our previous work (Frauscher et al., 2015); and

- (iv) *sampling frequency of a minimum of 200 Hz. This minimum sampling frequency was chosen to include as many patients as possible for the analysis of frequencies in the classical Berger frequency bands (0.3–70 Hz).*

From 106 patients, a total of 1785 iEEG channels were identified (1520 from SEEG and 265 from grids/strips, left hemisphere, 1066; right hemisphere, 719) (Figure 5-8). The average number of channels per cm³ of cortical grey matter volume was 2.7 channels/ cm³. For each channel, a 60-second artifact-free section during wakefulness was selected during eyes closed.

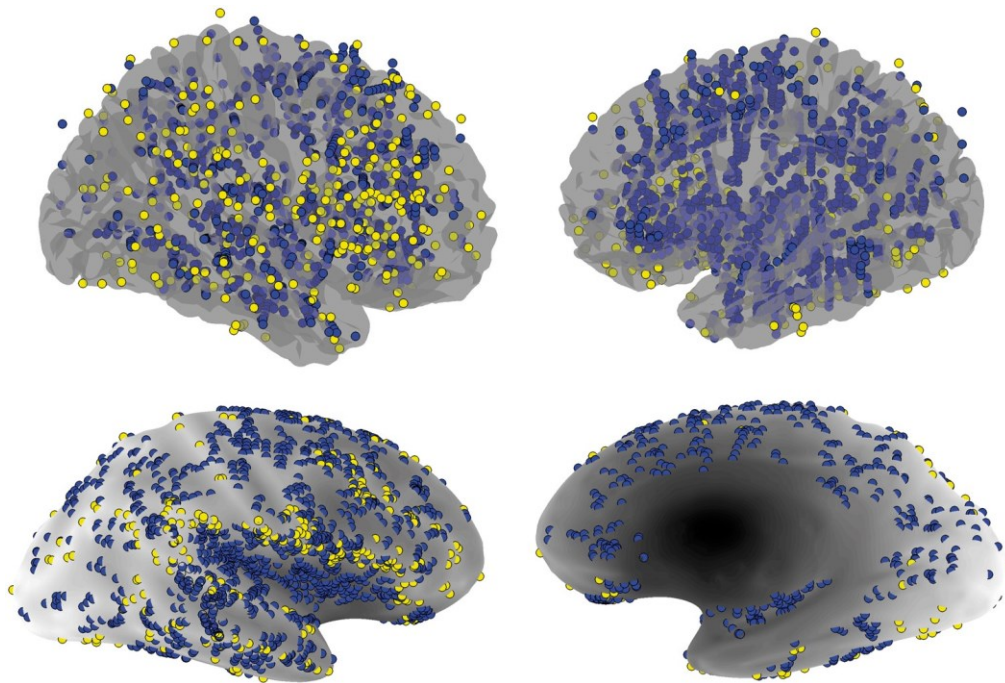


Figure 5-8 Localization of the 1785 EEG channels with normal physiological activity analyzed for this study. The 1520 channels from stereo-EEG electrodes are visualized in blue, and the 265 channels from cortical grids and strips are in yellow. Note that for the ‘inflated’ brain display at the bottom, the electrodes are projected on the cortical surface. Figure from *Atlas of the normal intracranial electroencephalogram: neurophysiological awake activity in different cortical areas* by Frauscher et al. (2018). Reprinted with permission from Oxford University Press.

This atlas provides a unique opportunity to study the characteristics of normal brain activity at a group level. This atlas will be used as ground truth to validate the MEG source imaging of resting state activity from a group of healthy participants in terms of oscillatory (Chapter 6) and connectivity patterns (Chapter 8).

Another normative atlas of intracranial EEG activity has been developed by merging data from the iEEG atlas developed by Frauscher et al. (2018) and data from the Penn Epilepsy Center, reporting data from 166 subjects with over 5000 channels (Bernabei et al., 2022). A similar normative iEEG atlas was also developed by Taylor et al. (2022) that included 21598 channels across 234 participants. Both atlases, like that of Frauscher et al. (2018), still suffer from the unavoidable weakness of not being recorded in healthy brains.

5.6 Conclusion

In this chapter, I briefly described the validation techniques of EEG/MEG source imaging using simulations and using iEEG as the ground truth. Both these techniques are extensively used for this thesis and will be discussed again in chapters 6, 7, 8 and 9. I also discussed the challenges when comparing EEG/MEG source imaging with intracranial EEG. Finally, the atlas of intracranial EEG of the resting state is introduced, which will be used as ground truth to validate resting-state MEG source imaging for a group of healthy subjects in chapters 6 and 8.

6 Manuscript 1: Validating MEG source imaging of resting state oscillatory patterns with an intracranial EEG atlas

6.1 Preface

EEG/MEG source imaging involves solving an ill-posed inverse problem, which necessitates careful validation. This need for validation is even more crucial when dealing with low signal-to-noise ratio resting-state activity. In the first study of this thesis, we aimed to validate MEG source localization of resting-state oscillations in a healthy group, using as gold standard, an intracranial EEG atlas of normal brain activity developed by Frauscher et al. (2018). The atlas data were collected from 110 patients with refractory epilepsy who underwent iEEG implantation for clinical evaluation; it includes only electrodes implanted in healthy brain regions. We used the wMEM source localization method, which had previously been evaluated for its ability to recover oscillations (Avigdor et al., 2021; Aydin et al., 2020; Lina et al., 2012; Pellegrino et al., 2016; von Ellenrieder et al., 2016). We propose several adaptations to wMEM to improve the localization of resting-state oscillations and we aim to create a brain atlas highlighting regions and frequencies where MEG source localization of resting state oscillations is accurate. We also compared the wMEM method with two widely used source imaging methods: minimum norm estimate (Hämäläinen & Ilmoniemi, 1994; Lin et al., 2006) and beamformer (Van Veen et al., 1997). MEG sources estimated from each method were then converted into virtual intracranial EEG data, by applying an iEEG forward model to MEG sources along the cortical surface (Abdallah et al., 2022; Grova et al., 2016), providing an ideal framework to compare quantitatively oscillations in MEG sources and real iEEG data. This chapter includes the published abstract, introduction, materials and methods, results, and discussions. The methodological adaptations of wMEM to localize resting state data are detailed in Appendix A for Manuscript 1 in Chapter 6 which is reported at the very end of this thesis.

This manuscript was published as:

Afnan, J., von Ellenrieder, N., Lina, J.M., Pellegrino, G., Arcara, G., Cai, Z., Hedrich, T., Abdallah, C., Khajehpour, H., Frauscher, B., Gotman, J., Grova, C., 2023. Validating MEG source imaging of resting state oscillatory patterns with an intracranial EEG atlas. *NeuroImage*, 274,p.120158. <https://doi.org/10.1016/j.neuroimage.2023.120158>

6.2 Abstract:

Background: Magnetoencephalography (MEG) is a widely used non-invasive tool to estimate brain activity with high temporal resolution. However, due to the ill-posed nature of the MEG source imaging (MSI) problem, the ability of MSI to identify accurately underlying brain sources along the cortical surface is still uncertain and requires validation.

Method: We validated the ability of MSI to estimate the background resting state activity of 45 healthy participants by comparing it to the intracranial EEG (iEEG) atlas (<https://mni-open-ieegatlas.research.mcgill.ca/>). First, we applied wavelet-based Maximum Entropy on the Mean (wMEM) as an MSI technique. Next, we converted MEG source maps into intracranial space by applying a forward model to the MEG-reconstructed source maps, and estimated virtual iEEG (ViEEG) potentials on each iEEG channel location; we finally quantitatively compared those with actual iEEG signals from the atlas for 38 regions of interest in the canonical frequency bands.

Results: The MEG spectra were more accurately estimated in the lateral regions compared to the medial regions. The regions with higher amplitude in the ViEEG than in the iEEG were more accurately recovered. In the deep regions, MEG-estimated amplitudes were largely underestimated and the spectra were poorly recovered. Overall, our wMEM results were similar to those obtained with minimum norm or beamformer source localization. Moreover, the MEG largely overestimated oscillatory peaks in the alpha band, especially in the anterior and deep regions. This is possibly due to higher phase synchronization of alpha oscillations over extended regions, exceeding the spatial sensitivity of iEEG but detected by MEG. Importantly, we found that MEG-estimated spectra were more comparable to spectra from the iEEG atlas after the aperiodic components were removed.

Conclusion: This study identifies brain regions and frequencies for which MEG source analysis is likely to be reliable, a promising step towards resolving the uncertainty in recovering intracerebral activity from non-invasive MEG studies.

Keywords: Intracranial EEG; Magnetoencephalography; Source imaging; Validation; Resting state; Spectral analysis.

6.3 Introduction

Neuronal oscillations are fundamental properties of brain activity and are considered to play an important role in processing and regulating neuronal communication in physiological (Giraud & Poeppel, 2012; Pellegrino et al., 2021; Voytek et al., 2010; Wang, 2010) and pathological conditions (Buzsáki et al., 2013; Hirano & Uhlhaas, 2021; Schnitzler & Gross, 2005b). Electro/magneto-encephalography (EEG/MEG) are widely used non-invasive electrophysiological methods to measure neuronal activity. They provide excellent temporal resolution in the order of milliseconds, which enables us to study spontaneous brain activity and oscillations in different frequency bands. Due to their non-invasive nature, EEG/MEG have been used in many studies of brain dynamics and networks, not only during well controlled tasks but also during the resting state, a state when the brain activity is spontaneous (thinking of nothing/not performing any task) (Matthew J. Brookes et al., 2011; Hipp et al., 2012; Keitel & Gross, 2016; Mellem et al., 2017). EEG/MEG have also been widely used as a presurgical tool for drug-resistant epilepsy and basic epilepsy research (Dalal et al., 2013; Hamandi et al., 2016; Pellegrino et al., 2018; von Ellenrieder et al., 2016). Compared to other invasive and non-invasive modalities, EEG/MEG have limited spatial resolution, since they consist in scalp recordings and source localization requires solving an ill-posed inverse problem (Darvas et al., 2004a). The source leakage associated with source imaging is defined as the influence of a source on the estimation of the generators in its neighborhood (Brookes et al., 2012; Hedrich et al., 2017). The source leakage and the challenges of localizing signals from deep brain structures are of great concern, especially when considering clinical applications such as pre-surgical planning for epilepsy (Aydin et al., 2020; Hedrich et al., 2017) and particularly while interpreting results from resting state activity due to its low signal-to-noise ratio, which is even lower for deep sources. Validation is thus necessary for non-invasive EEG/MEG techniques, to accurately interpret the results. In this study, we aimed to validate the ability of MEG source imaging to estimate resting state oscillations in

healthy subjects. Due to the frequent lack of a ground truth, validation of source imaging techniques using realistic simulations are common and often useful, such as in the context of epileptic spikes (Becker et al., 2015; Chowdhury et al., 2016; Grova et al., 2006) and connectivity studies (Wang et al., 2014). However, generating realistic simulations of brain activity is challenging and even more so for resting state activity.

The gold standard to validate non-invasive methods is intracerebral EEG (iEEG), an invasive technique employed in some patients with epilepsy during pre-surgical evaluation. In iEEG, electrodes are placed on or into brain tissue (Jayakar et al., 2016). They are subdural grid/strip or depth electrodes (freehand or using stereoecephalography, SEEG introduced by Bancaud and Talairach in the 1950s (Enatsu & Mikuni, 2016)). iEEG thus can measure brain activity directly from the regions of interest, however, at a cost of requiring a surgical procedure to implant the electrodes and of having a limited spatial coverage. iEEG can record brain activity with excellent spatial accuracy, however validation can only be partial because of the limited spatial sampling, due to the invasiveness of the procedure.

Simultaneous recordings of EEG/MEG and iEEG provide an excellent opportunity to validate non-invasive results (De Stefano et al., 2022; Koessler et al., 2010; Pizzo et al., 2019). However, acquiring simultaneous MEG and iEEG is technically challenging (Badier et al., 2017; Dubarry et al., 2014; Kakisaka et al., 2012; Pigorini et al., 2024; Rampp et al., 2010; Santiuste et al., 2008) and not many groups have the access and technical resources to conduct such acquisitions. Also, only the patients who are candidates for epilepsy surgery undergo such invasive iEEG procedures. The implantation of intracranial electrodes is usually limited to affected regions, with a few electrodes placed in healthy regions, thus providing very limited coverage of the brain. Our group developed an atlas of healthy iEEG (Frauscher et al., 2018) at the Montreal Neurological Institute (MNI) (<https://mni-open-ieegatlas.research.mcgill.ca/>). This MNI iEEG atlas was generated by pooling iEEG data from 110 patients with refractory epilepsy who underwent iEEG implantation for clinical evaluation for epilepsy, only keeping the data from the electrodes implanted in healthy brain regions. With a dense coverage of all regions, this atlas provides us with the unique opportunity to study the spectral characteristics of normal brain oscillations at a group level. We took this opportunity to validate the non-invasive modality, MEG, to localize the spectral properties of the normal brain in wakefulness, in a group of healthy participants and compare those

with the MNI iEEG atlas as ground truth, assuming both modalities represent the activity of the healthy brain at a group level.

We assessed MEG source imaging of resting state oscillatory patterns of healthy subjects at a group level and validated with the MNI iEEG atlas. We expect that MEG source imaging can recover the spectral patterns observed in the MNI iEEG atlas more accurately in some regions than in others. To investigate this question, we applied wavelet-based Maximum Entropy on the Mean (wMEM) (Aydin et al., 2020; Lina et al., 2012; Pellegrino et al., 2016; von Ellenrieder et al., 2016). wMEM is an EEG/MEG source imaging technique we developed and adapted to localize resting state oscillatory patterns, which proved its unique ability to recover the location and the spatial extent of the underlying oscillatory generators (Avigdor et al., 2021; Aydin et al., 2020; Pellegrino et al., 2016; von Ellenrieder et al., 2016). An original method proposed by our group (Abdallah, et al., 2022; Grova et al., 2016) to estimate iEEG signals from MEG sources was then applied to support a quantitative comparison between the MNI iEEG atlas (electrical potentials) and MEG sources (cortical current densities), at the location of each iEEG electrode contact of the atlas. This is the first study to provide a group level validation with iEEG spectral characteristics across the human cortex, of non-invasive resting state MEG recordings from the healthy brain.

6.4 Material and methods

6.4.1 Experimental design

Our analysis pipeline is summarized in Figure 6-1. We used the MNI iEEG atlas as ground truth to validate MEG source imaging of resting state oscillatory patterns for healthy subjects. The MEG data were collected from 45 healthy subjects. To solve the inverse MEG problem, we applied the wMEM, developed by our group (Lina et al., 2012). The reconstructed MEG data along subject specific cortical surface were projected to the positions of iEEG electrodes used in the atlas, to generate virtual iEEG (ViEEG) data using a method proposed by (Grova et al., 2016). To do this, the positions of the intracranial electrodes were projected from the template ICBM152 anatomy to the anatomy of each healthy subject. By applying an iEEG forward model from the sources localized along the cortical surface to all iEEG channel positions, this method allowed a quantitative comparison between the spectral properties of MEG-estimated ViEEG with actual iEEG atlas for each region of interest (ROI) for each frequency band of interest.

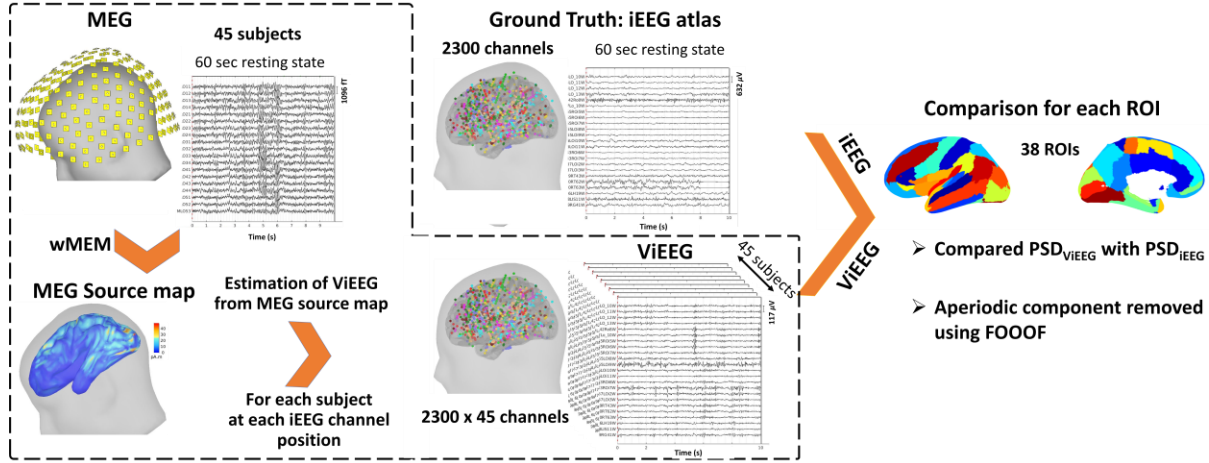


Figure 6-1 : Analysis pipeline to compare the spectral properties estimated by MEG with the MNI iEEG atlas, as ground truth. **Ground truth MNI iEEG atlas** (Frauscher et al., 2018) consists of 2300 channels collected from 110 subjects with epilepsy, retaining only the healthy brain regions. For each iEEG channel, 60 seconds of resting state data during wakefulness were used. **MEG pipeline:** MEG data were collected from 45 healthy participants, each having 60 seconds of resting state data during wakefulness (only 10 seconds of data are shown in this figure). We applied wavelet-MEM (wMEM) to solve the MEG inverse problem. For each source map, we estimated virtual iEEG (ViEEG) data at each position of 2300 channels (positions obtained from the MNI iEEG atlas). We compared the spectral characteristics (spectra and oscillatory peaks) between iEEG and ViEEG for 38 ROIs (MICCAI atlas). To consider only the oscillatory components, the aperiodic components were removed from the spectra using the FOOOF toolbox (Donoghue et al., 2020).

6.4.2 Ground truth: MNI iEEG atlas

The data in the MNI iEEG atlas (Frauscher et al., 2018) were collected from 110 patients with refractory epilepsy who underwent iEEG implantation for clinical evaluation for epilepsy surgery. The key features of the data are: i) some electrodes were implanted in brain regions that turned out to be healthy and only those were retained to construct the atlas, ii) recordings were controlled with subjects having their eyes closed, and iii) electrodes were projected on the standard ICBM152 template. In the intracranial atlas, a total of 2300 channels from 110 patients (age: 31 ± 10 Y, range: 13-62 Y, M:54) were selected. iEEG data in each patient were re-referenced to a common average reference, calculated by taking the average of 5% of the total channels exhibiting the lowest power and subtracting that value from each channel. Sixty seconds of resting state data during wakefulness were available for each of the 2300 channels. The iEEG channels in the atlas were

classified into 38 regions of interest (ROIs) based on the Medical Image Computing and Computer-Assisted Intervention (MICCAI) (Landman & Warfield, 2019) atlas. The channels from the left and the right hemispheres were considered together. The number of channels in each ROI was variable but ensured sufficient coverage of all regions: mean \pm standard deviation: 60 ± 47 channels in each ROI. More details on the data, centers, patient information, and inclusion criteria can be found in Frauscher et al. (2018).

6.4.3 Subject selection criteria for MEG

57 healthy participants who underwent MEG acquisition were included in this study (Pellegrino et al., 2022). MEG data were collected at the MEGLab of the IRCCS San Camillo Hospital in Venice, Italy. Eight minutes of resting state were acquired with eyes closed. The participants did not have any history of neurological or psychiatric disorders or any irregularity in the cycle of sleep-wakefulness. After preprocessing and sleep scoring of data, we finally included 45 participants (age: 28.67 ± 4.13 Y, range: 20-38 Y, M: 10). Of the participants, one was excluded for sleeping during the acquisition and 11 for coregistration issues such as issues with segmentation, or very noisy data.

6.4.4 MEG data acquisition

MEG data were acquired using a CTF-MEG system (VSM MedTech Systems Inc., Coquitlam, BC, Canada) with 275 axial gradiometers with a sampling rate of 1200 Hz. Bipolar electrodes were added to record Electrocardiogram (ECG) and electrooculogram (EOG). The coils were positioned on three anatomical landmarks (left and right preauricular points and nasion). These positions, along with the shape of the head of each participant were recorded with a 3D Polhemus localizer (Pellegrino et al., 2022), which were used for coregistration of MEG sensors with individual anatomical MRI of the participants.

6.4.5 Anatomical MRI, MEG-MRI co-registration and forward model estimation

For each participant, a T1-weighted-3D-TFE anatomical MRI was performed with a 3T Ingenia CX Philips scanner (Philips Medical Systems, Best, The Netherlands). The following parameters were used for MRI acquisition: [TR]=8.3 ms, [TE]=4.1 ms, flip angle=8°, acquired matrix resolution=288 \times 288, slice thickness=0.87 mm) (Pellegrino, 2022). Freesurfer (Dale et al., 1999) was used for subsequent brain segmentation and reconstruction of the white/gray matter interface.

The coregistration of MEG sensors with anatomical MRI was performed in Brainstorm (Tadel et al., 2011), applying a surface fitting between the head shape from MRI and the positions of coils and head shape recorded using 3D Polhemus during MEG acquisition. We considered the cortical mesh of the mid layer which is equidistant from the white and grey matter interface as source space, consisting of around 8000 vertices. The forward model was computed using OpenMEEG software (Gramfort et al., 2010; Kybic et al., 2005) implemented in Brainstorm (Tadel et al., 2011). We used a 3-layer Boundary Element model (BEM) consisting of brain, skull, and scalp surfaces with conductivity values of 0.33, 0.0165, and 0.33 S m⁻¹, respectively (Zhang et al., 2006).

6.4.6 MEG data preprocessing

MEG preprocessing was performed with Brainstorm software (Tadel et al., 2011). Preprocessing of MEG data included (i) filtering within the 0.5-80 Hz band, (ii) applying a notch filter at 50 Hz, (iii) downsampling to 200 Hz, (iv) applying third-order spatial gradient noise correction and (v) removal of cardiac and eye movement artifacts using Signal Space Projection (SSP) (Uusitalo & Ilmoniemi, 1997) routine available in Brainstorm. A sixty-second segment was extracted for each subject, continuous or concatenated (minimum length of the continuous segment: 10 seconds), where no artifact was visibly present, ensuring with an EEG expert that the subject was awake during this segment. To assess the data for sleep score, some scalp EEG channels were provided (F4, C4, O2, Ref left mastoid, Ground left shoulder).

6.4.7 MEG source imaging using wavelet Maximum Entropy on the Mean (wMEM)

The MEG inverse problem was solved using the Maximum Entropy on the Mean (MEM) (Amblard et al., 2004), which we carefully validated in the context of EEG/MEG source imaging (Chowdhury et al., 2013). The key feature of this framework is a spatial prior model, assuming that brain activity is organized within cortical parcels. MEM is a Bayesian framework, where the activity of every parcel is tuned by the probability of activation of a hidden state variable. When the parcel is active, a Gaussian prior is assumed to model a priori the activity within the parcel. Starting from such a prior “reference” distribution, inference to ensure data fit is then obtained using entropic techniques. As a result, MEM is able to either switch off or switch on the corresponding parcels during the localization process, while allowing local contrast along the

cortical surface within the active parcels. Parcellation of the whole cortical surface ($K \sim 228$ parcels) and initialization of the probability of being active were obtained using a data driven approach, based on a Multivariate Source Pre-localization (MSP) method (Mattout et al., 2005), a projection technique allowing to define the probability of every source to contribute to the data. The MEM specific prior model, using the entropic technique to fit the data, allows accurate localization of the underlying generators together with their spatial extent, as previously demonstrated by our studies for the standard version of MEM (cMEM) (Abdallah et al., 2022; Chowdhury et al., 2016; Chowdhury et al., 2013; Grova et al., 2016; Heers et al., 2016a; Pellegrino, Hedrich, et al., 2020), as well as the wavelet-based extension of MEM (wMEM) (Lina et al., 2012). wMEM was specifically designed to localize brain oscillatory patterns. wMEM applies a discrete wavelet transformation (Daubechies wavelets) to characterize the oscillatory patterns in the data before applying the MEM solver (Lina et al., 2012). We validated wMEM for localizing oscillatory patterns at seizure onset (Pellegrino et al., 2016), interictal bursts of high frequency oscillations (Avigdor et al., 2021; von Ellenrieder et al., 2016) and MEG resting state fluctuations (Aydin et al., 2020). Both wMEM and cMEM implementations are available within the Brain Entropy in space and time (Best) plugin of Brainstorm software (<https://neuroimage.usc.edu/brainstorm/Tutorials/TutBEst/>).

We incorporated a few changes in standard wMEM implemented in Brainstorm, to localize specifically oscillatory patterns in resting state data (more details in the Appendix A). (i) Spatial prior model: Our main adaptation of the wMEM spatial prior model consisted in considering one stable whole brain parcellation of the cortical surface, following the strategy proposed for cMEM (Chowdhury et al., 2013), whereas in our previous wMEM implementation the parcellation was varying for every time frequency samples. To do so, we proposed data-driven whole brain parcellation informed by the MSP method (Mattout et al., 2005), a projection technique allowing to estimate the probability of every source to contribute to the data, before region growing around local MSP peaks. The main adaptation of our current implementation is that the MSP projector is applied on all wavelet coefficients of Daubechies time-frequency representation of our data, instead of using signals in the time domain (see details in the Appendix A). (ii) Initialization of the probability of being active for each parcel: Following the parcellation, we initialized the probability of each parcel of being active, using normalized energy calculated for each time frequency sample. (iii) Selection of baseline for resting state localization: There is no ideal baseline

definition when localizing ongoing resting state data. We proposed to compute the sensor level noise covariance matrix from the ongoing resting state data. To do this, we generated a quasi-synthetic baseline from the signal of interest by randomly modifying the Fourier phase at each frequency (Prichard & Theiler, 1994). We also adopted a sliding window approach to generate the baseline for a more accurate estimation of the noise covariance matrix for each time frequency sample along the time scale. More details of these adaptations are described in the Appendix A.

Before applying this new implementation of wMEM on resting state MEG data, we validated it within a controlled environment with realistic simulation of epileptic spikes and oscillations on realistic MEG background, as previously proposed in Chowdhury et al. (2013) and Lina et al. (2012) (see supplementary material S.1 and Fig S1).

6.4.8 Estimation of virtual iEEG (ViEEG) data from the MEG source map

MEG and iEEG are two modalities each measuring brain activity in different units, MEG measurements after source imaging are current densities (in nanoAmpere-meters), whereas iEEG measurements are electrical potentials in μ Volts. To allow quantitative comparison between these two modalities, we converted MEG-reconstructed source maps into iEEG channel space, by estimating corresponding iEEG potentials that would correspond to those MEG sources on each electrode contact (channel) of the atlas (Abdallah et al., 2022; Grova et al., 2016). To do so, we first localized the position of all channels of the atlas within the native MRI referential system of all healthy subjects from whom we analyzed MEG data. Co-registration between anatomical MRI of each subject and the ICBM152 template where the atlas is defined was obtained using Minctracc program (Collins et al., 1994). This is obtained in three steps: (1) estimation of a linear registration to account for the linear part of the transformation (using `bestlinreg_s` tool), (2) estimation of a non-linear transformation to account for the variability between the two maps (using `minctracc` tool); (3) application of the resulting non-linear transformation to the coordinates of the electrode contacts of MNI iEEG atlas, to convert them from the ICBM152 anatomy to the anatomy of each healthy subject.

Then, for each subject, to estimate the virtual iEEG potentials from MEG-estimated current density, J_{MSI} , we calculated a subject specific iEEG forward model, G_{iEEG} that estimates the influence of each dipolar source of the cortical surface on each iEEG channel (Grova et al., 2016). Since we did not intend to solve the inverse problem of source localization from iEEG data, we

used a simplified iEEG forward model G_{iEEG} assuming an infinite volume conductor characterized by a conductivity σ of 0.25 S.m⁻¹. For a total number of iEEG contacts c , ($c = 2300$) and n number of cortical sources ($n = 8000$). G_{iEEG} is a $c \times n$ matrix that estimates the electrical potential located at each iEEG electrode i ($i = 1, 2 \dots c$) corresponding to an equivalent current dipole of unit activity located on the vertex S_j and oriented along \vec{n}_j , normal to the cortical surface ($j = 1, 2, \dots, n$), calculated as:

$$G_{iEEG}(i, j) = \frac{\vec{n}_j \cdot \vec{u}_{ij}}{4\pi\sigma r_{ij}^2} \quad (1)$$

where \vec{u}_{ij} is a unit vector oriented from the source S_j to the iEEG contact i and r_{ij} is the Euclidean distance between S_j and contact i . To avoid numerical instabilities, when the sources on the cortical surface were too close to the iEEG contacts ($r_{ij} < 3$ mm), the distance r_{ij} was set to 3 mm instead, keeping the orientation \vec{u}_{ij} . Finally, we applied the iEEG forward model, G_{iEEG} to the MEG-reconstructed source map (J_{MSI}) to estimate iEEG potentials on each iEEG channel, ViEEG as:

$$ViEEG = G_{iEEG}J_{MSI} \quad (2)$$

Here, we applied a simplified iEEG forward model because Cosandier-Rim    et al. (2007) showed that it could estimate accurately real iEEG measurements. Moreover, von Ellenrieder et al. (2012) showed that the use of finite-element models considering the actual size and the shape of the iEEG electrodes had almost no influence on local electrical potentials at 2 mm from the electrodes.

As for each source map obtained for all 45 participants, we estimated ViEEG for each iEEG channel in the atlas, we generated more ViEEG channels compared to the MNI iEEG atlas (2300 channels in the iEEG atlas vs 2300 x 45 channels in ViEEG).

6.4.9 Frequency specific brain maps of relative power

For each of the iEEG and ViEEG channels, the power spectral density (PSD) was estimated using Welch's method (Time duration: 0-60 seconds, 2s sliding Hamming windows, overlap: 50%). For each channel, a relative PSD was obtained by dividing each PSD value by the total power across the whole frequency range. The group average of relative PSD was calculated across all channels within a ROI and all frequency bins in each frequency band of interest: δ (0.5-4Hz), θ (4-8Hz), α (8-13Hz), β (13-30Hz), and γ (30-80Hz).

To compare the relative PSD before and after applying the conversion from MEG source maps into virtual intracranial space, we also calculated the relative PSD after MEG source imaging directly along the cortical surface (Fig S12). To obtain a group average of relative PSD for 45 subjects, we followed the approach described in Niso et al. (2019). We first projected individual relative PSD to a default template, ICBM152 (Fonov et al., 2009) and then obtained a group average of 45 relative PSD in each frequency band of interest.

6.4.10 Analysis of spectral oscillatory components

In this study, we applied FOOOF (Fitting Oscillations & One-Over-F) (Donoghue et al., 2020), a commonly used algorithm (Huang et al., 2021; Mahjoory et al., 2020; Ramsay et al., 2021; Senoussi et al., 2022; Wiesman et al., 2022) to separate periodic components from the aperiodic components of the spectra by parameterizing the power spectra as a composition of these two components. Using an iterative fit-refit method, the FOOOF algorithm models a PSD as a combination of an aperiodic component and several periodic component/s, where the aperiodic component is modeled as an exponential function and each periodic component is modeled as a Gaussian function (Donoghue et al., 2020). The central frequency extracted from each Gaussian fit was then considered as an ‘oscillatory peak’.

For each of the iEEG and ViEEG channels, we decomposed the spectra into periodic and aperiodic components using the FOOOF algorithm. The following FOOOF parameters were used: frequency range = 0.5–80 Hz; peak type: Gaussian; peak width limits (minimum bandwidth, maximum bandwidth) = 1 – 8 Hz; maximum number of peaks = 8; peak threshold: 3.0 dB; proximity threshold = 2 SD; aperiodic mode: *knee*. As we concentrated only on the rhythmic activities of the spectra, we subtracted (in the log-log scale) the aperiodic component from the raw PSD. The remaining oscillatory component of the spectra (PSD_{iEEG} and PSD_{ViEEG}) was considered for further analysis and comparison between iEEG and ViEEG. We also identified the oscillatory peaks during the process of finding aperiodic components.

6.4.11 Comparison of ViEEG spectra with iEEG

For each ROI, we calculated the median of PSD_{iEEG} (\overline{PSD}_{iEEG}) across all available channels within the ROI (N_{ROI}). The median of PSD_{ViEEG} (\overline{PSD}_{ViEEG}) for each ROI was obtained across a total

number of channels = $N_{ROI} \times \text{Number of healthy subjects}$. The overlap between PSD_{iEEG} and PSD_{ViEEG} was calculated for each frequency bin as:

$$overlap = \begin{cases} 1 - \frac{|\overline{PSD}_{iEEG} - \overline{PSD}_{ViEEG}|}{SD_{ViEEG}}; & \text{if } \overline{PSD}_{ViEEG} - SD_{ViEEG} \leq \overline{PSD}_{iEEG} \leq \overline{PSD}_{ViEEG} + SD_{ViEEG} \\ 0; & \text{otherwise} \end{cases} \quad (3)$$

Where SD_{ViEEG} is the standard deviation of PSD_{ViEEG} , across all available channels within the ROI (N_{ROI}). We calculated the *average overlap* for each ROI before and after removing the aperiodic components of the spectra. Average overlap quantifies the distance between \overline{PSD}_{ViEEG} and \overline{PSD}_{iEEG} at each frequency bin. The value of this metric ranges between 0 and 1 (calculated for 160 frequency bins). If the \overline{PSD}_{ViEEG} perfectly coincides with the \overline{PSD}_{iEEG} at a specific frequency bin, the *overlap* is 1, and if the \overline{PSD}_{iEEG} is greater or less than one SD_{ViEEG} , the *overlap* is zero at that frequency bin. We then obtained average overlap across all the frequency bins within each frequency band of interest: δ (0.5-4Hz), θ (4-8Hz), α (8-13Hz), β (13-30Hz), and γ (30-80Hz).

6.4.12 Comparison of ViEEG with iEEG in terms of peak frequency

We also compared the oscillatory peaks between the MEG-estimated ViEEG and the MNI iEEG atlas. Using FOOF, we identified all oscillatory peaks in each iEEG and ViEEG channel. For each ROI, the number of channels (out of the total number in each ROI N_{ROI}) exhibiting an oscillatory peak in a specific frequency band was calculated for the iEEG and ViEEG of each subject. Then we calculated the percentage difference of the number of channels exhibiting peak in a specific frequency band as:

$$Peak_estimated_{SUBi} = \frac{N_{peak_ViEEG_i} - N_{peak_iEEG}}{N_{ROI}} \times 100 \quad (4)$$

Where $N_{peak_ViEEG_i}$ is the number of channels exhibiting peaks in ViEEG in subject i and N_{peak_iEEG} is the number of channels exhibiting peaks in iEEG, in a specific frequency band. This measure was obtained for each ROI and each frequency band for each subject i . To obtain a group level estimation of channels exhibiting peaks per ROI per frequency band, we calculated the median of $Peak_estimated_{SUBi}$ over 45 subjects. This metric is a percentage assessing the overestimation or underestimation of MEG-estimated ViEEG channels showing oscillatory peaks, when compared to iEEG. The value of the Median ($Peak_estimated_{SUBi}$) ranges from -100% to

100%. For a particular ROI and frequency band, Median ($Peak_estimated_{SUBi}$) = +100% indicates that all the ViEEG channels in that ROI (N_{ROI}) showed peaks in that frequency band, whereas no peak was identified in any of the iEEG channels in that ROI and frequency band. We called it a 100% overestimation of peaks by MEG-estimated ViEEG in that ROI. On the contrary, a -100% estimation (underestimation) is obtained when all the iEEG channels in a ROI exhibit peaks, but ViEEG fails to identify any peak in that ROI. The peaks are well estimated by ViEEG if the Median ($Peak_estimated_{SUBi}$) is close to zero.

6.4.13 Comparison with minimum norm estimate (MNE) and LCMV beamformer

To check whether the choice of the source imaging method, wMEM, had influenced the results, we applied two other source imaging methods: (1) depth-weighted minimum norm estimate (MNE) (Hämäläinen & Ilmoniemi, 1994), and (2) Linearly Constrained Minimum Variance (LCMV) Beamformer (Van Veen et al., 1997). MNE: To calculate the noise covariance for MNE, we used 2 seconds of resting state data from each subject. We estimated the regularization hyperparameter λ by using the signal-to-noise ratio (SNR) of the data, as $\lambda = 1/SNR^2$, with the SNR set to 3 (default value in Brainstorm software). After source reconstruction on the cortical surface, we estimated ViEEG potential following the method described in section 6.4.8. LCMV beamformer: The source space for the beamformer consisted of the actual iEEG locations from the iEEG atlas (after coregistration in each subject native MRI space). The forward model was created using OpenMEEG (1-layer boundary element model). Data covariance was calculated from the entire resting state data segment (60 seconds) in each subject. Unlike the distributed source imaging methods, wMEM and MNE, LCMV beamformer reconstructed the virtual time series as MEG current density, directly at the location of iEEG contacts (Tamilia et al., 2021; Van Klink et al., 2016). For each position, the dipole was modeled with unconstrained orientation. The dipole orientation which maximizes the spatial filter output was selected for the final filter computation. The forward and inverse solutions for LCMV beamformer were calculated using fieldtrip toolbox (Oostenveld et al., 2011).

6.5 Results

6.5.1 Frequency specific brain maps of relative power

In Figure 6-2, the group average of relative PSD is plotted for 38 ROIs for iEEG and MEG-estimated ViEEG, as well as a map of the t-statistic comparing PSD in iEEG and ViEEG for each ROI and frequency band. For each frequency band in Figure 6-2, we used a common color bar for both modalities, thus highlighting how much MEG could estimate relative power when compared to iEEG. Fig S2 shows another representation of the same data, the color bar ranging from minimum to maximum value for each modality in each frequency band. Fig S2 highlights the regions exhibiting the strongest activation of average relative power within each modality.

Overall, similar patterns of power distribution were observed between iEEG and MEG-estimated ViEEG, such as high power in delta, theta, and gamma bands in the anterior ROIs, and high power in the alpha band in posterior ROIs. Beta power was strong around the primary and supplementary motor regions in both iEEG and ViEEG. However, for all frequency bands in Figure 6-2, the relative PSD in each iEEG ROI was very distinct, showing important contrasts and a larger range from strongest to weakest activity among ROIs, whereas MEG-estimated ViEEG maps were smoother among the neighboring ROIs spanning a smaller range of activity. This was evident especially in deeper regions such as the hippocampus and amygdala, which were very distinguished in iEEG showing very strong or weak activity, whereas these regions showed smoother activation in ViEEG, almost undistinguishable from the neighboring ROIs. We also observed high delta power and weak beta power in iEEG in lateral posterior ROIs, which were not well estimated by ViEEG. Figure 6-2B and Fig S3 show the difference of relative PSD between iEEG and ViEEG for the regions that are statistically different (*Welch's* unequal variances t-test, $p < 0.05$, Bonferroni corrected for 38 ROIs and 5 frequency bands), further illustrating regions where MEG overestimated relative power in alpha, beta and gamma band, and regions where MEG underestimated relative power in theta band.

Comparison of MEG-estimated average relative PSD with MNI iEEG atlas

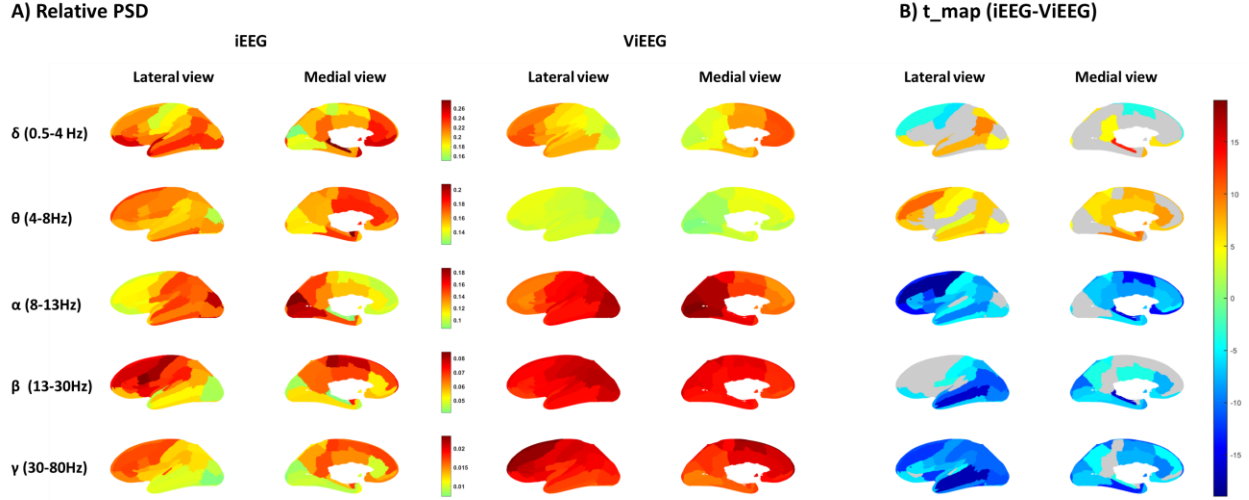


Figure 6-2: Group average of relative PSD values across each frequency band and over all the available channels in each ROI of the iEEG atlas, the ground truth, the MEG-estimated ViEEG using wavelet-MEM (wMEM) method. The number of channels in each ROI (N_{ROI}) in iEEG varies. For each ROI, ViEEG was estimated for $45 \times N_{\text{ROI}}$ channels, where the total number of subjects is 45. The relative PSD for each channel is calculated as the ratio of the power of the signal in each frequency bin relative to the total power of the signal. Relative PSD value for a channel range between 0 and 1. The color bar ranges from minimum to maximum value among iEEG and ViEEG in each frequency band, such that the scale is the same for both modalities in a given band. The corresponding t_{map} is shown in (B). We showed with color the ROIs which were statistically different (*Welch's* unequal variances *t*-test, $p < 0.05$, Bonferroni corrected for 38 ROIs and 5 frequency bands, positive t corresponding to larger PSD in iEEG when compared to ViEEG).

6.5.2 Analysis of spectral oscillatory components

In Figure 6-3, for four typical example ROIs selected at different depths (two in the lateral and two in the medial side), we show the decomposition of spectra into periodic and aperiodic components for iEEG and ViEEG. The spectra are plotted as median \pm standard deviation across all available channels within a ROI, N_{ROI} channels for iEEG, and the *number of healthy subjects* $\times N_{\text{ROI}}$ channels for ViEEG. Figure 6-3 also shows the probability histogram of all identified oscillatory peaks in the ROI for ViEEG and iEEG. For comparison between the ViEEG and iEEG spectra, we only considered the periodic components of the spectra, after removing the aperiodic components from

the original spectra. The comparison between iEEG and ViEEG spectra is discussed in the following sections.

Decomposition of the spectra into periodic and aperiodic components

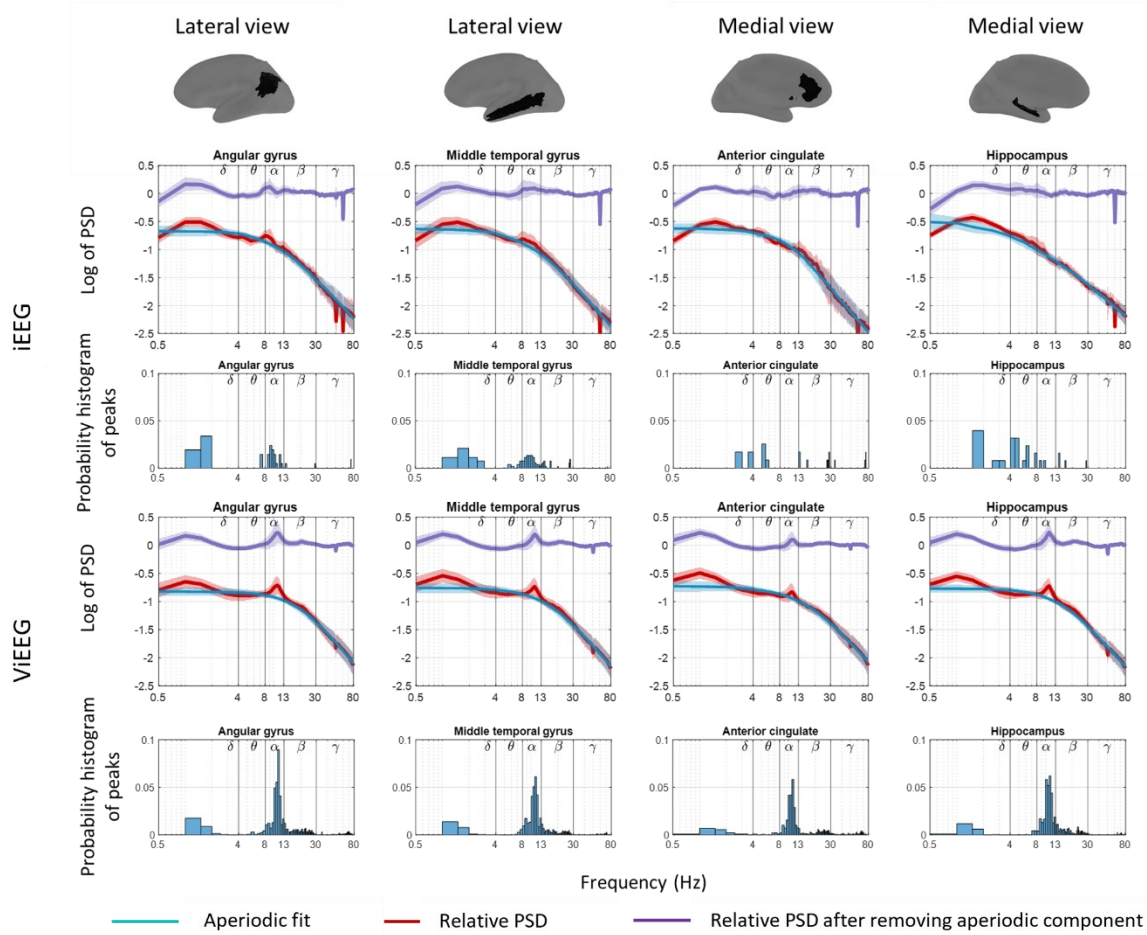


Figure 6-3: Decomposition of spectra into periodic and aperiodic components shown in a few example ROIs for iEEG and ViEEG. For both iEEG and ViEEG, the top panel shows the relative PSD before and after removing the aperiodic component and the bottom panel shows the probability histogram of identified peaks in δ (0.5-4Hz), θ (4-8Hz), α (8-13Hz), β (13-30Hz) and γ (30-80Hz). The aperiodic fits and oscillatory peaks are identified using the FOOOF toolbox (Donoghue et al., 2020).

6.5.3 Comparison of ViEEG spectra with iEEG

We show the comparison between iEEG and ViEEG spectra for four example ROIs (two in the lateral and two in the medial side) in Figure 6-4, before and after removing aperiodic components. We selected these four ROIs based on how MEG estimated the spectra compared to iEEG, quantified by the metric average overlap (performance worsening from left to right, after removing

the aperiodic components). The figure shows the value of average overlap quantified for each frequency band for a ROI. For all four ROIs, the average overlap improved after removing the aperiodic components (Figure 6-4C).

For *angular gyrus*, the MEG estimated the spectra quite well compared to iEEG, in most frequency bands after removing the aperiodic components. The similarity between spectra was quantified by average overlap (δ : 0.53, θ : 0.74, α : 0.31, β : 0.77, γ : 0.52). Before removing the aperiodic components, the average overlap values in all frequency bands were clearly lower δ : 0.13, θ : 0.13, α : 0.16, β : 0.01, γ : 0.08.

In the *middle temporal gyrus*, the average overlap in all frequency bands after removing the aperiodic spectra are δ : 0.2, θ : 0.55, α : 0.55, β : 0.47, γ : 0.48. Here we chose another ROI for which MEG-estimated ViEEG exhibited similar spectra to gold standard iEEG spectra, for all bands except delta. Before removing the aperiodic spectra, those values were much worse: δ : 0.14, θ : 0.3, α : 0.33, β : 0.01, γ : 0.03.

The example medial ROI *anterior cingulate* also showed improvement after removing the aperiodic components. The average overlap values in all frequency bands before and after removing aperiodic components are δ : 0.09, θ : 0.29, α : 0.38, β : 0.18, γ : 0.0 and δ : 0.27, θ : 0.3, α : 0.61, β : 0.2, γ : 0.3, respectively. For this medial structure, more difficult to localize in MEG because of its depth, average overlap values were good in the alpha band but lower in other bands (around 0.3), when compared to previous examples.

Finally, we showed an example of deep ROI, the *hippocampus*. MEG estimated the spectra in the *hippocampus* very poorly compared to iEEG. The average overlap values in all frequency bands before and after removing aperiodic components are δ : 0.1, θ : 0.32, α : 0, β : 0, γ : 0.47 and δ : 0.13, θ : 0.04, α : 0.29, β : 0.2, γ : 0.37, respectively. Although the spectral comparison improved after removing the aperiodic components, they remained inaccurate compared to other lateral superficial ROIs. It is worth mentioning that with MEG we estimated a clear peak in the alpha band in the hippocampus, whereas iEEG data were exhibiting no alpha band peak.

For each ROI, Figure 6-4 also shows the frequency bins at which iEEG and ViEEG were statistically different using the Mann Whitney U test ($p < 0.05$, Bonferroni corrected for 38 ROIs and 160 frequency bins), before (Figure 6-4A) and after (Figure 6-4B) removing the aperiodic

components from the spectra, which is in agreement with the overall improvement in average overlap after removing the aperiodic components (Figure 6-4C).

The comparison between iEEG and ViEEG spectra after removing the aperiodic components for all 38 ROIs is shown in Fig S4.

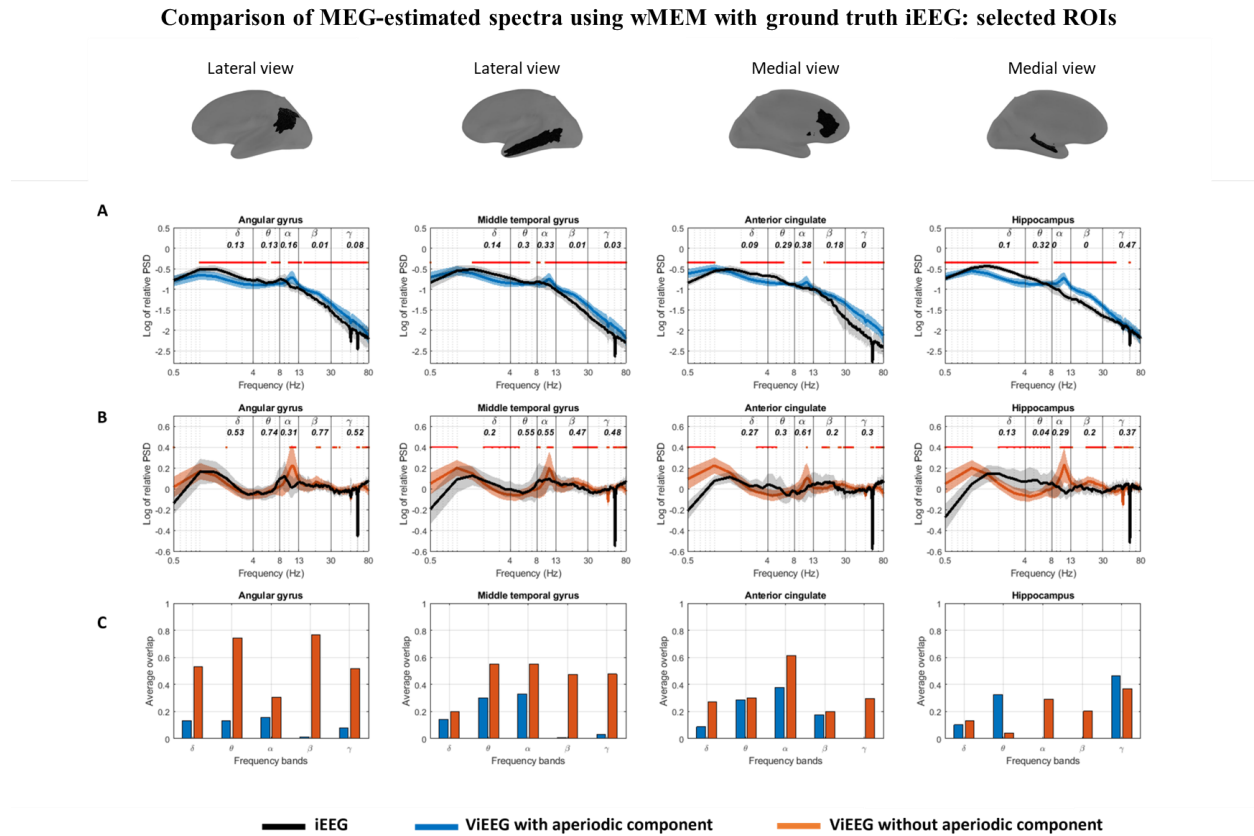


Figure 6-4: Comparison of periodic components of MEG-estimated spectra with ground truth iEEG, with aperiodic components (A) and without aperiodic components (B) shown for a few selected ROIs. For each spectrum, we are reporting the median value (black, blue and orange straight lines) together with corresponding standard deviation (shaded area) over all channels. Average overlaps between ViEEG and iEEG spectra across each spectral band are shown in (C). The value of overlap is calculated at each frequency bin and ranges from 0 to 1. For a ROI, if the median of PSD_{ViEEG} perfectly coincides with the median of PSD_{iEEG} at all frequency bins within a specific frequency band, the average overlap is 1. In A and B frequency bins are marked as red dots when iEEG and ViEEG are statistically different (Mann Whitney U Test, $p < 0.05$, Bonferroni corrected for 38 ROIs and 160 frequency bins).

In Figure 6-5, we summarized the average overlap for all 38 ROIs before and after removing the aperiodic components. It shows that for all frequency bands, the average overlap values improved after we removed the aperiodic components. If we compare the ROIs after removing the aperiodic spectra, we observe that the spectra in lateral regions are overall better estimated when compared to the medial ROIs. It was clearly the case for deeper regions like the hippocampus and amygdala, for which MEG-estimated ViEEG spectra did not accurately recover the actual iEEG spectra. On the other hand, the PSD in lateral temporal and parietal regions were localized accurately for all bands, as well as the medial posterior cingulate region. Especially, the medial ROIs in the theta band were very poorly estimated compared to other frequency bands. The delta band was very poorly estimated in occipital ROIs. This was also the case when we compared relative power in Figure 6-2, iEEG showed high activation in the delta band in the occipital regions which were not well estimated by MEG. Fig S5 shows the difference of relative PSD between iEEG and ViEEG before and after removing the aperiodic components for the regions that are statistically different (*Welch's* unequal variances t-test, $p < 0.05$, Bonferroni corrected for 38 ROIs and 5 frequency bands).

Spectral components estimated by MEG compared to MNI iEEG atlas: 38 ROIs

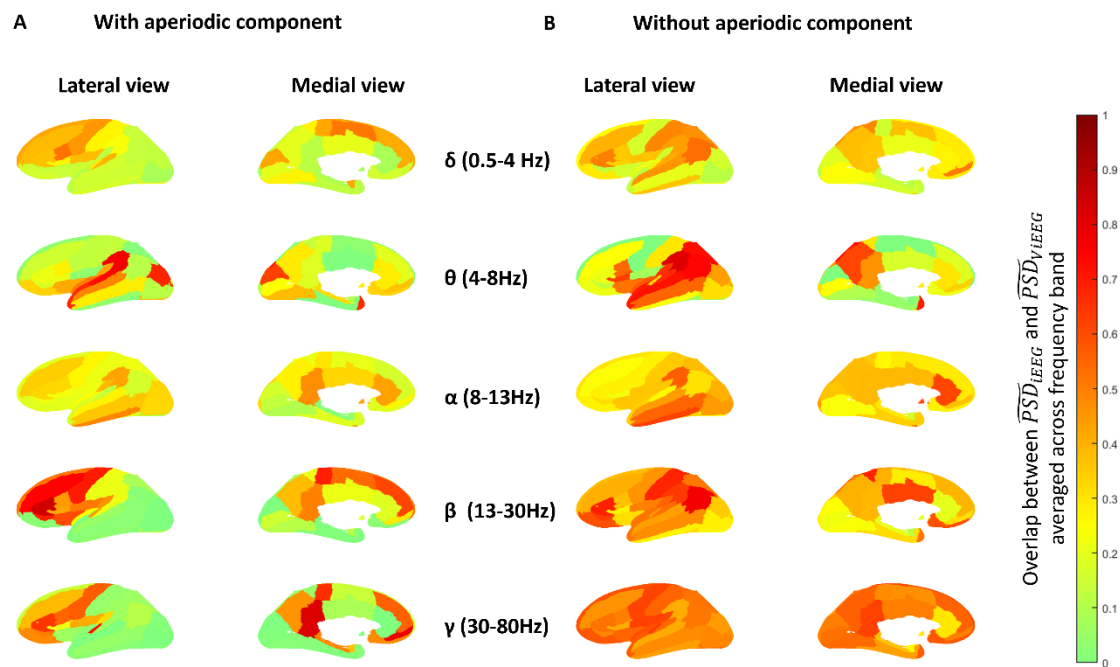


Figure 6-5: Average overlap between ViEEG and iEEG spectra across each spectral band for each of the 38 ROIs, (A) with and (B) without aperiodic components. The value of overlap is calculated at each frequency bin and ranges from 0 to 1. For a ROI, if the median of PSD_{ViEEG} perfectly coincides with the median of PSD_{iEEG} at all frequency bins within a specific frequency band, the average overlap is 1.

6.5.4 Comparison of ViEEG with iEEG in terms of oscillatory peaks

Oscillatory peaks in each band were estimated using the FOOOF algorithm, after removing the aperiodic component. When we compared MEG-estimated spectra with the MNI iEEG atlas in terms of oscillatory peaks, we found that the probability histogram of peaks from all ROIs (Figure 6-6A) in iEEG has more variability in all frequency bands, whereas MEG-estimated peaks are more narrowly concentrated within each frequency band, especially exhibiting high concentration in the alpha band. Also, the MEG-estimated peaks in the theta band were much fewer than in iEEG. Figure 6-6B shows the probability histogram of peaks identified in iEEG, and ViEEG for an example ROI (hippocampus) for one subject. It also shows the value of the percentage difference of the number of channels exhibiting peaks in a specific frequency band, as a proportion of the total number of channels in that ROI ($Peak_estimated_{SUBi}$) (Eq. 4). For instance, iEEG found peaks in the theta band, whereas no peak was found in ViEEG channels in this band. This was quantified in terms of the percentage difference of the number of channels exhibiting peak, $Peak_estimated_{SUBi} = -40\%$ (underestimation) in the theta band. Thus, in the hippocampus, MEG clearly underestimated peaks in the delta, theta, and gamma band by 36%, 40%, and 31% respectively. On the other hand, we observed a large overestimation of channels exhibiting peaks in ViEEG in the alpha band by 83%. In the beta band, the estimation of peaks by ViEEG was comparable with those in iEEG ($Peak_estimated_{SUBi} = 0$). The probability histograms of peaks identified in iEEG and ViEEG for all 38 ROIs are shown in Fig S6.

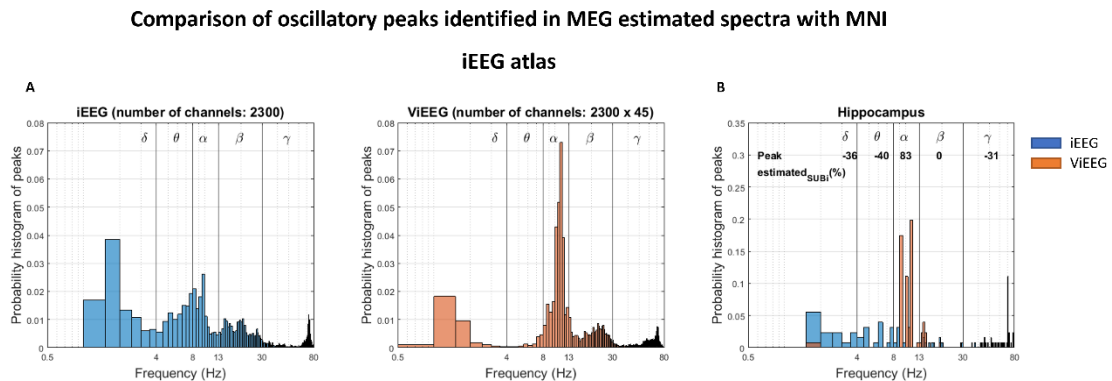


Figure 6-6: (A) Probability histogram of all identified peaks in all ROIs for iEEG and ViEEG using the FOOF toolbox. (B) Probability histogram for all identified peaks in hippocampus for iEEG and ViEEG for one subject. We also show the percentage difference of the number of channels exhibiting spectral peaks in ViEEG compared to iEEG in each spectral band, as a proportion of the total number of channels in the ROI. The value of $Peak_estimated_{SUBi}$ ranges from -100% to 100%. The peaks are well estimated by ViEEG in comparison with iEEG, for a specific frequency band, if $Peak_estimated_{SUBi}$ is close to zero.

In Figure 6-7, we summarized the percentage difference of the number of channels exhibiting a peak in a specific frequency band for 45 subjects, by plotting the median of $Peak_estimated_{SUBi}$ (calculated for each subject) over 45 subjects and shown for 38 ROIs. Warmer colors indicate an overestimation and cooler colors indicate an underestimation of channels exhibiting peaks by MEG when compared to the MNI iEEG atlas. We observe that MEG overestimated peaks in the alpha band for most ROIs, especially higher in frontal (lateral and medial) ROIs (>40%) and deeper ROIs such as hippocampus and amygdala (~100% overestimation). The peaks in the delta band were well estimated in most ROIs except the occipital ROIs (like Figure 6-2 and Figure 6-5), and deep ROIs such as the hippocampus and posterior cingulate, where peaks were underestimated by MEG (<-35%). We observe an underestimation of peaks in beta and theta bands, in frontal and central ROIs (both lateral and medial) (<-35%). MEG moderately overestimated beta peaks in posterior regions and gamma peaks all over the brain regions. Those regions also showed higher relative power in MEG (Figure 6-2) compared to iEEG.

Estimation of peaks by MEG in all spectral bands compared to iEEG: 38 ROIs

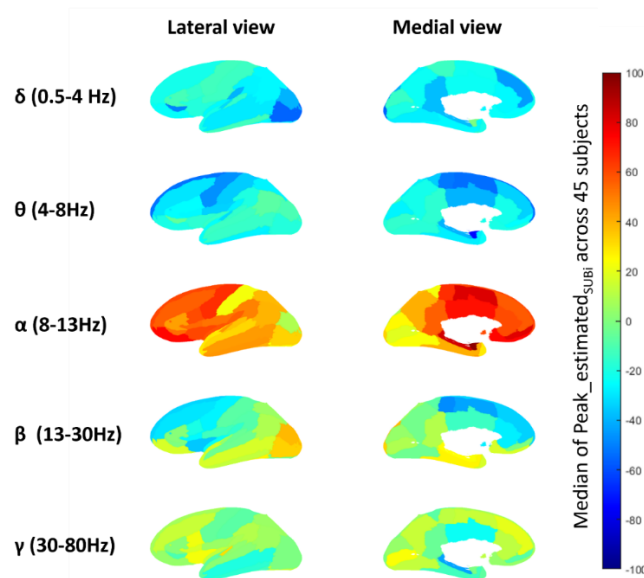


Figure 6-7: Median values of $Peak_estimated_{SUBi}$ over 45 subjects are plotted for 38 ROIs. $Peak_estimated_{SUBi}$ measures the percentage difference of the number of channels exhibiting spectral peaks in ViEEG compared to iEEG, as a proportion of the total number of channels in each ROI, for each spectral band and ROI, calculated for each subject i . The value of the median $Peak_estimated_{SUBi}$ over all subjects ranged from -100% to 100%. Median ($Peak_estimated_{SUBi}$) = +100% indicates that all the channels from ViEEG in a ROI (N_{ROI}) showed a peak in that frequency band, whereas no peak was identified in any of the iEEG channels in that ROI. We called it a 100% overestimation of oscillatory peaks by MEG-estimated ViEEG in this ROI. On the contrary, a -100% estimation is obtained when all the iEEG channels in a ROI exhibit peaks, but no peak was identified in ViEEG in that ROI, resulting in a 100% underestimation. The peaks were better estimated by ViEEG for the ROIs if the median ($Peak_estimated_{SUBi}$) was close to zero. The values in the color bar are ranging from underestimation (-100%, negative values, cooler color) to overestimation (+100%, positive values, warmer color) of channels exhibiting peak by MEG-estimated ViEEG.

It is also important to mention that all our results were reported in a common average montage. We also produced these results for bipolar montage and a similar pattern was found. Please see supplementary Fig S7 and Fig S8 comparing the results from the two montages. Although the spectral components recovered by both montages were very reproducible, bipolar montage was slightly better at estimating the oscillatory peaks in the alpha band, especially in the frontal regions.

6.5.5 iEEG and ViEEG amplitude

In Figure 6-8, the average amplitude across the iEEG and ViEEG channels in each ROI is plotted for the 38 ROIs, where each ROI amplitude was normalized by the average amplitude of all 38 ROIs (supplementary Fig S9 shows actual values in μV). The mean amplitude across 38 ROIs was $28.4 \mu V$ for iEEG, and $0.67 \mu V$ for ViEEG, since underestimation of the amplitude after solving the MEG inverse problem was expected by the regularization procedure. Thus, we normalized iEEG and ViEEG amplitudes to be comparable. A strong positive correlation (Spearman's $R = 0.69$, $p < 0.001$) was found for the amplitudes of 38 ROIs between iEEG and ViEEG. In Figure 6-8, we also plotted the difference of normalized amplitudes between iEEG and ViEEG for each ROI and the corresponding t_map (the ROIs with color which were statistically different, *Welch's* unequal variances t -test, $p < 0.05$, Bonferroni corrected for 38 ROIs). We represented the absolute value of amplitude difference in the bar plot and showed the signed amplitude difference on the inflated cortical surface. In the lateral parietal and lateral temporal regions, the ViEEG amplitudes

were significantly larger than the iEEG amplitudes ($p < 0.05$, Bonferroni corrected for 38 ROIs). On the other hand, in the medial frontal regions and some deep regions such as the hippocampus, the iEEG amplitudes were significantly higher than the MEG-estimated ViEEG amplitudes ($p < 0.05$, Bonferroni corrected for 38 ROIs).

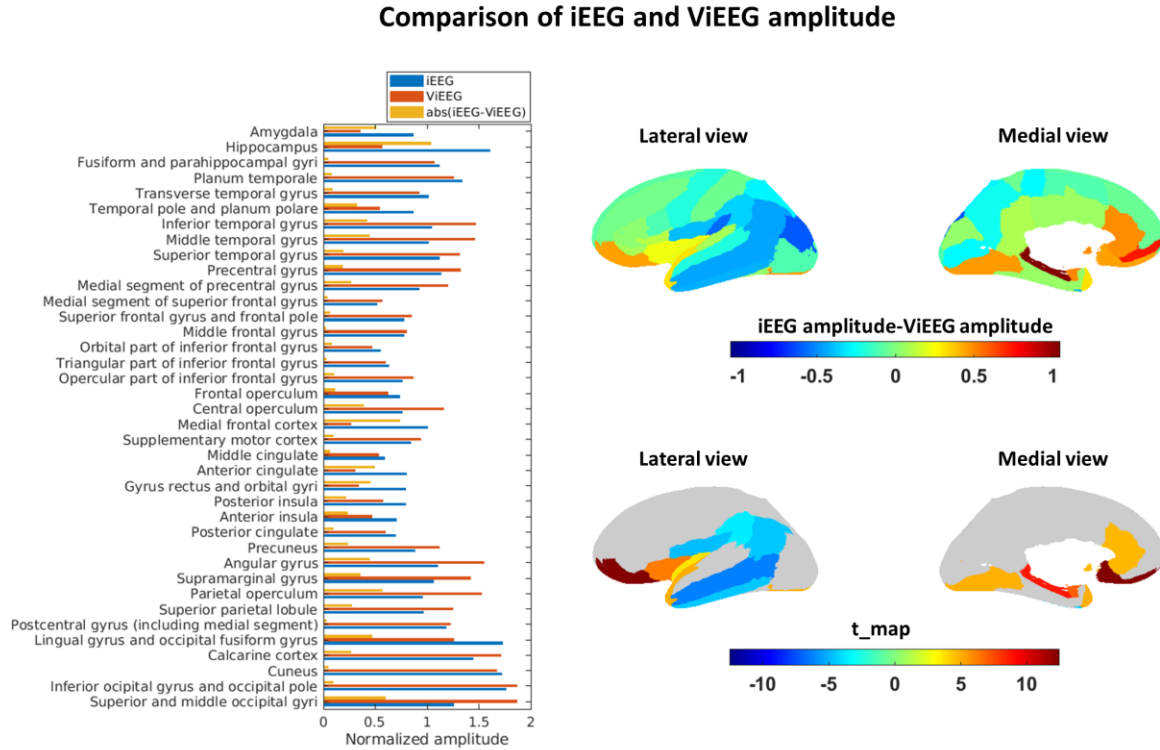


Figure 6-8: Average amplitude across the channels in each ROI, normalized by the average amplitude across all ROIs. The bar plot shows the absolute difference of normalized amplitude between iEEG and ViEEG. The right panel shows the difference of normalized amplitude between iEEG and ViEEG on the inflated cortical surface (lateral and medial views) (top) and the corresponding t_{map} (bottom). For t_{map} , we showed the ROIs which were statistically different (*Welch's* unequal variances t -test, $p < 0.05$, Bonferroni corrected for 38 ROIs, positive t corresponding to larger amplitude in iEEG when compared to ViEEG).

We calculated the correlation between the signed *amplitude difference* and the average overlap (calculated in Figure 6-5) for 38 ROIs in all frequency bands. It showed moderate negative correlation in alpha band (Spearman's $R = -0.33$, $p = 0.04$) and beta band (Spearman's $R = -0.3$, $p = 0.08$). A negative correlation indicates that for regions exhibiting higher ViEEG amplitude when compared to iEEG amplitudes, the average overlap between ViEEG and iEEG spectra was better.

In delta and theta frequency bands, weak negative correlation was found (δ : Spearman's $R = -0.19$, $p = 0.25$, θ : Spearman's $R = -0.22$, $p = 0.18$). No correlation was found in gamma band (Spearman's $R = -0.03$, $p = 0.8$).

6.5.6 Comparison with minimum norm estimate (MNE) and LCMV beamformer

The comparison among three source imaging methods (i.e. wMEM, MNE and LCMV Beamformer) is described in detail in the supplementary material. In Fig S10 and Fig S11, the group average of relative PSD is plotted for 38 ROIs for iEEG, and MEG-estimated ViEEG from wMEM, MNE, and beamformer. Fig S10 shows that the group average of PSD maps estimated from wMEM, MNE, and beamformer are overall similar. Compared to the iEEG atlas (Fig S11), ViEEG estimated from MNE underestimated the theta band when compared to wMEM and beamformer. An overestimation in the gamma band was found in ViEEG estimated using MNE and beamformer. In contrast, ViEEG power in the theta and gamma bands estimated from wMEM was in a closer range to iEEG (see details in the supplementary material section S.3). The relative PSD estimated by the distributed source imaging methods, wMEM and MNE on the cortical surface (Fig S12) also showed similar patterns in all frequency bands, except for gamma (see details in the supplementary material section S.2). We also showed a detailed comparison between iEEG and ViEEG spectra for four example ROIs (the same presented in Figure 6-4) using MNE (Fig S13) and beamformer (Fig S14), before and after removing aperiodic components. Overall, for all three methods, MEG-estimated spectra were more comparable to iEEG spectra after we removed the aperiodic components (as demonstrated by increased average overlap). The spectra provided by wMEM were more accurately estimated in beta and gamma bands when compared to the beamformer and MNE (Figure 6-4A, Fig S13A and Fig S14A). In Fig S15, we also plotted the aperiodic components estimated from wMEM, MNE and beamformer for those four example ROIs, and assessed them using the average overlap metric calculated as described in section 6.4.11. We can see that wMEM is performing better than MNE and beamformer in beta and gamma bands. Fig S16 summarizes the overlap between the aperiodic components estimated from iEEG and ViEEG for all 38 ROIs for wMEM, MNE and beamformer. Further details are found in the supplementary materials.

6.6 Discussion

We aimed to assess the reliability of MEG source imaging of awake resting state oscillations by comparing with the MNI iEEG atlas as ground truth (Frauscher et al., 2018). We compared MEG-estimated ViEEG spectra from a healthy group of participants (Pellegrino et al., 2022) with the atlas of healthy brain activity, in terms of (i) oscillatory components of the spectra, (ii) oscillatory peaks, and (iii) relative power. This is the first study using an iEEG atlas of healthy awake activity to validate quantitatively the accuracy of MEG source imaging of resting state activity. We investigated the performance of our source imaging technique, the wavelet based Maximum Entropy on the Mean (wMEM) (Aydin et al., 2020; Lina et al., 2012; Pellegrino et al., 2016). A quantitative comparison between iEEG and ViEEG spectra showed that the ViEEG spectra were closer to the iEEG spectra after the aperiodic components were removed from the spectra (Figure 6-5). The estimation of the ViEEG spectra was more accurate in the lateral regions compared to the medial regions (Figure 6-5B). Especially better estimation was found in the regions exhibiting higher ViEEG amplitude compared to iEEG (Figure 6-8), such as the lateral parietal, lateral temporal, and some lateral occipital regions (Figure 6-5B). We found that the estimation of ViEEG resting state spectra was particularly inaccurate in deep regions such as the hippocampus and amygdala, for most frequency bands. Our study also found that MEG-estimated spectra were dominated by oscillations in the alpha band, especially in anterior and deeper regions, unlike the actual in situ measurements from the atlas (Figure 6-4, Figure 6-7, Fig S4). This observation is consistent with the finding of dominance in alpha oscillations reported in previous studies (Capilla et al., 2022; Keitel & Gross, 2016; Mahjoory et al., 2020). In our study, the MNI iEEG atlas as ground truth enabled us to quantify the extent of overestimation or underestimation of alpha dominance in MEG-estimated spectra. A quantitative comparison of oscillatory peaks showed that MEG overestimated peaks in the alpha band in most brain regions, especially in the frontal and deep regions (Figure 6-7). In the delta, theta, and gamma bands, the peaks in the deep regions were underestimated, whereas they were more accurately estimated in lateral cortical regions. In terms of relative power, the distribution of MEG relative power reported in our study was consistent with the previous MEG studies in different frequency bands (Figure 6-2, Fig S2, Fig S12) (Hillebrand et al., 2012; Mahjoory et al., 2020; Mellem et al., 2017; Niso et al., 2016; Niso et al., 2019). However, when compared to the MNI iEEG atlas (Figure 6-2, Fig S3), important differences in average relative power were observed in the anterior regions for alpha, in the

posterior regions for delta, beta and gamma, and in deep regions (such as hippocampus and amygdala) for all bands. Especially in theta, MEG largely underestimated relative power compared to iEEG in all brain regions.

We also calculated the relative power for MEG and performed the spectral comparison using two other source imaging methods, depth-weighted MNE and LCMV beamformer (Fig S10-S16), to determine if our findings were not mainly driven by our source imaging method, wMEM. Indeed, results were overall similar when depth-weighted MNE and beamformer were applied. Investigating carefully the comparison between MNE, beamformer and wMEM, ViEEG estimated using wMEM exhibited better performance (i.e., closer to iEEG) in relative power, when compared to MNE and beamformer, especially in beta and gamma (Fig S11).

6.6.1 Removing the aperiodic component improves the spectral comparison between ViEEG and iEEG

Electrophysiological power spectra are composed of periodic components, typically characterized by spectral peaks and aperiodic components, also known as 1/f-like or arrhythmic components (He, 2014). While analyzing electrophysiological power spectra of neuronal oscillations, the separation of periodic and aperiodic components allows a better estimation of the periodic component (Donoghue et al., 2021; Wen & Liu, 2016). We applied FOOOF (Donoghue et al., 2020) to separate the periodic and aperiodic components of the spectra from iEEG and ViEEG. We quantitatively compared the iEEG and ViEEG spectra before and after removing the aperiodic components. The spectra estimated by MEG became more comparable to iEEG after the aperiodic components were removed (Figure 6-5). This is reflected by the metric *average overlap*, which quantifies the overlap between iEEG and ViEEG spectra. In Figure 6-5A, the average overlap values of the spectra, which include the aperiodic components, were very low for all frequency bands, with most ROIs exhibiting an average overlap < 0.2 . The average overlap values of the ROIs were much improved after removing the aperiodic components (Figure 6-5B). This indicates that the discrepancies between iEEG and ViEEG spectra were mostly driven by the variations in the aperiodic components between the two modalities (Fig S16A). The aperiodic component might be generated by spatial interactions among neuronal populations (Aguilar-Velázquez & Guzmán-Vargas, 2019). The iEEG records brain activity locally, with a spatial sensitivity of less than 1cm (von Ellenrieder et al., 2021), and would therefore not pick up all the spatial interactions, leading

to a different aperiodic component from the one recorded by the more spatially spread sensitivity of scalp EEG or MEG. Moreover, in a recent study based on computational modeling using the virtual brain project, we found that anatomical and forward model properties of EEG and MEG resulted in different aperiodic components between EEG and MEG (Bénar et al., 2019).

The differences in the aperiodic components between MEG and iEEG could also result from the differences in the inherent mechanism of generation of the signals in those two modalities. The local bioelectrical environment contributes to the generation of the local field potential of iEEG (Bédard & Destexhe, 2009), whereas MEG mainly originates from the activation of pyramidal sources.

6.6.2 MEG spectra were better estimated in lateral regions than in medial regions

MEG-estimated spectra were better estimated in lateral regions compared to the medial regions in most frequency bands (Figure 6-5B). The lateral parietal and lateral temporal regions in most frequency bands showed average overlap values greater than 0.5. In contrast, for most of the medial ROIs, the average overlap values were less than 0.5 in all frequency bands (except gamma). We found a negative correlation between the signed difference of iEEG and ViEEG amplitude (Figure 6-8) and the average overlap values (Figure 6-5B) in all bands except gamma. These negative correlations were moderate in the alpha and beta bands, and weak in the delta and theta bands. Such negative correlations indicate that average overlap values were better in regions having ViEEG amplitudes greater than iEEG amplitudes, which means MEG could estimate the spectra from these ROIs more accurately when underlying signals were of larger amplitudes for those regions. Example regions include the lateral parietal, lateral temporal, and some lateral occipital regions, which exhibited ViEEG amplitudes much higher than iEEG amplitudes (Figure 6-8) and also resulted in higher average overlap (Figure 6-5B). Overall, an important finding was that deep regions were not well estimated by MEG; results were similar for wMEM, MNE and beamformer (section 6.6.5 and supplementary material). For instance, the average overlap values were less than 0.3 in the hippocampus for all bands except gamma, and less than 0.25 in the amygdala for all bands. The reason for such poor estimation could be the large underestimation of the ViEEG amplitude compared to iEEG (Figure 6-8). Similarly, in the lingual gyrus and occipital fusiform gyrus, the ViEEG amplitude was largely underestimated compared to iEEG (Figure 6-8). The average overlap in this ROI was less than 0.25 in all bands except gamma.

6.6.3 Dominance of alpha oscillations in MEG

Oscillatory peaks in the alpha band were largely overestimated by MEG, especially in frontal regions ($Median (Peak_estimated_{SUBi}) = \sim 45-84\%$) and deep regions such as the hippocampus ($Median (Peak_estimated_{SUBi}) = 86\%$) and amygdala ($Median (Peak_estimated_{SUBi}) = 100\%$). We found widespread alpha oscillations in all brain regions (Figure 6-7, Fig S4, Fig S6). A quantitative comparison between the spectra from MEG-estimated ViEEG and the atlas (Figure 6-5B) showed, in most of the lateral frontal and medial regions, an average overlap in alpha of less than 0.5. A similar dominance of alpha oscillations in MEG was also reported in MEG resting state studies (Capilla et al., 2022; Keitel & Gross, 2016; Mahjoory et al., 2020). Using eyes open MEG data, Capilla et al. (2022) reported the dominance of alpha oscillations in all posterior regions. Alpha is of much higher amplitude with eyes closed than with eyes open. Thus, with eyes closed data, the dominance of alpha oscillations is expected to be more widespread and could explain why we found an overestimation of the alpha peak identified in MEG in most frontal regions. On the other hand, the large predominance of alpha oscillations found in deeper regions, which also had weak amplitudes, could be explained by source leakage from cortical signals getting localized with very low amplitude in deep regions. Nunez et al. (2001) and Srinivasan et al. (2006) also reported alpha dominance in brain regions with scalp recordings, including frontal regions. It is quite evident from intracranial EEG that alpha is not as prominent and widespread as seen from scalp recordings, especially not in the frontal regions (Groppe et al., 2013; Penfield & Jasper, 1954).

With electrocorticography (ECoG) recordings in patients with epilepsy, Groppe et al. (2013) reported that most dominant oscillations tended to be around ~ 7 Hz (in the theta range), not in the alpha range (8-13Hz) typically reported in scalp recordings. This is also evident from the peak histogram of iEEG and MEG (Figure 6-5A), iEEG tends to have the highest number of peaks around ~ 7 Hz, within theta and alpha bands, whereas MEG peaks were around $\sim 10-12$ Hz, in much higher proportions. Compared to iEEG, MEG underestimated theta and overestimated alpha, which was also evident in the relative power calculated in Figure 6-2. The reason EEG/MEG sees higher alpha oscillations might be a phase synchronization over larger extents than other bands (Groppe et al., 2013). The iEEG having a very local sensitivity profile, would pick up the activity from the alpha band, but also from other bands with low spatial phase synchronization. MEG, on

the other hand, having a more extended spatial profile, would pick up the generators of synchronous alpha activity interfering constructively, but generators of theta activity (or other poorly synchronized bands) would partially cancel out, leading to a dominant alpha rhythm.

To tackle the dominance of alpha oscillations, a few previous studies normalized each ROI spectrum by considering the average spectra of all other brain regions. Such normalization gives a measure of the characteristic features of each ROI spectrum compared to other brain regions, resulting in a less widespread influence of alpha oscillations in all brain regions (Capilla et al., 2022; Keitel & Gross, 2016). We did not incorporate such normalization in this study, as we aimed to compare the MEG-estimated spectra for each ROI with the MNI iEEG atlas, not with other ROIs. We also investigated iEEG and ViEEG data in a bipolar montage (Fig S7 and Fig S8). The spectral components estimated by MEG compared to the MNI iEEG atlas were very similar for bipolar and average montages (Fig S7). However, the peaks estimated by MEG were less dominant in the frontal regions in the alpha band in the bipolar montage, when compared to an average reference montage (Fig S8).

6.6.4 Differences in signal relative power

A qualitative comparison of relative power between MEG-estimated spectra and the atlas (Figure 6-2, Fig S2) showed that in general, both modalities have similar brain distributions, such as strong delta and theta power in frontal regions, alpha power in posterior regions, beta power in motor and frontal regions, and gamma power in frontal areas. However, when compared to the MNI iEEG atlas, the MEG-estimated relative power was spatially much more smoothly distributed. For instance, the atlas showed low power in the hippocampus in theta, alpha, and beta bands, in contrast to strong power in its neighboring region the para-hippocampal gyrus. In MEG, due to source leakage, such separation was not possible, resulting in similar distributions in the para-hippocampal gyrus, the hippocampus, and the neighboring regions for all frequency bands (Figure 6-2, Fig S2). The contrast between strong and weak relative power was reflected in MEG only where an extended area in iEEG exhibited a similar contrast. For instance, frontal regions showed weak alpha power compared to posterior regions in iEEG, a pattern that was also found in ViEEG (Fig S2). Similarly, posterior regions in theta and the orbito-frontal region in beta showed weak power compared to other regions within the specific band in iEEG, which were also reflected in ViEEG (Fig S2). Due to the source leakage in MSI, subtle changes in relative power in brain

regions (as seen in the atlas) were not accurately retrieved using MEG (Figure 6-2). This was particularly the case for deep regions localized with small amplitude in MEG. Similar mislocalization patterns were found with wMEM, MNE and beamformer (section 6.6.5, supplementary S.3).

Our MEG relative power maps were quite consistent with previous MEG studies (Niso et al., 2016; Niso et al., 2019). We also compared the MEG relative power on the cortical surface and MEG-estimated ViEEG relative power in the intracranial space in Fig S12 (described in the supplementary material). Fig S12 confirms that the conversion from the MEG source map to intracranial space (ViEEG) did not add any discrepancy, and the relative power in the virtual intracranial space (ViEEG) was concordant with the MEG relative power on the cortical surface.

6.6.5 wMEM for resting state localization and comparison with MNE and beamformer

We implemented and validated an adapted version of wavelet MEM to solve the inverse problem in the context of resting state source imaging. wMEM is a MEM framework specifically designed to localize oscillatory brain patterns in the context of EEG/MEG signals utilizing discrete wavelet transformation (Daubechies wavelets). Taking advantage of the MEM specific prior model (Chowdhury et al., 2013), wMEM can accurately localize the oscillatory patterns together with their spatial extent. We further adapted wMEM to localize wide band oscillations in resting state EEG/MEG data.

We observed that this new wMEM demonstrated improvement in localizing the underlying spatial extent of the generators when compared to the previous wMEM implementation (Lina et al., 2012) (results not shown) and depth-weighted MNE (Fig S1), therefore justifying our rationale for incorporating the adaptations when localizing resting state data.

We also included additional results when considering depth-weighted MNE and beamformer source localization in the supplementary material (Fig S10-S16). Overall, we show that the findings were not driven by our source imaging method, wMEM. Both MNE and beamformer are widely used source imaging methods. For MNE, we performed first source imaging on the cortical surface and then applied a forward model to convert MEG current density into intracranial electrical potential in μV , for each iEEG contact, as done for wMEM. On the other hand,

beamformer estimated the virtual time courses directly on the iEEG contacts locations, consisting in local estimates of current density as proposed in Tamilia et al. (2021). For all methods, we found an overall similar pattern in terms of relative PSD, and removal of the aperiodic component made the spectra estimated from MEG more comparable to iEEG spectra. When compared to iEEG spectra, wMEM performed better than MNE and beamformer in the beta and gamma bands (see spectra shown in Figure 6-4, Fig S13, Fig S14 and the estimated aperiodic components shown in Fig S15). It is worth mentioning that our method consisting in converting MEG sources into virtual iEEG potentials (Abdallah et al., 2022; Grova et al., 2016) offers a solid quantification approach to compare MEG sources estimated using different source imaging techniques with actual iEEG in situ recordings, taking into account spatial sampling of iEEG data..

6.6.6 Limitations

One limitation of this study is that the normative MNI iEEG atlas was collected from patients with epilepsy, although by including only the iEEG electrodes implanted in the brain regions which turned out to be healthy. This limitation cannot be overcome, as iEEG data are never collected from healthy subjects. Such normative iEEG atlas data are so far the best ground truth and provide us with a unique opportunity to validate non-invasive source imaging techniques. Another limitation is the heterogeneity of iEEG channels in different ROIs. The sampling of iEEG channels was higher in lateral temporal, parietal, and frontal regions compared to medial and occipital regions. This might have biased our results, but not severely. We found a mild to moderate positive correlation between the number of channels in a ROI and the average overlap value (calculated in Figure 6-5B) in delta and beta bands (results not shown). It is worth mentioning that the distribution of patients' age in the iEEG atlas (31 ± 10 Y, range: 13-62 Y) was wider when compared to our MEG dataset (28.67 ± 4.13 Y, range: 20-38 Y), and such a difference could affect our spectral comparison due to the age-dependency of spectral characteristics (Hoshi & Shigihara, 2020). However, these effects are small (Hoshi & Shigihara, 2020) and given the fact that in the iEEG atlas, only three patients were above 55 and that the healthy subjects were covering the range between the 25% (25 Y) and the 75% (40 Y) quartile of the patients' age distribution, we believe our results to be minimally biased by age. We also combined channels in both hemispheres to maximize the sampling and the coverage of the brain. Thus, any effect of hemispheric asymmetry on oscillatory characteristics was lost. Also, the MEG data and iEEG data in this study were not

simultaneously recorded. Simultaneous iEEG-MEG recordings would give us more opportunities to validate region specific spectral components (De Stefano et al., 2022; Pizzo et al., 2019), which we plan to do in the future. However simultaneous iEEG-MEG recordings have limited spatial sampling, whereas we could study the whole brain with the normative MNI iEEG atlas.

6.7 Conclusion

We aimed to address the reliability of MEG source imaging by validating source imaging results with the MNI iEEG atlas as ground truth. We quantitatively estimated the concordance of MEG-estimated spectral components with the atlas and identified the regions for which MEG-estimated spectra are reliable and regions for which we should be cautious while interpreting MEG results. We found widespread source leakage in the alpha band oscillations in MEG-estimated spectra in frontal and deep brain regions, which was present before and after the removal of aperiodic components. In the future, we are planning to investigate these issues on simultaneous MEG-iEEG data and validate MEG source imaging of spectral components at the single-subject level.

6.8 Acknowledgment

This work was supported by Natural Sciences and Engineering Research Council of Canada (NSERC) Discovery grant, grant from Canadian Institutes of Health Research (CIHR) (PJT-159448 and FDN 143208), and the Fonds de recherche du Québec—Nature et technologies (FRQNT) Research team grant. JA was partially supported by The Canadian Open Neuroscience Platform scholarship and Irma Bauer Fellowship, Faculty of Medicine and Health Sciences, McGill University. GP and AG were supported by the Italian Ministry of Health (GR-2019-12368960 and GR-2018-12366092). BF was supported by CIHR project grant (PJT-175056), salary award (Chercheur-boursier clinicien Senior) of the Fonds de Recherche du Québec – Santé. The authors would like to thank Samuel Medina Villalon for his help in the data analysis for the revision of this manuscript.

Supplementary file for Manuscript 1:

<https://ars.els-cdn.com/content/image/1-s2.0-S1053811923003099-mmc1.docx>

7 Manuscript 2 EEG/MEG source imaging of deep brain activity within the Maximum Entropy on the Mean framework: simulations and validation in epilepsy

7.1 Preface

Localizing deep brain activity with EEG/MEG is challenging. In Study 1, when we validated MEG source imaging of resting-state oscillations using an intracranial EEG atlas, we found that MEG estimation was inaccurate for sources in deep structures such as the hippocampus. Although MEM-based techniques like cMEM and wMEM have been demonstrated to accurately estimate spatial extent, they did not incorporate depth weighting, limiting their ability to localize deep brain activity. In this second study of the thesis, we proposed a depth-weighted adaptation of cMEM and wMEM to improve the localization of deep generators. We also included an accurate surface segmentation of bilateral hippocampi in our source space, to more realistically recover these deep generators. We evaluated this method and the required tuning for depth weighting using realistic MEG/high-density EEG simulations of epileptic activity across various spatial extents, source depths, and signal-to-noise ratio (SNR) levels, as well as actual MEG/HD-EEG recordings from patients with focal epilepsy. We compared the proposed method with previous MEM techniques and depth-weighted minimum norm estimate (MNE). This chapter includes the published abstract, introduction, materials and methods, results, and discussions. Details of the depth-weighted MEM implementations are provided in Appendix B for manuscript 2 in Chapter 7 which is reported at the very end of this thesis.

This manuscript was published as:

Afnan, J; Cai, Z; Lina, J.M.; Abdallah, C; Delaire, E.; Avigdor, T.; Ros, V.; Hedrich, T.; von Ellenrieder, N.; Kobayashi, E.; Frauscher, B; Gotman, J., and Grova, C., 2024. EEG/MEG source imaging of deep brain activity within the Maximum Entropy on the Mean framework: simulations and validation in epilepsy. *Human Brain Mapping*. 2024 Jul 15;45(10):e26720. doi: <https://doi.org/10.1002/hbm.26720>

7.2 Abstract

Electro/Magneto- EncephaloGraphy (EEG/MEG) source imaging (EMSI) of epileptic activity from deep generators is often challenging due to the higher sensitivity of EEG/MEG to superficial regions and to the spatial configuration of subcortical structures. We previously demonstrated the ability of the coherent Maximum Entropy on the Mean (cMEM) method to accurately localize the superficial cortical generators and their spatial extent. Here, we propose a depth-weighted adaptation of cMEM to localize deep generators more accurately. These methods were evaluated using realistic MEG / high-density EEG (HD-EEG) simulations of epileptic activity and actual EEG/HD-MEG recordings from patients with focal epilepsy.

We incorporated depth-weighting within the MEM framework to compensate for its preference for superficial generators. We also included a mesh of both hippocampi, as an additional deep structure in the source model. We generated 5400 realistic simulations of interictal epileptic discharges for MEG and HD-EEG involving a wide range of spatial extents and signal-to-noise ratio (SNR) levels, before investigating EMSI on clinical HD-EEG in 16 patients and MEG in 14 patients. Clinical interictal epileptic discharges were marked by visual inspection. We applied 3 EMSI methods: cMEM, depth-weighted cMEM and depth-weighted minimum norm estimate (MNE). The ground truth was defined as the true simulated generator or as a drawn region based on clinical information available for patients.

For deep sources, depth-weighted cMEM improved the localization when compared to cMEM and depth-weighted MNE, whereas depth-weighted cMEM did not deteriorate localization accuracy for superficial regions. For patients' data, we observed improvement in localization for deep sources, especially for the patients with mesial temporal epilepsy, for which cMEM failed to reconstruct the initial generator in the hippocampus. Depth weighting was more crucial for MEG (gradiometers) than for HD-EEG. Similar findings were found when considering depth weighting for the wavelet extension of MEM.

In conclusion, depth-weighted cMEM improved the localization of deep sources without or with minimal deterioration of the localization of the superficial sources. This was demonstrated using extensive simulations with MEG and HD-EEG and clinical MEG and HD-EEG for epilepsy patients.

7.3 Introduction

In addition to seizures, patients with epilepsy present inter-ictal epileptic discharges (IED), characterized by spontaneous abnormal neuronal discharges usually generated from regions overlapping with the regions generating seizures (Hauf et al., 2012), but without clinical manifestation. IEDs occur more frequently than seizures and the localization of IED generators is crucial during the pre-surgical evaluation of patients with drug-resistant epilepsy (Bautista et al., 1999; Hufnagel et al., 2000).

Electro/Magneto- EncephaloGraphy (EEG/MEG) are widely used non-invasive techniques to detect IEDs and delineate the seizure onset zone and irritative zone (Rosenow & Lüders, 2001). The ability of EEG/MEG to detect deep brain activity is often debated, especially for MEG (Barkley & Baumgartner, 2003; Kaiboriboon et al., 2010; Leijten et al., 2003; Rampp & Stefan, 2007; Shigeto et al., 2002). Detection and localization of deep subcortical sources by EEG/MEG is challenging for several reasons: (i) rapid attenuation of the signals generated from deep structures as a function of the distance of the generator to the EEG/MEG sensors, which is more pronounced for MEG when considering gradiometers (Barkley & Baumgartner, 2003; Malmivuo & Plonsey, 1995). (ii) ‘closed field’ structure of the subcortical regions such that the generators cancel each other (Lorente De Nó, 1947; Murakami & Okada, 2006) and are difficult to detect by distant sensors and (iii) signals from deep structures propagate rapidly to the lateral cortex resulting in the superposition of the low signal to noise ratio (SNR) signals from deep structures and high SNR signals from superficial regions; this makes it difficult to disentangle those sources (Attal & Schwartz, 2013; Benar et al., 2021). This is especially true for mesial temporal lobe epilepsy, a common type of epilepsy where the IEDs generated in mesial temporal regions propagate to neocortical temporal regions with a 10 to 50 ms delay (Merlet & Gotman, 1999). However, compelling evidence is available now suggesting that deep brain activity can be recorded by EEG (Seeber et al., 2019) and MEG (Alberto et al., 2021; Kaiboriboon et al., 2010), as demonstrated by simultaneously recorded intracranial EEG (Dalal et al., 2009; Koessler et al., 2015; Pizzo et al., 2019).

The spatiotemporal localization of underlying neuronal generators from EEG/MEG sensors, called EEG/MEG source imaging (EMSI), is an ill-posed inverse problem. Solving the ill-posed EMSI problem requires making assumptions (constraints added for regularization), which vary for different methods. Minimum-norm estimate (MNE) is a widely used EMSI method (Hämäläinen & Ilmoniemi, 1994) choosing the solution that best fits the sensor data with a minimum overall energy of brain activity. As the amplitude of electrical potentials or magnetic fields decreases with the square of the distance from generators to sensors, EEG and MEG sensors have a higher sensitivity to superficial compared to deep generators (Heller & van Hulteyn, 1992). Because of the constraint of minimum energy, standard MNE solutions have natural preferences toward localizing activity in superficial sources for which the sensors are more sensitive (Jeffs et al., 1987; Uutela et al., 1999), resulting in an underestimation of deep sources. A depth-weighted version of MNE was proposed (Fuchs et al., 1999; Jeffs et al., 1987; Lin et al., 2006) to improve the accuracy of source localization for deep sources, by weighting the covariance structure of the source to allow enhancing activity from deep generators. In parallel, two noise-normalized versions of MNE have been proposed, dynamic statistical parametric mapping (dSPM) (Dale et al., 2000) and standardized low-resolution electromagnetic tomography (sLORETA) (Pascual-Marqui, 2002). These noise-normalized versions of MNE also allow for enhancing the contribution of deep sources when solving the EMSI problem (Lin et al., 2006). Exploiting the depth-weighted and noise-normalized versions of MNE, while using a realistic anatomical and electrophysiological model of deep brain activity, Attal and Schwartz (2013) showed that signals from subcortical sources can be detected by MEG with good accuracy, especially when considering single source activation. The localization from subcortical regions becomes more challenging when a cortical source is simultaneously active. In Attal and Schwartz (2013), for accurate localization, the simulated subcortical activity had an energy SNR of 20 (amplitude SNR of ~ 4.5 or 13dB), which roughly corresponds to an evoked cortical MEG response obtained after averaging ~ 100 to 200 trials. In a low SNR scenario, which is usually the case for single events generated from deep structures, EEG/MEG source localization remains quite challenging. In addition, to study deep brain activity, an interesting anatomical and electrophysiological model was proposed by Attal et al. (2009) and Attal and Schwartz (2013). Depending on the types of neural generators (open and closed field cells) and their preferred orientation, subcortical structures were modeled as volume grids or surface meshes. The thalamus, striatum, and amygdala were modeled by placing current

dipoles on the volume grid with random orientation; the hippocampus was modeled as a surface mesh placing the current dipoles orthogonally to the surface (similar to cortical source space) (Attal & Schwartz, 2013; Meyer et al., 2017).

In the context of epilepsy, recovering the spatial extent of the generator is also of importance in addition to localizing its origin. It has been reported that the generators of IEDs often are associated with a large area of cortex, for instance with a minimum area of 4-8 cm² for EEG (Ebersole, 1997; Merlet & Gotman, 1999; Tao et al., 2007; Von Ellenrieder et al., 2014) and 3-4 cm² for MEG (Hari, 1990; Mikuni et al., 1997; Oishi et al., 2002). The Maximum Entropy on the Mean (MEM) is an EMSI technique that can accurately localize the superficial generators together with their spatial extent, which we previously demonstrated for coherent MEM (cMEM), the standard variant of MEM, assuming a stable parcellation of the brain along time in the prior model and which is ideal for localization of epileptic spikes (Abdallah et al., 2022; Chowdhury et al., 2016; Chowdhury et al., 2013; Grova et al., 2006). Our team also developed the wavelet MEM (wMEM) which is another variant of MEM, designed to localize the oscillatory components by transforming the data in the time-frequency domain before applying MEM localization (Afnan et al., 2023; Lina et al., 2012). In the present study, we propose a depth-weighted extension of cMEM and wMEM, following the depth-weighted strategy implemented by Cai et al. (2022) to reconstruct functional Near-InfraRed Spectroscopy data. We also added the hippocampus as a surface mesh in our source model, as proposed by Attal et al. (2009). Our objective is to demonstrate the ability of depth-weighted MEM methods to localize deep generators accurately while largely retaining their ability to localize superficial generators. We considered high-density EEG (HD-EEG) and MEG realistic simulations of single-source epileptic activity (Chowdhury et al., 2013; Grova et al., 2006) as well as more complex scenarios involving epileptic activity in the hippocampus and neocortical regions. The mixed sources scenario was generated to mimic IEDs in mesial temporal lobe epilepsy characterized by initial mesial activity followed by propagated neocortical activity (Merlet & Gotman, 1999). Finally, we evaluated the performance of depth-weighted MEM methods with IEDs recorded from HD-EEG and MEG in patients with focal epilepsy for whom the presumed localization of the focus was defined as a region along the cortical surface (including the hippocampus) using all available information from presurgical evaluation.

7.4 Materials and methods

7.4.1 Experimental design

The analysis pipeline is summarized in Figure 7-1. We propose depth-weighting in cMEM implementation (section 7.4.2). The depth-weighted cMEM was first evaluated using realistic simulations of IED on MEG and HD-EEG (section 7.4.3), before localizing actual IEDs from MEG, and HD-EEG (section 7.4.6) from patients with drug-resistant focal epilepsy. The proposed method was compared with standard cMEM and depth-weighted MNE. We included a surface of both hippocampi, as an additional deep structure in the source model (section 7.4.7).

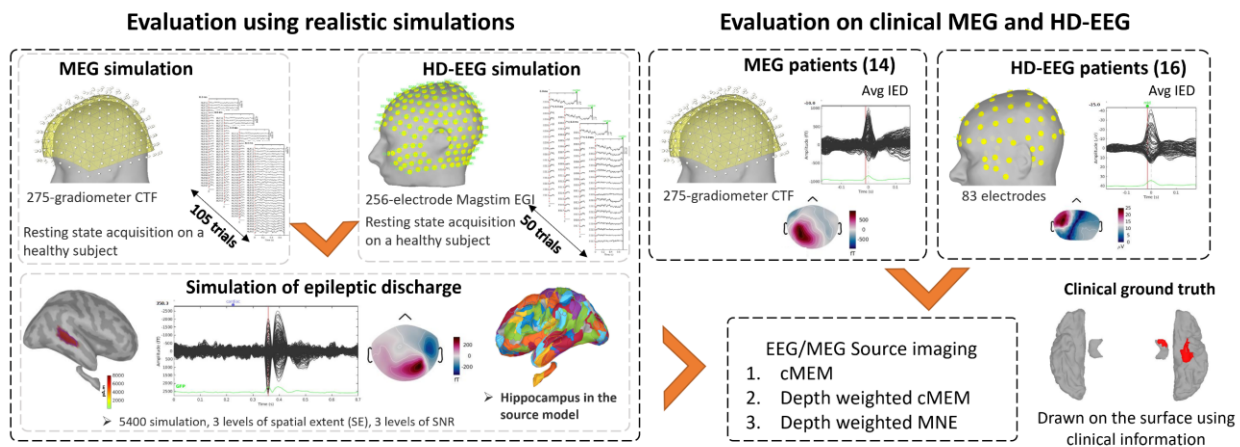


Figure 7-1 Analysis pipeline to evaluate depth-weighted cMEM compared to standard cMEM and depth-weighted MNE using MEG and HD-EEG simulations of epileptic discharges, as well as actual interictal epileptic discharges from MEG and HD-EEG in patients with focal epilepsy.

7.4.2 Maximum entropy on the mean method and depth weighting

The EEG/MEG inverse problem was solved using the Maximum Entropy on the Mean (MEM) (Amblard et al., 2004; Chowdhury et al., 2013). The key feature of this method is that it relies on a flexible spatial prior, assuming that brain activity is organized in cortical parcels. The activity of every parcel is scaled by the probability of activation of every parcel, which is tuned through a hidden state variable. When the parcel is active, a Gaussian distribution is used as the prior of the activity within the parcel. When the parcel is inactive, a Dirac distribution is considered that allows to shut down the activity from this parcel. Starting from such a prior “reference” distribution, the model is fitted

to data by maximizing the relative entropy between the solution and the prior. As a result, MEM can either switch off or switch on the parcels during the localization process, while still allowing local contrast on the cortical surface within the active parcels. MEM provides accurate localization of the generators together with their spatial extent, as demonstrated by the standard variant of MEM, cMEM (Abdallah et al., 2022; Chowdhury et al., 2016; Chowdhury et al., 2013; Grova et al., 2016), as well as the wavelet-based extension, wMEM (Lina et al., 2012; Pellegrino et al., 2016; von Ellenrieder et al., 2016). For coherent MEM (cMEM), the term “coherent” refers to the fact that we are using a coherent spatial prior, i.e. a data driven parcellation which is fixed along time (Abdallah et al., 2022; Chowdhury et al., 2016; Chowdhury et al., 2013; Grova et al., 2016). wMEM consists in applying first a discrete wavelet transformation (Daubechies wavelets) to characterize the oscillatory patterns in the data before considering the MEM solver to solve the EMSI problem (Lina et al., 2012). cMEM and wMEM implementations are available in the BrainEntropy plugin of Brainstorm software (Tadel et al., 2011) (<https://neuroimage.usc.edu/brainstorm/Tutorials/TutBEst/>).

cMEM/wMEM for EMSI have a preference toward superficial solutions (Afnan et al., 2023; Grova et al., 2006), since so far, we have not considered any depth-weighted strategy for both methods. On the other hand, depth weighted strategy is commonly considered for MNE (Hämäläinen & Ilmoniemi, 1994) and Beamformer (Van Veen et al., 1997). To solve the EMSI inverse problem for each source location, the uncertainty of the activity of the underlying sources is modeled by the source covariance matrix. Deeper sources tend to have greater uncertainty in EMSI, resulting in higher values in the covariance matrix compared to superficial sources. Therefore, an *a priori* source covariance matrix should appropriately account for the variance differences across source locations. To do so, the diagonal of the source covariance can be weighted by the forward model of each source, quantifying the influence of source depth of each source at a specific power ω . This standard approach is used as a default implementation of depth-weighted MNE (Fuchs et al., 1999; Lin et al., 2006). A similar depth-weighted strategy was implemented within the cMEM framework by Cai et al. (2022) for the reconstruction of functional Near-InfraRed Spectroscopy data. We weighted the source covariance for each parcel when generating the spatial prior (see additional details in the Appendix B). The depth weighting parameter was set to $\omega = 0.5$ as this is also used as a default value for depth-weighted MNE implemented in Brainstorm. We also

investigated the depth weighting parameter ω for a range of values: $\omega = 0.1, 0.3, 0.5, 0.7$ and 0.9 . The results are presented in the supplementary material.

Here, we evaluated the newly proposed depth-weighted cMEM (cMEM_ω , ω being the depth weighting factor) and compared with original cMEM (no depth-weighted) and depth-weighted MNE (MNE_ω) using first simulated IEDs (section 7.4.3) and then actual IEDs from MEG and HD-EEG (section 7.4.6). To calculate the noise covariance, we used two seconds of resting state data from each subject. For MNE_ω , we estimated the regularization hypermeter λ by using the SNR of the data, as $\lambda = 1/\text{SNR}^2$, with the SNR set to 3 (default value in Brainstorm).

We applied a similar depth weighting strategy for wMEM and validated it using the same dataset of simulated IEDs. Since wMEM considers discrete wavelets and is designed to localize oscillatory components of the signals, IEDs signals might not be ideal for validation of wMEM. However, our focus was on the improvement of depth-weighted wMEM (wMEM_ω) compared to original wMEM, not on the comparison between wMEM and cMEM. We compared wMEM_ω with cMEM, wMEM, cMEM_ω and MNE_ω in section 7.5.5 and Supplementary material S1. However, since this study focuses mainly on cMEM and cMEM_ω , the wMEM results are reported in the Supplementary Material.

7.4.3 MEG and HD-EEG realistic simulations

7.4.3.1 Realistic simulation parameters

The realistic simulation framework was developed by adding simulated epileptic activity to a real MEG or HD-EEG resting state background (Chowdhury et al., 2016; Grova et al., 2006; Lina et al., 2012) using the following steps: (i) the time course of an interictal epileptic spike was modeled with three gamma functions for each vertex within a specific generator defined along the cortical surface (ii) the simulated time courses of the generator defined in the source space were multiplied by the forward model to obtain sensor level data (more details in Chowdhury et al. (2013) and Grova et al. (2006)); (iii) the simulated sensor level data was finally superimposed on real resting state MEG or HD-EEG background obtained from a healthy subject. The maximum amplitude of each vertex of the simulated source was set to 2.85 nA.m. This value has been chosen to mimic the realistic amplitude of a typical epileptic spike. In each simulation, one trial of background HD-EEG/MEG was used, thus mimicking the occurrence of a single non-averaged epileptic spike. The

simulations were prepared separately for MEG and HD-EEG using resting state data and head models obtained from two different healthy subjects.

The *spatial extent (SE)* of the generator was obtained by expanding the region around a randomly chosen location (called the seed) in a geodesic manner on the cortical surface (or hippocampus surface), using different spatial neighborhood order. The actual SNR of the simulated sensor signal was defined as the ratio of maximum activity at the peak of the simulated epileptic activity to the standard deviation estimated within 300 ms background activity for the channel exhibiting this peak (Eq 1).

$$SNR (dB) = 20 \log_{10} \frac{|\text{maximum activity at the peak}|}{\text{standard deviation for 300 ms background}} \quad (1)$$

Depending on the location and spatial extent of the generator, the SNR of the sensor-level signal varied, although the signal strength of the generators for each vertex was kept equal to $S_0 = 2.85$ nA.m at the peak of the simulated spikes. In other words, the SNR of the simulations varied depending on the location, spatial extent and orientation of the sources. As expected, it was higher for the superficial sources and lower for the deep sources and resulted in relatively realistic SNR expected at the sensor level (see supplementary Fig S1 and S2 for actual sensor level SNR of the simulated signals).

Simulation of a single epileptic source: For each modality (MEG/HD-EEG), we generated 2700 simulations for 3 levels of the spatial extent (i.e. spatial neighborhood order around the seed) of the generators (SE=2 ($\sim 5\text{cm}^2$), 3 ($\sim 10\text{cm}^2$), 4 (20cm^2)) and 3 levels of source amplitude strength ($2S_0$, $3S_0$, $4S_0$ where $S_0 = 2.85$ nA.m), while keeping the amplitude of sensor level background at the same level. Since changing source amplitude strength directly impacted SNR at the sensor level, for simplification purposes, we denoted these 3 levels of source strengths as the SNR of 2,3,4 in this document. For each combination of SE and SNR, 300 simulations were performed where the location of each generator was selected randomly on the cortical or hippocampal surfaces. The proportion of simulated generators involving the hippocampus for each combination was 2.2 ± 0.8 % for MEG and 1.9 ± 0.3 % for HD-EEG. The resulting sensor level SNRs of those hippocampal generators were 11.3 ± 4.09 dB for MEG and 18 ± 4.6 dB for HD-EEG. In Fig S3, we showed all the single hippocampal sources generated among the total 300 MEG simulations, considering one combination of SE and SNR (SE3 SNR2). We also reported the amplitude of the sensor exhibiting the highest amplitude and the corresponding sensor-level SNR. In addition, Fig

S4 illustrates the decomposition of the simulated signals into the simulated spike and the MEG background for two examples in Fig S3.

Simulation of the mixture of cortical and hippocampal sources in MEG: We also simulated 100 sets of epileptic activity on MEG, involving a mixture of two generators, one in the hippocampus and the other in the lateral temporal cortex with a 15ms delay. These simulations mimicked typical epileptic discharges in a mesial temporal epilepsy case, where the signal is generated in the hippocampus and rapidly propagates to the lateral part of the temporal cortex (Merlet & Gotman, 1999). The seeds were chosen randomly but restricted to the hippocampus and the ipsilateral temporal cortex. Unlike the single source simulations in the hippocampus (low SNR), we generated higher SNR signals in the hippocampus for this set by increasing the number of vertices in the hippocampus (see section 7.4.7). The resulting sensor level SNR of the simulated signals was 14 ± 4.3 dB for the hippocampal generators and 20 ± 5.4 dB for the cortical generators. The average spatial extent was ~ 6 cm² for hippocampal sources and ~ 10 cm² for cortical sources.

7.4.4 Resting-state data acquisition for simulation

The resting state MEG and HD-EEG trials were acquired from two different healthy subjects (Hedrich et al., 2017). These studies (Principal Investigator: Dr. C. Grova) were approved by the Research Ethics Board of the Montreal Neurological Institute and Hospital and a written informed consent was signed by all participants before the procedures. MEG: We acquired MEG in a magnetically shielded room at the MEG center of the Montreal Neurological Institute (MNI) using a 275-channel CTF system (MISL, Vancouver, Canada) with a sampling rate of 1200 Hz. The participant was seated and instructed to keep eyes open. Continuous head localization was obtained using three localization coils attached to the nasion and left and right peri-auricular points on each subject. The exact position of the localization coils, as well as the shape of the head of the subject, were digitized with a 3D Polhemus localizer for subsequent coregistration with the anatomical MRI. The co-registration was done using the skin surface segmented from a high-resolution T1 weighted MRI acquired on the same subject at the MRI center of the MNI. The iterative closest point algorithm implemented in Brainstorm (Tadel et al., 2019) was used to ensure accurate coregistration between the skin mesh segmented from the MRI and the head shape digitized using the 3D Polhemus localizer, to estimate a rigid transformation matrix (3 rotations, 3 translations). HD-EEG: HD-EEG was recorded using a 256-electrode EGI system (Magstim Electrical

Geodesics Inc., Eugene, Oregon) with a sampling rate of 1000 Hz. A high-resolution T1-weighted MRI was acquired on the same subject using the scanner located at the MNI. Co-registration was done using individual T1 MRI and EEG sensor positions estimated using the Geodesic Photogrammetry System (GPS, Electrical Geodesic Inc., Eugene, OR) (Hedrich et al., 2017). The same coregistration approach employed for MEG was applied to HD-EEG and MRI.

7.4.5 Data preprocessing

The selected data were investigated to remove artifacts from eye blinks and muscle activity. Cardiac artifact and eye movement artifacts were removed from HD-EEG and MEG using Signal Space Projection method (Uusitalo & Ilmoniemi, 1997). The preprocessing included applying a bandpass filter between 0.3-70Hz, a notch filter at 60Hz, noisy channels removal, and downsampling to 600Hz. For MEG, the third-order gradient compensation was also applied. A total of 103 segments each lasting 0.7s were extracted from the clean MEG data. A total of 50 segments of 0.7s were extracted from the clean HD-EEG data. These segments were selected to be added as background realistic noise to simulated epileptic spikes.

7.4.6 IEDs from patients with focal epilepsy

For patients' data, both MEG and HD-EEG studies were approved by the Research Ethics Board of the Montreal Neurological Institute and Hospital and a written informed consent was signed by all participants before the procedures.

MEG: MEG from 14 patients with focal epilepsy (7 F; mean age, 31.4 ± 11.0 Y, 8 mesial temporal) were acquired in supine position on the same 275-channel CTF system as mentioned in section 7.4.4 at 1200Hz sampling rate. MEG data were acquired between 2008 and 2018 for presurgical evaluation (see Supplementary Table 1). We included patients for whom at least 5 IEDs were marked by visual inspection and enough clinical information was available to estimate a reasonable ground truth (by C.A and V. R). MEG was performed with the patient lying down in a supine position, lasting ~1 hour (10 runs of 6 minutes each). HD-EEG: The HD-EEG patient cohort included 16 patients (7 F; mean age, 33.6 ± 10.9 Y, 9 mesial temporal) with drug-resistant focal epilepsy who underwent 24 - 48 hour long HD-EEG recordings (83 electrodes, sampling 1000Hz) during presurgical evaluation at the MNI epilepsy unit between 2019 and 2022 (see Supplementary Table 2). The HD-EEG dataset was part of another study published by our group (Avigdor et al.,

2024). HD-EEG was performed using the Nihon Kodan system (Tokyo, Japan) using 83 collodion glued electrodes (10-10 EEG system). Note that we used a different HD-EEG system (256-electrode Magstim EGI system) for recording background activity from healthy participants. Co-registration for MEG and HD-EEG with corresponding anatomical MRI was done as described in section 7.4.4. Preprocessing of data included: bandpass filtered between 0.3-70Hz, notch filter at 60Hz, downsampling to 600 Hz and removal of channels with artifacts by visual inspection. EEG data were analyzed using average reference montage.

Marking of IEDs and clinical ground truth: IEDs were visually marked by a board-certified epileptologist (MEG: C.A. and V.R., HD-EEG: C.A and B.F.). The number of IEDs marked for each patient is summarized in Supplementary Tables 1 and 2. We analyzed the average IED for each patient, considering a 200ms window around the peak of the IED. To quantify the accuracy of source imaging, the presumed clinical ground truth for each patient was drawn as a region on the cortical surface (including the hippocampus) using all clinical information available from presurgical evaluation with long-term video EEG monitoring, anatomical MRI, fluorodeoxyglucose-positron emission tomographic, neuropsychological evaluation, intracranial EEG results or surgical cavity drawn using pre- and post-surgical MRI for patients who became seizure-free (for MEG), varying based on the availability of the information. Our evaluation was therefore performed based on a semi-quantitative definition of the presumed ground truth, as reported in our previous studies (Pellegrino et al., 2018; Pellegrino, Xu, et al., 2020).

7.4.7 Source space and forward model estimation

Brain segmentation and reconstruction of the white/gray matter interface for the cortex were obtained using recon-all from FreeSurfer software package (Dale et al., 1999). The subcortical structures were also segmented using FreeSurfer. The subsequent analysis to create the source model and forward model was conducted in Brainstorm (Tadel et al., 2011). We considered the cortical mesh of the middle layer which is equidistant from the white matter and pial surfaces consisting of ~300,000 vertices. We included the two hippocampi from the subcortical structures. Each hippocampus consisted of ~3000-4000 vertices (depending on the subject anatomy). For both the cortex and the hippocampus, the sources were located on the surface of the structures with a fixed orientation orthogonal to the surface at each point. Then we merged the cortical and hippocampal surfaces and downsampled the source space to ~8000 vertices. This resulted in ~4

vertices/cm² on the cortical and the hippocampal surface. A uniform density of vertices was used for both surfaces for simulations of single source generators and patients' data. Only for the simulations of mixed sources in MEG (section 7.4.3), we used a source model where the density of vertices was double in the hippocampus (~ 8 vertices/cm²). The reason was to generate higher SNR simulations in the hippocampus while keeping other simulation parameters similar compared to single source simulations. Once our source space was defined, the forward model was computed using OpenMEEG software using a 3-layer Boundary Element model (BEM) (Kybic et al., 2005) consisting of brain, skull, and scalp surfaces with conductivity values of 0.33, 0.0165, and 0.33S m⁻¹, respectively (Zhang et al., 2006).

7.4.8 Validation metrics

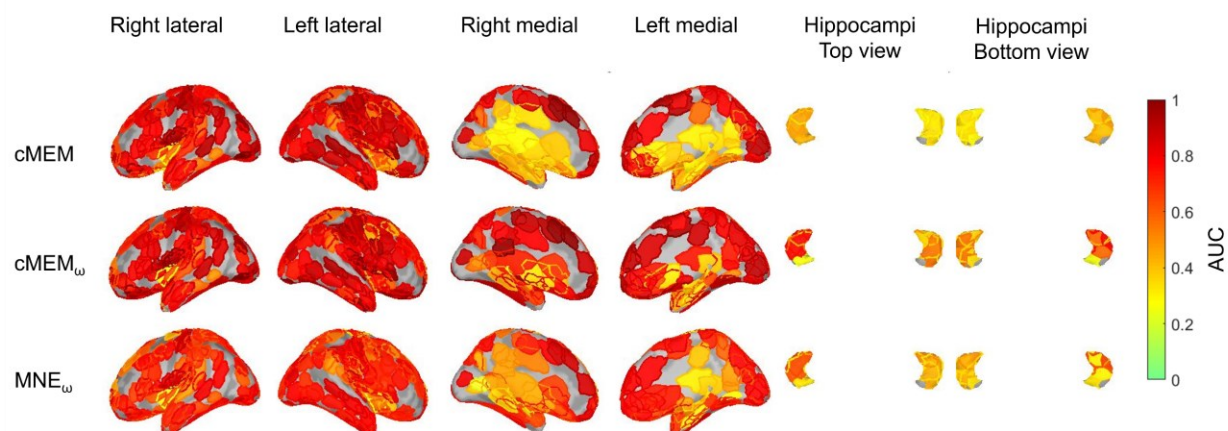
The performance of three source imaging methods (cMEM, cMEM_ω and MNE_ω) was assessed using the following three validation metrics (i) Area Under the ROC Curve (AUC): A detection accuracy index to assess the sensitivity to the spatial extent of the sources in the context of distributed sources model (adapted by Grova et al. (2006) for the specific problem of EMSI validation while allowing unbiased estimates, more details provided in Chowdhury et al. (2013)). (ii) D_{min}: the minimum distance localization error was the Euclidean distance in mm from the maximum of the map to the closest vertex belonging to the ground truth. When this maximum was located inside the simulated source, D_{min} was set to 0 mm (Hedrich et al., 2017) (iii) Spatial dispersion (SD): the SD metric measured the spatial spread (in mm) of the localization around the Ground Truth. To estimate SD, we considered the root mean square of the square of the distance from the estimated source to the ground truth weighted by the energy of the source localization map at each vertex (Hedrich et al., 2017). For each IED, we estimated those metrics at the peak of the IEDs for simulations, and at the midpoint of the rising spike for patients' averaged IEDs. We assessed AUC, SD, and D_{min} of each simulated source as a function of the eccentricity of the source, defined as the mean of the distance between all the vertices in the ground truth and the center of the head. Deep sources have therefore low eccentricity and superficial sources have high eccentricity. We applied the non-parametric Friedman test to compare the three source imaging methods (Durbin-Conover test for pair-wise comparisons, p-value corrected for multiple comparisons using Bonferroni). Similar analyses were also performed to evaluate wMEM and wMEM_ω methods, results are reported in the supplementary material.

7.5 Results

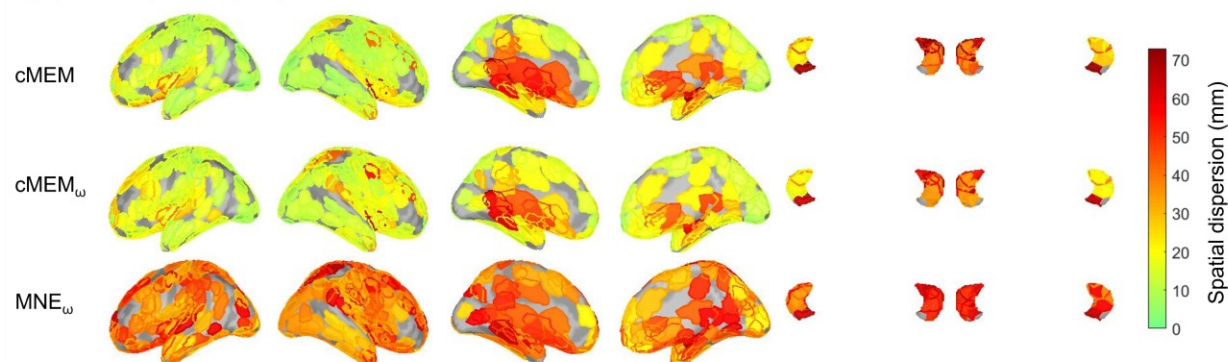
7.5.1 Simulation of single epileptic source: MEG

Figure 7-2 summarizes the performance of our three validation metrics – AUC, SD and D_{\min} for cMEM, cMEM_ω and MNE_ω estimated for 300 MEG simulations with spatial extent SE=3 ($11.8 \pm 2.1 \text{ cm}^2$) and SNR=2 ($11.6 \pm 5.4 \text{ dB}$). Figure 7-2D shows the average eccentricity values for those 300 generators. In Figure 7-2, the metrics are shown as colormap for 300 generators, where all the vertices within a generator are represented by one color associated with the value of the corresponding metric. The AUC values were overall improved when considering cMEM_ω in comparison to cMEM, especially in mesial regions. cMEM_ω performances in terms of SD and D_{\min} were also improved in deeper regions when compared to cMEM. Both cMEM and cMEM_ω exhibited smaller SD values when compared to MNE_ω.

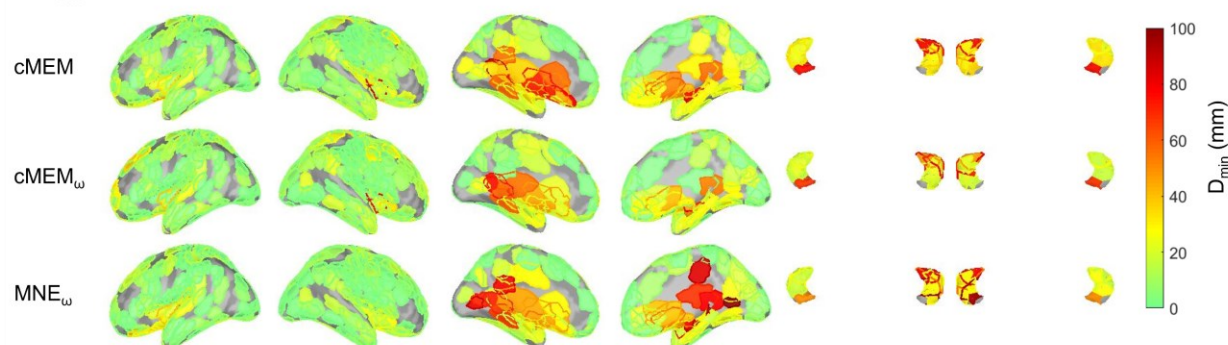
A) AUC



B) Spatial Dispersion (mm)



C) D_{min} (mm)



D) Eccentricity (mm)

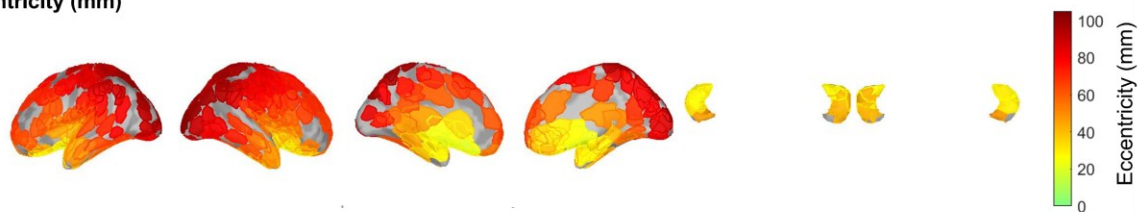


Figure 7-2: (A) AUC, (B) SD, and (C) D_{\min} for three source imaging methods are shown on the cortical surface at the locations of 300 simulated sources in MEG. The average eccentricity values for those 300 generators are shown in (D). Each parcel is one simulated source with the color representing the metric value associated with it. Regions where no sources were generated are shown as grey. When there was overlap between sources, a line was superimposed on the new color to illustrate the overlap from the previous source. Increases in AUC and decreases in SD and D_{\min} by cMEM_{ω} were observed mostly for the medial regions, whereas cMEM_{ω} and cMEM presented similar performances for superficial sources. Brain maps are shown for 6 views: right lateral, left lateral, right medial, left medial, hippocampi top and hippocampi bottom.

The improvement in localization for deep sources by cMEM_{ω} compared to cMEM is more clearly presented in Figure 7-3, which illustrates that cMEM_{ω} improved the localization mostly on the medial side (deep sources) without or with minimal worsening of the localization in the lateral and superficial regions. The statistical comparisons for these maps are presented in Figure 7-4 for deep sources and Fig S5 for superficial sources.

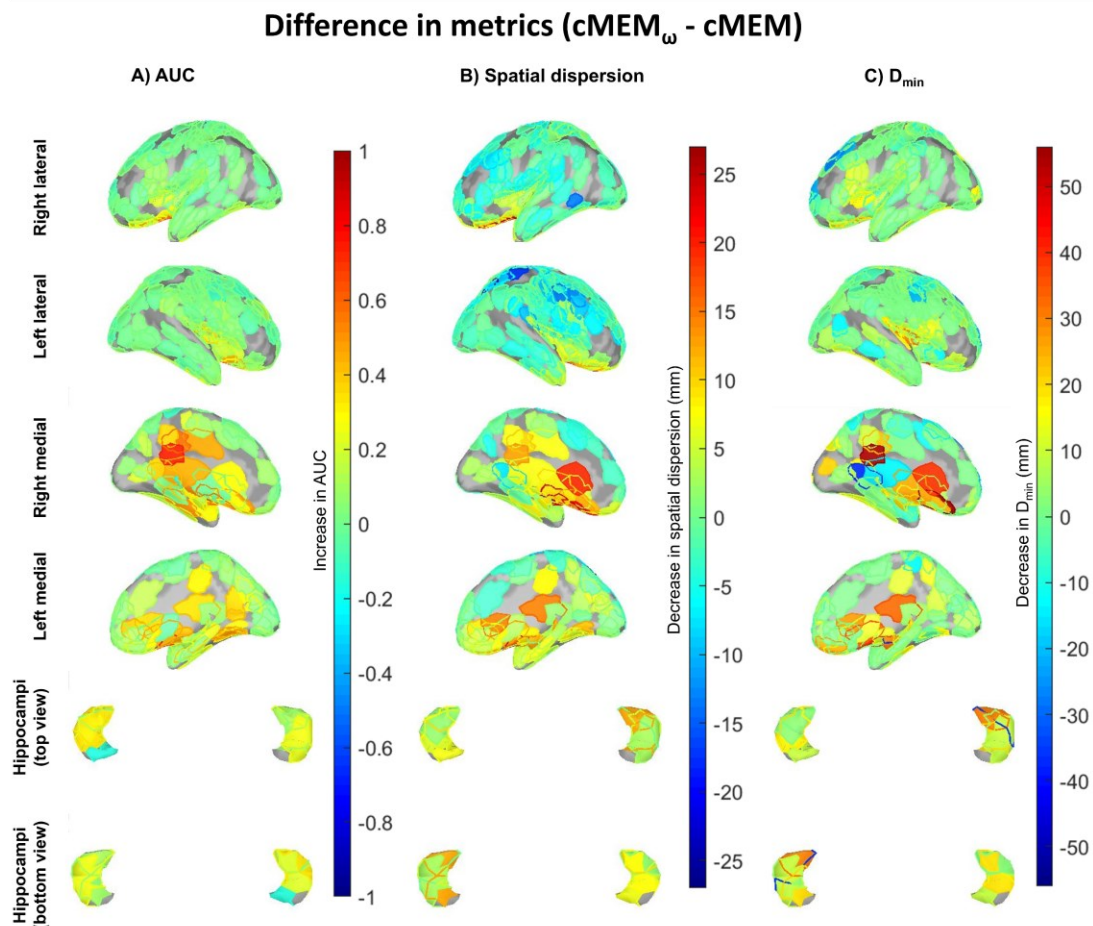


Figure 7-3: The differences in AUC, SD, and D_{\min} between $cMEM_{\omega}$ and $cMEM$ ($cMEM_{\omega} - cMEM$) are shown on the cortical surface at the locations of 300 simulated sources in MEG. Increases in AUC and decreases in SD and D_{\min} (warmer color) were observed mostly for the deeper regions. Regions where no sources were generated are shown as grey. When there was overlap between sources, a line was superimposed on the new color to illustrate the overlap from the previous source. Brain maps are shown for 6 views: right lateral, left lateral, right medial, left medial, hippocampi top and hippocampi bottom.

Figure 7-4A presents the detailed distributions of validation metrics AUC, SD and D_{\min} as a function of eccentricity for the 300 MEG simulations shown in Figure 7-2 and Figure 7-3. Similar to Figure 7-3, Figure 7-4 shows that the localization improved for regions with low eccentricity (0 - 60 mm, deep sources). We compared the metrics for $cMEM_{\omega}$, $cMEM$ and MNE_{ω} for regions with eccentricity less than 60 mm (Figure 7-4 B1, B2, B3). The localization for those regions was significantly improved by $cMEM_{\omega}$ compared to $cMEM$ in terms of AUC, SD and D_{\min} ($p < 0.001$, $AUC_{cMEM_{\omega}-cMEM}$: 0.14 ± 0.11 , $SD_{cMEM-cMEM_{\omega}}$: 3.9 ± 2.8 mm, $Dmin_{cMEM-cMEM_{\omega}}$: 3.1 ± 3.3 mm, the effect being reported as median \pm median absolute deviation of the difference between $cMEM_{\omega}$ and $cMEM$. Compared to MNE_{ω} , the localization was also significantly improved by $cMEM_{\omega}$ in terms of AUC and SD ($p < 0.001$, $AUC_{cMEM_{\omega}-MNE_{\omega}}$: 0.11 ± 0.07 , $SD_{MNE_{\omega}-cMEM_{\omega}}$: 19.5 ± 5.6 mm). D_{\min} by $cMEM_{\omega}$ was also improved when compared to MNE_{ω} but did not pass the significance threshold ($Dmin_{MNE_{\omega}-cMEM_{\omega}}$: 0.3 ± 7.6 mm).

For regions with eccentricity > 60 mm (Fig S5), the AUC and D_{\min} for $cMEM_{\omega}$ were overall similar to $cMEM$ ($AUC_{cMEM_{\omega}-cMEM}$: -0.01 ± 0.02 , $Dmin_{cMEM-cMEM_{\omega}}$: 0.0 ± 0.0 mm). The SD was slightly worsened by $cMEM_{\omega}$ when compared to $cMEM$ ($p < 0.001$, $SD_{cMEM-cMEM_{\omega}}$: -2.9 ± 1.8 mm). However, the SD was significantly improved by $cMEM_{\omega}$ compared to MNE_{ω} ($p < 0.001$, $SD_{MNE_{\omega}-cMEM_{\omega}}$: 23.8 ± 5.3 mm). In terms of SD, both $cMEM$ and $cMEM_{\omega}$ were still largely significantly lower than MNE_{ω} ($p < 0.001$, $SD_{MNE_{\omega}-cMEM}$: 26.0 ± 4.9 mm). The lowest median D_{\min} was found for MNE_{ω} , however, it was not significantly lower than $cMEM_{\omega}$. See also supplementary figures S6 -S16 for 2400 MEG simulations with other combinations of SE and SNR. Similar improvement by $cMEM_{\omega}$ was found compared to $cMEM$ and MNE_{ω} for all combinations.

Supplementary Fig S17 presents the distribution of AUC, SD and D_{\min} for 300 MEG simulations as a function of eccentricity for $cMEM_{\omega}$ for five different values of depth weighting parameter ω ($\omega = 0.1, 0.3, 0.5, 0.7$, and 0.9). As ω increases, the localization accuracy for deep sources

improves. However, for higher ω values, localization for superficial sources deteriorates, as observed in SD for $\omega = 0.7, 0.9$, and in AUC, SD, and D_{\min} for $\omega = 0.9$.

Improvement in localization by depth weighted cMEM: MEG

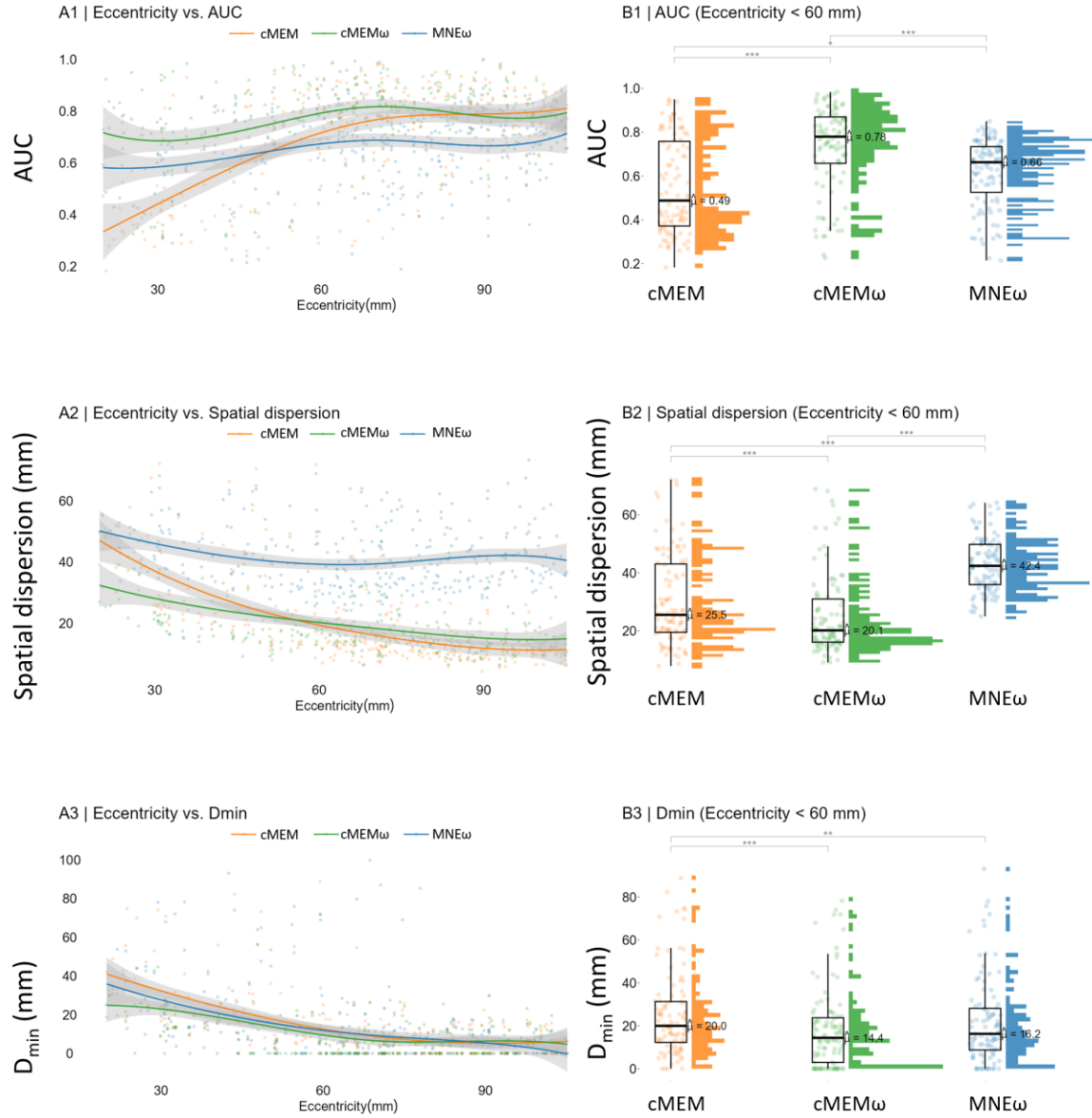


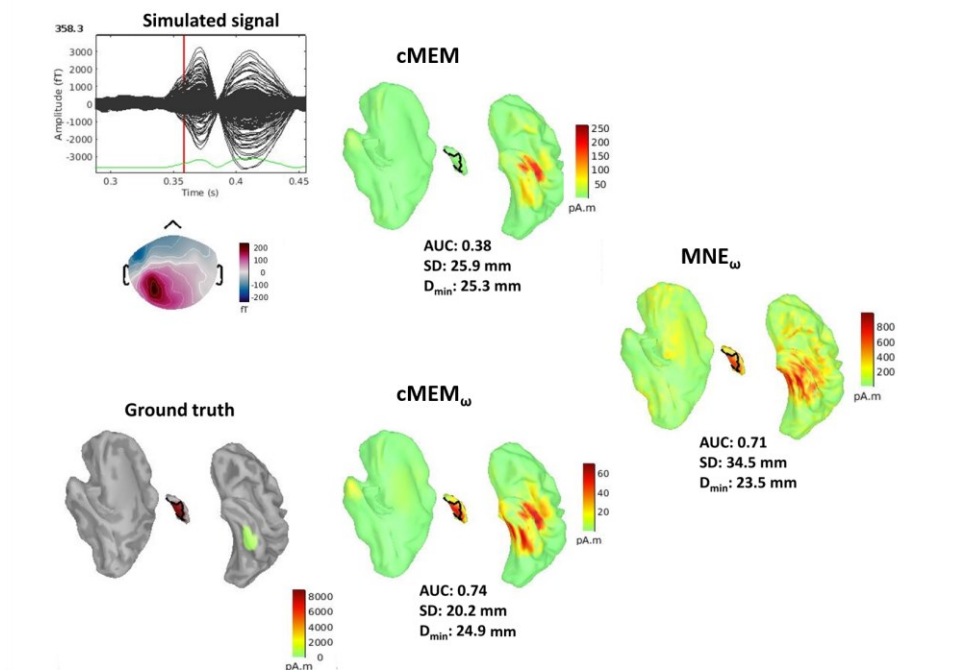
Figure 7-4: For 300 MEG simulations at SE=3 and SNR =2, the plot of AUC (A1), SD (A2), and D_{\min} (A3) as a function of eccentricity for cMEM, cMEM ω and MNE ω . The comparison of the three methods is summarized for AUC (B1), SD (B2), and D_{\min} (B3) for 99 (out of 300) sources with an eccentricity of less than 60 mm. On each boxplot, the central mark indicates the median, and the bottom and top edges of the

box indicate the 25th and 75th percentiles, respectively. If the groups are statistically different after post-hoc analysis, the significance levels are shown as: ‘***’ for $p < 0.001$, ‘**’ for $p < 0.01$, and ‘*’ for $p < 0.05$.

7.5.2 Simulation of mixed sources in the hippocampus and the neocortex in MEG

Figure 7-5 shows an example simulation of a complex or mixed source scenario, the first simulated generator is in the hippocampus (peak at 358 ms) and is followed by another generator along the lateral temporal cortex after a 15 ms delay (peak at 373 ms), mimicking a situation likely occurring in patients with mesial temporal lobe epilepsy. We calculated the metrics at 358 ms for the hippocampus and at 373 ms for the neocortex, considering the two sources are independent. We considered the whole cortex when estimating the metrics for both sources. For the hippocampal source, cMEM_ω localized the generator whereas cMEM failed, as reflected by AUC, SD and D_{min}. The metrics by cMEM and cMEM_ω were (cMEM/cMEM_ω): AUC:0.38/0.74, SD: 25.9mm/20.2mm, D_{min}: 25.3mm/24.9mm. The metrics for MNE_ω for the hippocampal source were: AUC: 0.71, SD: 34.5mm, D_{min}: 23.5mm. For the superficial source at 373 ms, both cMEM and cMEM_ω localized the generator. The metrics for cMEM and cMEM_ω were (cMEM/ cMEM_ω): AUC:0.93/0.90, SD: 12.2mm/15.3mm, D_{min}: 0mm/0mm. The metrics for MNE_ω for the superficial source were: AUC: 0.81, SD: 28.8mm, D_{min}: 0mm.

A) Simulated generator in the hippocampus (peak at 358 ms)



B) Simulated generator in the lateral neocortex (peak at 373 ms)

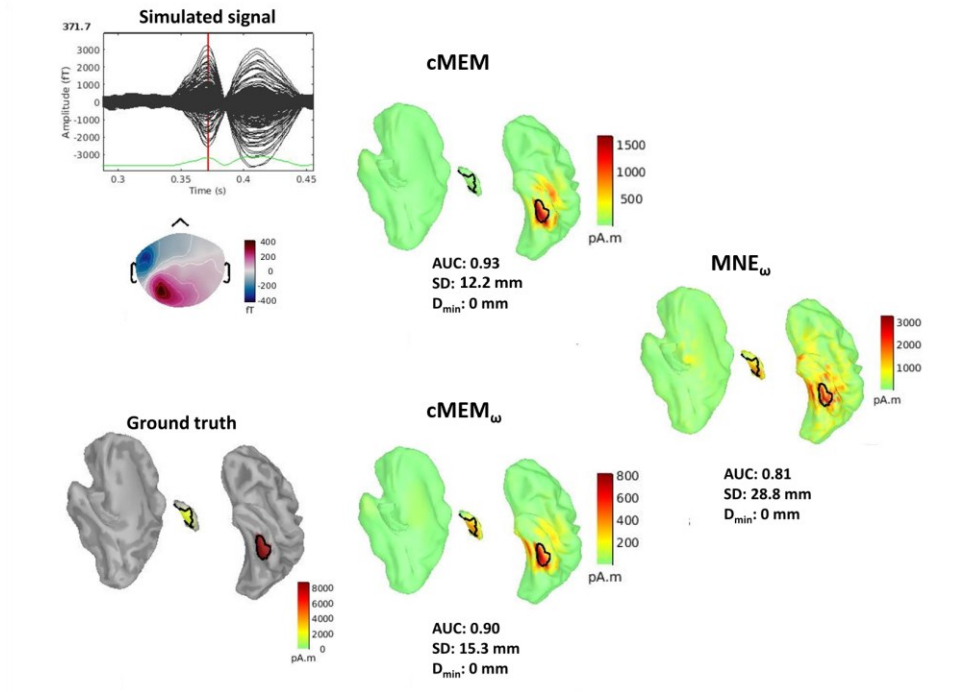


Figure 7-5: Example of two simulated generators first in the hippocampus (A) and then in the lateral neocortex after 15 ms delay (B). Three source imaging methods were applied to the averaged interictal epileptic discharges. The surface of the hippocampus is included in the source model (and presented in the figure as separate structures). The metrics AUC, SD, and D_{min} were calculated at 358 ms (peak of the source

in the hippocampus) and at 373 ms (peak of the neocortical source). The scale is different for the 3 methods but source maps have been interpreted relatively for each method.

Figure 7-6 summarizes the metrics for 100 simulations of mixed sources, following a complex scenario similar to the one illustrated in Figure 7-5. The first column shows the AUC, SD and D_{\min} at 358 ms for the source simulated in the hippocampus. AUC and SD were significantly improved by $cMEM_{\omega}$ compared to cMEM and MNE_{ω} ($p < 0.001$, $AUC_{cMEM_{\omega}-cMEM}$: 0.26 ± 0.08 , $AUC_{cMEM_{\omega}-MNE_{\omega}}$: 0.11 ± 0.09 , $SD_{cMEM-cMEM_{\omega}}$: 4.3 ± 2.6 mm, $SD_{MNE_{\omega}-cMEM_{\omega}}$: 17.6 ± 6.2 mm). D_{\min} was significantly improved by $cMEM_{\omega}$ compared to cMEM ($p < 0.001$, $D_{\min cMEM-cMEM_{\omega}}$: 3.3 ± 3.3 mm). Compared to MNE_{ω} , D_{\min} was also significantly improved by $cMEM_{\omega}$ ($p < 0.05$, $D_{\min MNE_{\omega}-cMEM_{\omega}}$: 5.2 ± 8.1 mm).

For the neocortical generator simulated at 373 ms, $cMEM_{\omega}$ showed similar AUC but slightly decreased SD compared to cMEM ($AUC_{cMEM_{\omega}-cMEM}$: 0.01 ± 0.03 , $SD_{cMEM-cMEM_{\omega}}$: -1.7 ± 2.6 mm). Both cMEM and $cMEM_{\omega}$ showed improved AUC and SD compared to MNE_{ω} ($p < 0.001$, $AUC_{cMEM_{\omega}-MNE_{\omega}}$: 0.09 ± 0.05 , $AUC_{cMEM-MNE_{\omega}}$: 0.06 ± 0.06 , $SD_{MNE_{\omega}-cMEM_{\omega}}$: 20.6 ± 5.1 mm, $SD_{MNE_{\omega}-cMEM}$: 21.5 ± 5.3 mm). D_{\min} was slightly improved in $cMEM_{\omega}$ compared to cMEM ($p < 0.01$, $D_{\min cMEM-cMEM_{\omega}}$: 0.0 ± 2.8 mm). Similar D_{\min} was found for $cMEM_{\omega}$ and MNE_{ω} ($D_{\min MNE_{\omega}-cMEM_{\omega}}$: 0.0 ± 3.7 mm).

Simulated mixed generators in the hippocampus and the neocortical regions at 15 ms delay

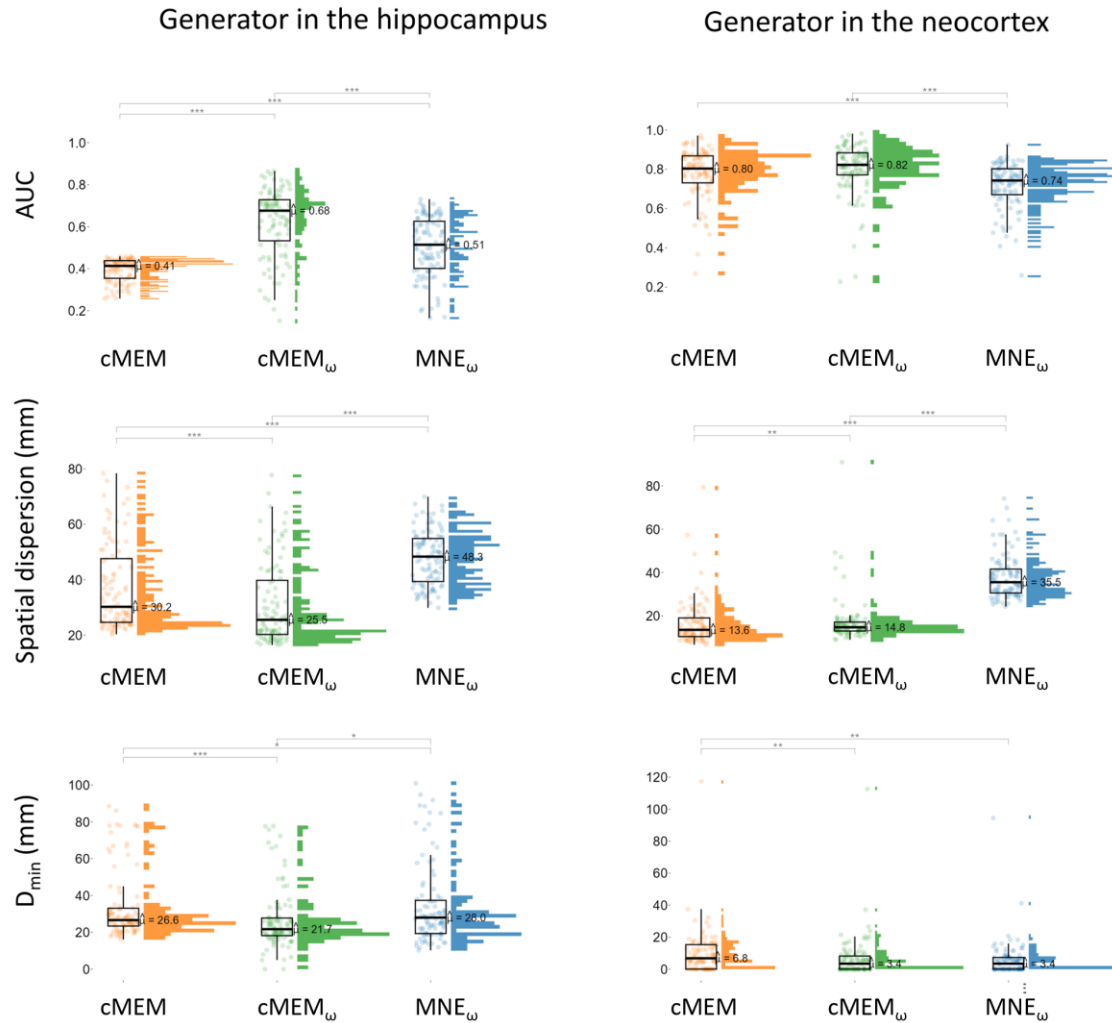


Figure 7-6: Source imaging for 100 simulations of mixed generators in the hippocampus and the ipsilateral neocortex after 15 ms delay. AUC, SD and D_{\min} are calculated separately for each generator at the peak of the spike (358 ms for hippocampal generator and 373 ms for neocortical generator). On each boxplot, the central mark indicates the median, and the bottom and top edges of the box indicate the 25th and 75th percentiles, respectively. If the groups are statistically different after post-hoc analysis, the significance levels are shown as: ‘***’ for $p < 0.001$, ‘**’ for $p < 0.01$, and ‘*’ for $p < 0.05$.

7.5.3 Simulation of single epileptic source: HD-EEG

Similar to the MEG results in Figure 7-3, Figure 7-7 shows the improvement in AUC, SD and D_{\min} for 300 EEG simulations of epileptic activity ($SE=3$, $SNR=2$). The HD-EEG equivalent of

Figure 7-2 is shown in supplementary Fig S18. Figure 7-7 illustrates that HD-EEG localization improved mostly on the medial side (deep sources) without or with minimal worsening of the localization in the lateral and superficial regions.

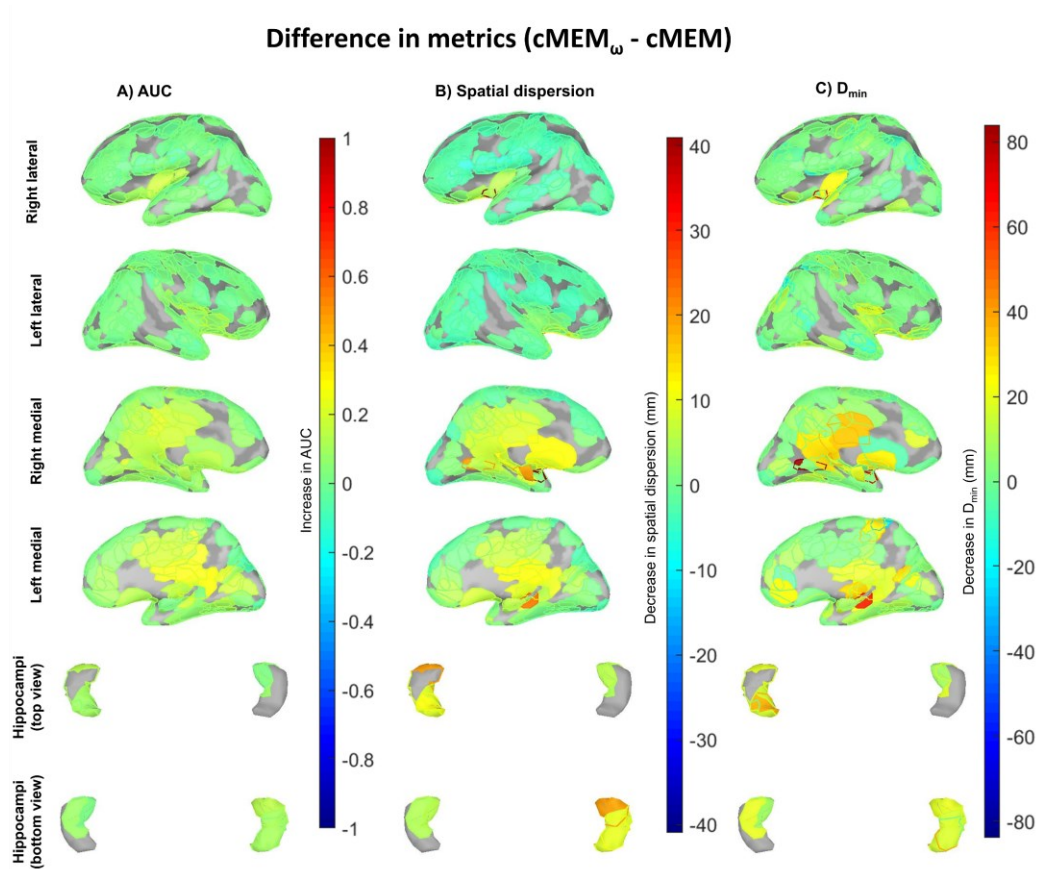


Figure 7-7: The differences in AUC, SD, and D_{\min} between $cMEM_{\omega}$ and $cMEM$ ($cMEM_{\omega} - cMEM$) are shown on the cortical surface at the locations of 300 simulated sources in HD-EEG. Increases in AUC and decreases in SD and D_{\min} (presented warmer color) were observed mostly for the deeper regions. Regions where no sources were generated are shown as grey. When there was overlap between sources, a line was superimposed on the new color to illustrate the overlap from the previous source. Brain maps are shown for 6 views: right lateral, left lateral, right medial, left medial, hippocampi top and hippocampi bottom.

Figure 7-8 presents the metrics as a function of eccentricity for the 300 EEG simulations ($SE=3$ and $SNR=2$), showing that the localization accuracy improved with $cMEM_{\omega}$ for regions with low eccentricity (deep sources, eccentricity < 45 mm). The eccentricity threshold was chosen based on the results from 2700 HD-EEG simulations where the localization accuracy from $cMEM$ and $cMEM_{\omega}$ started to converge at ~ 45 mm, (Figure 7-8, and Fig S19-21). For MEG, this threshold

was ~ 60 mm. We summarized the results from cMEM, cMEM $_{\omega}$ and MNE $_{\omega}$ as boxplots for regions with eccentricity < 45 mm (Figure 7-8) and regions with eccentricity > 45 mm (Fig S22).

Improvement in localization by depth weighted cMEM: HD-EEG

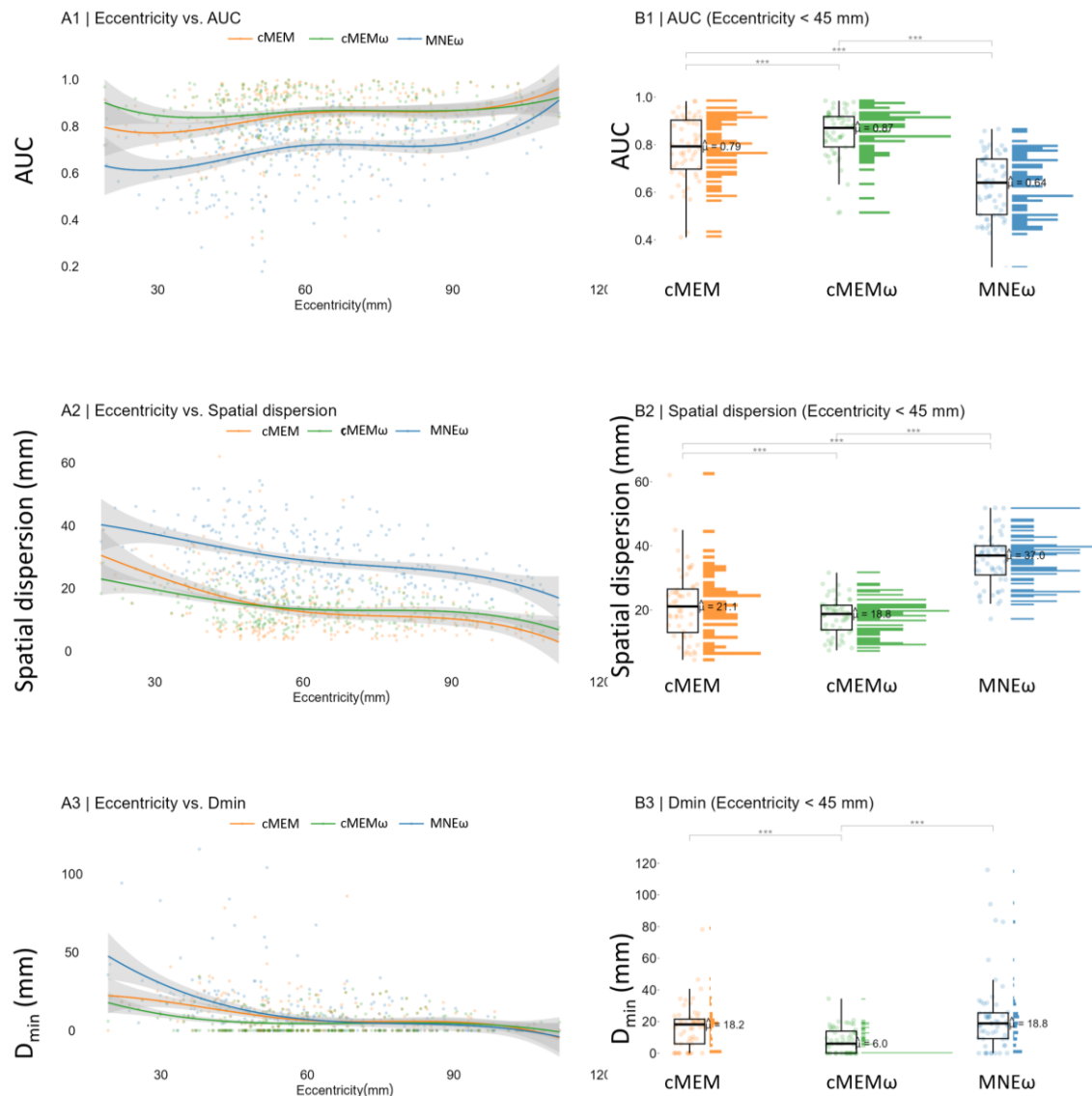


Figure 7-8: For 300 HD-EEG simulations at SE=3 and SNR =2, the plot of AUC (A1), SD (A2), and D $_{\min}$ (A3) as a function of eccentricity for three source imaging methods. The comparison of the three methods is summarized for AUC (B1), SD (B2), and D $_{\min}$ (B3) for 56 (out of 300) deep sources with an eccentricity less than 45 mm. For each boxplot, the central mark indicates the median, and the bottom and top edges of the box indicate the 25th and 75th percentiles, respectively. If the groups are statistically different after

posthoc analysis, the significance levels are shown as: ‘***’ for $p < 0.001$, ‘**’ for $p < 0.01$, and ‘*’ for $p < 0.05$.

For sources with eccentricity < 45 mm, the localization was significantly improved by $cMEM_{\omega}$ in terms of all 3 metrics compared to $cMEM$ ($p < 0.001$, $AUC_{cMEM_{\omega}-cMEM}$: 0.05 ± 0.03 , $SD_{cMEM-cMEM_{\omega}}$: 2.4 ± 2.8 mm, $D_{min_{cMEM-cMEM_{\omega}}}$: 5.5 ± 5.0 mm) and MNE_{ω} ($p < 0.001$, $AUC_{cMEM_{\omega}-MNE_{\omega}}$: 0.20 ± 0.05 , $SD_{MNE_{\omega}-cMEM_{\omega}}$: 17.1 ± 3.2 mm, $D_{min_{MNE_{\omega}-cMEM_{\omega}}}$: 11.8 ± 10.0 mm).

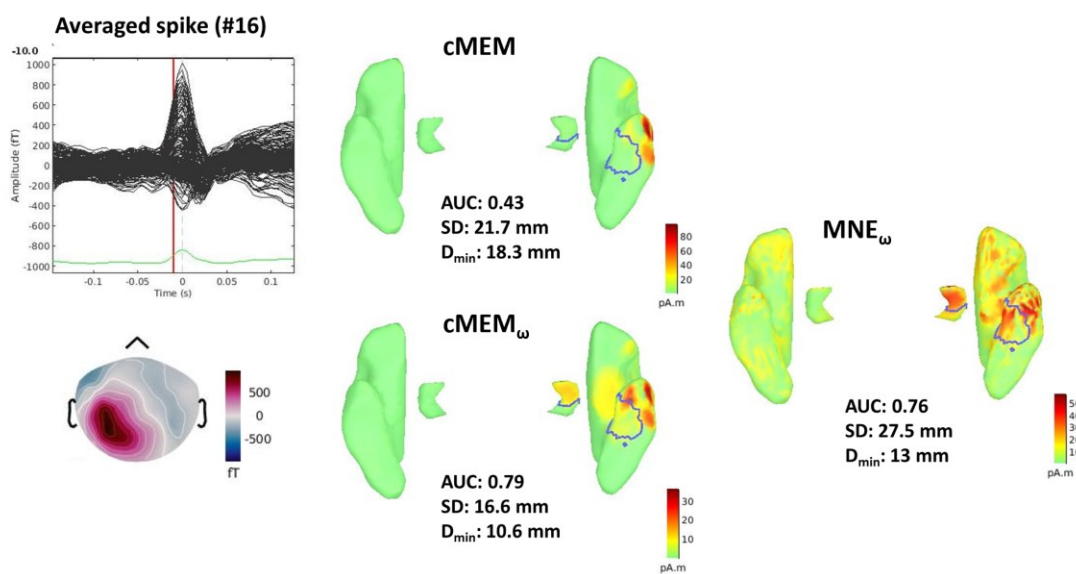
For regions with eccentricity > 45 mm (Fig S22), AUC and D_{min} for $cMEM_{\omega}$ were similar to $cMEM$ ($AUC_{cMEM_{\omega}-cMEM}$: 0.00 ± 0.02 , $D_{min_{cMEM-cMEM_{\omega}}}$: 0 ± 0 mm). In terms of SD, $cMEM_{\omega}$ worsened slightly but significantly compared to $cMEM$ ($p < 0.001$, $SD_{cMEM-cMEM_{\omega}}$: -2.1 ± 1.1 mm). On the other hand, AUC and SD for $cMEM_{\omega}$ were significantly improved compared to MNE_{ω} ($p < 0.001$, $AUC_{cMEM_{\omega}-MNE_{\omega}}$: 0.13 ± 0.05 , $SD_{MNE_{\omega}-cMEM_{\omega}}$: 13.3 ± 3.8 mm). Even if we observed slight worsening of $cMEM_{\omega}$ compared to $cMEM$ for SD ($SD_{cMEM-cMEM_{\omega}}$: -2.1 ± 1.1 mm), SD values remained low for both $cMEM$ and $cMEM_{\omega}$ when compared to MNE_{ω} ($SD_{MNE_{\omega}-cMEM}$: 15.2 ± 3.0 mm, $SD_{MNE_{\omega}-cMEM_{\omega}}$: 13.3 ± 3.8 mm). In terms of D_{min} , all 3 methods exhibited similar accuracy ($D_{min_{cMEM-cMEM_{\omega}}}$: 0.0 ± 0.0 mm, $D_{min_{MNE_{\omega}-cMEM_{\omega}}}$: 0.0 ± 3.8 mm, $D_{min_{cMEM-MNE_{\omega}}}$: 0.0 ± 1.8 mm). See also supplementary Fig S23 - 30 for 2400 HD-EEG simulations with other combinations of SE and SNR. Similar improvement by $cMEM_{\omega}$ was found compared to $cMEM$ and MNE_{ω} for all combinations.

7.5.4 Evaluation on clinical MEG/HD-EEG data from patients with focal epilepsy

MEG: Figure 7-9A shows an example of MEG source localization for a patient with mesial temporal lobe epilepsy. The source imaging methods were applied on an averaged IED (number of IEDs: 16, sensor level SNR at the peak: 30dB). The metrics were calculated at the midpoint of the rising phase of the spike (-10ms, sensor level SNR at -10ms: 26dB). $cMEM$ was not able to localize the underlying hippocampal generator, whereas the depth-weighted methods, $cMEM_{\omega}$ and MNE_{ω} could localize this deep generator during the rising phase of the averaged IED. The metrics for $cMEM/cMEM_{\omega}$ were: AUC: 0.43/0.79, SD: 21.7/16.6 mm and D_{min} : 18.3/10.6mm. The results for MNE_{ω} were: AUC: 0.76, SD: 27.5mm, D_{min} : 13.0mm. All three methods mainly retrieved the propagated activity within temporal neocortical regions. Figure 7-9B compares the metrics for 3 source imaging methods in MEG for 8 patients with mesial temporal lobe epilepsy, where the clinical ground truth involved the mesio-temporal structures including the hippocampus. The

sensor level SNR of the averaged IEDs were $22.7 \pm 6.6\text{dB}$ at the peak and $20.33 \pm 7.05\text{dB}$ at the midpoint of the rising phase of the spike. The localization was significantly improved by cMEM_ω compared to cMEM in terms of AUC, SD ($\text{AUC}_{\text{cMEM}_\omega - \text{cMEM}}: 0.19 \pm 0.04$, $\text{SD}_{\text{cMEM} - \text{cMEM}_\omega}: 4.9 \pm 0.3\text{ mm}$, $p < 0.001$) and D_{\min} ($\text{Dmin}_{\text{cMEM} - \text{cMEM}_\omega}: 7.6 \pm 6.3\text{ mm}$, $p < 0.05$). Compared to MNE_ω , cMEM_ω improved the localization significantly in terms of AUC ($p < 0.05$, $\text{AUC}_{\text{cMEM}_\omega - \text{MNE}_\omega}: 0.13 \pm 0.04$) and SD ($p < 0.001$, $\text{SD}_{\text{MNE}_\omega - \text{cMEM}_\omega}: 11.7 \pm 1.7\text{ mm}$). The median D_{\min} was lower for cMEM_ω compared to MNE_ω ($\text{Dmin}_{\text{MNE}_\omega - \text{cMEM}_\omega}: 0.0 \pm 2.8\text{ mm}$), but not statistically significant.

A) Source localization of averaged MEG spike (averaged 16 spikes)



B) MEG source imaging methods for 8 patients with mesial temporal lobe epilepsy

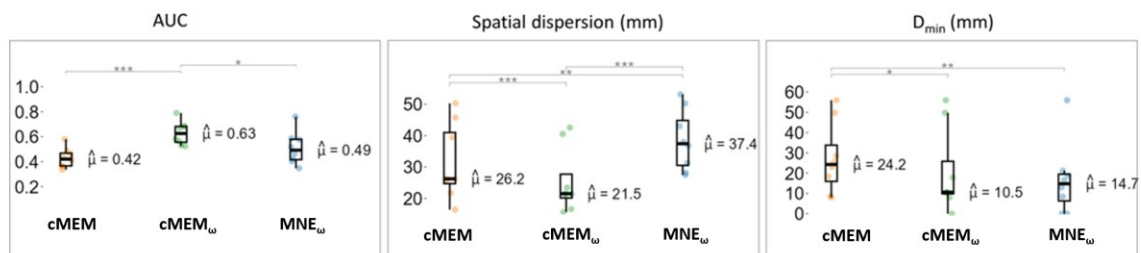


Figure 7-9: (A) Example of a MEG patient with mesial temporal lobe epilepsy. The source imaging methods were applied to the average of 16 selected interictal epileptic discharges. The surface of the hippocampus is included in the source model (shown as separate structures). The metrics AUC, SD, and D_{\min} were calculated at the midpoint of the rising phase of the spike (-10ms). The scale is different for the 3 methods,

but source maps are interpreted relatively for each method. (B) Comparison of the MEG source imaging methods in terms of the validation metrics AUC, SD and D_{\min} for 8 patients with mesial temporal lobe epilepsy. Each boxplot represents metrics from one source imaging method. On each boxplot, the central mark indicates the median, and the bottom and top edges of the box indicate the 25th and 75th percentiles, respectively. If the groups are statistically different after post-hoc analysis, the significance levels are shown as: ‘***’ for $p < 0.001$, ‘**’ for $p < 0.01$, and ‘*’ for $p < 0.05$.

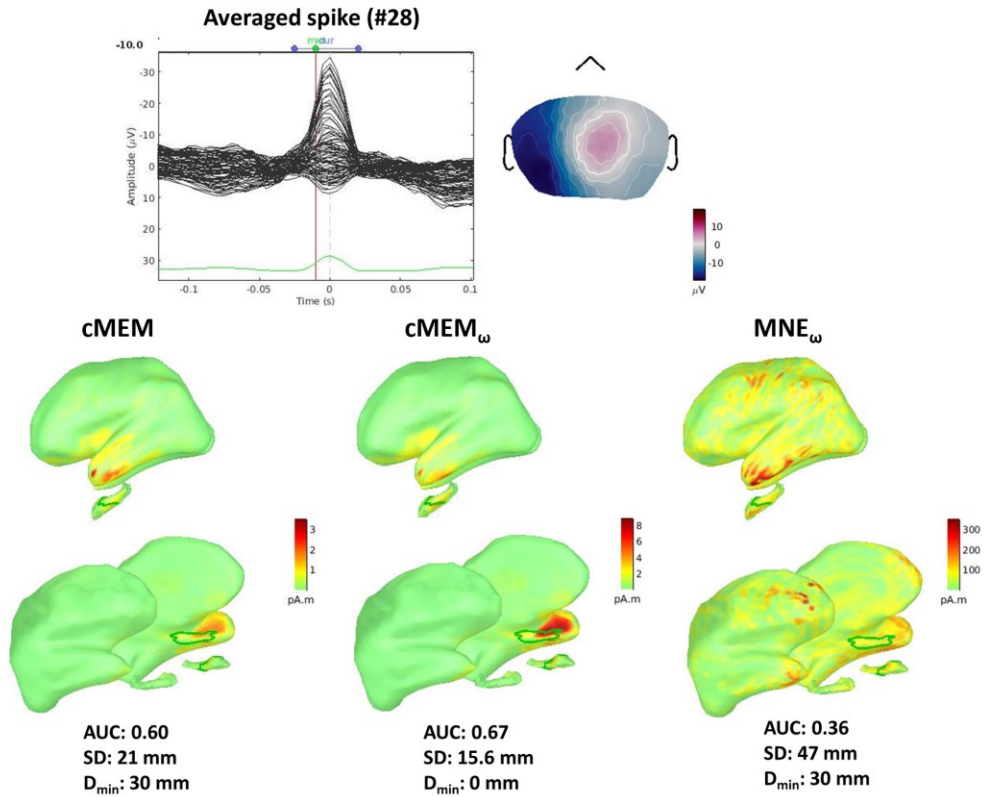
Fig S31 (A) summarizes the metrics estimated for 14 patients including the mesial temporal cases and also other superficial cases. The sensor level SNR of the averaged IEDs were $24.0 \pm 7.7\text{dB}$ at the peak and $20.7 \pm 7.4\text{dB}$ at the midpoint of the rising phase of the spike. Overall improvement by cMEM_{ω} was observed compared to cMEM (not statistically significant). Compared to MNE_{ω} , cMEM_{ω} slightly improved the localization in terms of AUC (not statistically significant) and SD ($p < 0.001$). The lowest median of D_{\min} was found for MNE_{ω} when compared to cMEM and cMEM_{ω} . We also verified that the improvement brought by depth weighting was not dependent on the overall quality of the ground truth data, when comparing results between the seizure-free group and the other group for both MEG and HD-EEG data (see details in the Supplementary material S2).

HD-EEG: Figure 7-10A presents an example of HD-EEG source localization for a patient with mesial temporal lobe epilepsy. Unlike the MEG result shown in Figure 7-9A, cMEM could localize the hippocampal generator for HD-EEG. cMEM_{ω} improved the localization compared to cMEM in terms of AUC, SD and D_{\min} . The metrics for cMEM/ cMEM_{ω} were: AUC: 0.60/0.67, SD: 21.0/15.6 mm and D_{\min} : 30/0mm. The results for MNE_{ω} were: AUC: 0.36, SD: 47mm, D_{\min} : 30mm.

Figure 7-10B shows the boxplots summarizing the metrics for cMEM, cMEM_{ω} and MNE_{ω} for 9 patients with mesial temporal lobe epilepsy, for which the ground truth involved the mesio-temporal structures that include the hippocampus. The sensor level SNR of the averaged IEDs were $28.60 \pm 4.95\text{dB}$ at peak and $26.92 \pm 5.88\text{dB}$ at the midpoint of the rising phase of the spike. cMEM_{ω} significantly improved the localization compared to cMEM in terms of AUC ($p < 0.001$, $\text{AUC}_{\text{cMEM}_{\omega}-\text{cMEM}}$: 0.04 ± 0.01) and SD ($\text{SD}_{\text{cMEM}_{\omega}-\text{cMEM}}$: 2.9 ± 0.7 mm). D_{\min} was also improved by cMEM_{ω} compared to cMEM ($\text{Dmin}_{\text{cMEM}_{\omega}-\text{cMEM}}$: 0.4 ± 1.1 mm) but not statistically significant. Compared to MNE_{ω} , cMEM_{ω} provided improved AUC ($p < 0.001$, $\text{AUC}_{\text{cMEM}_{\omega}-\text{MNE}_{\omega}}$: 0.10 ± 0.03), SD ($p < 0.001$, $\text{SD}_{\text{MNE}_{\omega}-\text{cMEM}_{\omega}}$: 16.0 ± 3.2 mm) and slightly improved D_{\min} ($\text{Dmin}_{\text{MNE}_{\omega}-\text{cMEM}_{\omega}}$: 3.2 ± 5.2 mm, not statistically significant).

Fig S31 (B) summarizes the metrics for all 16 HD-EEG patients including mesial temporal cases and other extra-temporal cases. The sensor level SNR of the averaged IEDs were $28.09 \pm 4.40\text{dB}$ at the peak and $25.40 \pm 5.00\text{dB}$ at the midpoint of the rising phase of the spike. Overall improvement by cMEM_ω was observed compared to cMEM (not statistically significant). Compared to MNE_ω , cMEM_ω significantly improved the localization in terms of AUC ($\text{AUC}_{\text{cMEM}_\omega - \text{MNE}_\omega}$: 0.11 ± 0.06), SD ($\text{SD}_{\text{MNE}_\omega - \text{cMEM}_\omega}$: $16.7 \pm 6.0\text{ mm}$) and D_{\min} ($D_{\min \text{MNE}_\omega - \text{cMEM}_\omega}$: $3.0 \pm 9.0\text{ mm}$).

A) Source localization of averaged EEG spike (averaged 28 spikes)



B) EEG source imaging methods for 9 patients with mesial temporal lobe epilepsy

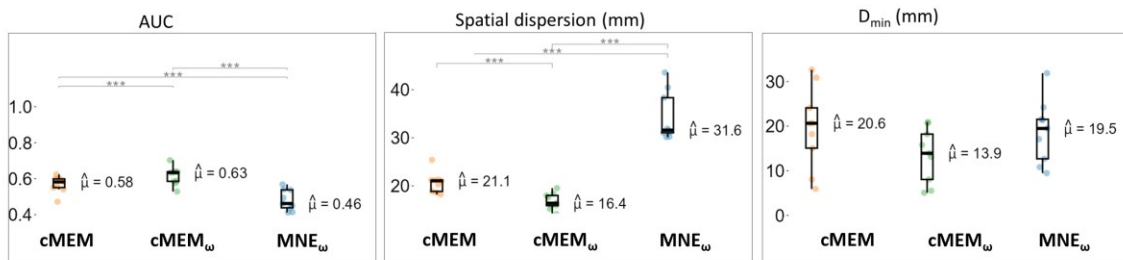


Figure 7-10: (A) Example localization of HD-EEG source imaging methods for a patient with mesial temporal lobe epilepsy. The source imaging methods were applied to an average of 28 interictal epileptic discharges. The surface of the hippocampus is included in the source model (shown as separate structures). The metrics AUC, SD, and D_{\min} were calculated at the midpoint of the rising phase of the spike (-10ms). The scale is different for the 3 methods but source maps are interpreted in a relative manner for each method. (B) Comparison of the EEG source imaging methods in terms of the validation metrics AUC, SD and D_{\min} for 9 patients with mesial temporal lobe epilepsy. Each boxplot represents metrics from one source imaging method. On each boxplot, the central mark indicates the median, and the bottom and top edges of the box indicate the 25th and 75th percentiles, respectively. If the groups are statistically different after posthoc analysis, the significance levels are shown as: ‘***’ for $p < 0.001$, ‘**’ for $p < 0.01$, and ‘*’ for $p < 0.05$.

7.5.5 Depth-weighted wMEM

Similar to cMEM, depth weighting improved the localization for deep sources for wMEM method as well. Fig S32 shows the metrics AUC, SD and D_{\min} as a function of eccentricity for the 300 MEG simulations presented in Figure 7-4, but also this time considers wMEM and its depth weighted implementation, wMEM_ω. Overall, the findings for wMEM versus wMEM_ω were similar to cMEM versus cMEM_ω. Detailed statistical comparisons are presented in the Supplementary material (section S1, Fig S32 and Fig S33). We also provided wMEM results as a function of eccentricity for all combinations of SE and SNR levels for MEG simulations in Fig S34-36 and HD-EEG simulations in Fig S37-39. For all combinations of MEG and HD-EEG, similar trends were found as described in Fig S32 and Fig S33. We decided not to provide detailed statistical comparisons for wMEM results for other combinations of HD-EEG and MEG simulations. Our results were overall similar to the ones reported in Fig S32 and Fig S33, suggesting that depth weighting also improved the ability of wMEM to localize deep generators, while preserving good accuracy when localizing superficial generators, which could be of great interest when localizing specific oscillations using this wavelet extension of MEM framework.

7.6 Discussion

In this study, we proposed a depth-weighted implementation of cMEM for EEG/MEG source imaging to localize deep source activity accurately, while maintaining cMEM's ability to recover the spatial extent of the underlying generators for both deep and cortical generators. We assessed the ability of the depth-weighted method, cMEM_ω to localize simulated epileptic activity at

different locations on the cortical and hippocampal surface. Compared to cMEM and MNE as benchmarks, the new version could estimate the deep generators more accurately, without or with minimal worsening of the localization for superficial regions. This was robust for HD-EEG and MEG, different spatial extents of the generator, and different SNR levels. A similar improvement was found for the wavelet version of the MEM method. We also demonstrated the utility of cMEM_ω in localizing EEG/MEG epileptic spikes from patients with mesial temporal lobe epilepsy.

7.6.1 Including hippocampus in the source model

The source model included the surface mesh of the cortex, with an additional subcortical structure, the hippocampus. The sources were located along the surface of the structures, with a fixed orientation normal to the surface as proposed by Attal and Schwartz (2013) and used in other studies (Calvetti et al., 2019; Meyer et al., 2017). Such modeling is motivated by the morphological and organizational similarity of the layer of the pyramidal cells in the hippocampus and neocortex (Meyer et al., 2017). Other subcortical structures such as the thalamus, amygdala, or brainstem can be modeled as a volume grid for better anatomical approximation (Attal & Schwartz, 2013). Including those structures in the volume grid would require handling parcellation in both surface and volume for the MEM framework, which was out of the scope of this study, as in MEM the parcellation is guided along the surface in a geodesic manner.

7.6.2 Depth-weighted cMEM improved localization for deep sources

For MEG and HD-EEG simulations of epileptic activity involving different locations covering the whole brain, cMEM_ω provided more accurate localizations for deep sources than cMEM and MNE_ω. For superficial regions, cMEM_ω exhibited similar performance as cMEM in terms of AUC and D_{min}, but worsened slightly the SD. Compared to MNE_ω, cMEM_ω localizations for superficial regions were also better in terms of AUC and SD, along with our previous findings comparing non depth-weighted cMEM to MNE_ω (Chowdhury et al., 2016; Chowdhury et al., 2013; Chowdhury et al., 2018). Although cMEM_ω slightly worsened the SD compared to cMEM (by ~3mm), it still provided improved SD compared to MNE_ω (by ~24mm in MEG and ~14mm for HD-EEG) and therefore excellent sensitivity to the spatial extent of the generators.

Our simulation results showed that the cMEM_ω was sensitive to mesial sources, and we found rare spurious localization of deep structures when they were not simulated. MEG and HD-EEG source imaging results were robust for all other combinations of spatial extent and SNR levels. Compared

to HD-EEG, we observed high variance in SD and D_{\min} for MEG simulations and worsening of SD and D_{\min} for some superficial regions (Fig S5, Fig S22, Figure 7-3, Figure 7-7). This was related to the lower level of sensor level SNR for MEG simulations compared to HD-EEG. The sensor level SNR of the simulated signal for MEG/HD-EEG is reflective of the sensitivity of the sensors to different source locations and orientations. For instance, EEG is more sensitive to radial and deep sources whereas MEG using gradiometers is more sensitive to tangential and superficial sources (Goldenholz et al., 2009; Kakisaka et al., 2013). This is also why the improvement in MEG due to depth weighting was more pronounced compared to HD-EEG (Figure 7-3 and Figure 7-7). However, the low SNR of MEG simulations also resulted from the simulation model used in this study. As we used a uniform signal strength for all the vertices within a patch, the generators that consisted of two opposite walls of the sulcus would lead to more signal cancellation for MEG than EEG (Chowdhury et al., 2016; Chowdhury et al., 2015). Therefore, several MEG sources simulated in this study resulted in lower sensor level SNR when compared to HD-EEG. This could explain the large variance observed in SD and D_{\min} in MEG localizations for both deep and superficial sources even after applying depth weighting.

Although $cMEM_{\omega}$ improved localization accuracy for deep sources compared to $cMEM$ and MNE_{ω} , the localization accuracy was still associated with source depth (i.e. lower accuracy for deeper sources). This is consistent with the findings reported in previous studies using EEG (Krings et al., 1999; Mikulan et al., 2020; Unnwongse et al., 2023; Whittingstall et al., 2003) and MEG (Chowdhury et al., 2015). Using simultaneously acquired HD-EEG and intracerebral stimulation as ground truth, Pascarella et al. (2023) compared ten source imaging methods and explored different depth weighting parameters. They found the lowest localization error (within 10mm) was obtained for dipolar and sparsity-promoting localization methods. Larger localization errors (mean ~15-20 mm) were found for distributed source imaging methods such as the MNE_{ω} , sLORETA, eLORETA (Pascual-Marqui et al., 2006) and Beamformer (Van Veen et al., 1997), with large localization errors associated with deeper sources, even after applying depth weighting. In our HD-EEG simulations, we observed a similar range of localization error and SD for MNE_{ω} as reported by Pascarella et al. (2023). We found the lowest localization error (4.8 ± 6.8 mm) for $cMEM_{\omega}$. Both $cMEM$ and $cMEM_{\omega}$ provided much lower SD compared to MNE_{ω} , consistent with our previous studies (Chowdhury et al., 2016; Chowdhury et al., 2013; Pellegrino, Hedrich, et al., 2020) reporting the ability of the MEM method to recover the spatial extent accurately. Pascarella

et al. (2023) used real intracerebral stimulations resulting in very focal generators associated with high SNR, whereas we used realistic numerical simulations involving spatially extended generators and different SNR levels. Another important difference is we considered a fixed value of depth weighting factor ($\omega = 0.5$) for cMEM_ω and MNE_ω in the whole study. However, we also investigated the depth weighting parameter ω for a range of values: $\omega = 0.1, 0.3, 0.5, 0.7$ and 0.9 for one set of 300 MEG simulations (Fig S17). For deep sources, increasing the depth weighting parameter ω improved localization accuracy as expected, but choosing higher ω values penalized the localization of superficial sources. This observation aligns with Pascarella et al. (2023), who investigated different depth weightings between 0 and 5 in MNE, Mixed Norm Estimate (Gramfort et al., 2012), dSPM and Beamformer for various sources and found optimal localizations with either $\omega = 0$ or 1. This suggests that for superficial sources, $\omega = 0$ would provide the best localization, while for deep sources, $\omega = 1$ would be optimal. Without a ground truth, determining whether a source is superficial or deep is unknown. Therefore, choosing $\omega = 0.5$ appears as a reasonable compromise, whereas using 0 or 1 could potentially lead to complete mislocalization of sources. Moreover, the depth weighting factor also depends on the sensitivity of the modality. For instance, Lin et al. (2006) reported the best localization accuracy for MNE_ω for a depth weighting factor ranging from 0.6 to 0.8 for MEG, and from 2 to 5 for EEG. Recently, in Cai et al. (2022), our group evaluated a range of ω when reconstructing functional Near-Infrared Spectroscopy data using cMEM_ω , most accurate results were found for depth weighting factors ranging between 0.3 and 0.5.

The simulations generated in this study were controlled to remain within a realistic range. Most of the hippocampal IEDs were nearly obscured by the background (as depicted in Supplementary Figs S3 and S4). In contrast to single simulations in MEG, for the mixture of cortical and hippocampal sources, we intentionally applied a higher SNR for the hippocampus to highlight that even with a good SNR signal, the standard cMEM failed to localize accurately to the hippocampus. In scenarios with very low SNR, none of the methods would be able to effectively localize deep sources when they are obscured by the superficial component. However, this limitation would be due to the low SNR of deep sources rather than the methods themselves.

We also demonstrated the applicability of cMEM_ω by evaluating the source localization of actual IEDs from patients with focal epilepsy. For the patients with mesial temporal lobe epilepsy, localization was significantly improved by cMEM_ω compared to cMEM and MNE_ω . The MEG

localizations of IEDs by cMEM were almost blind to the deep hippocampal or the mesial part of the sources. Depth weighting was necessary to localize these hippocampal sources during the rising phase of the spike. In contrast, HD-EEG localizations by cMEM were still behaving better (when compared to MEG) and some activity in the hippocampus and other deep regions was localized with cMEM, but incorporating depth weighting improved the localization accuracy.

7.6.3 Complex simulations involving mesial and neocortical sources

It is evident from simultaneous recording of scalp EEG/MEG and intracerebral EEG that the IEDs generated in deep mesial structures are hardly observable (often missed during visual interpretation) from scalp measurements when confined to mesial structures only (Merlet & Gotman, 1999). The spikes generated from mesial structures are more detectable on the sensors when they propagate and involve the activation of neocortical sources (Koessler et al., 2015; Merlet & Gotman, 1999). To mimic such concurrent activation of mesial plus neocortical interictal spikes, we simulated complex epileptic spikes on MEG, including the first generator at the hippocampus propagating to a second generator on the temporal neocortex after 15ms. We only ran these simulations for MEG, not HD-EEG, because it was more difficult for MEG data acquired with gradiometers to localize deep sources without depth weighting, when compared to our HD-EEG results. We considered source imaging at the peak of the hippocampal sources, which corresponded approximately to the midpoint of the rising phase of the spike we used when localizing clinical data. Compared to cMEM and MNE_{ω} , $cMEM_{\omega}$ was more accurate when localizing the hippocampal source. cMEM could not localize the hippocampal source, mistakenly placing it on the lateral neocortex. $cMEM_{\omega}$ localized the source in the hippocampus, but also exhibited spurious localizations on the lateral neocortex, reflected by a large localization error ($\sim 20\text{mm}$) and SD ($\sim 25\text{ mm}$). MNE_{ω} also showed this spurious localization on the lateral neocortex reflected by large localization error ($\sim 28\text{mm}$) and spatial spread (SD: $\sim 48\text{mm}$). For superficial regions, localizations by both MEM methods were more accurate than MNE_{ω} in terms of AUC and SD, not in terms of D_{\min} , as we previously reported (Hedrich et al., 2017).

Although $cMEM_{\omega}$ was more accurate than cMEM in localizing the deep hippocampal activity, the maximum activity was mostly found on the lateral cortex (see D_{\min} in Figure 7-6). This activation in the lateral cortex was also contributed by the simulation of the neocortical generator that already started at that point. However, we also observed spurious activity on the lateral neocortex for the

single sources simulated in the hippocampus only, which was reflected by high SD. Thus, the challenge to completely disentangle the mesial from neocortical sources remains (Benar et al., 2021; Krishnaswamy et al., 2017), even if depth weighting shows improved accuracy in localizing deep generators. Independent component analysis (ICA) based source separation techniques could be employed to disentangle deep versus superficial sources (Pizzo et al., 2019). However, ICA-based approach has been found to worsen MEG source localization accuracy for interictal activity and is suggested to be applied with caution (Pellegrino, Xu, et al., 2020).

7.6.4 Sensitivity of EEG/MEG sensors to deep activity

As the simulations for MEG and HD-EEG were implemented using background activity and anatomical head models from two different subjects, it was difficult to compare different source localization methods between these modalities directly. However, MEG was found overall less sensitive to deep sources than HD-EEG. One of the main reasons is that we considered gradiometers only, whereas magnetometers have a higher sensitivity to deep sources, at the price of more sensitivity to environmental noise (Malmivuo & Plonsey, 1995; Parkkonen et al., 2009). Our results are therefore consistent with studies using MEG gradiometers and suggesting that MEG is less sensitive to deep sources (Agirre-Arrizubieta et al., 2009; Baumgartner et al., 2000; Leijten et al., 2003; Shigeto et al., 2002; Wennberg et al., 2011). Few studies localizing subcortical activity using gradiometers benefitted from evoked responses with large SNR data (Barry et al., 2019; Coffey et al., 2016; Taylor et al., 2011). In contrast, most studies reporting that deep activity is indeed detectable by MEG, used magnetometers (Dalal et al., 2013; López-Madrona et al., 2022; Pizzo et al., 2019; Plummer et al., 2019; Santiuste et al., 2008). Fusion of EEG and MEG can also be exploited to recover some deep activity which we previously demonstrated using cMEM (Chowdhury et al., 2018; Chowdhury et al., 2015). Even though gradiometers are less sensitive to deep sources, we showed that the proposed cMEM_ω method would be useful for localizing deep source activity, even for gradiometers.

7.6.5 Depth-weighted wMEM

wMEM represents the data on the time-frequency domain, using discrete wavelets, before applying MEM solver for localization. Since discrete wavelets only consider the oscillatory part of the signal, wMEM was therefore proposed as a method particularly adapted to localize brain oscillations (Lina et al., 2012). The depth-weighted wMEM (wMEM_ω), the wavelet version of

cMEM_ω, showed similar improvement for MEG and HD-EEG simulations. Compared to cMEM_ω, wMEM_ω results exhibited similar performances in terms of AUC and D_{\min} , but slightly larger SD values. We expect that wMEM localization of epileptic spikes, mainly characterized by a transient shape and not by oscillations, will often result in higher SD than cMEM. The depth-weighted version of wMEM is more suitable for the localization of resting state oscillations (Afnan et al., 2023), epileptic burst activity, or high-frequency oscillations from deep sources (Avigdor et al., 2021; von Ellenrieder et al., 2016) and oscillatory activity at seizure onset (Pellegrino et al., 2016).

7.6.6 Limitations

One limitation of this study is that the MEG and EEG simulations were generated using anatomical head models and background recordings from different subjects, thus it was difficult to directly compare these two modalities. Simultaneous recording of EEG and MEG on the same subject would allow a comparison of the sensitivity of detecting deep source activity by EEG versus MEG. Moreover, the ground truth used for patients was still semi-quantitative. Further examination showed that the differences in localization improvement by depth weighting between the seizure-free group and the other group were not likely influenced by the quality of ground truth and possibly by the number of patients with deep generators included in that group (see Supplementary material S2, Tables 1 and 2). Comparison of simultaneous scalp recording with intracranial EEG will be considered in our future investigations.

7.7 Conclusion

We proposed depth-weighted cMEM (cMEM_ω) source imaging and demonstrated that it improved the EEG/MEG localization of deep sources compared to standard cMEM and depth-weighted MNE. We validated this method using extensive MEG and EEG realistic simulations of epileptic spikes, covering all brain regions including the hippocampus. We demonstrated the improvement by cMEM_ω in localizing deep brain activity, especially in a low SNR environment. Finally, we showed that cMEM_ω could localize the hippocampal activity more accurately for patients with mesial temporal lobe epilepsy, in cases for which standard cMEM would fail in recovering these deep generators. It is notable that the localization of superficial sources was hardly affected by depth weighting both for MEG and HD-EEG.

7.8 Acknowledgment

This work was supported by Natural Sciences and Engineering Research Council of Canada (NSERC) Discovery grant, grant from Canadian Institutes of Health Research (CIHR) (PJT-159448 and FDN 143208), and the Fonds de recherche du Québec—Nature et technologies (FRQNT) Research team grant. JA was partially supported by The Canadian Open Neuroscience Platform scholarship, Irma Bauer Fellowship, Faculty of Medicine and Health Sciences, McGill University and Fonds de Recherche du Québec – Santé Doctoral scholarship. BF was supported by CIHR project grant (PJT-175056), salary award (Chercheur-boursier clinicien Senior) of the Fonds de Recherche du Québec – Santé.

Supplementary file for Manuscript 2:

<https://pmc.ncbi.nlm.nih.gov/articles/instance/11240147/bin/HBM-45-e26720-s001.docx>

8 Manuscript 3: Validating MEG estimated resting state connectome with intracranial EEG

8.1 Preface

This is the third study of this thesis and the second part of our group-level validation of MEG source imaging of resting-state activity using the intracranial EEG atlas. The first part, covered in Study 1, focused on resting-state oscillations, while this second part now examines estimation of functional connectivity from MEG data. In Chapter 4, we addressed the challenges of estimating connectivity from EEG/MEG source localization due to source leakage issues. Previous studies have recommended metrics that remove zero-lag connectivity to mitigate this issue, but such metrics can also eliminate some genuine zero-lag connectivity.

In this study, we applied the same methodology proposed in Study 1 (Chapter 6), converting MEG sources into virtual intracranial EEG data, using the intracranial EEG electrode position of the MNI intracranial EEG atlas. We are proposing an original resampling methodology to take into account the limited spatial sampling of the MNI intracranial EEG atlas when assessing functional connectivity (since only paired electrodes from the same subjects could be considered), proposing for the first time spatial correlations between functional connectomes estimated from MEG sources and intracranial EEG data at the group level. We evaluated four widely used connectivity metrics to determine which ones more accurately estimate MEG-derived connectomes compared to the intracranial EEG atlas. We used the same healthy datasets from MEG and the intracranial EEG atlas as in Study 1 but applied the depth-weighted wMEM method for MEG source localization, which was proposed and validated in Study 2. This chapter includes the following sections: abstract, introduction, materials and methods, results, and discussion.

This manuscript is in press, *Network Neuroscience* as:

Afnan, J., Cai, Z., Lina, J. M., Abdallah, C., Pellegrino, G., Arcara, G., Khajehpour, H., Frauscher, B., Gotman, J., & Grova, C. (in press). Validating MEG estimated resting state connectome with intracranial EEG. *Network Neuroscience*.

8.2 Abstract

MEG is widely used for studying resting-state brain connectivity. However, MEG source imaging is ill-posed and has limited spatial resolution. This introduces source-leakage issues, making it challenging to interpret MEG-derived connectivity in resting states. To address this, we validated MEG-derived connectivity from 45 healthy participants using a normative intracranial EEG (iEEG) atlas.

The MEG inverse problem was solved using the wavelet-Maximum Entropy on the Mean method. We computed four connectivity metrics: Amplitude Envelope Correlation (AEC), orthogonalized AEC (OAEC), Phase Locking Value (PLV), and weighted-phase lag index (wPLI). We compared spatial correlation between MEG and iEEG connectomes across standard canonical frequency bands.

We found moderate spatial correlations between MEG and iEEG connectomes for AEC and PLV. However, when considering metrics that correct/remove zero-lag connectivity (OAEC/wPLI), the spatial correlation between MEG and iEEG connectomes decreased. MEG exhibited higher zero-lag connectivity compared to iEEG.

The correlations between MEG and iEEG connectomes suggest that relevant connectivity patterns can be recovered from MEG. However, since these correlations are moderate/low, MEG connectivity results should be interpreted with caution. Metrics that correct for zero-lag connectivity show decreased correlations, highlighting a trade-off; while MEG may capture more connectivity due to source-leakage, removing zero-lag connectivity can eliminate true connections.

Keywords: MEG source imaging, Intracranial EEG, connectivity, source leakage, resting state connectome

8.3 Introduction

The study of brain connectomes is a rapidly growing field in neuroscience which explores both the structural and functional patterns of resting-state brain connectivity, whereas electrophysiology plays a key role in disentangling static versus dynamic aspects of resting-state functional connectivity (Sadaghiani et al., 2022). Historically, MRI has been widely employed to investigate

brain connectomes, encompassing structural connectivity assessed through diffusion MRI and functional connectome evaluated using functional MRI (fMRI). In contrast, the utilization of electrophysiological methods, such as non-invasive electro/magneto-encephalography (EEG/MEG), in connectome research has experienced a notable surge in recent years. Due to their high temporal resolution and accessibility, EEG/MEG-based connectome studies have been undertaken to address a broad spectrum of questions in physiological and pathological conditions (Aydin et al., 2020; Xie & He, 2012). However, the main limitation of EEG/MEG-based connectome studies is that, as they involve scalp recordings and source localization, they require solving an ill-posed inverse problem (Darvas et al., 2004), and are therefore susceptible to source leakage. Source leakage, defined as the influence of a source on the estimation of the generators within its neighborhood (Brookes et al., 2012; Hedrich et al., 2017), is a significant concern, particularly for resting-state activity due to its low signal-to-noise ratio (SNR) condition. This affects the spatial accuracy of EEG/MEG estimated sources and introduces false positives in connectivity measures. Additionally, use of connectivity measures that are insensitive to true near-zero-lag synchronization leads to false negatives (Palva et al., 2018; Palva & Palva, 2012). Validation is thus essential for non-invasive EEG/MEG resting-state source imaging techniques to ensure appropriate interpretation of connectome results.

Researchers have investigated EEG/MEG connectivity for resting-state activity, using simulations to study source leakage (Palva et al., 2018) or to assess the effect of source imaging parameters or the choice of regions of interest extraction on connectivity (Brkić et al., 2023; Hincapié et al., 2016; Vallarino et al., 2023), or when comparing networks derived from EEG/MEG sources with those from fMRI (Brookes et al., 2011; Rizkallah et al., 2020). Recently, a few studies have compared whole-brain EEG connectomes with fMRI-derived ones and found moderate spatial correlations between the two modalities in canonical frequency bands (Wirsich et al., 2020; Wirsich et al., 2021; Wirsich et al., 2017). However, because these modalities capture different brain mechanisms, electrophysiology in EEG versus hemodynamic activity in fMRI, direct comparisons are limited, particularly for specific frequency bands.

Compared to EEG/MEG, intracranial EEG (iEEG), commonly used in epilepsy presurgical evaluation, offers highly accurate estimation of brain activity with excellent spatial and temporal resolution, including good SNR from deep structures. iEEG measurements are also negligibly

affected by volume conduction (Arnulfo et al., 2015; O'Reilly & Elsabbagh, 2021). However, it requires an invasive implantation procedure and has intrinsically limited spatial coverage, targeting only suspected regions of abnormal epileptic activity (Jayakar et al., 2016). Simultaneously recording EEG/MEG and iEEG provides probably the most reliable validation for non-invasive measurements (Koessler et al., 2010; Pizzo et al., 2019), as both modalities capture the same brain activity at the same temporal scale. However, validating whole-brain connectome estimates from EEG/MEG with iEEG is not feasible, as iEEG implantation covers the brain only partially. Therefore validation is limited to the implanted brain regions only (Nir et al., 2008).

In this context, the iEEG atlas of resting-state human activity developed by Frauscher et al. (2018) at the Montreal Neurological Institute (MNI) (<https://mni-open-ieegatlas.research.mcgill.ca/>) offers a unique opportunity for validating whole-brain connectome estimates from non-invasive EEG/MEG at the group level. This atlas pools data from many patients with epilepsy monitored during presurgical evaluation, retaining only iEEG electrodes implanted in healthy regions, i.e. regions not exhibiting any epileptic discharges. We have successfully used this atlas to validate how the power spectra of resting-state oscillations could accurately be localized using MEG (Afnan et al., 2023). In this study, we propose a similar methodology to validate the resting-state connectome estimated from MEG within a group of healthy participants against the resting-state iEEG connectome derived from the MNI iEEG atlas. To our knowledge, this is the first study to compare cross-modal correlations between MEG and iEEG at a group level to validate MEG-derived connectivity in widespread brain regions. Even though MEG and iEEG data were not recorded simultaneously, they both represent connectivity of the healthy adult brain and should ideally be strongly correlated.

8.4 Materials and methods

8.4.1 Experimental design

The iEEG connectome was constructed from the MNI iEEG atlas (110 subjects) of resting state data (sec 2.2). For MEG, resting state data were obtained from 45 healthy subjects (Pellegrino et al., 2022). Wavelet-based Maximum Entropy on the Mean (wMEM) was applied to solve the MEG inverse problem (sec 2.3.2) (Afnan et al., 2023; Lina et al., 2012). MEG was reconstructed on subject-specific cortical surfaces and then projected to the positions of iEEG electrodes specified

in the MNI iEEG atlas, using a method proposed by Grova et al. (2016) (sec 2.3.3). Projecting the MEG source maps to the intracranial space facilitated a quantitative comparison between MEG and iEEG (sec 2.3.3). MEG connectomes were constructed using a bootstrapping approach described in sec 2.3.4. Finally, we quantified the cross-modal spatial correlations between these two connectomes for six frequency bands: delta (0.5-4Hz), theta (4-8Hz), alpha (8-13Hz), beta (13-30Hz), low gamma (30-55Hz) and high gamma (55-80Hz). For each frequency band, the connectomes were constructed for four connectivity metrics; amplitude envelope correlation (AEC), AEC after pairwise orthogonalization (OAEC) (Hipp et al., 2012), phase locking value (PLV) and a modified version of weighted phase lag index (wPLI) (Vinck et al., 2011) keeping only phase information (sec 2.5). We will denote the 'MNI iEEG atlas' as the 'iEEG atlas' for the remainder of the article.

8.4.2 Ground truth: iEEG atlas

The iEEG atlas (Frauscher et al., 2018) was developed from 110 patients (age: 31 ± 10 years, range: 13-62 years, Male: 54) with refractory epilepsy who underwent iEEG implantation for presurgical epilepsy evaluation. The number of patients in the original paper was 106. However, by the time we started our project, additional patient data had been added. The atlas included electrodes in confirmed healthy brain regions, i.e. channels that did not exhibit any epileptic discharges. It comprises 1712 channels in a bipolar configuration. Each of the 1712 channels has 60 seconds of resting-state data, recorded with eyes closed (sampling rate: 200Hz). Preprocessing of iEEG data included filtering within the 0.5-80 Hz band and applying a notch filter at 50 Hz and 60Hz to remove the line noise considering in which center (North America or Europe) the data were acquired. iEEG data were downsampled to 200 Hz if the original sampling rate was higher (original sampling rates were 200, 256, 512, 1000, 1024, and 2000 Hz). The 60-second data were selected visually (either continuous or consecutive discontinuous > 5-second segments after artifact exclusion) (Frauscher et al., 2018). The iEEG channels were grouped into 76 regions of interest (ROIs) based on the MICCAI atlas (38 ROIs in each hemisphere) (Landman & Warfield, 2019). More details can be found in Frauscher et al. (2018).

8.4.2.1 Construction of iEEG connectome

To compute connectivity between two ROIs in the iEEG atlas, it is necessary to have at least one pair of channels connecting them in the same subject (connectivity cannot be computed for pairs

of ROIs recorded in different subjects). We identified all pairs of ROIs that exhibited at least one pair of channels between them. All local connections within the same ROI were discarded from further analysis. The number of channels between the ROI pairs and the number of subjects contributing to each ROI pair varied. For instance, some ROI pairs featured one or more pairs of channels from a single subject, while others could be contributed by up to 10 subjects, each providing one or more pairs of channels. Therefore, the average number of channels in all ROI pairs was 14 ranging from 1 to 217 channel pairs. For each pair of channels (between ROIs), connectivity was calculated using the four connectivity metrics described in section 8.4.5. The connectivity values for each ROI pair were then averaged, irrespective of whether they belonged to the same or different subjects, resulting in a single connectivity value per ROI pair. This process resulted in a connectome covering 44% of the whole connectome, consisting of 1278 pairs of ROIs, involving 100% of the MICCAI atlas (i.e. all 76 ROIs). Most connections were intra-hemispheric, covering 62% of the left hemispheric connectome, 59% of the right hemispheric connectome and 28% of interhemispheric connectome (see Supplementary Fig S1 for more details).

8.4.3 MEG

This study included 57 healthy participants who underwent MEG acquisition (resting state, with eyes closed), collected at the MEGLab of the IRCCS San Camillo Hospital in Venice, Italy (Pellegrino et al., 2022). MEG was acquired using a CTF-MEG system (VSM MedTech Systems Inc., Coquitlam, BC, Canada) with 275 axial gradiometers with a sampling rate of 1200 Hz. MEG preprocessing was performed with Brainstorm software (Tadel et al., 2011). Preprocessing of MEG data included (i) filtering within the 0.5-80 Hz band, (ii) applying a notch filter at 50 Hz, (iii) downsampling to 200 Hz, (iv) applying third-order spatial gradient noise correction and (v) removal of cardiac and eye movement artifacts using Signal Space Projection (SSP) (Uusitalo & Ilmoniemi, 1997) routine available in Brainstorm. A sixty-second segment was extracted for each subject, continuous or concatenated (minimum length of the continuous segment: 10 s), where no artifact was visibly present, ensuring with an EEG expert that the subject was awake during this segment. Following data preprocessing and sleep scoring, a total of 45 participants were ultimately included in the analysis (age: 29 ± 4 years, range: 20-38 years, Male: 10). Notably, 1 participant was excluded due to sleeping during the acquisition, while 11 were excluded for coregistration, segmentation issues, or exceptionally noisy data.

8.4.3.1 Source space and forward model estimation

For each participant, a T1-weighted-3D-turbo field-echo (TFE) anatomical MRI was performed with a 3T Ingenia CX Philips scanner (Philips Medical Systems, Best, The Netherlands). Freesurfer (Dale et al., 1999) was used for subsequent brain segmentation and reconstruction of the cortical surfaces. The coregistration of MEG sensors with anatomical MRI and analysis for creating the source model and forward model were performed in Brainstorm (Tadel et al., 2011). The cortical mesh of the middle layer (white/gray matter interface), equidistant between the white matter and pial surfaces and comprising approximately 300,000 vertices, was considered as the source space. Additionally, the two hippocampi from the subcortical structures were included, each hippocampus consisting of around 3,000-4,000 vertices depending on the subject's anatomy. For the cortex and hippocampus, sources were placed on the surface of the structures with a fixed orientation orthogonal to the surface at each point. The cortical and hippocampal surfaces were then combined as the source space and was downsampled to approximately 8,000 vertices. The forward model was computed using OpenMEEG software (Gramfort et al., 2010; Kybic et al., 2005) implemented in Brainstorm. We used a 3-layer Boundary Element model (BEM) consisting of brain, skull, and scalp surfaces with conductivity values of 0.33, 0.0165, and 0.33 S m⁻¹ (Zhang et al., 2006).

8.4.3.2 MEG source imaging using wavelet Maximum Entropy on the Mean (wMEM)

The MEG inverse problem was solved using the Maximum Entropy on the Mean (MEM) framework (Amblard et al., 2004), a Bayesian approach validated in the context of EEG/MEG source imaging (Chowdhury et al., 2013). The key feature of MEM is a spatial prior model, assuming that brain activity is organized within cortical parcels, where the activity of every parcel is tuned by the probability of activation of a hidden state variable. When the parcel is active, a Gaussian prior is assumed to model a priori the activity within the parcel. Starting from such a prior “reference” distribution, inference is then obtained by maximizing the relative entropy to the prior. MEM can either switch off or switch on the corresponding parcels during the localization process while allowing local contrast along the cortical surface within the active parcels. Wavelet MEM (wMEM) is a variant of the MEM method specifically designed to localize brain oscillatory patterns (Afnan et al., 2023; Amblard et al., 2004; Lina et al., 2012). wMEM applies a discrete wavelet transformation (Daubechies wavelets) to characterize the oscillatory patterns in the data before applying the MEM solver for source imaging (Lina et al., 2012). wMEM was validated for

localizing oscillatory patterns at seizure onset (Pellegrino et al., 2016), interictal bursts of high-frequency oscillations (Avigdor et al., 2021; von Ellenrieder et al., 2016) and MEG resting state fluctuations (Aydin et al., 2020). We proposed and implemented several changes in standard wMEM to localize specifically oscillatory patterns in the resting state (details in Afnan et al. (2023)), and evaluated the accuracy of reconstructions with the MNI iEEG atlas. In the current study, we used the wMEM version proposed by Afnan et al. (2023) adding the depth weighting parameter proposed and validated in Afnan et al. (2024) to localize deep brain activity more accurately.

To estimate a noise-covariance model from resting state data, we created a quasi-synthetic baseline from the signal of interest to compute the noise covariance by randomly shuffling the Fourier phase at each frequency (Prichard & Theiler, 1994). We employed a sliding window approach (window length: 1 second) to generate the baseline, ensuring a more precise estimation of the noise covariance matrix for each wavelet sample across the time scales (Afnan et al., 2023). wMEM implementation is available within the *BEST* plugin of Brainstorm software (<https://neuroimage.usc.edu/brainstorm/Tutorials/TutBEST/>).

8.4.3.3 *Estimation of virtual iEEG data from the MEG source map*

MEG measures current densities (in nanoAmpere-meters) after source imaging, while iEEG records electrical potentials in μ Volts. For a quantitative comparison, we converted MEG-reconstructed source maps into iEEG channel space by estimating corresponding electrical potentials for each electrode channel on the iEEG atlas (Abdallah et al., 2022; Grova et al., 2016). This involved localizing iEEG channels in the native MRI of MEG healthy subjects, by co-registering each subject MRI with the ICBM152 template using Minctracc (Collins et al., 1994), and applying a linear and non-linear transformation to align electrode coordinates from the iEEG atlas to each subject's anatomy. More details about this projection can be found in the Supplementary material S1. For each source map acquired from all 45 participants, we obtained MEG data converted into μ Volts to the corresponding locations of 1712 channels available in the iEEG atlas. This resulted in a larger number of MEG channels compared to the iEEG atlas (1712 channels in the iEEG atlas versus 1712×45 channels in MEG). We used a bipolar montage for both iEEG and MEG-converted virtual iEEG. In our comparison of MEG-estimated oscillations with the iEEG atlas in Afnan et al. (2023), we used a common average montage and found similar

results for a bipolar montage. However, we used a bipolar montage for the connectivity analysis as a common average montage can introduce spurious connections between channels (Bastos & Schoffelen, 2016; Shi et al., 2024).

8.4.3.4 Construction of reliable MEG connectomes using Bootstrap resampling

We constructed 45 MEG connectomes, retaining only the connections present in the iEEG connectome (see Fig S1). The key contrast between the iEEG connectome and MEG connectomes is that the iEEG connectome can reflect contributions from multiple subjects, while each MEG connectome represents contributions solely from one subject. To address this, we employed a bootstrapping approach to develop a MEG connectome contributed by a group of participants, similar to the one considered when using the iEEG atlas. The iEEG connectome consists of connectivity metrics between channel pairs, obtained by pooling the contribution from 110 patients. For example, consider two regions of interest (ROIs) - the hippocampus and angular gyrus, including four iEEG pairs of electrodes: The first and fourth connection pairs were obtained from one subject (iEEG_subject-1), while the second was obtained from iEEG_subject-2 and the third one from iEEG_subject-3. On the other hand, in each of 45 MEG connectomes, all connections would originate from a single subject. To create a MEG connectome mimicking the one obtained when using the iEEG atlas, we randomly select MEG subjects to contribute connection pairs between these two ROIs (hippocampus and angular gyrus). For instance, the first and fourth connection pairs came from one randomly selected MEG subject (e.g. MEG_subject-40), while the second and third connections were sampled from two other randomly selected MEG subjects (e.g. MEG_subject-8 and MEG_subject-1). As illustrated in Figure 8-1, this process was repeated for all ROI pairs to generate a bootstrap resampled MEG connectome, mimicking the same subjects group distribution as our original iEEG connectome. This overall process was repeated 5000 times and resulted in 5000 bootstrap resampled MEG connectomes (Figure 8-1).

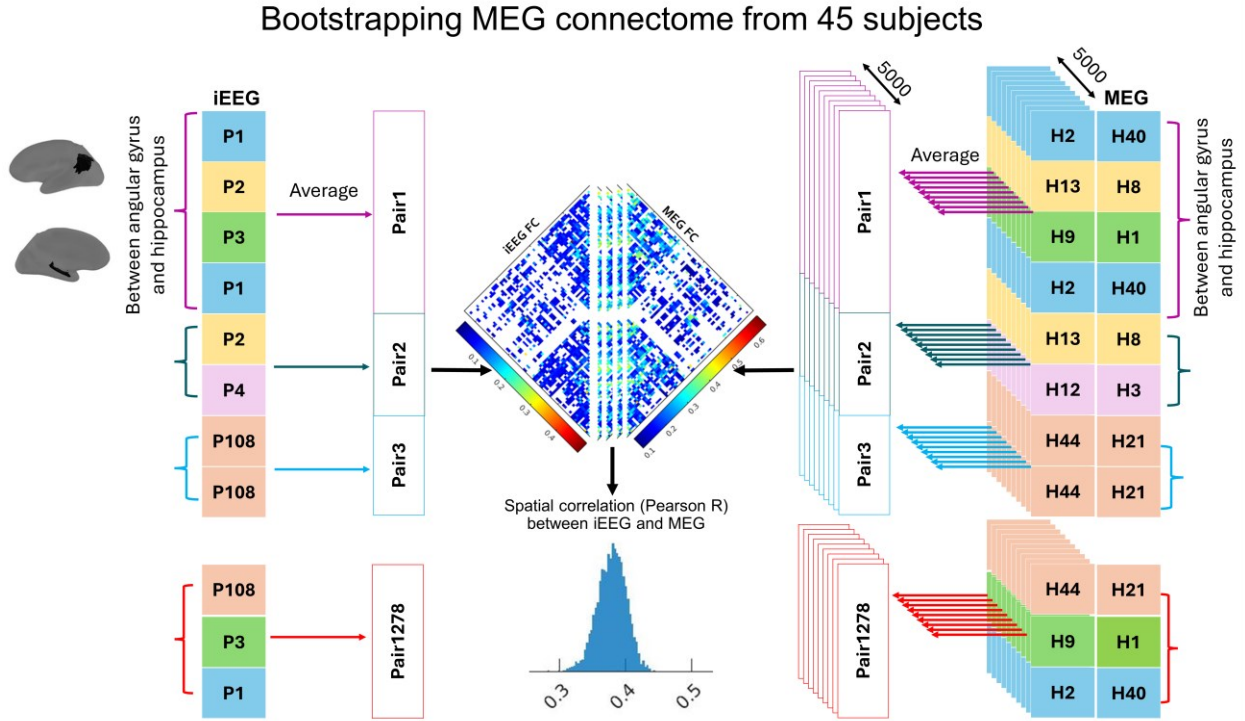


Figure 8-1: The iEEG connectome consists of connectivity metrics between pairs of channels, obtained from a total of 110 patients. In each of 45 MEG connectomes, all connections originated from a single subject. To generate a new MEG connectome comparable to the original iEEG connectome, MEG subjects were randomly chosen to contribute connections between ROIs while preserving spatial information. This process was repeated for all ROI pairs, resulting in a bootstrap resampled MEG connectome, mimicking the same subjects group distribution as our original iEEG connectome. The spatial Pearson correlation between the original iEEG connectome and the bootstrap resampled MEG connectome was computed. This overall process was iterated 5000 times, yielding 5000 correlation values.

8.4.4 Cross-modal correlation

We computed the spatial Pearson correlation between the original iEEG connectome and the 5000 bootstrap resampled MEG connectomes. As a result, we obtained 5000 Pearson correlation values, representing the spatial cross-modal correlation between iEEG and MEG data. To statistically assess the significance of cross-modal correlations, we also generated 5,000 cross-modal correlation values to build an empirical null distribution. To do so, for each iteration, we permuted randomly the anatomical labels of the channel pairs in the bootstrapped MEG connectomes, therefore effectively destroying the underlying spatial correlation structure. Then, we calculated the Pearson correlation between the iEEG connectome and the spatially permuted MEG

connectomes, creating an empirical null distribution from those 5000 correlation values. We defined a range for the null distribution, known as the Region of Practical Equivalence, which included 95% of the distribution centered around the median of the null. A cross-modal (MEG connectome-iEEG connectome) correlation was considered significant if less than 2.5% of the actual distribution lay inside the null range (equivalent to a 5% two-tailed threshold, with 2.5% in each tail).

8.4.5 Estimation of connectivity metrics

For analyzing electrophysiological data, various connectivity metrics are available, mainly classified into two categories: amplitude-based and phase-based metrics. In this study, we employed a widely-used amplitude-based metric—the amplitude envelope correlation (*AEC*) (Matthew J Brookes et al., 2011) and a phase-based metric, the phase locking value (*PLV*) (Mormann et al., 2000). Additionally, we utilized two metrics that correct/remove zero-lag connectivity: orthogonalized AEC (*OAEC*) (Hipp et al., 2012) and a modified version of the weighted phase lag index (*wPLI*) (Vinck et al., 2011), which was modified to consider only the phase information.

Let us consider two signals X and Y . To obtain their corresponding amplitude envelope and instantaneous phases, we computed the Hilbert transform for the entire 60-second signals. The Hilbert transform was initially calculated for each 0.5 Hz frequency band and then averaged to obtain one transform for six canonical frequency bands (delta (0.5-4Hz), theta (4-8Hz), alpha (8-13Hz), beta (13-30Hz), low gamma (30-55Hz) and high gamma (55-80Hz)) (Aydin et al., 2020).

$X_{BP,H}$ and $Y_{BP,H}$ (BP stands for bandpass and H stands for Hilbert) are the Hilbert analytical signals of each narrow frequency band for signals X and Y , described as $X_{BP,H}(t) = |X_{BP,H}(t)|e^{j\varphi_X(t)} = A_X(t)e^{j\varphi_X(t)}$ and $Y_{BP,H}(t) = |Y_{BP,H}(t)|e^{j\varphi_Y(t)} = A_Y(t)e^{j\varphi_Y(t)}$ respectively. Here, $A_X(t)$ and $A_Y(t)$ denote the instantaneous amplitude of $X_{BP,H}(t)$ and $Y_{BP,H}(t)$, $\varphi_X(t)$ and $\varphi_Y(t)$ denote the instantaneous phase of $X_{BP,H}(t)$ and $Y_{BP,H}(t)$, respectively. We considered the whole 60-second dataset to estimate AEC and OAEC. For PLV and wPLI, we used 6-second epochs and averaged the connectivity over the epochs.

Amplitude Envelope Correlation (AEC): AEC between two signals, X and Y , is obtained by computing the Pearson correlation between the envelopes of $X_{BP,H}$ and $Y_{BP,H}$. (Matthew J Brookes et al., 2011).

$$AEC = \frac{\sum_{t=1}^T (A_X(t) - \bar{A}_X)(A_Y(t) - \bar{A}_Y)}{\sqrt{\sum_{t=1}^T (A_X(t) - \bar{A}_X)^2 \sum_{t=1}^T (A_Y(t) - \bar{A}_Y)^2}} \quad (1)$$

Where T is the length of the signal (we considered 60-sec at 200 Hz sampling, $T = 12000$ samples) and \bar{A}_X and \bar{A}_Y are the mean values of $A_X(t)$ and $A_Y(t)$ respectively.

Orthogonalized Amplitude Envelope Correlation (OAEC): OAEC was proposed by Hipp et al. (2012) following a pairwise orthogonalization between two signals.

$$Y_{\perp X} = \text{imag}(Y_{BP,H} \frac{X_{BP,H}^*}{|X_{BP,H}|}) \quad (2)$$

$$X_{\perp Y} = \text{imag}(X_{BP,H} \frac{Y_{BP,H}^*}{|Y_{BP,H}|}) \quad (3)$$

Here $*$ means complex conjugate and *imag* means the imaginary part of the complex number.

We calculated the Pearson correlation between the envelopes of $X_{BP,H}$ and $Y_{\perp X}$. Similarly, the correlation between the envelopes of $Y_{BP,H}$ and $X_{\perp Y}$ is calculated and then the average of these two correlation values is considered as the final OAEC value.

Phase Locking Value (PLV): PLV was originally proposed in Lachaux et al. (1999) in the context of evoked activity considering a stable phase-difference along trials. We calculated PLV for each epoch of 6 seconds using an extended definition of PLV (Equation 3), a version proposed by Mormann et al. (2000) in the context of resting-state data, by assessing phase locking as a stable phase difference over time:

$$PLV_{X,Y} = \frac{1}{T} |\sum_{t=1}^T \exp(j(\varphi_X(t) - \varphi_Y(t)))| \quad (4)$$

Where T is the length of the signal (we considered 6-sec epochs at 200 Hz sampling, $T = 1200$ samples), j denotes the imaginary unit, $\varphi_X(t)$ and $\varphi_Y(t)$ are respectively the corresponding instantaneous phases of signals X and Y at time point t . We implemented PLV following the derivation proposed by Bruña et al. (2018) as:

$$PLV_{X,Y} = \frac{1}{T} \left| \sum_{t=1}^T \dot{X}_{BP,H}(t) \cdot (\dot{Y}_{BP,H}(t))^* \right| \quad (5)$$

Where $\dot{X}_{BP,H}(t) = \frac{X_{BP,H}(t)}{|X_{BP,H}(t)|}$ and $\dot{Y}_{BP,H}(t) = \frac{Y_{BP,H}(t)}{|Y_{BP,H}(t)|}$.

Finally, we averaged the PLV values across all the epochs.

Modified Weighted Phase Locking Index (wPLI*):

The original formula of wPLI is proposed by Vinck et al. (2011):

$$wPLI = \frac{|\sum_{t=1}^T A_X(t)A_Y(t)\sin(\varphi_X(t)-\varphi_Y(t))|}{\sum_{t=1}^T |A_X(t)A_Y(t)\sin(\varphi_X(t)-\varphi_Y(t))|} \quad (6)$$

If we consider the amplitudes of the channels in a particular frequency band are stable in time and not involved in the coupling of the channels, the coupling will be strictly described by the phase synchronization and driven by the constant phase shift. Under this assumption, the modified version of wPLI becomes:

$$wPLI^* = \frac{|\sum_{t=1}^T \sin(\varphi_X(t)-\varphi_Y(t))|}{\sum_{t=1}^T |\sin(\varphi_X(t)-\varphi_Y(t))|} \quad (7)$$

Where T is the length of the signal (we considered 6s epochs at 200 Hz sampling, $T = 1200$ samples). We averaged the $wPLI^*$ values across all the epochs.

The results obtained when considering the original wPLI formula are also provided in the Supplementary material.

8.5 Results

8.5.1 Connectivity estimated by MEG versus iEEG

Figure 8-2 shows the distribution of connectivity values estimated by MEG and iEEG for four connectivity metrics over the whole available iEEG connectome. Here we used all the original MEG connectomes estimated from 45 subjects, not the resampled MEG connectome as described in section 8.4.3.4. In this figure, iEEG connectivities were averaged across 6 frequency bands and MEG connectivities were averaged across 45 subjects and 6 frequency bands. Each boxplot shows 1278 connectivity values (from 1278 ROI pairs) for iEEG and MEG.

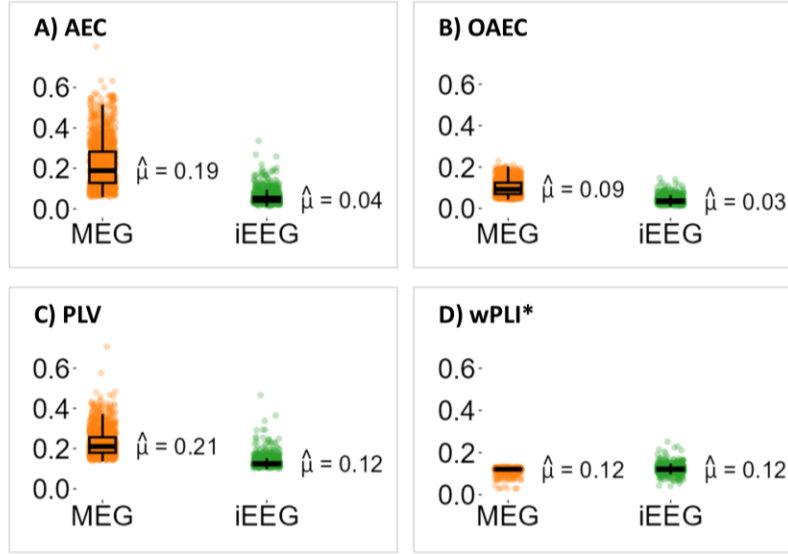


Figure 8-2: Connectivity averaged across frequency bands estimated by MEG and iEEG calculated using (A) *AEC*, (B) *OAEC*, (C) *PLV*, and (D) *wPLI**. For iEEG, we considered all 1278 iEEG ROI pairs available from all patients of the iEEG atlas and showed the averaged connectivity across six frequency bands. For MEG we considered 1278 virtual iEEG ROI pairs from each of the 45 subjects and showed the averaged connectivity across 45 subjects and six frequency bands. The median value of each distribution is displayed.

This figure provides a general overview of the scale of connectivity values one could expect from MEG versus iEEG connectomes. We found large differences in *AEC* and *PLV* connectivity values estimated from MEG when compared to iEEG, given that those two metrics are sensitive to volume conduction leakage. For *OAEC* and *wPLI** which removed zero-lag connectivity, MEG and iEEG connectivity values were found within a more similar range, but both were very low. We will investigate those connectivity values as a function of the distance between two ROIs in section 8.5.5.

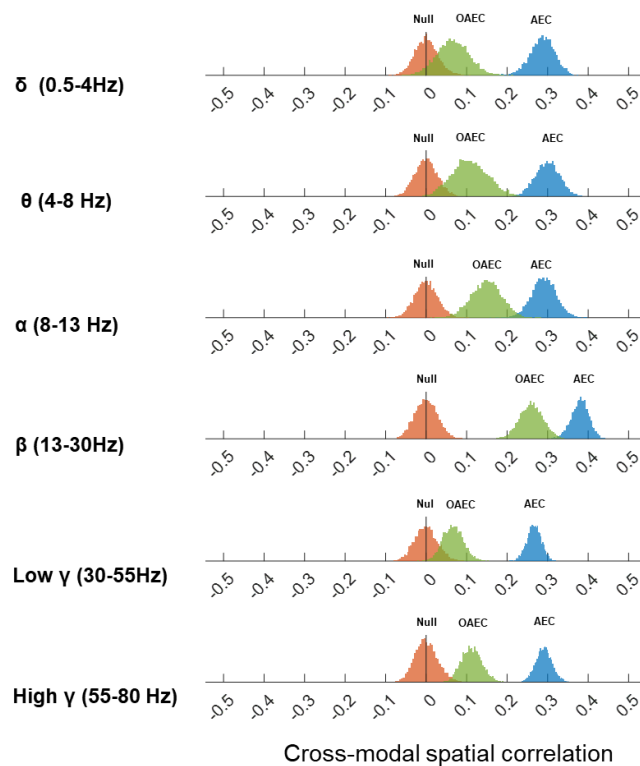
8.5.2 Cross-modal spatial correlation: AEC and OAEC

After considering 5000 bootstrap resampled MEG connectomes mimicking the same spatial/population distribution as our original iEEG connectome, Figure 8-3A presents the results of cross-modal spatial correlations between MEG and iEEG connectomes for six frequency bands calculated from *AEC* and *OAEC*, when compared to null distributions obtained by spatial permutation of the ROI pairs. The differences between the cross-modal correlations and the null distributions were as follows: For *AEC*: δ : 0.29 ± 0.03 , θ : 0.30 ± 0.03 , α : 0.29 ± 0.03 , β : 0.38 ± 0.02 ,

low γ : 0.27 ± 0.02 and high γ : 0.29 ± 0.02 (values reported as median \pm median absolute deviation). For OAEC: δ : 0.06 ± 0.03 , θ : 0.11 ± 0.03 , α : 0.15 ± 0.03 , β : 0.26 ± 0.03 , low γ : 0.07 ± 0.03 and high γ : 0.11 ± 0.03 .

Fig 3B displays the median value of the distribution for each cross-modal correlation and highlights correlations that were significantly larger than null. Unless specified otherwise, the correlation was considered significant if its overlap with the null range was less than 2.5% (equivalent to a 5% two-tailed threshold, with 2.5% in each tail). When considering *AEC* metric, MEG-estimated connectomes were moderately correlated with iEEG connectomes across all frequency bands (~ 0.25 - 0.37), with the highest correlation observed in the beta band (0.37). When considering *OAEC* metric, the median of cross-modal correlations decreased compared to *AEC*, but they remained significantly higher than null distribution in the alpha, beta and high gamma bands, with the highest correlation still observed in the beta band (0.26).

A) Cross-modal correlation between MEG and iEEG connectomes for AEC and OAEC



B)

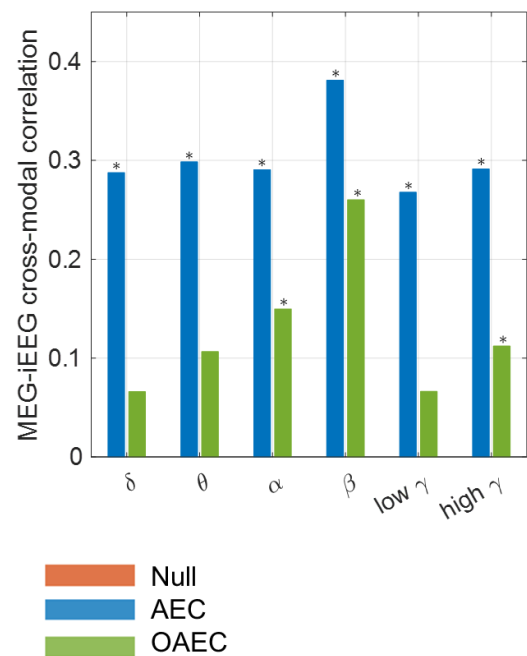


Figure 8-3: (A) Distribution of cross-modal correlations as well as the null distribution (red) between MEG and iEEG for six frequency bands calculated for AEC (blue) and OAEC (green). (B) The medians of the distribution of cross-modal correlations are shown in the bar plot. The correlation was considered significant if its overlap with the null range was less than 2.5% (equivalent to a 5% two-tailed threshold, with 2.5% in each tail). The frequency bands that showed significantly higher correlations than the null distribution are marked with an asterisk (*)

Figure 8-4 further presents intra-hemispheric and inter-hemispheric connections, alongside all available connections. Similarly to Figure 8-3, intra-hemispheric connectomes estimated from MEG using *AEC* were moderately correlated to those from iEEG across all frequency bands (significantly higher than the null distribution). Inter-hemispheric cross-modal correlations were significantly higher than the null distribution in all bands except alpha. For *OAEC*, inter- and intra-hemispheric correlations decreased compared to *AEC* in all frequency bands (Figure 8-4B). Intra-hemispheric correlations were significantly higher than the null distribution for the beta band, whereas inter-hemispheric correlations were not found statistically significant in any band.

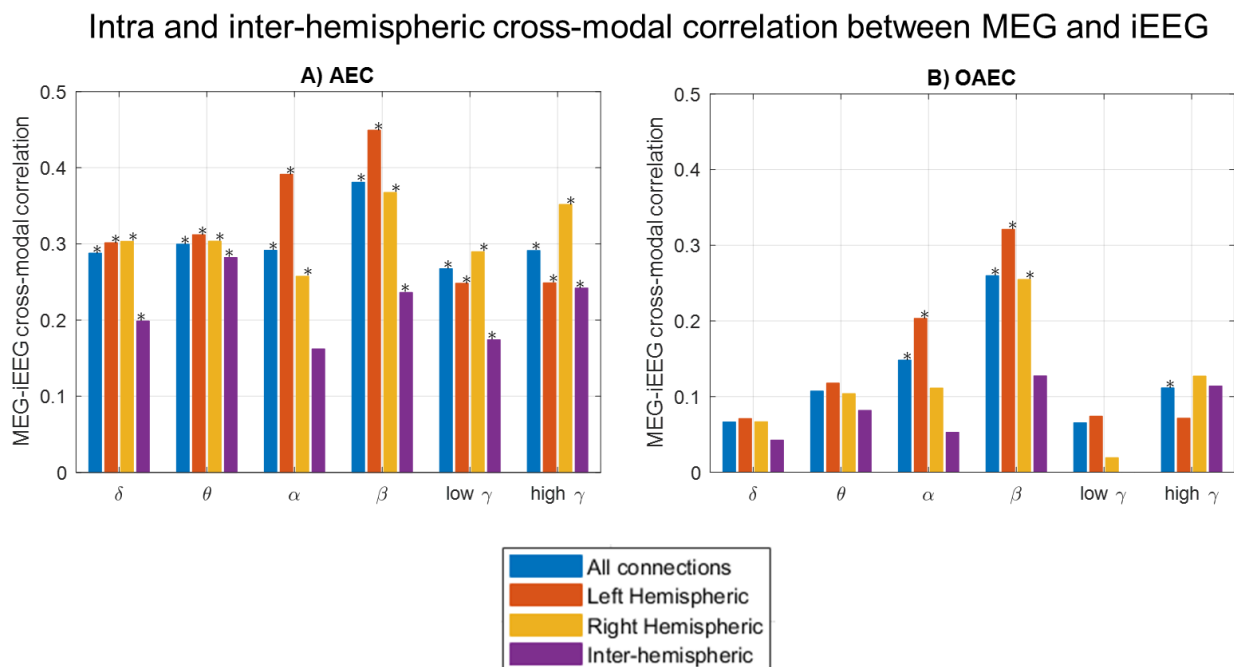


Figure 8-4: The median of the distribution of cross-modal correlations is depicted, considering all connections, intra-hemispheric connections, and inter-hemispheric connections for (A) AEC and (B) OAEC. The correlation was considered significant if its overlap with the null range was less than 2.5%

(equivalent to a 5% two-tailed threshold, with 2.5% in each tail). Frequency bands with significantly higher correlations than the null distribution are marked with an asterisk (*).

To assess the reliability of our findings, we conducted a supplementary investigation using a bootstrap resampling strategy to generate the iEEG connectomes. We divided the 60 seconds of iEEG data into ten 6-second segments and performed bootstrapping with replacement 100 times (similarly to the approach we proposed in Aydin et al. (2020)). More details are provided in Supplementary material S2. The spatial correlations between MEG and iEEG for AEC and OAEC, computed from the 100 bootstrapped iEEG datasets, are shown in Fig S2. The patterns for AEC and OAEC were similar to those shown in Figure 8-3B, suggesting robustness of our findings.

8.5.3 Cross-modal spatial correlation: *PLV* and *wPLI**

Figure 8-5A presents the cross-modal correlation between MEG and iEEG connectomes, depicted for 6 frequency bands, using the connectivity metrics *PLV* and *wPLI**. *PLV* exhibited moderate cross-modal spatial correlation across all frequency bands, with the highest correlation in the beta band. The differences between the cross-modal correlation and the null distribution for all frequency bands were as follows: δ : 0.29 ± 0.03 , θ : 0.34 ± 0.03 , α : 0.25 ± 0.04 , β : 0.36 ± 0.03 , low γ : 0.31 ± 0.03 , and high γ : 0.34 ± 0.03 . For *wPLI**, these differences were: δ : 0.14 ± 0.03 , θ : 0.2 ± 0.03 , α : 0.13 ± 0.04 , β : 0.15 ± 0.03 , low γ : 0.12 ± 0.03 , and high γ : 0.25 ± 0.03 .

In Figure 8-5B, the median values of each cross-modal correlation distribution are presented as a bar plot for both *PLV* and *wPLI**, highlighting correlations significantly larger than the empirical null distribution. For *PLV*, MEG-estimated connectomes were moderately correlated to iEEG connectomes across all frequency bands (~ 0.3). With *wPLI**, the median of cross-modal correlations decreased compared to *PLV*, but remained significantly higher than the null distribution for all frequency bands.

The spatial correlations between MEG and iEEG for intra- and inter-hemispheric connectomes for *PLV* and *wPLI** are presented in Supplementary Fig S3. For *PLV*, significant cross-modal correlations were observed for both intra-hemispheric connectomes in all frequency bands. Inter-hemispheric correlations were statistically significant in all frequency bands except alpha. Interestingly for *wPLI**, the inter-hemispheric correlations were statistically significantly higher than the null distribution in all frequency bands, whereas the left hemispheric correlations were

not significantly higher than null in any band. Moreover, the right hemispheric correlations were found higher than the left hemispheric correlations in all frequency bands. To further investigate this surprising result, we also evaluated the raw *wPLI** separately for iEEG and MEG for left-hemispheric versus right-hemispheric connectomes, and the distributions of *wPLI** did not show such laterality differences.

A) Cross-modal correlation between MEG and iEEG connectomes for PLV and *wPLI**

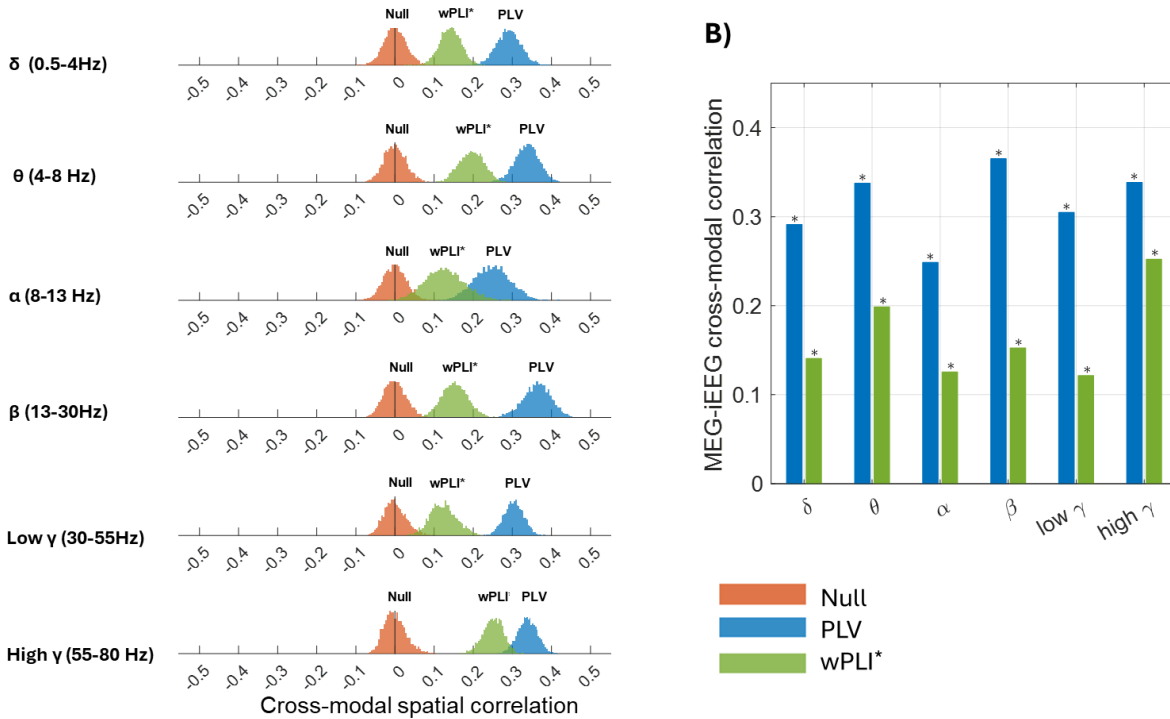


Figure 8-5: Distribution of cross-modal correlations as well as the null distribution (red) between MEG and iEEG for six frequency bands calculated for *PLV* (blue) and *wPLI** (green) (A). The medians of the distribution of cross-modal correlations were shown as a bar plot (B). The correlation was considered significant if its overlap with the null range was less than 2.5% (equivalent to a 5% two-tailed threshold, with 2.5% in each tail). The frequency bands that showed significantly higher correlations than the null distribution were marked with an asterisk (*).

To assess if the left versus right and inter-hemispheric asymmetry found by *wPLI** could be influenced by the choice of the source imaging method (wMEM), we also repeated this analysis using another standard source imaging method, the minimum norm estimate (Hämäläinen & Ilmoniemi, 1994). We found a similar trend, i.e., the inter-hemispheric correlations were higher than left/right hemispheric correlations and right hemispheric correlations were higher than left

hemispheric correlations (result not shown). In Supplementary Fig S4, we also provided the correlations between MEG and iEEG for intra- and inter-hemispheric connectomes for *wPLI*, calculated using the original definition, which also included envelope amplitudes, as described in equation (7). Using this implementation, the resulting correlations were overall very low and not statistically significant in any frequency bands.

8.5.4 Cross-modal spatial correlation for superficial versus deep sources

In Figure 8-6, we investigated the cross-modal correlations between MEG and iEEG for superficial and deep ROI pairs. For each iEEG channel, we measured the eccentricity, defined as the distance between the channel location and the center of the head. Deep channels have therefore low eccentricity and superficial channels have high eccentricity. Figure 8-6A shows the distribution of eccentricity values for all the channels, using 80% transparency of the cortical mesh so that all channels are visible in the figure. A threshold of 85 mm eccentricity was selected to classify the channels into superficial and deep channels. We used this threshold of 85 mm to have a similar number of ROI pairs in superficial versus deep connectomes. The distributions of the distance between ROI pairs for two groups (eccentricity > 85 mm for both ROIs of the pair and eccentricity < 85 mm for both ROIs of the pair) are shown in Figure 8-6B. The cross-modal correlations between MEG and iEEG connectomes for these two groups are depicted for the 6 frequency bands for *AEC*, *OAEC*, *PLV*, and *wPLI** (Figure 8-6C-F). For *AEC* and *PLV*, the cross-modal correlations were significantly higher than the null distribution for all frequency bands for both groups. However, the cross-modal correlations for deep ROI pairs had a trend of decrease when compared to superficial ROI pairs for delta, theta, alpha, and beta bands. For *OAEC*, the cross-modal correlations were significantly higher than the null distribution in the beta band for both superficial and deep ROI pairs. On the other hand, the correlation for deep ROI pairs in the alpha band was found significantly higher than null whereas the correlation for superficial ROI pairs did not reach the significant threshold. Interestingly for *wPLI**, the correlations for superficial ROI pairs were significantly higher than the null distribution for all frequency bands except low gamma, whereas the correlations for deep ROI pairs were very low and did not reach the significant threshold in any frequency band.

Cross-modal correlations between MEG and iEEG for superficial and deep sources

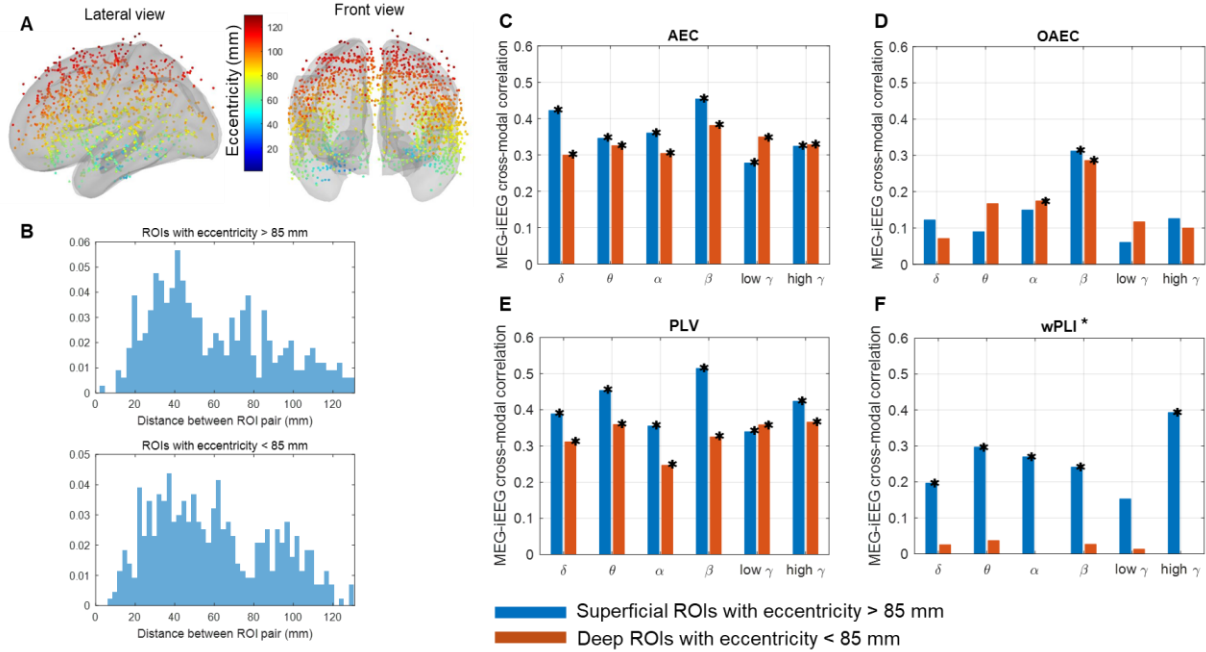


Figure 8-6: (A) Eccentricity of iEEG channels shown on the brain cortex with 80% transparency to ensure all deep iEEG channels are visible. (B) Distribution of the distances between ROI pairs for all pairs exhibiting either an eccentricity > 85 mm (top) or < 85 mm (bottom). The cross-modal correlation between MEG and iEEG for two groups (both eccentricity values > 85 mm in blue and both eccentricity values < 85 mm in red) for *AEC* (C), *OAEC* (D), *PLV* (E), and *wPLI** (F). The correlation was considered significant if its overlap with the null range was less than 2.5% (equivalent to a 5% two-tailed threshold, with 2.5% in each tail). The frequency bands that showed significantly higher correlations than the null distribution were shown with a *.

8.5.5 Connectivity as a function of distance between two ROIs

In this section, we investigated raw connectivity values from iEEG and MEG. Figure 8-7A shows the *AEC* and *OAEC* values as a function of the distance between two ROIs for iEEG and MEG for beta band results. For MEG, the connectivity values were averaged over 45 subjects. As expected, both *AEC* and *OAEC* decreased as a function of distance between the two ROIs. However, for *AEC*, MEG connectivity values were greater than iEEG. After orthogonalization, both MEG and iEEG connectivity values decreased, but the decrease in MEG was higher than iEEG, which was quantified and plotted in Figure 8-7B. The *AEC* and *OAEC* for all frequency bands are presented in Supplementary Fig S5. Across all frequency bands, the reduction in MEG connectivity

following orthogonalization exceeded that of iEEG (see Fig S6). The raw *PLV* and *wPLI** values as a function of distance between ROIs for all frequency bands are presented in Fig S7. Similar to *AEC* and *OAEC*, *PLV* also decreased as a function of the distance between two ROIs for both MEG and iEEG. *PLV* estimated by MEG were greater than iEEG. However for *wPLI**, the relationship of the values as a function of the distance between ROI pairs is not as clear as found for other metrics.

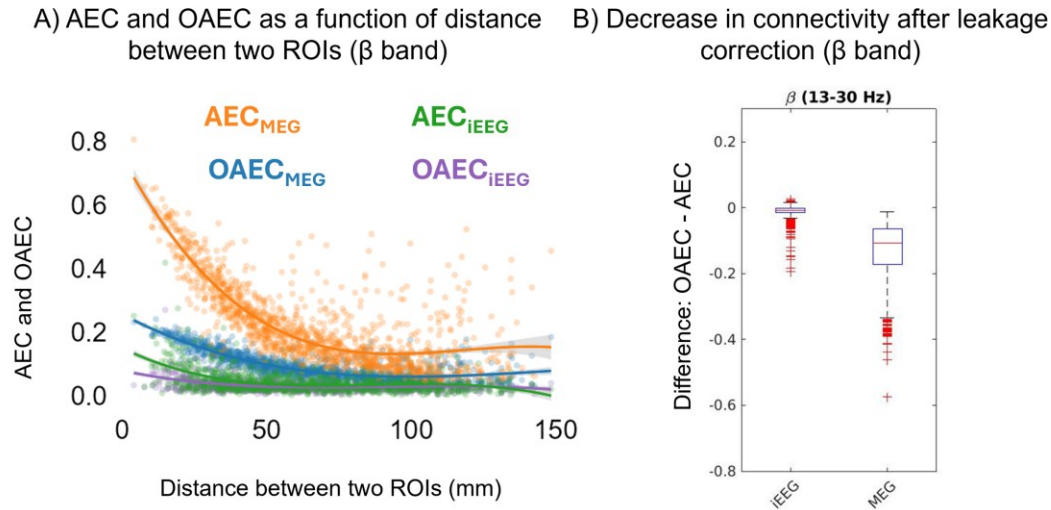


Figure 8-7: (A) *AEC* and *OAEC* as a function of distance between two ROIs plotted for iEEG and MEG in the beta band. (B) The distribution of differences between *OAEC* and *AEC* (*OAEC* minus *AEC*) for MEG and iEEG.

8.5.6 Cross-modal spatial correlation and the number of subjects averaged in ROI pairs

In previous results, we actually estimated the iEEG connectomes (real or virtual) by averaging all possible pairs of channels between each ROI pair (section 8.4.2.1). The results shown so far were produced using this criterion: at least one pair of channels connecting the ROI pair, which resulted in a connectome containing 1,278 ROI pairs (out of 2,888 possible ROI pairs, resulting in 44% coverage of the whole connectome). To assess the effect of the number of subjects having an ROI pair, we further investigated the cross-modal spatial correlations between MEG and iEEG connectomes while increasing the minimum number of subjects to be averaged for each ROI pair. However, increasing the minimum number of subjects in each ROI pair limits the coverage of the iEEG connectome we could consider (some ROI pairs have only one subject, some have two, etc).

Cross-modal correlation when number of subject averaged in each ROI pair increases
 β (13 - 30 Hz)

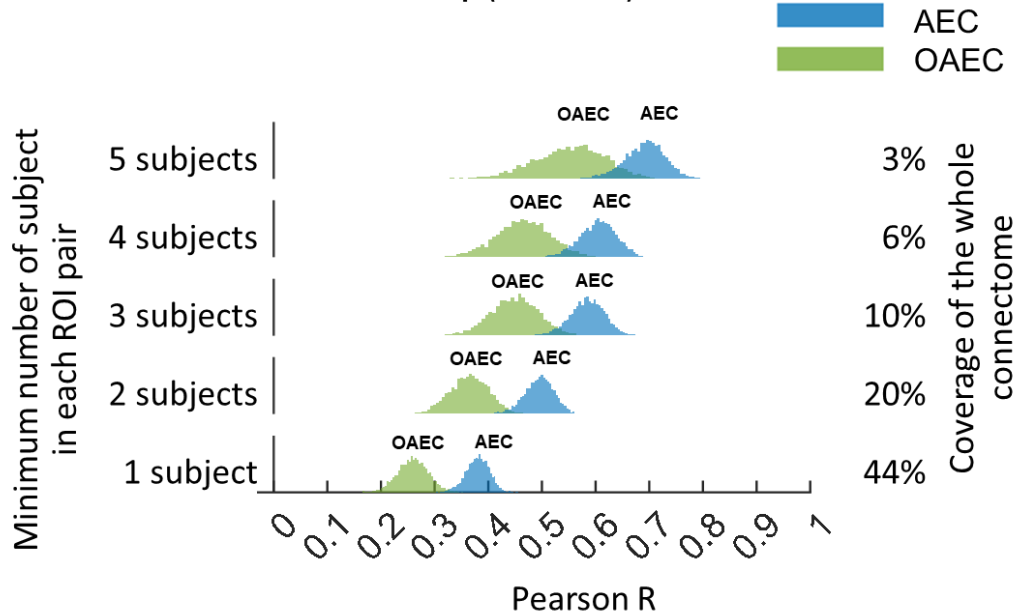


Figure 8-8: Distribution of cross-modal spatial correlations between MEG and iEEG connectomes in the beta band obtained using *AEC* and *OAEC* (obtained from 5000 bootstrap MEG samples), as we increase the minimum number of subjects from 1 to 5 in each ROI pair. Increasing the minimum number of subjects in each ROI pair (as shown on the left) decreases the available coverage of the iEEG connectome from 44% to 3% (as shown on the right). For example, the bottom row displays histograms of the correlations between MEG and iEEG connectomes when the iEEG connectome was created with ROI pairs that include at least 1 patient, covering 44% of the connectome.

Figure 8-8 shows the cross-modal correlations for *AEC* and *OAEC* in the beta band as an example. On the y-axis, we show the minimum number of subjects on the left and the percentage coverage of the whole connectome on the right. The cross-modal correlations between MEG and iEEG increased as the minimum number of subjects included in each ROI pair increased. The lowest value of the minimum number of patients (= 1) means including all possible ROI pairs, thus maximizing the connectome coverage. Using a minimum number of patients of 1 provided 1,278 ROI pairs, covering 44% of the whole connectome. Increasing the minimum number of patients in each ROI pair to 2, 3, 4, and 5 decreased the connectome coverage to 20%, 10%, 6%, and 3% of the whole connectome, respectively. We did not show results for a minimum number of patients greater than 5, as the coverage of the connectome decreases to less than 1%.

The cross-modal correlations for six frequency bands as we increased the minimum number of subjects in each ROI pair are shown in Supplementary Fig S8. A similar trend of increased cross-modal correlation was found for *AEC* and *OAEC* in delta, theta, alpha, beta and low gamma bands.

In Supplementary Fig S9, the cross-modal correlations obtained using *PLV* and *wPLI** are shown for all six frequency bands as we increased the minimum number of subjects in each ROI pair. For all frequency bands, the cross-modal correlations for *PLV* increased as the minimum number of subjects in each ROI pair increased. However for *wPLI**, we did not find the trend of increasing cross-modal correlation as we increased the minimum number of subjects.

8.6 Discussion

Our objective was to validate the ability of MEG to estimate resting state connectomes for healthy subjects by comparing them with an iEEG atlas. To compare the two modalities in the same space, we converted MEG sources into virtual iEEG potentials (Abdallah et al., 2022; Grova et al., 2016). As opposed to estimating virtual channels using beamforming approaches (Tamilia et al., 2021), our strategy is to combine a MEG source imaging method that was evaluated for its ability to localize accurately resting-state MEG data and notably oscillations, the wavelet-based MEM (wMEM) (Afnan et al., 2023), followed by applying an iEEG forward problem to estimate virtual iEEG potentials in microVolts that correspond to our MEG sources (Abdallah et al., 2022; Grova et al., 2016). This offers a solid quantification approach to compare MEG sources (estimated by solving an inverse problem) with actual iEEG in situ recordings. Consequently, the two modalities were associated with different distributions of available data when estimating connectomes. For MEG, we were able to estimate 45 connectomes, each coming from one subject, and providing virtual iEEG data on all channels of the iEEG atlas. Thus each connectome was contributed by the same subject. In contrast, when considering the multicentric iEEG atlas, we were able to estimate one iEEG connectome, which was obtained by pooling data from 110 subjects, each subject contributing to a subset of the connectome. To address the discrepancy between MEG and iEEG data distribution when estimating connectomes, we proposed a bootstrap resampling approach to create a MEG connectome spatially sampled in the same way as the iEEG connectome, such that each bootstrapped MEG connectome was built by pooling data in a similar way of constructing iEEG connectome.

Spatial cross-modal correlations between MEG and iEEG ranging from ~ 0.25 to 0.38 were observed for *AEC* and *PLV*. As expected, we found that considering *OAEC* or *wPLI**, as metrics that correct/remove zero-lag connectivity, led to a reduction in cross-modal correlations. This highlights the trade-off: while MEG may exhibit more connectivity due to source leakage, removing zero-lag connectivity also eliminates genuine connections, thereby decreasing overall cross-modal correlation. These results are also supported by the fact that even for the original iEEG, we found a small decrease in connectivity when removing zero-lag connectivity. This suggests that the observed connectivity is more likely to be genuine time-locked zero phase connectivity (see Figure 8-7), as iEEG, being local in-situ measurements, are less sensitive to source leakage and volume conduction (O'Reilly & Elsabbagh, 2021). These findings are consistent with prior studies (Colclough et al., 2016; Palva et al., 2018) that were conducted using simulations. In addition, there was a general trend of higher cross-modal spatial correlations between MEG and iEEG for superficial ROI pairs compared to deep ROI pairs, with a few exceptions. The decrease in correlations for deep ROI pairs was more prominent in phase-based metrics compared to amplitude-based metrics. The differences in cross-modal correlations for amplitude- and phase-based metrics also highlight that those metrics are capturing distinct information, more likely supported by different underlying mechanisms (Siems & Siegel, 2020).

Moreover, to the best of our knowledge, our study is the first to quantify the extent of overestimation of MEG connectivity when compared to ground truth iEEG data, at the population level. This overestimation was consistently observed across all frequency bands. This is also the first study to quantify and compare MEG and iEEG connectomes. For both MEG and iEEG, *AEC* and *PLV* values decreased with increasing distance between two ROIs, consistent with previous studies with animal electrophysiology (Leopold et al., 2003) and human iEEG (Arnulfo et al., 2015). The decrease in connectivity with increasing distance between regions was also found for *OAEC*, but not much for *wPLI** for which we mainly found very small connectivity values on those resting state data.

8.6.1 Moderate correlations between MEG and iEEG connectome

The cross-modal correlations between MEG and iEEG connectomes for different metrics across all frequency bands were generally moderate to low (~ 0.12 to 0.37 for all connections, when statistically significant). It is however important to note that we did not expect very high

correlations between these two modalities due to several factors contributing to the differences, such as: (i) non-simultaneous data from two different groups, (ii) different subjects contributing to the single iEEG connectome versus each of the 45 participants contributing to the MEG connectome (45 MEG connectomes), although we attempted to address this by adopting a bootstrap resampling approach, and (iii) different levels of averaging for different ROI pairs (ranging between 1 to 217 channel pairs). Considering these variabilities, the cross-modal correlations found between MEG and iEEG suggest that we can recover some relevant connectivity patterns from MEG. However, since these correlations are moderate to low and vary across different metrics, the choice of metrics is important and the results of MEG connectivity should be interpreted with caution.

For connectivity metrics that do not remove zero-lag connectivity (*AEC/PLV*), moderate but significant cross-modal correlations (~ 0.25 to 0.45) between MEG and iEEG were found in all frequency bands. For connectivity metrics that corrected/removed the zero-lag connectivity, the cross-modal correlations decreased. When compared to the empirical null distribution of cross-modal correlation, the resulting correlations were found significant in alpha and beta bands for *OAEC*. For *wPLI**, although the correlations were low (~ 0.15 to 0.25), they were statistically significant in all frequency bands. Overall, we observed the highest cross-modal correlation in the beta band for *AEC*, *OAEC*, and *PLV*.

Previous studies suggested that intrinsic networks estimated by MEG show the strongest correlation with fMRI-derived networks in the alpha and beta bands estimated by amplitude envelope correlation (Brookes et al., 2011). They proposed that the frequency of the amplitude envelope in these bands might better match slower fMRI signal fluctuations. Similarly, Wirsich et al. (2020) estimated the cross-modal correlation between simultaneous fMRI and EEG connectome generated using imaginary coherence (Nolte et al., 2004) and reported similar cross-modal correlations as those we obtained (~ 0.29 - 0.36), with the highest correlations also found in the beta band. They found consistent results with multiple datasets using imaginary coherence (Wirsich et al., 2020; Wirsich et al., 2017) and across different MRI systems using *AEC/OAEC* and imaginary coherence (Wirsich et al., 2021). In Wirsich et al. (2021), the cross-modal correlations between fMRI and EEG connectivity using *OAEC* were lower compared to *AEC*, which is consistent with our findings.

In contrast to the studies mentioned above, where two modalities were compared across various frequency bands, Shafiei et al. (2022) adopted a different approach to compare fMRI and MEG-derived connectivity using OAEC. They illustrated that MEG oscillations across multiple bands might combine to give rise to the fMRI functional networks. They reported that while all frequency bands contribute to forming fMRI networks, beta band connectivity made the largest contribution, followed by theta and alpha connectivity. This was consistent with previous studies (Matthew J. Brookes et al., 2011; Deligianni et al., 2014; Sadaghiani et al., 2022) suggesting that the frequency of the slower oscillation (i.e. extracted from the envelope of the alpha/beta oscillations) would be more similar to the fMRI fluctuations.

Unlike those studies, which compared hemodynamic correlations measured with fMRI with EEG/MEG connectivities, known to capture different brain mechanisms at varying time scales, we aimed to compare two modalities, iEEG and MEG, capturing essentially the same brain dynamics at the same time scale. For this reason, it is surprising that the cross-modal correlations between MEG and iEEG were in a similar range as, and not higher than those observed in studies comparing fMRI with EEG/MEG. The reasons for the frequency-specific cross-modal similarities, as well as why correlations in the beta band were higher than in other bands, remain unclear and pose important questions for future studies.

However, it is interesting to observe higher cross-modal correlations between MEG and iEEG for *AEC*, *OAEC*, and *PLV* when we increase the number of subjects to average in each ROI pair to construct the connectome, but at the cost of reducing overall connectome coverage. For instance, when we ensured at least 3 subjects in each ROI pair to construct the connectome, the cross-modal correlations between MEG and iEEG for *AEC*, *PLV* and *OAEC* were 0.6, 0.6, and 0.45 (Figure 8-8, Fig S8, S9), respectively, compared to 0.37, 0.36, and 0.26 (Figure 8-3, Figure 8-5), values found when we used at least one subject for each ROI pair. However, even if we found larger cross-modal correlations when averaging more subjects, we could hardly consider this a comprehensive connectome because it covered only 10% of the entire connectome. Thus, we chose to use at least one subject to create the connectome, which maximized connectome coverage (44%). More surprisingly, *wPLI** did not follow this trend.

Increasing the minimum number of subjects to create the connectome likely removes noisy connections contributed by single subjects. In another study using simultaneous EEG-fMRI

(Wirsich et al., 2021), the authors compared cross-modal correlations between EEG and fMRI. Although the data were simultaneous, the cross-modal correlation between EEG and fMRI for individual subjects was very low across all frequency bands. They found moderate cross-modal correlations (~ 0.3 to 0.4) when averaging at least 7-12 subjects. This finding is interesting, and we expect that cross-modal correlations between MEG and iEEG connectomes could similarly benefit from averaging more subjects to reduce noisy connections. However, drawing such conclusions from our iEEG data is challenging, as increasing the number of subjects in each ROI pair drastically decreases the coverage of the iEEG connectome. We would require more subjects in the iEEG atlas to fully assess this. Nevertheless, our results suggest that cross-modal correlations between MEG and iEEG connectomes may increase when the iEEG connectome includes more subjects in each ROI pair.

8.6.2 Compromise between removing spurious connectivity and genuine zero-lag connectivity

The issue of source leakage or volume conduction in EEG/MEG connectivity, as well as the search for the best connectivity metric, has been a topic of discussion for the past few years. Several studies reported the source leakage issue involved with EEG/MEG-derived connectivity and recommended to use connectivity metrics that remove zero-lag connections for obtaining interpretable results (Hipp et al., 2012; Palva & Palva, 2012; Schoffelen & Gross, 2009). Garcés et al. (2016) investigated the test-retest reliability of MEG resting-state functional connectivity for *PLV*, *PLI*, *AEC*, and *OAEC* by evaluating the within- and between-subject variability using the intraclass correlation coefficient. They found higher reliability for *PLV* across theta to gamma bands and for *OAEC* and *AEC* in the beta band. They suggested that volume conduction effects could contribute to high reliability for *PLV* and *AEC*. Rizkallah et al. (2020) compared resting-state EEG/MEG connectomes with fMRI-derived connectomes and reported significant correlations (but very low) between EEG/MEG connectomes and fMRI connectomes for *AEC* and *PLV*, whereas metrics that remove zero-lag connectivity exhibited no significant spatial cross-modal correlations. Finger et al. (2016) proposed a computational model and structural data from diffusion MRI tractography to simulate functional connectivity in the alpha band and compared it with empirical EEG functional connectivity for six connectivity metrics. They found high correlations between simulated and empirical functional connectivity for *PLV* and coherence

(~0.6), whereas the other metrics that remove zero-lag connectivity including *PLI* and *wPLI* exhibited low correlations (~0.18). While they did not rule out the possibility that the high correlation found for *PLV* and coherence could be influenced by volume conduction, they questioned the use of metrics that remove zero-lag connectivity, as they might eliminate genuine neural synchrony mainly driven by the underlying anatomical structure.

Unlike previous studies that attempted to address this issue either through simulations or by comparing modalities known to detect different brain mechanisms at varying time scales, such as EEG/MEG with fMRI, we compared the MEG connectome with the iEEG connectome, both of which record similar brain activity. When compared to the iEEG connectome, we observed moderate correlations between the MEG connectome and iEEG connectome for *AEC* and *PLV*. The comparison of raw connectivity values revealed that MEG exhibited higher connectivity than iEEG across all frequency bands, confirming the inflated connectivity associated with EEG/MEG source leakage and volume conduction. However, for *OAEC* and *wPLI**, metrics that remove or correct zero-lag connectivity (recommended to avoid spurious connectivity), although the raw connectivity values were found more similar for both modalities (Figure 8-2), the spatial correlations between MEG and iEEG connectomes decreased (Figs 8-3,8-5). In addition, the quantification of the difference between *AEC* and *OAEC* for MEG versus iEEG provided a clear representation that MEG indeed exhibits more zero-lag connections compared to iEEG, consistently observed across all frequency bands (Fig 8-7, Fig S6).

Thus the question of which metric is best for EEG/MEG connectivity analysis remains difficult to answer. The choice of metric should depend on the research question. Based on our findings, for resting-state connectivity analysis at the connectome level, it may be important to use metrics that preserve zero-lag connections. If the study necessitates removing volume conduction, *OAEC* could be a good compromise as it corrects for zero-lag connectivity and also shows significant correlations between MEG and iEEG in the alpha and beta bands. Moreover, the cross-modal correlations for *OAEC* increased when we increased the minimum number of subjects to create the iEEG connectome, a trend also observed for *AEC* and *PLV*. For *wPLI**, we found significantly higher cross-modal correlations in all frequency bands, which were consistently significant when only superficial ROIs were included. However, *wPLI** for deep ROI pairs showed very low and statistically non significant correlations in all frequency bands. The number of subjects averaged

in each ROI pair also did not affect $wPLI^*$ results, unlike what was observed for AEC , $OAEC$, and PLV (Fig S8, S9). Unlike AEC , $OAEC$, and PLV , the $wPLI^*$ metric was also not affected by the distance between the two ROIs (Fig S7). Furthermore, it remains unclear why there was asymmetry in cross-modal correlations computed for left, right, and inter-hemispheric connectomes using $wPLI^*$. These surprising trends reported using $wPLI^*$ should be further investigated and this metric should therefore be considered with caution. Carefully assessing the reliability of $wPLI^*$ but also other metrics, using test/retest reliability (Garcés et al., 2016) could be very important but this was out of the scope of present study. It is important to note that we only considered the phase information to calculate the $wPLI^*$. When analyzed with the original definition, which includes the amplitude information of Hilbert, the cross-modal correlations were very low (clearly lower than $wPLI^*$ results) and not significant in any frequency band, suggesting some instabilities when considered this family of metric.

8.6.3 Cross-modal correlations for deep versus superficial ROIs

The raw connectivity values for superficial versus deep ROIs had similar distributions for both iEEG and MEG. However, the correlations between MEG and iEEG connectomes for superficial ROIs were higher than for deep ROIs. This is not surprising because detecting and localizing deep subcortical sources by EEG/MEG is challenging for several reasons, such as the rapid attenuation of signals generated from deep structures with the distance of the generator from the EEG/MEG sensors, a phenomenon more pronounced for MEG when considering gradiometers (Barkley & Baumgartner, 2003; Malmivuo & Plonsey, 1995). The spatial configuration of the deep/subcortical structures also results in signal cancellation (Lorente De Nó, 1947; Murakami & Okada, 2006) and are difficult to detect by distant sensors. In Afnan et al. (2024), we proposed a depth weighting parameter in MEM methods that significantly improved EEG/MEG localization from deep sources. In this study, we used the depth weighted wMEM proposed in Afnan et al. (2024). Although depth weighting in the source imaging methods can improve localization accuracy from deep generators (Lin et al., 2006), these are often associated with large localization errors compared to superficial sources (Pascarella et al., 2023; Unnwongse et al., 2023). Interestingly, we found that the decrease in correlations between MEG and iEEG for deep ROIs was more pronounced in phase-based metrics than in amplitude-based metrics. This could be because AEC is estimated from the signal envelope, which is associated with synchronization over a larger scale,

resulting in a higher SNR and reduced sensitivity to noise (Matthew J Brookes et al., 2011). *PLV* and *wPLI**, on the other hand, rely on instantaneous phases and are linked to local synchrony. Phase-based measures could be more sensitive to noise and would therefore be more difficult to estimate from resting-state and deep sources using EEG/MEG source imaging. The assessment of phase and amplitude-based connectivity for superficial versus deep sources could be investigated in future studies and was beyond the scope of the current study. For the deep ROIs estimated by *wPLI**, the cross-modal correlations between MEG and iEEG were very low and not statistically significant in any frequency bands. The reason why *wPLI** estimations from deep sources were more affected than *PLV* was not clear. We repeated this analysis using another source imaging method (minimum norm estimate) and found a similar trend (result not shown). Comparison with minimum norm estimate was to check whether the choice of the source imaging method, wMEM, had influenced the results.

8.6.4 Limitations

One limitation of this study is that the connectome available from the iEEG atlas covered only 44% of the whole brain. Despite not encompassing the entire brain, this approach represents the best means available to validate EEG/MEG-derived connectomes. Further validation could be considered with simultaneous EEG/MEG and iEEG recordings, although this can only provide even more limited spatial coverage unless it can be done on a large number of subjects. Another limitation is that we utilized a regularization parameter in wMEM which was optimized for source estimation. The spatial prior model used in wMEM initializes each parcel using the MNE energy of the sources, and therefore would be influenced by MNE regularization (Afnan et al., 2023). Through extensive MEG simulations, Vallarino et al. (2023) demonstrated that the regularization optimal for MEG source estimation was suboptimal for connectivity estimation. They showed an increased risk of being affected by spurious connections when using the regularization optimized for source estimation. Their findings suggested the need for less regularization to mitigate false positives. It may be necessary to reduce the regularization to improve the estimation of connectivity, a topic we plan to explore in future research. Additionally, since the study was conducted using simplistic simulated data, investigating how regularization could impact connectivity measures in the context of our multimodal real MEG/iEEG data could be valuable.

Another limitation is that the iEEG atlas, which is developed using iEEG channels from healthy brain regions, is still derived from patients with epilepsy. Studies using fMRI, EEG/MEG, and iEEG suggest that seizures or interictal epileptic activity can affect brain network properties even in regions distant from the epileptic focus (Aydin et al., 2020; DeSalvo et al., 2014; Lee et al., 2018; Taylor et al., 2022; van Diessen et al., 2013). However, this limitation is unavoidable since iEEG data are never collected from healthy subjects. Also, while regions may exhibit abnormalities in iEEG, these are unlikely to be consistent across patients as these are caused by the specific epileptic focus. Increasing the number of subjects/patients in each ROI pair (as illustrated in Fig 8-8, S7, and S8) could mitigate these effects, potentially explaining the increased cross-modal correlations between MEG and iEEG when averaging more subjects.

Our goal was to validate the assessment of functional connectivity of normal brain activity using healthy MEG data. Currently, the iEEG atlas of normal brain activity (i.e. using iEEG channels exhibiting no epileptic activity) provides the best available ground truth for such validation with global brain coverage. One could argue that a more comparable MEG cohort would be a group of patients with epilepsy, excluding pathological regions as done in the iEEG atlas. However, excluding pathological regions from MEG would imply that we already trust MEG source imaging to identify these regions, which would make our validation objective redundant. The ideal dataset for this validation would be to consider challenging simultaneous iEEG and MEG recordings (Pizzo et al., 2019), but from a large group of patients, allowing for whole-brain coverage. However, such data are not yet available.

Another limitation of this study is that the distribution of patients' ages in the iEEG atlas (31 ± 10 years, range: 13-62 years) was wider than that of the MEG dataset (28.67 ± 4.13 years, range: 20-38 years). We also acknowledge that the male-female ratio was balanced in the iEEG dataset (F: 56, M: 54), whereas there were more females than males in our MEG dataset (F: 35, M: 10). Age and sex could influence resting-state oscillation properties (Hoshi & Shigihara, 2020; Schäfer et al., 2014). However, these effects are small (Hoshi & Shigihara, 2020), and given that the healthy subjects covered the range between the 25th (25 years) and 75th (40 years) percentiles of the patients' age distribution, we believe our results to be minimally biased by age. Moreover, the effects of male-female differences were found to be less pronounced in eyes-closed conditions compared to eyes-open conditions (Hoshi & Shigihara, 2020), as this was the case for our study.

For the comparisons between metrics such as AEC versus orthogonalized AEC and PLV versus wPLI, both metrics are likely to be influenced by the same factors (age/sex), so we believe this should not bias our comparisons between metrics at the group level.

8.7 Conclusions

This is the first validation of the MEG-derived connectome with the iEEG connectome at a group level. Based on the moderate spatial correlations between the two modalities, we can conclude that they share some commonalities. Differences in correlations estimated from different metrics may suggest that these metrics capture different/complementary aspects of brain activity. Moderate correlations were found between MEG and iEEG connectomes for metrics that include zero-lag connectivity. For metrics that removed or corrected zero-lag connectivity, the cross-modal correlations between MEG and iEEG decreased. This suggests that although correction of zero-lag connections may help in removing false connectivity related to volume conduction, it also removes true connections, as reflected in the overall decrease in cross-modal correlation between MEG and iEEG. In addition, a higher prevalence of zero-lag connectivity in MEG compared to iEEG was quantitatively presented.

8.8 Acknowledgment

This work was supported by Natural Sciences and Engineering Research Council of Canada (NSERC) Discovery grant, grant from Canadian Institutes of Health Research (CIHR) (PJT-159448 and FDN 143208), and the Fonds de recherche du Québec—Nature et technologies (FRQNT) Research team grant. JA was partially supported by The Canadian Open Neuroscience Platform scholarship, Irma Bauer Fellowship, Faculty of Medicine and Health Sciences, McGill University, and Fonds de Recherche du Québec—Santé Doctoral scholarship. GP and AG were supported by the Italian Ministry of Health (GR-2019-12368960 and GR-2018-12366092). BF was supported by CIHR project grant (PJT-175056), salary award (Chercheur-boursier clinicien Senior) of the Fonds de Recherche du Québec – Santé.

9 Manuscript 4: Validating MEG source imaging of oscillations and connectivity using simultaneous MEG-intracerebral EEG

9.1 Preface

In Studies 1 and 3, we validated MEG source localization of resting-state oscillations and connectivity in healthy participants using an intracranial EEG atlas of normal brain activity. Since the groups in Studies 1 and 3 were drawn from different populations—healthy individuals and patients with epilepsy— and since the MEG and intracranial EEG recordings were obviously not performed simultaneously, there were some uncertainties in interpreting the differences between the two modalities. Additionally, across all three studies (1, 2, and 3), we also observed that EEG/MEG source localization of deep brain activity remains challenging, despite some significant improvement after applying depth weighting within the MEM and adding surface segmentation of bilateral hippocampi in the MEG source space.

In this final study, we considered simultaneous intracerebral EEG and MEG data acquired from five patients with epilepsy. Our overall objective was to validate at the single subject level, our group-level findings reported in Studies 1 (Chapter 6) and 3 (Chapter 8) and to further assess the ability of MEG source imaging to accurately estimate deep brain activity in the resting state, using the methodology proposed in Study 2 (Chapter 7). Access to these unique data was provided by our collaborators, the team of Dr. Christian Benar at Aix-Marseille University, France (Pizzo et al., 2019). Using resting state segments which did not feature any spontaneous epileptic discharges, we applied the same methodology proposed in Studies 1 and 3 to assess MEG's ability to recover oscillatory and connectivity patterns when compared to intracranial EEG findings. This chapter includes the following sections: abstract, introduction, materials and methods, results, and discussion. The manuscript is currently under preparation.

Afnan, J; Fratello, M.; Bonini, F.; Medina, S.; Cai, Z.; Badier, J.M.; Bartolomei, F.; Gotman, J.; Benar, C.; Grova, C., “Validating MEG source imaging of oscillations and connectivity patterns using simultaneous MEG-intracranial EEG” in preparation.

9.2 Abstract

Due to the ill-posed nature of EEG/MEG source imaging, the accuracy of EEG/MEG estimated sources requires validation, before considering localization of epileptic discharges and resting-state analysis for clinical applications. We previously validated MEG source imaging with an intracranial EEG atlas of physiological brain activity at a group level in terms of resting-state oscillations and connectivity. In this study, we aimed to validate MEG source imaging of resting-state activity at a single-subject level using simultaneous MEG and stereotaxic EEG (SEEG).

We considered simultaneous MEG and SEEG acquired from 5 patients with epilepsy. For each patient, a 1-min segment of data featuring resting state oscillations in a dominant frequency band was marked in MEG, where no artifact or epileptic discharge was visible. The MEG source imaging inverse problem was solved using wavelet Maximum Entropy on the Mean method. To quantitatively compare MEM results estimated along the cortical surface with SEEG, we projected MEG sources at each SEEG channel position using an SEEG forward model. We computed the relative power for MEG and SEEG data for each channel. The spatial correlation between the two modalities was calculated for the average relative power in the frequency band of interest. For connectivity analysis, we computed pairwise connectivity using Amplitude Envelope Correlation (AEC), orthogonalized AEC (OAEC), Phase Locking Value (PLV) and Weighted Phase Lag Index (wPLI). We compared the spatial correlation between MEG and SEEG connectomes for each metric.

For the 5 patients, when assessing the power of oscillatory patterns, the cross-modal correlations between SEEG and MEG estimates for average relative power was 0.31 ± 0.18 . When the correlation was computed for superficial and deep channels based on an eccentricity threshold of 60 mm (a measure of source depth, with low values indicating deep channels), the cross-modal correlation was 0.42 ± 0.25 for superficial and 0.12 ± 0.22 for deep channels. For functional connectivity, we found moderate correlations between MEG and SEEG connectomes for AEC (0.25 ± 0.06), OAEC (0.23 ± 0.04) and PLV (0.16 ± 0.07). For wPLI, the correlations between MEG

and SEEG connectomes were close to null or negative, indicating that the MEG-estimated connectome was inaccurate.

MEG retrieved oscillatory and connectivity patterns when compared to SEEG, although less accurately for deep activity. For connectivity, the decrease in cross-modal correlations found by the metrics corrected for zero-lag connectivity highlights a trade-off: although MEG may capture erroneous connectivity due to source leakage, removing zero-lag connectivity also eliminates true connections, leading to a decrease in cross-modal correlation. Our study suggests that MEG could still accurately estimate connectomes using the amplitude-based metric OAEC, but connectomes estimated using wPLI were inaccurate.

9.3 Introduction

Electro-/Magneto-EncephaloGraphy (EEG/MEG) are widely used non-invasive electrophysiological methods to measure neuronal activity in healthy subjects (Giraud and Poeppel (2012); (Pellegrino et al., 2021; Voytek et al., 2010; Wang, 2010) and pathological conditions (Buzsáki et al., 2013; Hirano & Uhlhaas, 2021; Schnitzler & Gross, 2005b). The high temporal resolution of EEG/MEG allows us to study brain activity in well-controlled tasks or spontaneous abnormal discharges in epilepsy (Dalal et al., 2013; Hamandi et al., 2016; Pellegrino et al., 2018; von Ellenrieder et al., 2016) as well as during the resting state, a state when the brain activity is spontaneous (thinking of nothing/not performing any task) (Matthew J. Brookes et al., 2011; Hipp et al., 2012; Keitel & Gross, 2016; Mellem et al., 2017; Wirsich et al., 2020). However, EEG/MEG has limited spatial resolution because it involves scalp recordings, and estimating the neuronal generators from these recordings (called source imaging) requires solving an ill-posed inverse problem (Darvas et al., 2004b). Localizing deep generators using EEG/MEG is more challenging because signals originating from these sources are often associated with low signal-to-noise ratio (SNR) data at the surface, due to the distance and the spatial configuration of subcortical structures (Attal & Schwartz, 2013). EEG/MEG source imaging is also affected by source leakage, defined as the influence of a source on the estimation of the generators within its neighborhood (Brookes et al., 2012; Hedrich et al., 2017). Source leakage introduces spurious false positives in EEG/MEG-derived connectivity measures. It also leads to false negatives in connectivity measures that are insensitive to true near-zero-lag synchronization (Palva et al., 2018; Palva & Palva, 2012). Thus, the validation of EEG/MEG source imaging is important when interpreting results from deep brain

structures and resting-state activity, as both cases are associated with low SNR data. This is especially critical in clinical applications, such as pre-surgical planning for epilepsy.

Due to the frequent lack of ground truth, validation of EEG/MEG source imaging techniques often relies on simulations. Realistic simulations have been useful in contexts such as validating source imaging for epileptic discharges (Becker et al., 2015; Chowdhury et al., 2016; Chowdhury et al., 2013; Grova et al., 2006) and in connectivity studies (Brkić et al., 2023; Palva et al., 2018; Vallarino et al., 2023). Neuronal computational models, that consider combined biophysical/physiological generative models to simulate realistic data are also useful for validating the performance of source imaging methods (Badier et al., 2007; Chowdhury et al., 2016; Wendling, 2005). However, generating realistic simulations of brain activity is difficult. Whereas simulations of pathological discharges mimicking epileptic discharges are more and more realistic (Cosandier-Rimélé et al., 2007; Cosandier-Rimélé et al., 2008), and it becomes even more difficult when considering background resting-state activity. Few studies have used functional MRI (fMRI) to compare with EEG/MEG-derived connectivity (Matthew J Brookes et al., 2011; Wirsich et al., 2020; Wirsich et al., 2021; Wirsich et al., 2017). Whereas assessing such multimodal concordance is interesting at a global level, these modalities capture different underlying brain mechanisms (electrophysiology in EEG/MEG versus slow hemodynamic activity in fMRI) and thus direct comparisons are impossible, since one-to-one local correspondence could not be expected.

The gold standard for validating EEG/MEG source imaging is intracerebral EEG or stereotaxic EEG (SEEG), an invasive technique commonly used in the presurgical evaluation of epilepsy. SEEG can record brain activity directly from brain tissue, including deep structures, with high SNR and high spatial and temporal resolution (Bartolomei et al., 2018; Lagarde et al., 2022). SEEG measurements are also negligibly affected by volume conduction (Arnulfo et al., 2015; O'Reilly & Elsabbagh, 2021). However, SEEG requires a surgical procedure to implant the electrodes and has limited spatial coverage. Normative atlases of intracranial EEG (iEEG) (Bernabei et al., 2022; Frauscher et al., 2018; Taylor et al., 2022) have been developed by pooling iEEG data from patients, but only including channels that were implanted in presumably healthy regions. Such atlases provide a unique opportunity to validate EEG/MEG source imaging at a group level. We previously leveraged the atlas of normal iEEG developed at the Montreal Neurological Institute (Frauscher et al., 2018) to validate MEG source imaging of resting-state oscillations and

connectivity patterns for a group of healthy subjects (Afnan et al., in press; Afnan et al., 2023). Although the normative iEEG atlas provided an excellent way to validate MEG source imaging at a whole-brain level, several limitations were unavoidable, such as the heterogeneity of iEEG sampling across the brain, variability in the number of channels contributed by different patients, and the non-simultaneity of the MEG and SEEG recordings (Afnan et al., 2023).

Simultaneous recording of EEG/MEG and SEEG provides the most reliable validation for EEG/MEG (Badier et al., 2017b; De Stefano et al., 2022; Koessler et al., 2010; Pigorini et al., 2024; Pizzo et al., 2019), although limited to the implanted brain regions. SEEG has been used to determine the detectability of epileptic abnormalities by simultaneously acquired scalp EEG/MEG (Cosandier-Rim    et al., 2012; Dubarry et al., 2014; Koessler et al., 2015; Merlet & Gotman, 1999; Ramantani et al., 2016). Using simultaneously acquired SEEG, two recent studies provided evidence of detectability from deep subcortical structures by high-density EEG (Seeber et al., 2019) and MEG (Pizzo et al., 2019). However, studies using simultaneous EEG/MEG and SEEG to investigate resting-state oscillations are very few (Hnazaee et al., 2020; Seeber et al., 2019), and connectivity was not investigated. To fill this gap, we aimed to validate MEG source imaging of resting-state oscillations and connectivity patterns by comparing them with simultaneously acquired SEEG as the ground truth in five patients with epilepsy.

9.4 Materials and methods

9.4.1 Experimental design

The analysis pipeline is summarized in Figure 9-1. Simultaneous MEG and SEEG acquired in 5 patients were considered (section 9.4.2). 60 seconds of resting period without artefact or epileptic discharge was marked in MEG by the epileptologist F. P; the predominant frequency band of that resting state section was also determined visually. Using the marker identified in MEG, we obtained the 60 seconds from simultaneously acquired SEEG. To solve the MEG inverse problem, we used the wavelet MEM (wMEM) method (Lina et al., 2012) that we recently adapted for resting state localization (Afnan et al., 2023) (section 9.4.6). The reconstructed MEG source map along the cortical surface was then projected to the positions of SEEG channels to generate virtual SEEG potentials using a method proposed by Grova et al. (2016) (section 9.4.7), using an SEEG forward model to link MEG sources and virtual SEEG potentials. This conversion allows a quantitative

comparison of MEG-estimated virtual SEEG and actual SEEG (Abdallah et al., 2022). Finally, we compared the relative oscillatory power (section 9.4.8) and connectivity patterns (section 9.4.9) between the two modalities in the frequency band dominant for the section.

9.4.2 Simultaneous SEEG-MEG data

Simultaneous MEG and SEEG were recorded at the Epileptology and Cerebral Rhythmology Unit of the Timone Hospital (Assistance Publique Hôpitaux de Marseille, APHM) in Marseille, France and provided by our collaborators (team of Drs. F. Bartolomei / C.G. Bénar). Technical setup of these challenging simultaneous MEG/SEEG recordings was described in previous publication from the group of Dr. Bénar (Badier et al., 2017; Dubarry et al., 2014; Pizzo et al., 2019). MEG was acquired using a 4D Neuroimaging™ 3600 whole-head system (248 magnetometers) at a sampling rate of 2034.51 Hz. The patients were lying down. They were instructed to be relaxed with their eyes closed. Simultaneous SEEG was recorded on 256 channels (256 channel BrainAmp, Brain Products GmbH, Munich, Germany), sampled at 1024 Hz. SEEG electrodes were implanted based on clinical hypotheses.

Experimental design

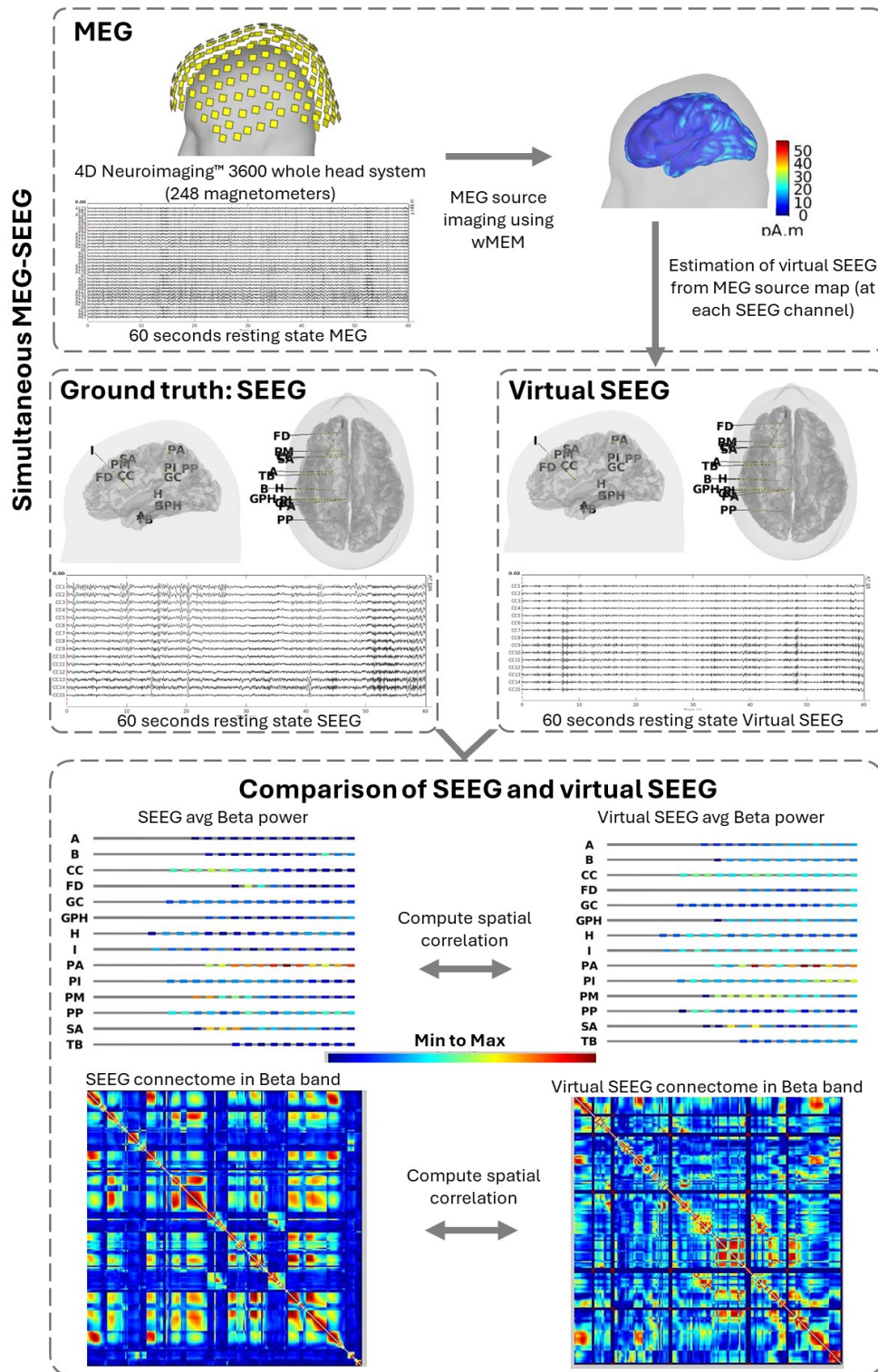


Figure 9-1 Analysis pipeline to compare the spectral and connectivity patterns estimated by MEG with the simultaneously acquired SEEG, as ground truth. MEG: 60 s of resting state data during wakefulness were

marked in MEG in a dominant frequency band. Using the marking from MEG, 60 s data were obtained from the simultaneously acquired SEEG, which is considered the ground truth. Virtual SEEG: The MEG source map, obtained with wMEM, was converted to virtual SEEG potentials for each SEEG channel. Comparison between virtual SEEG and SEEG: The virtual SEEG estimated from MEG were quantitatively compared with SEEG in terms of power spectral density and connectivity. For each SEEG and virtual SEEG channel, the relative power spectral density was computed and averaged across all the frequency bins within the dominant canonical frequency band. The spatial correlation between the SEEG and virtual SEEG relative power was computed. The spatial correlation between the SEEG and virtual SEEG connectomes was computed.

9.4.3 SEEG contact localization

Each patient underwent a pre-operative T1-weighted MRI on a 3T MRI system. Additionally, pre-implantation MRI and post-implantation CT scan were performed. The post-implantation CT scan was co-registered with the pre-implantation anatomical MRI to obtain the exact locations of the SEEG channels in each patient's individual MRI. Brain segmentation and reconstruction of the white/gray matter interface for the cortex were obtained using recon-all from FreeSurfer software package (Dale et al., 1999). Co-registration of anatomical MRI with post-implantation CT images was performed and the locations of the SEEG channels were estimated in patient-specific MRI space using GARDEL software (<https://meg.univ-amu.fr/wiki/GARDEL:presentation>) (Pizzo et al., 2019). The subsequent analysis for MEG source imaging and comparison between MEG and SEEG was performed in Brainstorm software (Tadel et al., 2011).

9.4.4 MEG Source space and forward model estimation

The coregistration of MEG sensors with anatomical MRI and analysis for creating the source model and forward model were performed in Brainstorm using the reconstructed cortical and subcortical surfaces using FreeSurfer, following the methodology described in (Afnan et al., 2024). The cortical mesh of the middle layer (white/gray matter interface), equidistant between the white matter and pial surfaces was considered as the source space. Additionally, the two hippocampi from the subcortical structures were also included in the source space. For the cortex and hippocampus, dipolar sources were placed along the surface of the structures with a fixed orientation orthogonal to the surface at each point. The cortical and hippocampal surfaces were combined and downsampled to reach a total ~8,000 vertices. The forward model was computed

using OpenMEEG software (Gramfort et al., 2010; Kybic et al., 2005) implemented in Brainstorm. We used a 3-layer Boundary Element model (BEM) consisting of brain, skull, and scalp surfaces with conductivity values of 0.33, 0.0165, and 0.33 S m⁻¹ (Zhang et al., 2006).

9.4.5 MEG and SEEG data preprocessing

Data preprocessing was performed with Brainstorm. Preprocessing included (i) online correction based on reference channels for MEG; (ii) filtering within the 0.5-80 Hz band, (iii) applying a notch filter at 50 Hz, and (iv) downsampling to 200 Hz.

9.4.6 MEG source imaging using wavelet Maximum Entropy on the Mean (wMEM)

The MEG inverse problem was solved using the Maximum Entropy on the Mean (MEM) framework (Amblard et al., 2004), a Bayesian approach validated in the context of EEG/MEG source imaging (Chowdhury et al., 2013). Wavelet MEM (wMEM) is a variant of the MEM method specifically designed to localize brain oscillatory patterns (Afnan et al., 2023; Amblard et al., 2004; Lina et al., 2012). wMEM applies a discrete wavelet transformation (Daubechies wavelets) to characterize the oscillatory patterns in the data before applying the MEM solver for source imaging (Lina et al., 2012). We proposed and implemented several changes in standard wMEM to localize specifically oscillatory patterns in the resting state (details in Afnan et al. (2023)), and evaluated the accuracy of reconstructions with the iEEG atlas (Afnan et al., 2023). In the current study, we used the wMEM version we proposed in Afnan et al. (2023) adding the depth weighting parameter we proposed and validated in Afnan et al. (2024) to localize deep brain activity more accurately. Since there does not exist a clear baseline when localizing resting state data, to estimate a noise-covariance model from resting state data, we created a quasi-synthetic baseline from the signal of interest to compute the noise covariance by randomly shuffling the Fourier phase at each frequency (Prichard & Theiler, 1994). We employed a sliding window approach (window length: 1 second) to generate the baseline, ensuring a more precise estimation of the noise covariance matrix for each wavelet sample across the time scales (Afnan et al., 2023). wMEM implementation is available within the *BES*t plugin of Brainstorm software (<https://neuroimage.usc.edu/brainstorm/Tutorials/TutBES/>).

9.4.7 Estimation of virtual SEEG data from the MEG source map

To compare MEG-estimated results with SEEG quantitatively, we converted MEG-reconstructed source maps (in nanoAmpere-meters) into SEEG channel space by estimating corresponding electrical potentials (μ Volts) for each SEEG channel of a patient (Abdallah et al., 2022; Grova et al., 2016). More details about this conversion method can be found in Grova et al. (2016). For each patient, to estimate the virtual SEEG potentials from MEG estimated current density along the cortical surface, $\mathbf{j}_{wMEM}(t)$, we calculated a patient-specific SEEG forward model, G_{SEEG} that estimates the influence of each dipolar source of the cortical surface on each SEEG channel. To do so, our proposed SEEG forward model G_{SEEG} assumes an infinite volume conductor characterized by a conductivity σ of 0.25 S.m^{-1} (Cosandier-Rim    et al., 2008). For each patient, for a total number of SEEG contacts c , and n number of cortical sources ($n = 8000$), G_{SEEG} is a $c \times n$ matrix that estimates the electrical potential at each SEEG channel i ($i = 1, 2 \dots c$) corresponding to an equivalent current dipole of unit activity located on the vertex S_j and oriented along \vec{n}_j , normal to the cortical surface, calculated as:

$$G_{SEEG}(i, j) = \frac{\vec{n}_j \cdot \vec{u}_{ij}}{4\pi\sigma r_{ij}^2} \quad (1)$$

where \vec{u}_{ij} is a unit vector oriented from the source S_j to the SEEG channel i and r_{ij} is the Euclidean distance between S_j and contact i . To avoid numerical instabilities, when the sources on the cortical surface were too close to the SEEG contacts ($r_{ij} < 3 \text{ mm}$), the distance r_{ij} was set to 3 mm instead, keeping the orientation (Grova et al., 2016). Finally, we applied this SEEG forward model, G_{SEEG} to the MEG reconstructed source map ($\mathbf{j}_{wMEM}(t)$) to estimate virtual SEEG potentials on each SEEG channel, V_{SEEG} as:

$$V_{SEEG}(t) = G_{SEEG} \mathbf{j}_{wMEM}(t) \quad (2)$$

9.4.8 Frequency specific relative power

For each SEEG and MEG estimated virtual SEEG channel, the power spectral density was estimated using Welch's method (time duration: 0-60 s, 2 s sliding Hamming windows, overlap: 50%). For each channel, the relative power spectral density was obtained by dividing the power at each frequency bin by the total power across the whole frequency range. Within the dominant frequency band marked for each patient, we averaged the relative power across all frequency bins

within that band. The dominant frequency bands were selected as follows: Patient #1: Beta (13-30 Hz), Patient #2 and #3: Alpha (8-13 Hz), and Patient #4 and #5: Theta (4-8 Hz).

9.4.9 Connectivity metrics

For SEEG and virtual SEEG estimated from MEG, connectivity between each channel pair was computed using amplitude envelope correlation (*AEC*) (Matthew J Brookes et al., 2011), phase locking value (*PLV*) (Mormann et al., 2000), orthogonalized AEC (*OAEC*) (Hipp et al., 2012) and a modified version of the weighted phase lag index (*wPLI*) (Vinck et al., 2011) considering only the phase information, as we proposed in (Afnan et al., in press). The details formulations are described in more detail in (Afnan et al., in press).

9.4.10 Cross-modal spatial correlation between MEG and SEEG results

We computed the spatial Pearson correlation between the SEEG and virtual SEEG estimated from MEG in terms of (i) the average power map for the selected dominant frequency band and (ii) connectome created using the four connectivity metrics. To statistically assess the significance of cross-modal correlations, we also generated 5,000 cross-modal correlation values to build an empirical null distribution. To do so, we permuted randomly the anatomical labels of the channel pairs in the MEG, therefore effectively destroying the underlying spatial correlation structure. Then, we calculated the Pearson correlation between the SEEG and the spatially permuted MEG, creating an empirical null distribution from those 5000 correlation values. We defined a range for the null distribution which included 95% of the distribution centered around the median of the null. A cross-modal (MEG-SEEG) correlation was considered significant if the actual correlation was positive and higher than the null range.

9.5 Results

We will present the results from each patient individually in their dominant frequency band. We will then summarize the common trends in the results. We need to be careful when interpreting the results from all five patients together due to the differences in their dominant frequency bands. For the result and discussion sections, we will now use the term ‘MEG’ instead of ‘virtual SEEG estimated for MEG’ for simplification wording purposes.

9.5.1 Relative power spectral density

Figure 9-2A shows the qualitative comparison of average relative power estimated by MEG and SEEG for each channel in patient #1 in the β band (13-30Hz). The quantitative representation of these values is shown in Figure 9-2B, suggesting a clear linear relationship between the relative power of all SEEG contacts as of function of all MEG virtual contacts. The spatial correlation between the two modalities was 0.54, significantly larger than the null distribution (Figure 9-2C).

Patient #1 Comparison of relative Beta power between MEG and SEEG

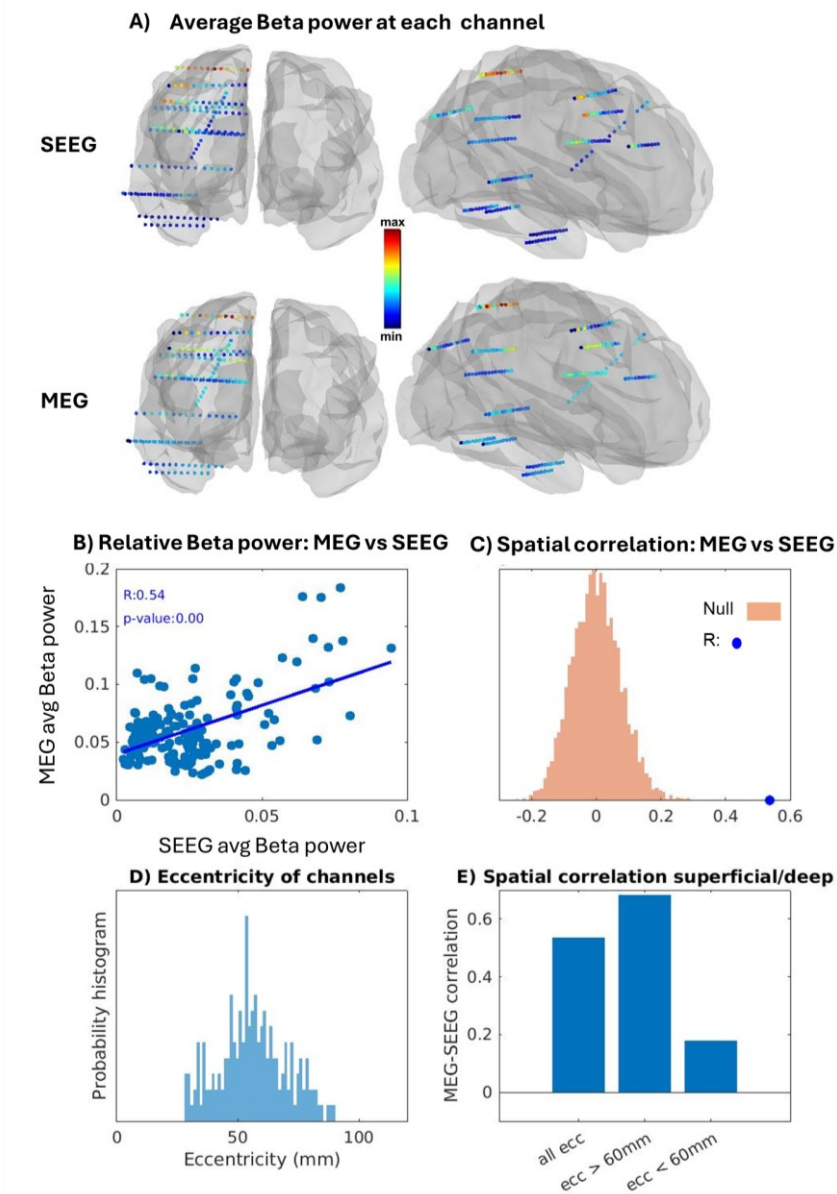


Figure 9-2 **(A)** Relative power spectral density averaged for all frequency bins within the frequency band of interest (Beta: 13-30Hz) for each channel of SEEG and MEG for patient #1 (two views). A threshold of 50% of the maximum activity is used for display. **(B)** MEG average relative power as a function of SEEG average relative power plotted for all channels in the beta band. The spatial correlation between MEG and SEEG average power was 0.54. **(C)** The observed spatial MEG/SEEG correlation of 0.54 is shown as a blue dot compared to the null distribution. **(D)** Distribution of eccentricity, which is a measure of the distance between the center of the head and the location of the SEEG channel. Low eccentricity and high eccentricity are associated with deep channels and superficial channels, respectively. **(E)** Using an eccentricity threshold of 60 mm, the correlations between MEG and SEEG relative power for channels > 60 mm and < 60 mm are shown. The spatial correlation between MEG and SEEG for superficial channels was higher than for deep channels.

In Figure 9-2D and Figure 9-2E, we investigated the cross-modal correlations between MEG and SEEG for superficial and deep channels. For each SEEG channel, we measured the eccentricity, defined as the distance between the channel location and the center of the head. Deep channels have therefore low eccentricity and superficial channels have high eccentricity. Fig 2D shows the distribution of eccentricity values for all the channels. A threshold of 60 mm eccentricity was selected to classify the channels into superficial and deep. The cross-modal correlations between MEG and SEEG for these two groups, along with all channels, are depicted in Fig 2E. The cross-modal correlation for superficial channels was 0.68, whereas it dropped to 0.17 for deep channels (still significantly higher than null). In this section, all correlations reported are significantly higher than null unless mentioned otherwise.

In Figure 9-3, following the same methodology, we present the cross-modal correlations between MEG and SEEG for Patients #2-5. For Patients #2 and #3, the dominant frequency band was the alpha band (8-13Hz). The spatial cross-modal correlations for Patients #2 and #3 for the average relative power considering all channels were 0.40 and 0.31, respectively. For both patients, the cross-modal correlations for deep channels were lower than for superficial channels (deep/superficial correlations in #2: 0.34/0.51 and #3: 0.12/0.14).

For Patients #4 and #5, the dominant frequency band was theta (4-8Hz) and the spatial cross-modal correlations for the average relative power were lower when compared to the three other patients, 0.19 and 0.12, respectively. For Patient #4, the correlations for superficial and deep channels were 0.25 and -0.03 (not significant), respectively. For Patient #5, the correlations for superficial and

deep channels were 0.42 and -0.03 (not significant), respectively. It is worth mentioning that the negative correlations for deep channels for those patients mean that the average power estimated using MEG was completely inaccurate. The cross-modal correlations for all 5 patients are also summarized in Table 9-1.

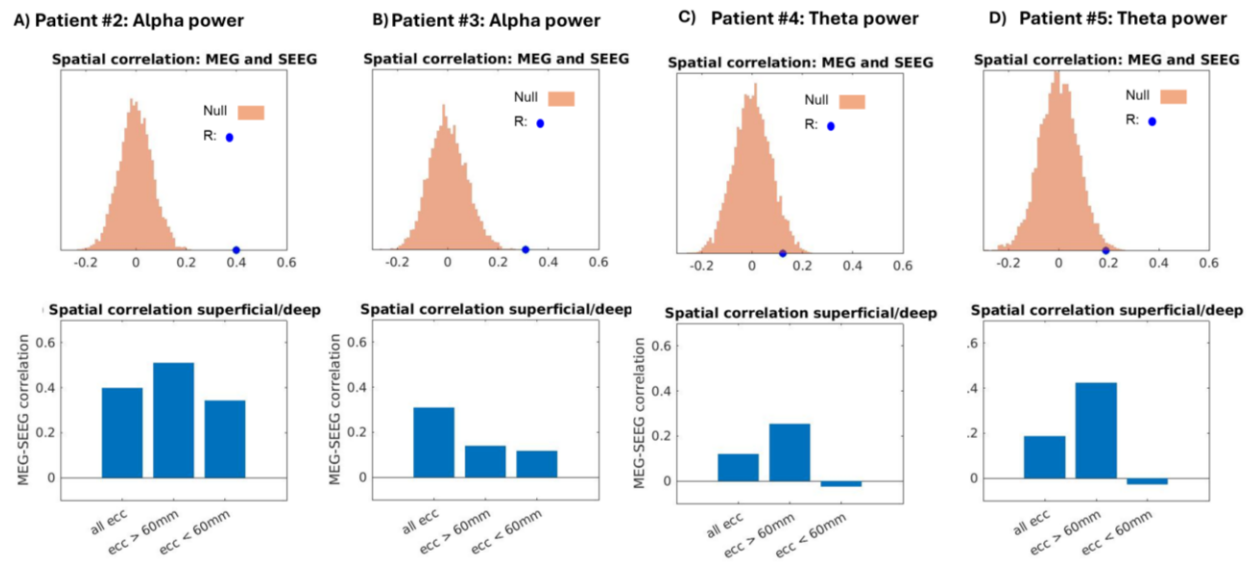


Figure 9-3(A-D) For patients #2-5, **(top)** The spatial correlation between MEG and SEEG relative power spectral density is shown as a blue dot compared to the null distribution. **(Bottom)** Using an eccentricity threshold of 60 mm, the correlations between MEG and SEEG relative power for channels > 60 mm and channels < 60 mm are shown. For Patients #2 and #3, the analysis was done in the alpha band (8-13Hz). For Patients #4 and #5, the analysis was done in the theta band (4-8Hz).

Table 9-1: Summary of spatial cross-modal correlations between MEG and SEEG for average relative power (correlations that were significantly higher than the null distribution are reported using bold font)

Patient ID	Frequency band	Spatial correlation between MEG and SEEG		
		All channels	Superficial channels	Deep channels
Patient #1	Beta	0.54	0.68	0.17
Patient #2	Alpha	0.40	0.51	0.34
Patient #3	Alpha	0.31	0.14	0.12
Patient #4	Theta	0.19	0.25	-0.03
Patient #5	Theta	0.12	0.42	-0.03

9.5.2 Connectivity

Fig 4A shows the connectivity values estimated by MEG and SEEG for four connectivity metrics for all possible channel pairs available from Patient #1. Patient #1 had 96 channels in bipolar montage resulting in 4560 possible channel pairs. The points in Figure 9-4A are 4560 connectivity values computed for those channel pairs. This figure provides a general overview of the scale of connectivity values retrieved from MEG versus SEEG connectomes. We found that the MEG connectivity values exhibited a larger distribution than SEEG, when not corrected for zero-lag connectivity using *AEC* and *PLV*. For *OAEC* and *wPLI** which removed zero-lag connectivity, MEG and SEEG connectivity values were within a more similar range.

In Figure 9-4B, the spatial cross-modal correlations between MEG and SEEG for these 4 metrics are shown. For amplitude-based metrics, the cross-modal correlations for *OAEC* decreased when *AEC* (*AEC* / *OAEC*: 0.37/0.24) but correlation remained significantly larger than the null distribution of connectivity values for both methods. For phase-based metrics, although a significant spatial cross modal correlation was found for *PLV*, for *wPLI**, the spatial correlation was close to null and not significant (*PLV* / *wPLI**: 0.28/-0.01).

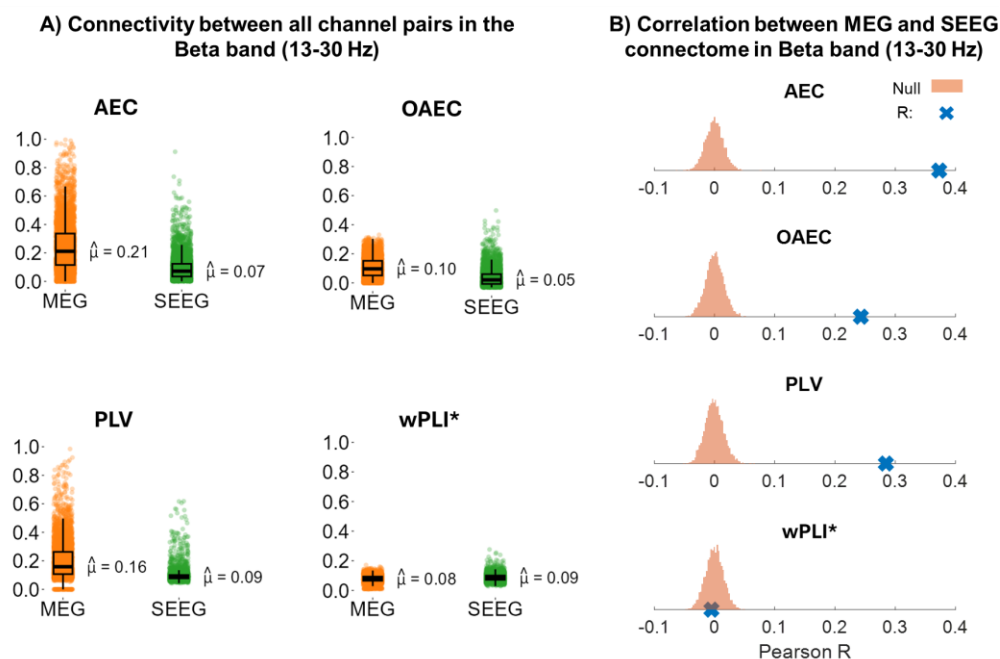


Figure 9-4 (A) Connectivity between all 4560 channel pairs estimated by MEG (orange) and SEEG (green) in Patient #1 calculated using *AEC*, *OAEC*, *PLV*, and *wPLI** in the Beta band (for a total of 96 channels

in bipolar reference montage). In addition to every channel pair connectivity values (every point on the graph), the underlying distribution of connectivity values is also presenting using a boxplot representation and the median value of every distribution is indicated. **(B)** The spatial cross-modal correlations between MEG and SEEG for *AEC*, *OAEC*, *PLV*, and *wPLI** in the Beta band is presented as a blue cross, whereas the connectivity null distribution estimated using surrogate data for each metric is shown in red.

Figure 9-5 summarizes the spatial cross-modal correlations for Patients #2-5. Except for Patient #2, all patients exhibited similar results as Patient #1. The correlations for *OAEC* were lower than *AEC* (*AEC* / *OAEC* for Patient#3: 0.29/0.23, Patient#4: 0.25/0.08, Patient#5: 0.21/0.12) but remained significantly larger than the null distribution. For Patient #2, the correlation for *OAEC* was slightly larger than *AEC* (*AEC* / *OAEC*: 0.23/0.26). For all 4 patients, although significant spatial correlations were found between the two modalities when considering *PLV*, *wPLI** did not show any significant spatial correlation (*PLV* / *wPLI** for Patient#2: 0.13/0.04, Patient#3: 0.21/0.03, Patient#4: 0.16/-0.09, Patient#5: 0.11/-0.05). The negative correlations for *wPLI** mean that the connectivity estimated by MEG was clearly inaccurate. The cross-modal correlations for all 5 patients are also summarized in Table 9-2.

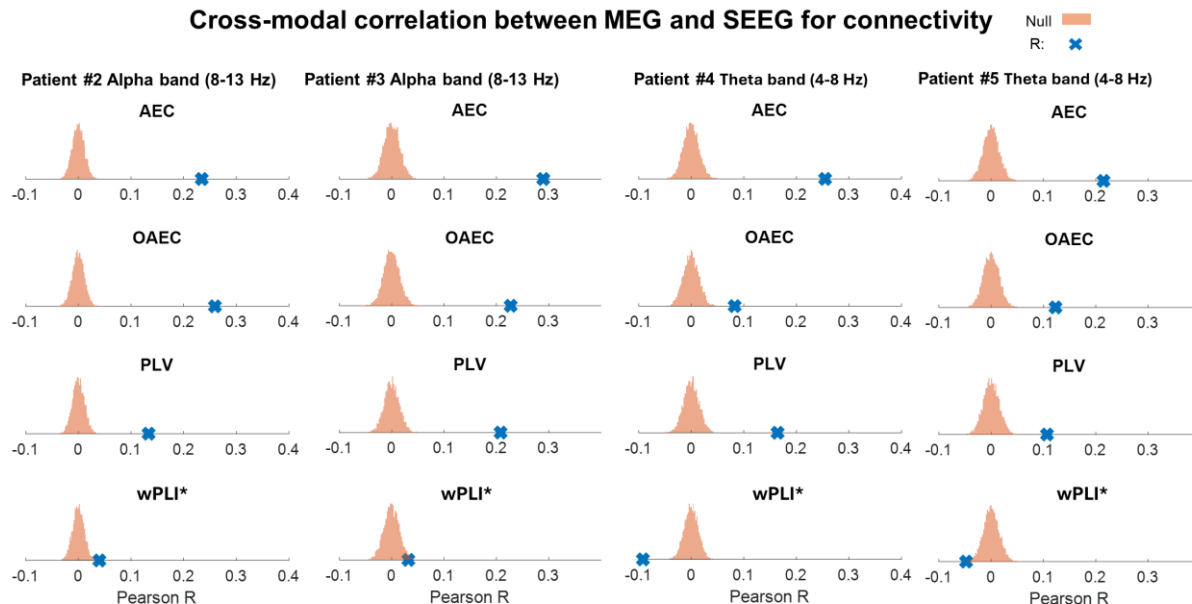


Figure 9-5 Spatial cross modal correlation between MEG and SEEG connectome for *AEC*, *OAEC*, *PLV*, and *wPLI** for patients #2 to #5. For Patients #2 and #3, the analysis was done in the alpha band (8-13Hz). For Patients #4 and #5, the analysis was done in the theta band (4-8Hz). The null distribution of connectivity values estimated from surrogate data for each metric is shown in red.

Table 9-2 Summary of spatial cross-modal correlations between MEG and SEEG for connectome (correlations that were significantly larger than the null distribution are reported using bold font))

		Spatial cross-modal correlations between MEG and SEEG			
Patient ID	Frequency band	<i>AEC</i>	<i>OAEC</i>	<i>PLV</i>	<i>wPLI*</i>
Patient #1	Beta	0.37	0.24	0.28	-0.01
Patient #2	Alpha	0.23	0.26	0.13	0.04
Patient #3	Alpha	0.29	0.23	0.21	0.03
Patient #4	Theta	0.25	0.08	0.16	-0.09
Patient #5	Theta	0.21	0.12	0.11	-0.05

9.6 Discussion

In this study, we aimed to validate MEG source imaging of resting state activity with simultaneously acquired SEEG data. We solved the MEG inverse problem using the wMEM method which was previously validated for accurately localizing oscillatory patterns at seizure onset (Pellegrino et al., 2016), interictal bursts of high-frequency oscillations (Avigdor et al., 2021; von Ellenrieder et al., 2016) and MEG resting state oscillations in epilepsy (Aydin et al., 2020) and healthy subjects (Afnan et al., 2023). By converting MEG source maps into virtual SEEG potentials using an SEEG forward model, we quantitatively compared MEG sources with actual SEEG recordings at each SEEG channel location (Abdallah et al., 2022; Afnan et al., 2023; Grova et al., 2016).

Results from the average power within the dominant frequency band showed that the MEG-estimated power retrieved accurately oscillatory patterns in superficial regions but was less accurate in deep channels for all five patients, even after adding depth-weighting to wMEM source imaging (Afnan et al., 2024). MEG source imaging of deep sources was quite inaccurate in two patients, resulting in negative cross modal correlations for Patients #4 and #5 for oscillations in the theta band. Thus, interpreting source imaging results from ongoing oscillatory patterns still requires caution for deep generators. Adding more realistic head modeling of underlying subcortical structures, as suggested in (Attal & Schwartz, 2013), could improve the localization accuracy of oscillation in deep structures. Such a development was out of the scope of this study and will be considered in our future developments.

Regarding functional connectivity, as expected, MEG exhibited larger connectivity values than SEEG for both amplitude and phase-based metrics that included zero-lag connectivity (*AEC/PLV*), in agreement with our previous findings at the group level (Afnan et al., in press). For *OAEC* and *wPLI**, the metrics that are corrected for zero-lag connectivity, the MEG and SEEG connectivities were found in a more similar range. However, the spatial cross-modal correlations for all connectivity pairs (connectome) between the two modalities revealed that the MEG-estimated connectome was more accurately estimated using *AEC* than *OAEC*, but in both cases spatial correlation were significantly larger than the null distribution suggesting that relevant patterns were retrieved by MEG using both metrics. For phase-based metrics, although MEG estimated connectome showed significant spatial correlations with SEEG when considering *PLV*, *wPLI**, surprisingly exhibited no correlations or even negative correlations, indicating that the MEG connectome estimated using *wPLI** was completely inaccurate when compared to SEEG connectomes. Our results are similar to the group-level findings we reported in Afnan et al. (in press) using non-simultaneous MEG and intracranial EEG (iEEG) atlas data.

Most studies investigating resting-state oscillations and connectivity in EEG/MEG use canonical frequency bands. However, in many cases, it is not initially confirmed whether oscillations exist in all these frequency bands. This makes it challenging to interpret results in frequency bands when there is actually no evidence of such oscillations. In this study, we only analyzed the dominant frequency band, which was carefully identified to confirm the presence of oscillations.

9.6.1 Deep source localization

The ability of EEG/MEG to detect deep brain activity has been debated for a long time, especially for MEG (Barkley & Baumgartner, 2003; Kaiboriboon et al., 2010; Rampp & Stefan, 2007; Shigeto et al., 2002). Recently, however, compelling evidence has been reported suggesting that deep brain activity can be recorded by high-density EEG (Seeber et al., 2019) and MEG (Alberto et al., 2021; Benar et al., 2021; Dalal et al., 2009; Koessler et al., 2015; Pizzo et al., 2019). Even if some signals from deep subcortical sources are detectable on the scalp EEG/MEG, they are often usually associated with very low SNR, hidden by higher amplitude signals from superficial regions. Source localization of low SNR signal remains difficult for any source imaging method. In addition, source localization underestimates deep sources because EEG and MEG sensors have a higher sensitivity to superficial than deep generators. To address this issue, a depth-weighting

approach is used in source imaging methods to enhance the contribution from deep sources (Lin et al., 2006). We used a depth-weighted version of wMEM, a method we recently proposed and validated to improve EEG/MEG localization of deep sources (Afnan et al., 2024). In (Afnan et al., 2024), we demonstrated significant improved accuracy of MEM source imaging techniques (cMEM and wMEM) by adding a depth-weighting strategy and including a surface mesh of bilateral hippocampi in our source space. Despite improved localization accuracy for deep structures, we also demonstrated that all source imaging techniques were also biased by spurious ghost localization on the superficial cortex adjacent to the deep generators. Therefore, even when localizing high amplitude spikes, it is still challenging to assess whether generators are only deep or associated with deep and superficial sources. In present study, when applying the same methods to localize ongoing resting state oscillations, MEG source imaging results were still poorly accurate for deep generators when compared for superficial generators. Our results were notably completely inaccurate for two patients, when considering localizations in the theta band. These results are however not surprising. Although depth weighting in source imaging methods can improve localization accuracy for deep generators (Lin et al., 2006), these methods are often associated with larger localization errors compared to superficial sources. This was demonstrated using focal brain stimulation or realistic simulations of epileptic discharges (Afnan et al., 2024; Pascarella et al., 2023; Unnwongse et al., 2023). With simultaneous SEEG data, it was evident that although some deep brain activity may be detected by EEG/MEG (Pizzo et al., 2019; Seeber et al., 2019), the source localization of resting state activity from deep sources needs to be interpreted with caution, as the localization of low SNR data may be inaccurate.

9.6.2 Compromise between removing spurious connectivity and genuine zero-lag connectivity

Due to the source leakage issue inherent with EEG/MEG-derived connectivity, it is often recommended to use connectivity metrics that remove zero-lag connections to obtain interpretable results (Hipp et al., 2012; Palva & Palva, 2012; Schoffelen & Gross, 2009). However, this approach also means accepting that these metrics could remove actual zero-lag connectivity. Several studies investigated the reliability of connectivity metrics based on the test-retest reliability (Garcés et al., 2016) or by comparing the EEG/MEG-estimated connectomes with fMRI-derived connectomes (Rizkallah et al., 2020). Those studies reported that connectivity metrics that are not corrected for

zero-lag connectivity are generally more reliable across subjects and trials compared to the metrics that are corrected for zero-lag connectivity.

Unlike studies that addressed source leakage issues in connectivity using numeric simulations or comparisons with modalities like fMRI that detect different brain mechanisms, we validated MEG-estimated connectivity using an iEEG atlas with data from a group of healthy participants (Afnan et al., in press). In our group-level comparison, we found that MEG exhibited higher connectivity than SEEG for *AEC* and *PLV*, although the spatial correlations between the two modalities for the entire connectome were moderate to low, but still significantly larger than the null distribution. Conversely, for metrics that corrected for zero-lag connectivity, *OAEC* and *wPLI**, the connectivity values between the two modalities were more similar, but the spatial correlation between the MEG and SEEG connectomes decreased, but still remained significantly different from the null distribution for *OAEC* in alpha, beta and high gamma bands, and for *wPLI** in all frequency bands. A key limitation of this group-level study was that MEG and SEEG data were acquired from two different groups of subjects, healthy subjects for MEG versus intracranial EEG contacts exhibiting normal activity in epilepsy contacts. To address this, we aimed to validate the group-level findings at a single-subject level using simultaneous SEEG and MEG.

Our current results align with the findings from our group-level study. The raw connectivity obtained in this study was similar to the values reported by (Afnan et al., in press). Comparing raw connectivity estimates from MEG with SEEG revealed that MEG connectivity, as estimated by *AEC* and *PLV*, was overestimated compared to SEEG, which was expected since those metrics are sensitive to volume conduction and source leakage. For metrics involving the correction or removal of zero-lag connectivity, the values from the two modalities were more similar. However, the spatial cross modal correlation between the connectomes derived from these four metrics showed that the connectomes were spatially more similar for metrics that did not correct or remove zero-lag connectivity (*AEC* versus *OAEC* and *PLV* versus *wPLI**). Although *OAEC* correlations decreased compared to *AEC* in 4 out of 5 patients, it is important to mention that results remained significantly higher than the null distribution, suggesting relevant connectivity information recovered using MEG. These findings were overall consistent with our group-level results, except for *wPLI**. While we obtained significant *wPLI** correlations in our group-level study in all frequency bands, the *wPLI** results in the current study showed close to zero or negative

correlations. A near-zero or negative correlation between the two modalities indicates that the connectome estimated from MEG was inaccurate.

9.6.3 Moderate to low correlations between MEG and SEEG connectome

The correlations between MEG and SEEG connectomes were moderate to low for *AEC*, *OAEC*, and *PLV* (0.08 to 0.37). To the best of our knowledge, the only study comparing MEG-derived connectomes with iEEG was conducted by our group (Afnan et al., in press). In that study, the cross-modal correlations for *AEC*, *OAEC*, and *PLV* ranged from 0.15 to 0.38 across theta, alpha, and beta frequency bands. Intuitively, the cross-modal correlations in the current study, which uses simultaneous data, should be higher than those in our group-level study with non-simultaneous data. However, several factors need to be considered before comparing the correlation values.

Although the two studies are methodologically similar, the datasets are very different. In (Afnan et al., in press), the data were non-simultaneous and acquired from two different populations. The iEEG connectome provided more coverage (44%) of the brain but was derived by combining data from different subjects. The comparison was therefore done at the region of interest (ROI) level, not at the channel level, considering 76 ROIs covering the whole brain (Afnan et al., in press). Each ROI was actually associated with a different number of channels that were averaged, and many ROIs were contributed by only a single pair of channels. In (Afnan et al., in press), we proposed an original resampling strategy to carefully take into account these sampling disparities when comparing both modalities. Despite these variabilities, the resulting cross-modal correlations ranged from 0.15 to 0.38. Therefore, we could expect higher cross-modal correlations for our simultaneous datasets at the single-subject level.

In another type of cross-modal comparisons using whole-brain EEG connectomes with simultaneously acquired fMRI connectomes, Wirsich et al. (2021) suggested that averaging connectomes across subjects before computing the cross-modal correlation results in a higher correlation than computing the cross-modal correlation for individuals and then averaging. Although the data were simultaneous, the cross-modal correlation between EEG and fMRI for individual subjects was still low (0.08 to 0.22) across all frequency bands. They found moderate cross-modal correlations (~ 0.3 to 0.4) when averaging at least 7 to 12 subjects. This suggests that averaging the connectomes separately for the two modalities before computing the cross-modal correlation may remove some noisy structures from individual subjects, thus providing a more

robust correlation between the modalities. Similarly, in our previous group-level comparison using the MEG and iEEG atlas, we observed higher cross-modal correlations between MEG and iEEG connectomes for *AEC*, *OAEC*, and *PLV* when we increased the number of subjects averaged in each ROI pair to construct the connectome (see Figure 8-8 in (Afnan et al., in press)). Increasing the minimum number of subjects likely removed noisy connections contributed by single subjects but came at the cost of reducing overall spatial coverage of the connectome. Therefore, concluding that averaging more subjects would increase the cross-modal correlation between the two modalities was not possible from the group-level comparison.

This could explain why we did not obtain higher correlations with our simultaneous data at the single-subject level compared to our previous group-level comparison. If we had an atlas of simultaneous SEEG and MEG that allows for ROI-level analysis, this effect could be tested.

9.6.4 Limitations

The limited number of patients reduces the generalizability of our findings. Comparison between different frequency bands was not possible as we only focused on the dominant frequency band in each patient. In this study, we focused on analyzing one minute of resting-state activity, averaging measures such as power and connectivity across that period. Benefitting from simultaneous MEG/SEEG recordings, one could assess the dynamic evolution of connectivity metrics across the two modalities. This interesting investigation was out of the scope of present study. Comparing cross modal MEG/SEEG correlations during ongoing low SNR resting state activity and high SNR signals measured during epileptic discharges (Pizzo et al., 2019) could be of great interest to assess the dependence of this cross modal correlation on the SNR of the data. The current sample size was insufficient to perform an ROI-based analysis, and the spatial coverage was overall limited. Recruiting more patients will enhance the spatial coverage, allowing for a more comprehensive analysis of whole-brain connectivity. Addressing these limitations in future studies will provide a more complete understanding of the correlation between MEG and SEEG, particularly in the context of source imaging and connectivity analysis.

9.7 Conclusions

To the best of our knowledge, this is the first study to validate MEG source imaging of resting state, particularly MEG-derived connectivity and source leakage issues, with simultaneously

acquired SEEG. Based on the moderate spatial correlations between the two modalities, we can conclude that MEG can estimate resting state activity with reasonable accuracy. However, MEG source imaging for deep sources is often inaccurate, and interpreting results from deep activity should be done with caution. For connectivity, MEG showed inflated connectivity compared to SEEG for metrics that include zero-lag connectivity (AEC/PLV). In contrast, for metrics that are corrected for zero-lag connections (OAEC/wPLI), MEG estimated connectivity values are more similar to SEEG. On the other, when measuring spatial correlation between MEG derived and SEEG connectomes, MEG-derived connectomes were more similar to SEEG when the metrics include zero-lag connectivity (AEC/PLV) than when using corrected ones (OAEC/wPLI). MEG could still accurately estimate connectomes using the amplitude-based metric OAEC, but wPLI results were inaccurate.

10 Overall discussion and conclusions

In this section, we begin by revisiting the primary question that motivated this thesis and assess how effectively it has been addressed. We will summarize the key contributions of each manuscript, noting the main findings and any limitations that should be considered. Finally, we will explore how these results can inform future research directions and studies. Additionally, we will discuss the role of intracranial EEG, not only as a validation tool but also as a complementary method with EEG/MEG in the study of brain activity.

10.1 Main methodological contributions and limitations

The aim of this thesis was to assess the reliability of EEG/MEG source localization for resting-state activity, particularly given the inherent uncertainties in these methods, which are even more pronounced when dealing with low signal-to-noise ratio signals, such as those associated during background resting-state activity or those involving deep generators of brain activity. While EEG/MEG source localization of resting-state brain activity is widely used in both healthy and diseased brain studies, there has been a lack of validation to guide the community on which brain regions, frequency bands, and connectivity metrics can be interpreted with confidence, and where caution is warranted. This thesis aims to address specifically these important questions.

EEG/MEG source localization requires incorporating prior knowledge to select a solution from the infinite number of possible solutions to the inverse problem. Based on the assumption it makes, each source imaging method has its strengths and limitations, as discussed in Chapter 3. For example, the MEM-based methods developed by our lab in the context of EEG/MEG have shown great accuracy in estimating the spatial extent of underlying neuronal generators, which is critical in applications like epilepsy, where the sources of interictal epileptic discharges are often spatially extended (Abdallah et al., 2022; Chowdhury et al., 2016; Chowdhury et al., 2013; Hedrich et al., 2017; Pellegrino, Hedrich, et al., 2020). However, MEM implementation was overall poorly sensitive to deep brain generators (Chowdhury et al., 2015), also combining EEG/MEG within a fusion scheme slightly improved depth accuracy according to our numerical simulations. Adapting MEM methods for localizing resting state activity and deep brain activity were important parts of this thesis, which are included in manuscripts 1 (Chapter 6) and 2 (Chapter 7).

In our first manuscript presented in Chapter 6 (Afnan et al., 2023), we evaluated MEG source imaging of resting-state oscillations in a healthy population by comparing MEG sources to an intracranial EEG atlas of normal brain activity. Although the intracranial EEG data were obtained from patients with epilepsy, only recordings from healthy brain regions were used. Given that intracranial EEG is never performed on healthy subjects, this atlas of normal brain activity serves as the best available ground truth for validating normal resting-state brain activity at a group level. This study was the first group-level validation of non-invasive source imaging methods, leveraging the dense coverage of intracranial EEG to study the whole brain at a spatial region of interest (ROI) level.

The key findings from this study were that, on a global brain level, MEG source imaging of resting-state power or amplitude correlates well with intracranial EEG, with some specific areas of difference. The distribution of MEG relative power in different brain regions reported in our study was consistent with the previous MEG studies for the different canonical frequency bands (Mahjoory et al., 2020; Mellem et al., 2017; Niso et al., 2016; Niso et al., 2019). We provided a brain map showing, for each region, a measure of overlap that indicates the similarity in power spectral density between MEG sources and intracranial EEG data, after carefully converting MEG sources into virtual intracranial EEG data for comparison purposes (Grova et al., 2016). Overall, our results suggested that for most cortical regions, MEG sources recovered oscillatory activity accurately when compared to data from the intracranial EEG atlas. In terms of oscillatory peaks, our comparison reflected the differences previously observed between EEG/MEG and intracranial ECoG recordings (Groppe et al., 2013). Specifically, MEG-estimated spectral peaks were dominated by 10-12 Hz alpha peaks, whereas intracranial EEG showed the highest alpha peaks around 7-8 Hz. In MEG, alpha peaks were actually present in most brain regions, including the frontal and deep regions (bilateral hippocampi), whereas these peaks were clearly absent in the frontal and deep regions in intracranial EEG. This is an important finding suggesting how source localization within deep structures, like the hippocampus, can be biased by source leakage, resulting in spurious high alpha power localized in those regions, whereas real in situ intracranial EEG are not exhibiting alpha oscillations in the hippocampus. Additionally, MEG estimates of theta band peaks were significantly underestimated compared to intracranial EEG. These differences could be attributed to the two distinct population involved in our comparison: one being completely healthy (MEG) and the other comprising normal intracranial EEG data from patients

with epilepsy. Although the intracranial EEG electrodes were located in healthy brain regions, they were still obtained from patients. This limitation can only be fully addressed with simultaneously acquired MEG and intracranial EEG data. For instance, using simultaneous MEG and intracerebral EEG data from five patients in Study 4, we observed that, when considering resting state data not exhibiting any epileptic discharges, MEG-estimated alpha peaks in patients were also found around 7-8 Hz (and not around 10-12 Hz as in our Study 1), similar to the alpha peaks measured using intracerebral EEG. This important issue needs to be investigated carefully with simultaneous recordings from more patients.

In this study, we focused on the ‘periodic component’ of the oscillations and removed the 1/f aperiodic components, which were estimated using the FOOOF algorithm (Donoghue et al., 2020). Our results are suggesting that after removing the aperiodic components, we found a better concordance between MEG sources and intracranial EEG data in different frequency bands. However, we did not thoroughly investigate the 1/f components, which are also of interest. A recent study (Bush et al., 2024) using intracranial EEG demonstrated that cortical regions typically exhibit a clear knee in the power spectra (in log-log space), whereas subcortical regions do not. Consistent with this, our findings showed that intracranial EEG revealed a distinct knee or bend in the spectra of cortical regions, while this feature was absent in subcortical regions such as the hippocampus. It is important to note that this distinction is not evident in MEG-estimated spectra, where, the knee was present in both cortical and subcortical regions when using the wMEM method for MEG estimation. We also observed that the 1/f component differed significantly between MEG and intracranial EEG and varied depending on the source imaging methods used. Compared to intracranial EEG, while wMEM more accurately estimated the spectra with a knee component, the spectra appeared more linear in the log-log space when using the other two source imaging methods (MNE and beamformer). The reason wMEM localized the 1/f component with a clear knee more accurately (similar to intracranial EEG) might be explained by the sparse/optimal data representation of oscillatory components obtained using Daubechies discrete wavelets. However, these discrepancies suggest that the 1/f component is influenced not only by different modalities but also by the choice of source imaging methods. Further research is needed to understand these differences and their implications.

Moreover, we found that all aspects of oscillations, including power in a frequency band, and oscillatory peaks were highly inaccurate in deep structures such as the hippocampus. Although this finding with the wMEM method was consistent with two other source imaging methods (depth-weighted MNE and beamformer), it highlighted some areas for improvement in the MEM method. We recognized that the wMEM (and cMEM) method are not sensitive to deep sources, leading to underestimation of medial brain regions. Moreover, our source model did not include the hippocampus, although we projected MEG-estimated source maps to the hippocampal intracranial EEG channels. These limitations led to our second study, which aimed to improve MEM-based methods for more accurate detection of deep brain activity.

In our second study presented in Chapter 7 (Afnan et al., 2024), we introduced a depth-weighting adaptation to the MEM method to improve its capability in localizing deep brain activity. We also included the hippocampus in the source model with the cortical surface. This newly adapted method accurately estimates the spatial extent of brain generators while addressing the previous limitations related to detecting deep brain activity. Through extensive realistic simulations of interictal epileptic discharges (IEDs) in high-density EEG and MEG, we demonstrated that this method significantly improves the localization of deep brain activity when compared to the previous MEM implementation and another source imaging method, the depth-weighted MNE.

The proposed method was further validated using high-density EEG and MEG data from patients with epilepsy. Significant improvements were obtained for patients with mesial temporal lobe epilepsy. Unlike the other three studies, Study 2 utilized both high-density EEG and MEG. The ability to detect deep brain activity was also influenced by the type of sensors used. Even after applying depth-weighting, deep brain activity was more challenging to localize with MEG gradiometers compared to high density EEG. It is well-known that MEG gradiometers are less sensitive to deep brain activity than MEG magnetometers (Malmivuo & Plonsey, 1995), meaning that studies relying on MEG gradiometers require further caution when interpreting deep brain localization.

Through extensive simulations, this study provides an improved method and offers recommendations for tuning the depth weighting parameter to effectively localize deep brain activity without compromising the superficial source localization. Compared to standard MEM and depth-weighted MNE as benchmarks, our new cMEM version could estimate deep generators

more accurately, with minimal or no worsening of localization for superficial regions. This improvement was robust across high-density EEG and MEG, different spatial extents of the generator, and varying SNR levels. The improvement in MEG by depth weighting was more pronounced/necessary compared to high density-EEG. This could be because EEG is more sensitive to radial and deep sources, whereas MEG using gradiometers is more sensitive to tangential and superficial sources (Goldenholz et al., 2009; Kakisaka et al., 2013). However, we acknowledge that the localization error associated with deep sources remains larger than that of superficial sources. This was consistent with the findings reported in previous studies (Chowdhury et al., 2015; Mikulan et al., 2020; Pascarella et al., 2023; Unnwongse et al., 2023). The key takeaway is that, while our method (and other source imaging methods with depth weighting) improves deep source localization, caution is still necessary when interpreting deep sources. Specifically, our simulations showed that while superficial sources can be accurately localized, deep sources, especially those with low SNR, may also produce superficial 'ghost localization'. Without a ground truth, it is challenging to determine whether a superficial component is merely a 'ghost localization' of an actual deep generator or if there are genuinely two generators, one deep and one superficial. Current distributed source imaging methods cannot resolve this uncertainty, highlighting the need for more sophisticated techniques in the future. Simultaneous intracranial EEG with scalp EEG or MEG recordings will be required to assess specifically this challenging localization problem.

In Study 3 presented in Chapter 8 (Afnan et al., in press), we validated MEG-derived resting-state connectivity in the healthy population from Study 1 using the intracranial EEG atlas. We applied the newly proposed depth weighted wMEM method (from Study 2) by adding depth weighting and incorporating the hippocampus into the source model. For this study, we applied the same methodology proposed in Study 1, converting MEG sources into virtual intracranial EEG data. We then proposed an original resampling methodology to take into account the limited spatial sampling of the intracranial EEG atlas when assessing functional connectivity (since only paired electrodes from the same subjects could be considered), proposing for the first time spatial correlations between functional connectomes estimated from MEG sources and intracranial EEG data at the group level. The challenges associated with conducting a group-level connectivity study using the intracranial EEG atlas have been detailed in Chapter 8 and will not be discussed here.

The goal of this study was to investigate MEG-derived connectivity and the issue of source leakage using four popular connectivity metrics.

In Chapter 4, we reviewed previous studies that recommended using connectivity metrics corrected for zero-lag connectivity to address the issue of EEG/MEG source leakage, often based on simulations or comparisons with fMRI-derived connectivity (Sadaghiani et al., 2022). It is worth mentioning that correcting those metrics for source leakage may remove real zero-lag connectivity measured using intracranial EEG. Our Study 3 presented in Chapter 8 was the first to validate non-invasive MEG-derived resting state connectivity with intracranial EEG as ground truth at a group level. Contrary to common recommendations, we found that using metrics corrected for zero-lag connectivity could be risky when analyzing brain connectomes. When using connectivity metrics not corrected for zero-lag connectivity, we found that MEG-derived connectivity values were inflated when compared to intracranial EEG connectivity values. When using connectivity metrics corrected for zero-lag connectivity, MEG-derived connectivity measures were closer to those of intracranial EEG. On the other, when measuring spatial correlation between MEG derived and intracranial EEG connectomes, MEG-derived connectomes were more similar to intracranial EEG when using uncorrected metrics than when using corrected ones. However, in both cases, spatial correlations between modalities were found significant when compared to surrogate data, notably in the alpha and beta bands, suggesting that MEG was able to retrieve some relevant connectivity patterns even when correcting for zero-lag connectivity. For the corrected metrics, we observed more consistent results when considering amplitude-based metrics compared to phase-based metrics. This finding aligns with the work of Colclough et al. (2016), which proposed orthogonalized amplitude envelope correlation as a superior metric to other metrics that are corrected for zero-lag connectivity.

Studies 1 (Chapter 6) and 3 (Chapter 8) provided a group-level validation of MEG source localization for resting-state activity, examining different aspects such as power, oscillatory peaks, 1/f components, and connectivity patterns. In Study 1, we were able to analyze the entire brain at the ROI level, while in Study 3, we explored nearly 46% of the whole-brain connectome at such a ROI level. However, the main limitation is that the MEG data and the intracranial EEG atlas were derived from two different population groups, introducing several variables that constrained a

direct one-to-one comparison between the two modalities. Despite these intrinsic limitations, our group-level comparison provided valuable insights.

In our last study (Study 4 presented in Chapter 9), we further validated MEG's ability to recover resting-state power and connectivity patterns more directly at the individual subject level using simultaneous MEG and intracerebral EEG data. As discussed in Chapter 5, integrating invasive intracerebral EEG with non-invasive EEG/MEG techniques has many challenges, and few groups have the resources to conduct such complex acquisitions (Badier et al., 2017). Through collaboration with Dr. Bénar's group in Aix-Marseille University (France), we investigated MEG localization of resting-state activity with simultaneous intracerebral EEG in five patients who underwent intracerebral EEG implantation during their presurgical evaluation. Unlike Studies 1 and 3, this study provided limited spatial coverage for each patient, considerably restricting ROI-level analysis but offering a better opportunity to directly validate MEG-estimated oscillations and connectivity, benefitting from simultaneous recordings. Despite the small sample size, our results were encouraging and supported our group-level findings. The study also demonstrated that MEG-estimated oscillatory power from deep channels may often be inaccurate.

To the best of our knowledge, no other study has validated EEG/MEG-derived connectivity from resting-state data with intracerebral EEG, either at a single-subject level with simultaneous data or at a group level with non-simultaneous data. A recent study by (Liu et al., 2024) investigated the effects of inverse methods and connectivity measures using simultaneous EEG and SEEG signals evoked by electrical stimulation applied on SEEG contacts. They reported that deep sources performed poorly across all source imaging methods. They identified wPLI as the most accurate connectivity measure among the six metrics studied. However, since they used stimulation-evoked data, the signals were much stronger than when considering resting-state brain activity. The direct applicability of these results to interpret connectivity measures in a resting-state context is therefore uncertain.

In our study 4, using simultaneous MEG and intracerebral EEG, we found that MEG-derived connectomes using wPLI were not accurate. A group-level connectome study using intracerebral EEG by Williams et al. (2023), computed with PLV, showed that the identified network modules consisted of anatomically contiguous regions. Unlike resting-state fMRI, intracerebral EEG-derived connectomes exhibited more local, anatomically contiguous connections rather than a

distributed pattern, indicating that intracerebral EEG connectivity patterns were more local. This could explain why MEG-derived connectomes using wPLI were inaccurate. If the connectome derived using a phase-based metric primarily consists of local connections, removing zero-lag connectivity would result in a noisy connectome that excludes actual zero-lag connections. In contrast, amplitude envelope-based metrics, which are derived from signal envelopes (associated with larger-scale synchronization) could capture more long-distance connections and thus reflect underlying distributed networks similar to the one we can retrieve from resting state fMRI data (Matthew J Brookes et al., 2011). In our study, even after correcting for source leakage (orthogonalized AEC), amplitude envelope-based metrics were able to accurately estimate MEG connectomes at a group level in alpha and beta bands (Study 3) and at a single-subject level in alpha, beta, and theta bands (Study 4). This finding is consistent with a previous study by Colclough et al. (2016) using resting-state MEG data, which compared different metrics to assess consistency across different sessions or subjects (without using any ground truth).

The spatial correlations we observed between connectomes estimated from MEG and the iEEG atlas, as well as between those estimated using simultaneous MEG and SEEG, were within the same range as those reported in previous studies comparing simultaneous EEG and fMRI derived connectomes (Wirsich et al., 2020; Wirsich et al., 2024; Wirsich et al., 2021). In Wirsich et al. (2021), after applying minimum norm source imaging to localize resting state EEG data acquired in the scanner, cross-modal correlations between fMRI and EEG connectivity using orthogonalized amplitude envelope correlation were lower compared to non-corrected amplitude envelope correlation, which aligns with our findings in Studies 3 and 4. They also found significant correlations between EEG and fMRI connectomes when EEG connectivity was estimated using imaginary coherence, a metric that excludes zero-lag connectivity. In our group-level comparison in Study 3, we found significant correlations between MEG and intracranial EEG atlas when MEG connectivity was estimated using wPLI. However, at a single-subject level comparison with simultaneous MEG and intracerebral EEG data in Study 4, no correlation was found between MEG and intracerebral EEG connectomes for wPLI. Detailed comparisons with these studies are presented in Chapters 8 and 9, where we also highlight the differences between our studies and those comparing EEG and fMRI connectomes. Although their studies used simultaneous data, EEG and fMRI capture different brain mechanisms, electrophysiology in EEG versus hemodynamic activity in fMRI, and thus direct comparisons are limited. In contrast, we compared

two modalities, iEEG and MEG, capturing essentially the same underlying generators and brain dynamics.

10.2 Future directions

We emphasize the need to develop a simultaneous intracerebral EEG and EEG/MEG atlas that combines data from multiple patients, similar to the existing atlas created using only intracranial EEG data. Such an atlas would be invaluable for validating results from non-invasive methods and for generating a brain map that highlights regions with greater accuracy and those associated with localization inaccuracies. This type of atlas would serve as the most reliable ground truth not only for validating resting-state oscillations but also for evaluating different source imaging methods and parameters.

In Study 2, we validated the depth-weighted MEM method by simulating a ground truth or using a ground truth in epilepsy patients based on presurgical clinical information or surgical resection outcomes in seizure-free patients. Simultaneous EEG/MEG and intracerebral EEG would actually be the most effective way to validate these method parameters. For instance, using data from a patient in Study 4, who had SEEG implantation in the left and right hippocampi and simultaneous MEG recording, we compared the performance of depth-weighted cMEM (cMEM_w) with standard MEM (Figure 10-1). The standard cMEM failed to localize IED activity in the hippocampus, whereas depth-weighted cMEM (cMEM_w) successfully localized the IED, consistent with the SEEG ground truth.

SEEG to validate MEG source imaging in deep source localization

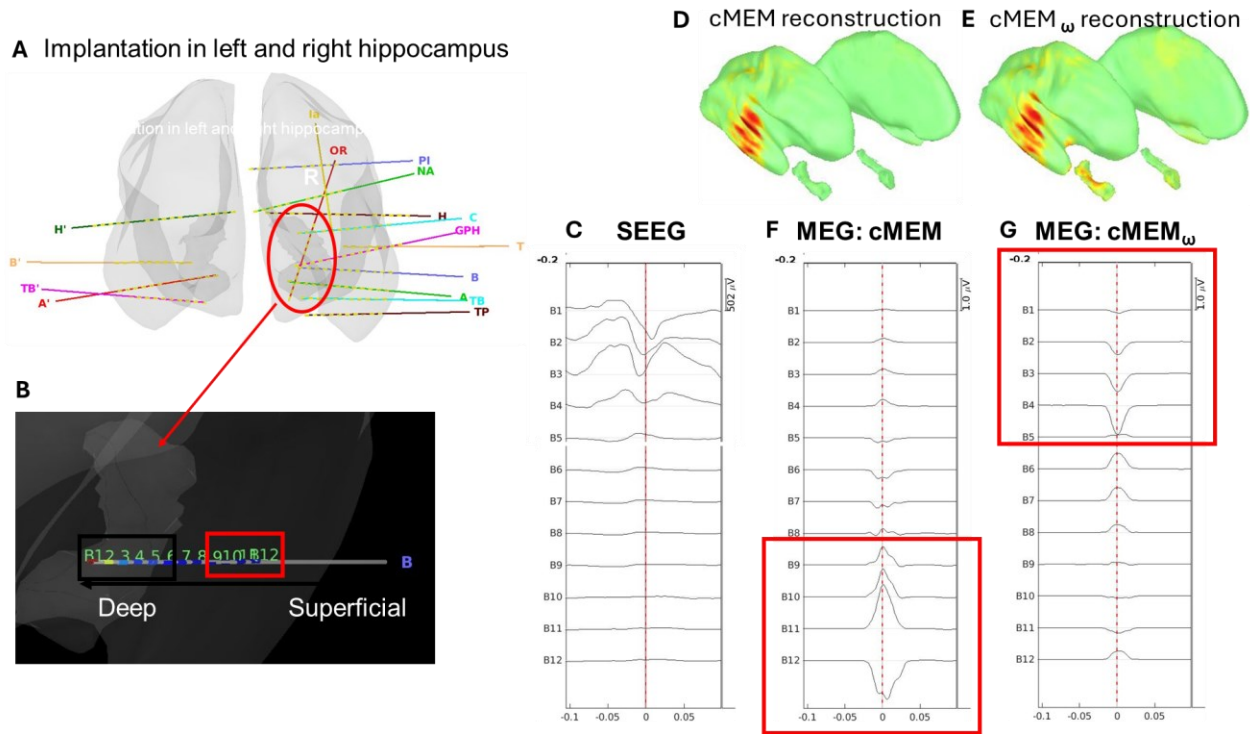


Figure 10-1: (A) A patient with intracerebral EEG (stereotaxic EEG or SEEG) implanted in left and right hippocampus. (B) Example SEEG electrode shown that has some contacts in deep hippocampus and some contacts in the superficial regions. (C) Example of an interictal epileptic discharge in SEEG. The same IED was marked in simultaneous MEG and reconstructed using (D) standard cMEM (no depth weighting) and (E) depth weighted cMEM ($cMEM_{\omega}$). The MEG source maps were finally converted to SEEG space for (F) cMEM and (G) depth weighted cMEM ($cMEM_{\omega}$). Compared to SEEG IED in C, cMEM could not localize the spike within deep contacts but depth weighted cMEM provided more accurate localization in deep hippocampus contacts.

However, it is important to note that, although the depth-weighted cMEM localized the hippocampal source, it also produced some ghost localizations on the lateral superficial cortex (Figure 10-2). Further investigation using more patients with simultaneous EEG/MEG and intracerebral EEG is necessary to thoroughly evaluate these challenging localization scenarios and compare with other source imaging techniques. Open-source datasets, such as the first publicly available dataset of simultaneous high-density EEG and SEEG recordings of IEDs by Zauli et al. (2024) (<https://osf.io/89ndr/>), are invaluable resources for such research.

SEEG to validate MEG source imaging in deep source localization

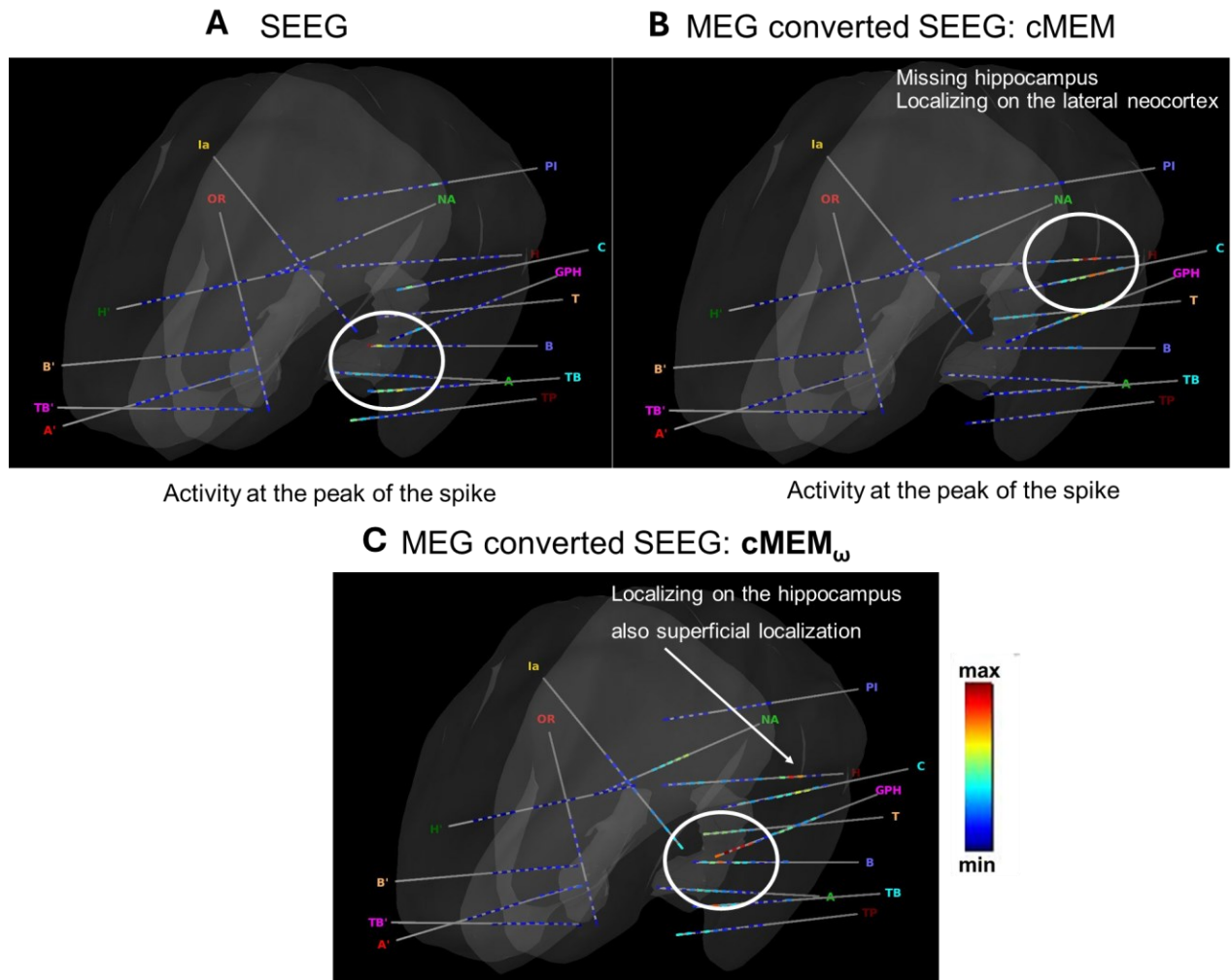


Figure 10-2 Interictal epileptic discharge (IED) for all electrodes (color shows activity thresholded at 50% of the maximum) for (A) stereotaxic EEG or SEEG, (B) MEG estimated using cMEM and converted to the SEEG space and (C) MEG estimated using depth weighted cMEM ($cMEM_{\omega}$) and converted to the SEEG space. cMEM failed to localize activity in the hippocampus, whereas the depth-weighted cMEM successfully localized it, consistent with the SEEG ground truth. However, depth-weighted cMEM also produced some ghost localizations on the lateral cortex.

Validation of non-invasive EEG/MEG methods has also been performed using electrical stimulation applied on intracranial EEG to generate ground truth data (Liu et al., 2024; Pascarella et al., 2023; Unnwongse et al., 2023). Pascarella et al. (2023) compared ten source imaging methods and explored various depth-weighting parameters using simultaneously acquired high-

density EEG and intracerebral ‘electrical stimulation pulses’ as ground truth. However, whereas these studies are valuable, it is worth mentioning that the generators of these stimulations are highly focal, and the resulting elicited signals feature high signal-to-noise ratios. In epilepsy, the generators are usually spatially extended and thus these focal electrical stimulations are not ideal for validation. When considering either electrical stimulation or recording of ongoing epileptic/resting state data, simultaneous EEG/MEG and intracerebral EEG provide the best framework for testing and validating source imaging methods.

While we have so far used intracerebral EEG as a ground truth to validate non-invasive EEG/MEG results, combining these modalities for complementary use has a great potential (Dubarry et al., 2014; Gavaret et al., 2016; Koessler et al., 2015; Pigorini et al., 2024; Zauli et al., 2024). EEG/MEG offers global recordings with limited spatial resolution but overall good spatial accuracy for most superficial cortical regions. On the other hand, intracerebral EEG provides high spatial resolution and signal-to-noise ratio (SNR) and can record almost anywhere in the brain, but with limited spatial coverage. By leveraging EEG/MEG for a broad coverage of superficial cortical regions and intracerebral EEG for deep regions, we can effectively investigate a larger fraction of the brain than with any modality by itself. The poor spatial coverage of intracerebral EEG may result in implantations missing the actual epileptogenic zone. For instance, Gavaret et al. (2016) utilized multi-modal EEG/MEG and stereotaxic EEG (SEEG) recordings to guide the localization of epileptogenic zones by leveraging the strengths of each modality while complementing information that might be missed by individual techniques. They selected IEDs from SEEG that were not visible in EEG/MEG, and by using these SEEG-marked IEDs in the EEG/MEG data (even if single events were not visually detectable), the localization of averaged EEG/MEG IEDs revealed a generator that was not captured by SEEG alone.

Multimodal fusion of source imaging applied on EEG/MEG and intracerebral EEG, could improve the issue of limited sampling in intracerebral EEG, particularly in cases of implantation missing the epileptogenic zone. For instance, this fusion source imaging could localize interictal epileptic discharges (IEDs) accurately that may be missed by intracerebral EEG alone. Our group previously implemented a fusion of EEG and MEG source imaging within the MEM framework (Chowdhury et al., 2015) and demonstrated that EEG/MEG fusion significantly improved the reliability of source localization results when localizing single non-averaged epileptic discharges (Chowdhury

et al., 2018). This fusion methodology framework we proposed within the context of MEM is sufficiently flexible and can therefore be extended to combine EEG/MEG with intracerebral EEG source imaging to optimally incorporate information measured from complementary recordings into the source imaging problem. We believe this is a topic of great interest that we will investigate in our future investigations.

In the future, we will also analyze the aperiodic components using simultaneous MEG and intracerebral EEG data, particularly to investigate whether there are significant differences in the estimation of these components between the two modalities. The difference observed in the 'knee' component between cortical and subcortical structures in intracerebral EEG spectra (Bush et al., 2024) should also be explored to determine whether EEG/MEG sources can similarly estimate these features. The origin of these differences in cortical and subcortical structures remains unclear, making this an important area for future research.

When incorporating subcortical structures into the source model, we included only the hippocampus alongside the cortical surface. Integrating the hippocampus was straightforward because it was modeled as a surface mesh, with current dipoles oriented orthogonally to the surface, similar to the cortical source space. Our results in Study 2 are demonstrating the relevance of adding a surface segmentation of bilateral hippocampi to improve source imaging accuracy. This is a modeling approach we are now considering in all our EEG/MEG source imaging studies. In contrast, structures like the thalamus, striatum, and amygdala should rather be modeled using a volume grid with current dipoles placed in random orientations (Attal et al., 2009; Attal & Schwartz, 2013). Other source imaging methods that can handle both cortical surface and volume grid models can incorporate these subcortical structures using a mixed source model. However, including these subcortical structures in the MEM framework would require adapting the parcellation process, which is currently guided along the surface in a geodesic manner. Extending the MEM method to handle a combination of surface models and volume grids would facilitate the inclusion of mixed hybrid models, allowing the integration of additional subcortical structures into the source space.

In this thesis, we focused on analyzing one minute of resting-state activity, averaging measures such as power spectra and connectivity across that period. However, brain activity is highly dynamic. Using simultaneous MEG and intracerebral EEG, future work will aim to explore brain

dynamics both during the resting state and in the context of epilepsy, including the propagation of interictal epileptic discharges and seizures. A recent study using intracerebral EEG and structural connections derived from diffusion weighted MRI data (Azeem et al., 2024) demonstrated that seizure propagation is mediated by white matter tracts. Previously, Azeem et al. (2021) showed that the epileptic network can be delineated through the propagation of interictal epileptiform discharges using intracerebral EEG. This relationship between structural connectivity and seizure propagation in epilepsy, as well as the detection of epileptic networks through interictal discharge propagation, could potentially be explored using non-invasive EEG/MEG connectivity based on source imaging and simultaneous EEG/MEG and intracerebral EEG. Similarly, simultaneous EEG/MEG and intracerebral EEG, associated with the methodological development proposed in this thesis would provide the ideal framework to study the dynamic of brain activity, during epileptic activity (interictal discharges or seizures), but also during ongoing resting state activity which is not always stationary.

Appendix A for manuscript 1 in Chapter 6

The maximum entropy on the mean (MEM) is a Bayesian inference technique that regularizes the inverse problem using prior information. This prior relies on the notion of functional parcellation of brain activity over the cortical surface, and hidden state variables describing each parcel being active or inactive. A data driven parcellization (DDP) based on Multivariate Source Pre-localization (MSP) method (Mattout et al., 2005) was used to guide the parcellation of the cortical surface into non-overlapping and functionally homogeneous parcels (Lapalme et al., 2006). For each parcel, the prior is then defined as a mixture of Gaussians, each Gaussian of each parcel will be related to a state as active and inactive controlled by a hidden state variable. In the context of resting state EEG/MEG, we adapted wMEM by incorporating a few changes in the prior model and initialization of the parcels.

Spatial prior model:

Parcellation of the whole cortical surface was obtained using a data driven approach, based on the Multivariate Source Pre-localization (MSP) method (Mattout et al., 2005), a projection technique allowing to estimate the probability of every source contributing to the data. The MEG data (M) were first normalized (across sensors) and then wavelet transformed (\tilde{W}). In the present implementation of wMEM, time expansion was thus substituted with a time-scale representation. The contribution of each source to the data (called the MSP score) is obtained using the normalized MEG data (\tilde{W}) and the normalized lead field matrix (\tilde{G}), where the normalization was performed by the norm of each column. \tilde{W} is the sensor space data in the wavelet domain (dimension: *number of sensors* \times *discrete wavelet time-frequency indices*), whereas the normalized lead field \tilde{G} is of dimension *number of sensors* \times n ; n is the total number of sources. The MSP score for each source (a_i), $i = 1, \dots, n$, is calculated in the following steps:

The normalized lead field matrix \tilde{G} is decomposed into d mutually orthogonal eigenvectors u_i using singular value decomposition (SVD). We selected a subspace, $U_s = [u_1, u_2, \dots, u_s]$, by projecting these orthogonalized projectors onto the normalized data \tilde{W} as $U^t \tilde{W} \tilde{W}^t U$ and taking the diagonal of $U^t \tilde{W} \tilde{W}^t U$ that captures 95% of the variability.

In the data subspace spanned by U_s , the data that can be explained within this subspace is calculated as:

$$W_s = U_s U_s^t \tilde{W} \quad (\text{A.1})$$

The projector in this subspace is defined by

$$P_s = W_s (W_s^t W_s)^{-1} W_s^t \quad (\text{A.2})$$

Finally, the MSP score between 0 and 1 for each source i is then calculated by the norm of the projection of its associated lead field,

$$a(i) = \tilde{g}_i^t P_s \tilde{g}_i \quad (\text{A.3})$$

where \tilde{g}_i is the i^{th} column of \tilde{G} .

Parcels are then constructed using a region-growing algorithm, selecting sources according to decreasing MSP scores. In this version of wMEM, assuming a stable parcellation of the cortex for all the time-frequency samples for resting state data, we followed the strategy proposed for cMEM (Chowdhury et al., 2013), ensuring that the same underlying parcellation was considered when localizing all the time-frequency samples (dimension of \tilde{W} as *number of sensors* \times *number of discrete time frequency boxes*). In our previous implementation (Lina et al., 2012), a specific parcellation was computed for each time-frequency box to localize.

Initialization of the parcels:

The probability α_k for each parcel k to be active was then initialized as the amount of ‘normalized energy’ in the parcel, for each time-frequency sample. Given the minimum norm estimated energy of the sources, for a specific time-frequency sample (a column in \tilde{W}) \tilde{w} ,

$$j = \tilde{G}^t (\tilde{G} \tilde{G}^t)^{-1} \tilde{w} \quad (\text{A.4})$$

$$\alpha_k = \sqrt{\frac{\sum_{i \in k} j(i)^2}{\sum_{i=1, \dots, n} j(i)^2}} \quad (\text{A.5})$$

Although the parcels were identical across time-frequency samples, this quantity initializing the probability of each parcel to be active changed with time and frequency.

Selection of baseline for resting state localization:

A baseline is needed to complete the initialization of the prior, to define the variance of the active state and inactive state, in comparison to the noise variance at the sensor level. This is an important feature that will allow switching off parcels in the model when they are not active. The idea of selecting a baseline is to choose a segment of data with an amplitude significantly lower than the signal of interest. However, the selection of such segments in resting state data is not straightforward. In Aydin et al. (2020), the baseline was defined as a two-second segment exhibiting low amplitude in the alpha band, since we were investigating amplitude envelope correlation in the alpha band, as a connectivity metric. This approach worked reasonably when localizing in a specific and narrow frequency band, however, becomes inappropriate when localizing in a wide frequency band. Here, we propose to generate a quasi-synthetic baseline from a segment of the signal of interest. The baseline was obtained by randomly modifying the Fourier phase at each frequency, for all the sensors (originally proposed by Prichard & Theiler 1994). This baseline preserves the coherence between the sensors and the power spectrum of the signals while destroying only the temporal coherence. To consider this new baseline, we adopted a sliding window approach to calculate the baseline. For each window with one second duration along the sixty second resting state MEG data, a quasi synthetic “shuffled” baseline was thus generated. To solve the inverse problem for each time frequency box, we selected the corresponding one second “shuffled” baseline along the time scale. We adopted this sliding window approach considering that the selection of baseline is an important aspect of the initialization of the prior, allowing the parcels to be active or not, and thus would be more reasonable to use the baseline which is temporally associated with the time frequency sample.

Appendix B for manuscript 2 in Chapter 7

Coherent Maximum Entropy on the mean (cMEM)

The relationship between source amplitudes and EEG/MEG measurements is expressed by the following linear model:

$$\mathbf{m}(t) = \mathbf{G}\mathbf{j}(t) + \mathbf{e}(t) \quad (\text{B.1})$$

$\mathbf{m}(t)$ is the q -dimensional measurement vector for EEG or MEG signal at time t where q denotes the number of EEG/MEG sensors, $\mathbf{j}(t)$ is the r -dimensional vector denoting current density of r dipolar sources at time t and \mathbf{G} is the lead field matrix with a dimension of $q \times r$. $\mathbf{e}(t)$ models an additive measurement noise at time t . We assume an anatomical constraint that the dipoles are orientated orthogonally to the surface of the cortex and hippocampus.

Within the MEM framework (Amblard et al., 2004), \mathbf{j} denoting the intensities of r dipolar sources is considered as a random variable described by the probability distribution $dp(\mathbf{j}) = p(\mathbf{j})d\mathbf{j}$. To regularize the inverse problem, we incorporate prior information on \mathbf{j} in the form of a reference distribution $d\nu(\mathbf{j})$. The Kullback Leibler divergence or v-entropy is defined by:

$$S_v(dp) = - \int_{\mathbf{j}} \log \left(\frac{dp(\mathbf{j})}{d\nu(\mathbf{j})} \right) dp(\mathbf{j}) = - \int_{\mathbf{j}} f(\mathbf{j}) \log (f(\mathbf{j})) d\nu(\mathbf{j}) \quad (\text{B.2})$$

Where f is a ν -density of dp defined as $dp(\mathbf{j}) = f(\mathbf{j})d\nu(\mathbf{j})$. The ν -entropy $S_v(dp)$ measures the amount of information brought by the data with respect to the prior $d\nu$. We introduce a data fit constraint as the set of probability distributions on \mathbf{j} that explains the data on average.

$$\mathbf{m} - [\mathbf{G}|\mathbf{I}_q] \begin{bmatrix} E_{dp}[\mathbf{j}] \\ \mathbf{e} \end{bmatrix} = 0, \quad dp \in C_M \quad (\text{B.3})$$

Where C_M is the set of probability distributions on \mathbf{j} that explains the data on average, $E_{dp}[\mathbf{j}] = \int_{\mathbb{R}} \mathbf{j} dp(\mathbf{j})$ is the mathematical expectation of \mathbf{j} with respect to the probability distribution dp and \mathbf{I}_q is a $q \times q$ identity matrix. Among all the possible distributions of $dp(\mathbf{j})$ that explain the data \mathbf{m} on average, MEM solution is derived from maximizing the ν -entropy (Amblard et al., 2004; Grova et al., 2006). More details on MEM formulations are described in Chowdhury et al. (2016). The key feature of this framework is a spatial prior model, assuming that brain activity is organized

within a set of K non-overlapping and independent parcels. The reference distribution $dv(\mathbf{j})$ for K parcels is defined as a joint distribution:

$$dv(\mathbf{j}) = dv_1(\mathbf{j}_1)dv_2(\mathbf{j}_2)dv_3(\mathbf{j}_3) \dots dv_k(\mathbf{j}_k) \dots dv_K(\mathbf{j}_K) \quad (\text{B.4})$$

The spatial parcellation used in MEM method uses a data driven parcellation technique (Lapalme et al., 2006). Each parcel k is characterized by an activation state S_k , which is a hidden state variable controlling the activation of the parcel. The reference distribution for each parcel is defined as:

$$dv_k(\mathbf{j}_k) = [(1 - \alpha_k)\delta(\mathbf{j}_k) + \alpha_k\mathcal{N}(\boldsymbol{\mu}_k, \boldsymbol{\Sigma}_k)(\mathbf{j}_k)]d\mathbf{j}_k \quad (\text{B.5})$$

Where α_k is the probability of the k^{th} parcel to be active ($Prob(S_k = 1)$). δ is a Dirac function which is used to switch off the parcel when $S_k = 0$. $\mathcal{N}(\boldsymbol{\mu}_k, \boldsymbol{\Sigma}_k)$ is a Gaussian distribution of the intensities of the k^{th} parcel, $\boldsymbol{\mu}_k$ describing the mean and $\boldsymbol{\Sigma}_k$ describing the covariance of all the sources within that k^{th} parcel.

In this study we considered the “coherent” version of MEM, entitled cMEM, originally introduced in Chowdhury et al 2013 and fully described in Chowdhury et al 2016. The term “coherent” refers to the fact that we are using a coherent spatial prior, i.e. a data driven parcellation in K parcels which is fixed along time, while the probability of being active α_k can evolve dynamically. In cMEM implementation, we also included local spatial smoothness within each parcel of the model.

Therefore, in cMEM, to initialize the spatial prior model, $\boldsymbol{\mu}_k$ is set to zero and $\boldsymbol{\Sigma}_k$ is defined as follows,

$$\boldsymbol{\Sigma}_k(t) = \eta_k(t)\mathbf{W}_k(\sigma)^T\mathbf{W}_k(\sigma) \quad (\text{B.6})$$

Where $\boldsymbol{\Sigma}_k(t)$ is the source covariance of parcel k at each time sample t , $\mathbf{W}_k(\sigma)$ is a spatial smoothness matrix which controls the local smoothness within the parcel (σ set to 0.6 (Chowdhury et al., 2013; Friston et al., 2008)) and $\eta_k(t)$ is defined as 5% of the energy of minimum norm estimate (MNE) solution (Lin et al., 2006) of all the r_k sources within the parcel k^{th} .

$$\eta_k(t) = 0.05 \frac{1}{r_k} \sum_{i \in r_k} \hat{\mathbf{j}}_{MNE}^2(i, t) \quad (\text{B.7})$$

The MNE solution $\hat{\mathbf{j}}_{MNE}$ was calculated using:

$$\hat{\mathbf{j}}_{MNE} = \operatorname{argmin}(\|\mathbf{m} - \mathbf{G}\mathbf{j}\|_{\Sigma_d}^2 + \lambda\|\mathbf{j}\|_{\Sigma}^2) = (\mathbf{G}^T\mathbf{\Sigma}_d\mathbf{G} + \lambda\mathbf{\Sigma})^{-1}\mathbf{G}^T\mathbf{\Sigma}_d\mathbf{m} \quad (\text{B.8})$$

Where $\mathbf{\Sigma}_d$ is the inverse of the noise covariance, $\mathbf{\Sigma}$ is the inverse of the source covariance ($\mathbf{\Sigma} = \mathbf{I}_r$, an $r \times r$ identity matrix), and λ is a hyperparameter to regularize the inversion. Standard L-Curve method was used to estimate λ .

After the reference distribution $d\mathbf{v}$ is initialized, the MEM solution is finally obtained through an optimization of a convex function obtained from the dual formulation of the maximum entropy principle (Amblard et al., 2004; Chowdhury et al., 2016; Chowdhury et al., 2013).

Depth-weighted cMEM (cMEM _{ω})

We are introducing a new parameter for cMEM implementation. Depth weighting within cMEM framework was first proposed and implemented by Cai et al. (2022) for functional Near InfraRed Spectroscopy 3D reconstruction. Similarly to the depth weighting strategy proposed for MNE (Lin et al., 2006), we introduced a location penalty in the source covariance by scaling it with the forward model and thus penalizing the superficial sources that exhibit larger amplitude and enhancing the contribution from deep sources. This penalization was tuned by the weighting parameter ω . Therefore, $\omega = 0.0$ refers to no depth weighting whereas increasing the value of ω would refer to more contribution from deep sources.

Therefore, in cMEM _{ω} depth weighting was implemented when initializing the spatial prior. The parcels are initialized using the source covariance of the parcel, $\mathbf{\Sigma}_k$ (Eq B.6). The source covariance in Equation B.6 was weighted by the forward model of each vertex, quantifying the influence of source depth, to a specific power ω . Therefore, following the method proposed and validated by Cai et al (2022), depth weighting was added at two levels:

- 1) To initialize the spatial prior model, we applied depth weighting in the source covariance for each parcel, $\mathbf{\Sigma}_k(t)_\omega$ as:

$$\mathbf{\Sigma}_k(t)_\omega = \mathbf{\Lambda}_{r_k}\eta_k(t)_\omega\mathbf{W}_k(\sigma)^T\mathbf{W}_k(\sigma) \quad (\text{B.9})$$

where $\mathbf{\Lambda}_{r_k}$ is the depth weighting matrix defined as the diagonal matrix of $(\mathbf{G}_k^T\mathbf{G}_k)^{-\omega}$, where \mathbf{G}_k is the gain matrix for r_k sources in parcel k .

2) For cMEM, $\eta_k(t)$ was defined as 5% of the energy of MNE solution of r_k sources within the parcel k (Eq. A.7). In cMEM $_{\omega}$, we replaced the MNE solution with the depth-weighted MNE solution. Equation B.7 and B.8 are modified as follows:

$$\eta_k(t)_{\omega} = 0.05 \frac{1}{r_k} \sum_{i \in r_k} \hat{\mathbf{j}}_{MNE_{\omega}}(i, t)^2 \quad (\text{B.10})$$

Where $\hat{\mathbf{j}}_{MNE_{\omega}}$ is the depth-weighted version of $\hat{\mathbf{j}}_{MNE}$ in equation B.8, where we used the diagonal of the source covariance matrix $\mathbf{\Sigma}$, weighted by the forward model, as follows:

$$\mathbf{\Sigma} = \mathbf{I}_r (\mathbf{G}^T \mathbf{G})^{-\omega} \quad (\text{B.11})$$

In this study, we considered a fixed depth weighting factor, $\omega = 0.5$ (zero would represent no depth-weighting) for the two levels reported in Equations B.9 and B.11. This is different from Cai et al. (2022), where they explored different pairs of weighting factors for Equations B.9 and B.11 using realistic simulations of Functional Near-infrared spectroscopy data and reported the best reconstruction accuracy for $\omega = 0.3$ for Equation B.9 and $\omega = 0.5$ for Equation A.11. In our EEG/MEG study, $\omega = 0.5$ was chosen to be consistent with the default value used in depth-weighted MNE (MNE $_{\omega}$) implementation for EEG/MEG source imaging in Brainstorm (Tadel et al., 2011). We also explored ω values ranging between 0.1 and 0.9 for one set of MEG simulations and observed that higher ω values enhanced the localization of deep sources but adversely affected the localization of superficial sources. Therefore, choosing $\omega = 0.5$ appeared as a reasonable compromise.

Wavelet Maximum Entropy on the mean (wMEM)

wMEM is another version of MEM specifically designed to localize brain oscillatory patterns. wMEM applies a discrete wavelet transformation (Daubechies wavelets) to characterize the oscillatory patterns in the data before applying the MEM solver (Lina et al., 2012). In this work, we are introducing a new parameter for wMEM implementation to allow depth weighting, resulting in the method wMEM $_{\omega}$ with $\omega=0.5$. wMEM $_{\omega}$ method was validated using the same simulation datasets as cMEM $_{\omega}$ and MNE $_{\omega}$ for localizing epileptic spikes. More details on wMEM implementation can be found in Lina et al. (2012) and Afnan et al. (2023).

In wMEM, the time expansion of data is substituted with a time-scale representation. In terms of wavelet expansion, equation A.1 can be written as:

$$\mathbf{d}_{s,n} = \mathbf{G}\mathbf{w}_{s,n} + \mathbf{w}^\epsilon_{s,n} \quad (\text{B.12})$$

Where $\mathbf{d}_{s,n}$, $\mathbf{w}_{s,n}$ and $\mathbf{w}^\epsilon_{s,n}$ are the wavelet coefficients for the data, the sources, and the measurement noise, respectively, for a particular discrete time index n and scale s ($s=1,2,3\dots$ with $s=0$ being the sampling scale). Depth weighting is implemented for the step when we initialize the spatial prior (as described for cMEM $_\omega$). The time-scale representation of Equation B.6 and B.7 are:

$$\mathbf{\Sigma}_k(s, n) = \eta_k(s, n) \mathbf{W}_k(\sigma)^T \mathbf{W}_k(\sigma) \quad (\text{B.13})$$

$$\eta_k(s, n) = 0.05 \frac{1}{r_k} \sum_{i \in r_k} \hat{\mathbf{j}}_{MNE}(i, s, n)^2 \quad (\text{A.14})$$

Where $\mathbf{\Sigma}_k(s, n)$ is the source covariance of parcel k at a particular discrete time index n and scale s . $\eta_k(s, n)$ is defined as 5% of the energy of MNE solution of all the sources (r_k) within the parcel k for a particular discrete time index n and scale s . The MNE solution $\hat{\mathbf{j}}_{MNE}$ is calculated in time-scale domain as:

$$\hat{\mathbf{j}}_{MNE} = \underset{\mathbf{j}}{\text{argmin}} \left(\|\mathbf{d}_{s,n} - \mathbf{G}\mathbf{w}_{s,n}\|_{\mathbf{\Sigma}_d}^2 + \lambda \|\mathbf{w}_{s,n}\|_{\mathbf{\Sigma}}^2 \right) = (\mathbf{G}^T \mathbf{\Sigma}_d \mathbf{G} + \lambda \mathbf{\Sigma})^{-1} \mathbf{G}^T \mathbf{\Sigma}_d \mathbf{d}_{s,n} \quad (\text{B.15})$$

Where $\mathbf{\Sigma} = \mathbf{I}_r$, an $r \times r$ identity matrix.

Depth-weighted wMEM (wMEM $_\omega$)

Similar to cMEM $_\omega$, the depth weighting was applied in wMEM at two levels. First, we applied depth weighting in the source covariance for each parcel, $\mathbf{\Sigma}_k(s, n)_\omega$ as:

$$\mathbf{\Sigma}_k(s, n)_\omega = \mathbf{\Lambda}_{r_k} \eta_k(s, n)_\omega \mathbf{W}_k(\sigma)^T \mathbf{W}_k(\sigma) \quad (\text{B.16})$$

where $\mathbf{\Lambda}_{r_k}$ is the depth weighting matrix defined as the diagonal matrix of $(\mathbf{G}_k^T \mathbf{G}_k)^{-\omega}$, where \mathbf{G}_k is the gain matrix for r_k sources in parcel k . Second, we defined $\eta_k(s, n)_\omega$ as 5% of the energy of the depth-weighted MNE solution, for which we modified equation A.15 by using the diagonal of the source covariance matrix $\mathbf{\Sigma}$, weighted by the forward model (see equation A.11: $\mathbf{\Sigma} = \mathbf{I}_r (\mathbf{G}^T \mathbf{G})^{-\omega}$). Similar to cMEM $_\omega$, we considered a fixed depth weighting factor, $\omega = 0.5$ for wMEM $_\omega$ at the two levels described by equations A.16 and A.11.

References

- Abdallah, C., Hedrich, T., Koupparis, A., Afnan, J., Hall, J. A., Gotman, J., Dubeau, F., von Ellenrieder, N., Frauscher, B., Kobayashi, E., & Grova, C. (2022). Clinical yield of electromagnetic source imaging and hemodynamic responses in epilepsy: Validation with intracerebral data. *Neurology*, 98(24), e2499-e2511.
- Abdallah, C., Maillard, L. G., Rikir, E., Jonas, J., Thiriaux, A., Gavaret, M., Bartolomei, F., Colnat-Coulbois, S., Vignal, J.-P., & Koessler, L. (2017). Localizing value of electrical source imaging: frontal lobe, malformations of cortical development and negative MRI related epilepsies are the best candidates. *NeuroImage: Clinical*, 16, 319-329.
- Adler, J., & Öktem, O. (2017). Solving ill-posed inverse problems using iterative deep neural networks. *Inverse Problems*, 33(12), 124007.
- Adrian, E. D., & Matthews, B. H. (1934). The Berger rhythm: potential changes from the occipital lobes in man. *Brain*, 57(4), 355-385.
- Afnan, J., Cai, Z., Lina, J. M., Abdallah, C., Delaire, E., Avigdor, T., Ros, V., Hedrich, T., von Ellenrieder, N., Kobayashi, E., Frauscher, B., Gotman, J., & Grova, C. (2024). EEG/MEG source imaging of deep brain activity within the maximum entropy on the mean framework: Simulations and validation in epilepsy. *Human Brain Mapping*, 45(10), e26720.
- Afnan, J., Cai, Z., Lina, J. M., Abdallah, C., Pellegrino, G., Arcara, G., Khajehpour, H., Frauscher, B., Gotman, J., & Grova, C. (in press). Validating MEG estimated resting state connectome with intracranial EEG. *Network Neuroscience*.
- Afnan, J., von Ellenrieder, N., Lina, J.-M., Pellegrino, G., Arcara, G., Cai, Z., Hedrich, T., Abdallah, C., Khajehpour, H., Frauscher, B., Gotman, J., & Grova, C. (2023). Validating MEG source imaging of resting state oscillatory patterns with an intracranial EEG atlas. *NeuroImage*, 120158.
- Agirre-Arrizubieta, Z., Huiskamp, G., Ferrier, C., Van Huffelen, A., & Leijten, F. (2009). Interictal magnetoencephalography and the irritative zone in the electrocorticogram. *Brain*, 132(11), 3060-3071.
- Aguilar-Velázquez, D., & Guzmán-Vargas, L. (2019). Critical synchronization and 1/f noise in inhibitory/excitatory rich-club neural networks. *Scientific reports*, 9(1), 1-13.
- Ahonen, A. I., Hämäläinen, M., Kajola, M., Knuutila, J., Laine, P., Lounasmaa, O. V., Parkkonen, L., Simola, J., & Tesche, C. D. (1993). 122-channel SQUID instrument for investigating the magnetic signals from the human brain. *Physica Scripta*, 1993(T49A), 198.
- Alarcon, G., Garcia Seoane, J., Binnie, C., Martin Miguel, M., Juler, J., Polkey, C., Elwes, R., & Ortiz Blasco, J. (1997). Origin and propagation of interictal discharges in the acute electrocorticogram. Implications for pathophysiology and surgical treatment of temporal lobe epilepsy. *Brain: a journal of neurology*, 120(12), 2259-2282.
- Alarcon, G., Guy, C., Binnie, C., Walker, S., Elwes, R., & Polkey, C. (1994). Intracerebral propagation of interictal activity in partial epilepsy: implications for source localisation. *Journal of Neurology, Neurosurgery & Psychiatry*, 57(4), 435-449.
- Alberto, G. E., Stapleton-Kotloski, J. R., Klorig, D. C., Rogers, E. R., Constantinidis, C., Daunais, J. B., & Godwin, D. W. (2021). MEG source imaging detects optogenetically-induced activity in cortical and subcortical networks. *Nature communications*, 12(1), 5259.

- Allouch, S., Kabbara, A., Duprez, J., Khalil, M., Modolo, J., & Hassan, M. (2023). Effect of channel density, inverse solutions and connectivity measures on EEG resting-state networks reconstruction: A simulation study. *NeuroImage*, 271, 120006.
- Allouch, S., Yochum, M., Kabbara, A., Duprez, J., Khalil, M., Wendling, F., Hassan, M., & Modolo, J. (2022). Mean-field modeling of brain-scale dynamics for the evaluation of EEG source-space networks. *Brain Topography*, 35(1), 54-65.
- Amblard, C., Lapalme, E., & Lina, J.-M. (2004). Biomagnetic source detection by maximum entropy and graphical models. *IEEE transactions on biomedical engineering*, 51(3), 427-442.
- Arnulfo, G., Hirvonen, J., Nobili, L., Palva, S., & Palva, J. M. (2015). Phase and amplitude correlations in resting-state activity in human stereotactical EEG recordings. *NeuroImage*, 112, 114-127.
- Asadzadeh, S., Rezaii, T. Y., Beheshti, S., Delpak, A., & Meshgini, S. (2020). A systematic review of EEG source localization techniques and their applications on diagnosis of brain abnormalities. *Journal of Neuroscience Methods*, 339, 108740.
- Attal, Y., Bhattacharjee, M., Yelnik, J., Cottureau, B., Lefèvre, J., Okada, Y., Bardinet, E., Chupin, M., & Baillet, S. (2009). Modelling and detecting deep brain activity with MEG and EEG. *IRBM* 30, 133–138. In.
- Attal, Y., & Schwartz, D. (2013). Assessment of subcortical source localization using deep brain activity imaging model with minimum norm operators: a MEG study. *PloS one*, 8(3), e59856.
- Avigdor, T., Abdallah, C., von Ellenrieder, N., Hedrich, T., Rubino, A., Russo, G. L., Bernhardt, B., Nobili, L., Grova, C., & Frauscher, B. (2021). Fast oscillations > 40 Hz localize the epileptogenic zone: An electrical source imaging study using high-density electroencephalography. *Clinical Neurophysiology*, 132(2), 568-580.
- Aydin, Ü., Pellegrino, G., Ali, O. B. K. b., Abdallah, C., Dubeau, F., Lina, J.-M., Kobayashi, E., & Grova, C. (2020). Magnetoencephalography resting state connectivity patterns as indicatives of surgical outcome in epilepsy patients. *Journal of Neural Engineering*, 17(3), 035007.
- Azeem, A., Abdallah, C., von Ellenrieder, N., El Kousseifi, C., Frauscher, B., & Gotman, J. (2024). Explaining slow seizure propagation with white matter tractography. *Brain*, awae192.
- Azeem, A., von Ellenrieder, N., Hall, J., Dubeau, F., Frauscher, B., & Gotman, J. (2021). Interictal spike networks predict surgical outcome in patients with drug-resistant focal epilepsy. *Annals of clinical and translational neurology*, 8(6), 1212-1223.
- Baccalá, L. A., & Sameshima, K. (2001). Partial directed coherence: a new concept in neural structure determination. *Biological cybernetics*, 84(6), 463-474.
- Badier, J.-M., Cosandier-Rimele, D., Bénar, C. G., Schwartz, D., Chauvel, P., & Wendling, F. (2007). Realistic synthetic background neuronal activity for the analysis of MEG probe configurations. 2007 29th Annual International Conference of the IEEE Engineering in Medicine and Biology Society,
- Badier, J.-M., Dubarry, A., Gavaret, M., Chen, S., Trébuchon, A., Marquis, P., Régis, J., Bartolomei, F., Bénar, C.-G., & Carron, R. (2017). Technical solutions for simultaneous MEG and SEEG recordings: towards routine clinical use. *Physiological Measurement*, 38(10), N118.
- Baillet, S., Mosher, J. C., & Leahy, R. M. (2001). Electromagnetic brain mapping. *IEEE Signal Processing Magazine*, 18(6), 14-30.

- Barborica, A., Mindruta, I., Sheybani, L., Spinelli, L., Oane, I., Pistol, C., Donos, C., López-Madróna, V. J., Vulliemoz, S., & Bénar, C.-G. (2021). Extracting seizure onset from surface EEG with independent component analysis: Insights from simultaneous scalp and intracerebral EEG. *NeuroImage: Clinical*, 32, 102838.
- Barkley, G. L., & Baumgartner, C. (2003). MEG and EEG in epilepsy. *Journal of Clinical Neurophysiology*, 20(3), 163-178.
- Barry, D. N., Barnes, G. R., Clark, I. A., & Maguire, E. A. (2019). The neural dynamics of novel scene imagery. *Journal of Neuroscience*, 39(22), 4375-4386.
- Bartolomei, F., Nica, A., Valenti-Hirsch, M. P., Adam, C., & Denuelle, M. (2018). Interpretation of SIEG recordings. *Neurophysiologie clinique*, 48(1), 53-57.
- Bastos, A. M., & Schoffelen, J.-M. (2016). A tutorial review of functional connectivity analysis methods and their interpretational pitfalls. *Frontiers in Systems Neuroscience*, 9, 175.
- Baumgartner, C., Koren, J. P., Britto-Arias, M., Zoche, L., & Pirker, S. (2019). Presurgical epilepsy evaluation and epilepsy surgery. *F1000Research*, 8.
- Baumgartner, C., Pataia, E., Lindinger, G., & Deecke, L. (2000). Neuromagnetic recordings in temporal lobe epilepsy. *Journal of Clinical Neurophysiology*, 17(2), 177-189.
- Bautista, R. E. D., Cobbs, M. A., Spencer, D. D., & Spencer, S. S. (1999). Prediction of surgical outcome by interictal epileptiform abnormalities during intracranial EEG monitoring in patients with extrahippocampal seizures. *Epilepsia*, 40(7), 880-890.
- Becker, H., Albers, L., Comon, P., Gribonval, R., Wendling, F., & Merlet, I. (2015). Brain-source imaging: From sparse to tensor models. *IEEE Signal Processing Magazine*, 32(6), 100-112.
- Bédard, C., & Destexhe, A. (2009). Macroscopic models of local field potentials and the apparent 1/f noise in brain activity. *Biophysical Journal*, 96(7), 2589-2603.
- Bellec, P., Rosa-Neto, P., Lyttelton, O. C., Benali, H., & Evans, A. C. (2010). Multi-level bootstrap analysis of stable clusters in resting-state fMRI. *NeuroImage*, 51(3), 1126-1139.
- Bénar, C.-G., Velmurugan, J., López-Madróna, V. J., Pizzo, F., & Badier, J.-M. (2021). Detection and localization of deep sources in magnetoencephalography: A review. *Current Opinion in Biomedical Engineering*, 18, 100285.
- Bénar, C. G., Grova, C., Jirsa, V. K., & Lina, J.-M. (2019). Differences in MEG and EEG power-law scaling explained by a coupling between spatial coherence and frequency: a simulation study. *Journal of computational neuroscience*, 47(1), 31-41.
- Bensaid, S., Modolo, J., Merlet, I., Wendling, F., & Benquet, P. (2019). COALIA: a computational model of human EEG for consciousness research. *Frontiers in Systems Neuroscience*, 13, 59.
- Berger, H. (1929). Über das elektroencephalogramm des menschen. *Archiv für Psychiatrie und Nervenkrankheiten*, 87(1), 527-570.
- Bernabei, J. M., Sinha, N., Arnold, T. C., Conrad, E., Ong, I., Pattnaik, A. R., Stein, J. M., Shinohara, R. T., Lucas, T. H., & Bassett, D. S. (2022). Normative intracranial EEG maps epileptogenic tissues in focal epilepsy. *Brain*, 145(6), 1949-1961.
- Besl, P. J., & McKay, N. D. (1992). Method for registration of 3-D shapes. Sensor fusion IV: control paradigms and data structures,
- Betzel, R. F., Medaglia, J. D., Kahn, A. E., Soffer, J., Schonhaut, D. R., & Bassett, D. S. (2019). Structural, geometric and genetic factors predict interregional brain connectivity patterns probed by electrocorticography. *Nature biomedical engineering*, 3(11), 902-916.

- Birot, G., Albera, L., Wendling, F., & Merlet, I. (2011). Localization of extended brain sources from EEG/MEG: the ExSo-MUSIC approach. *NeuroImage*, 56(1), 102-113.
- Biswal, B. B., Kylen, J. V., & Hyde, J. S. (1997). Simultaneous assessment of flow and BOLD signals in resting-state functional connectivity maps. *NMR in Biomedicine*, 10(4-5), 165-170.
- Blair, R. D. (2012). Temporal lobe epilepsy semiology. *Epilepsy research and treatment*, 2012(1), 751510.
- Blondel, V. D., Guillaume, J.-L., Lambiotte, R., & Lefebvre, E. (2008). Fast unfolding of communities in large networks. *Journal of statistical mechanics: theory and experiment*, 2008(10), P10008.
- Bódizs, R., Szalárdy, O., Horváth, C., Ujma, P. P., Gombos, F., Simor, P., Pótári, A., Zeising, M., Steiger, A., & Dresler, M. (2021). A set of composite, non-redundant EEG measures of NREM sleep based on the power law scaling of the Fourier spectrum. *Scientific reports*, 11(1), 1-18.
- Bosboom, J., Stoffers, D., Stam, C., Van Dijk, B., Verbunt, J., Berendse, H., & Wolters, E. C. (2006). Resting state oscillatory brain dynamics in Parkinson's disease: an MEG study. *Clinical Neurophysiology*, 117(11), 2521-2531.
- Brkić, D., Sommariva, S., Schuler, A.-L., Pascarella, A., Belardinelli, P., Isabella, S. L., Di Pino, G., Zago, S., Ferrazzi, G., & Rasero, J. (2023). The impact of ROI extraction method for MEG connectivity estimation: Practical recommendations for the study of resting state data. *NeuroImage*, 284, 120424.
- Brookes, M. J., Hale, J. R., Zumer, J. M., Stevenson, C. M., Francis, S. T., Barnes, G. R., Owen, J. P., Morris, P. G., & Nagarajan, S. S. (2011). Measuring functional connectivity using MEG: methodology and comparison with fMRI. *NeuroImage*, 56(3), 1082-1104.
- Brookes, M. J., Leggett, J., Rea, M., Hill, R. M., Holmes, N., Boto, E., & Bowtell, R. (2022). Magnetoencephalography with optically pumped magnetometers (OPM-MEG): the next generation of functional neuroimaging. *Trends in neurosciences*, 45(8), 621-634.
- Brookes, M. J., Stevenson, C. M., Barnes, G. R., Hillebrand, A., Simpson, M. I., Francis, S. T., & Morris, P. G. (2007). Beamformer reconstruction of correlated sources using a modified source model. *NeuroImage*, 34(4), 1454-1465.
- Brookes, M. J., Woolrich, M., Luckhoo, H., Price, D., Hale, J. R., Stephenson, M. C., Barnes, G. R., Smith, S. M., & Morris, P. G. (2011). Investigating the electrophysiological basis of resting state networks using magnetoencephalography. *Proceedings of the National Academy of Sciences*, 108(40), 16783-16788.
- Brookes, M. J., Woolrich, M. W., & Barnes, G. R. (2012). Measuring functional connectivity in MEG: a multivariate approach insensitive to linear source leakage. *NeuroImage*, 63(2), 910-920.
- Bruña, R., Maestú, F., & Pereda, E. (2018). Phase locking value revisited: teaching new tricks to an old dog. *Journal of Neural Engineering*, 15(5), 056011.
- Bruns, A., Eckhorn, R., Jokeit, H., & Ebner, A. (2000). Amplitude envelope correlation detects coupling among incoherent brain signals. *Neuroreport*, 11(7), 1509-1514.
- Bush, A., Zou, J. F., Lipski, W. J., Kokkinos, V., & Richardson, R. M. (2024). Aperiodic components of local field potentials reflect inherent differences between cortical and subcortical activity. *Cerebral Cortex*, 34(5), bhae186.
- Buzsáki, G., Logothetis, N., & Singer, W. (2013). Scaling brain size, keeping timing: evolutionary preservation of brain rhythms. *Neuron*, 80(3), 751-764.

- Cai, Z., Machado, A., Chowdhury, R. A., Spilkin, A., Vincent, T., Aydin, Ü., Pellegrino, G., Lina, J.-M., & Grova, C. (2022). Diffuse optical reconstructions of functional near infrared spectroscopy data using maximum entropy on the mean. *Scientific reports*, 12(1), 1-18.
- Calvetti, D., Pascarella, A., Pitolli, F., Somersalo, E., & Vantaggi, B. (2019). Brain activity mapping from MEG data via a hierarchical Bayesian algorithm with automatic depth weighting. *Brain Topography*, 32, 363-393.
- Capilla, A., Arana, L., García-Huésca, M., Melcón, M., Gross, J., & Campo, P. (2022). The natural frequencies of the resting human brain: an MEG-based atlas. *NeuroImage*, 119373.
- Catacuzzeno, L., Michelucci, A., & Franciolini, F. (2024). The Long Journey from Animal Electricity to the Discovery of Ion Channels and the Modelling of the Human Brain. *Biomolecules*, 14(6), 684.
- Chaoul, A. I., & Siegel, M. (2021). Cortical correlation structure of aperiodic neuronal population activity. *NeuroImage*, 245, 118672.
- Chatrian, G. E., Lettich, E., & Nelson, P. L. (1985). Ten percent electrode system for topographic studies of spontaneous and evoked EEG activities. *American Journal of EEG technology*, 25(2), 83-92.
- Cheyne, D., Bakhtazad, L., & Gaetz, W. (2006). Spatiotemporal mapping of cortical activity accompanying voluntary movements using an event-related beamforming approach. *Human Brain Mapping*, 27(3), 213-229.
- Chowdhury, R. (2017). *Localization of generators of epileptic activity in the brain using multimodal data fusion of EEG and MEG* [McGill University Libraries]. WorldCat. [Montreal]. <http://central.bac-lac.gc.ca/.redirect?app=damspub&id=05cfed08-74a1-4620-9071-ed0c244a63ca>
- Chowdhury, R., Merlet, I., Birot, G., Kobayashi, E., Nica, A., Biraben, A., Wendling, F., Lina, J.-M., Albera, L., & Grova, C. (2016). Complex patterns of spatially extended generators of epileptic activity: Comparison of source localization methods cMEM and 4-ExSo-MUSIC on high resolution EEG and MEG data. *NeuroImage*, 143, 175-195.
- Chowdhury, R. A., Lina, J. M., Kobayashi, E., & Grova, C. (2013). MEG source localization of spatially extended generators of epileptic activity: comparing entropic and hierarchical bayesian approaches. *PloS one*, 8(2), e55969.
- Chowdhury, R. A., Pellegrino, G., Aydin, Ü., Lina, J. M., Dubeau, F., Kobayashi, E., & Grova, C. (2018). Reproducibility of EEG-MEG fusion source analysis of interictal spikes: Relevance in presurgical evaluation of epilepsy. *Human Brain Mapping*, 39(2), 880-901.
- Chowdhury, R. A., Zerouali, Y., Hedrich, T., Heers, M., Kobayashi, E., Lina, J.-M., & Grova, C. (2015). MEG-EEG information fusion and electromagnetic source imaging: from theory to clinical application in epilepsy. *Brain Topography*, 28, 785-812.
- Coenen, A. (2024). The Erratic History of Electroencephalography. *Medical Research Archives*, 12(6).
- Coffey, E. B., Herholz, S. C., Chepesiuk, A. M., Baillet, S., & Zatorre, R. J. (2016). Cortical contributions to the auditory frequency-following response revealed by MEG. *Nature communications*, 7(1), 11070.
- Cohen, D. (1968). Magnetoencephalography: evidence of magnetic fields produced by alpha-rhythm currents. *Science*, 161(3843), 784-786.
- Cohen, D. (1972). Magnetoencephalography: detection of the brain's electrical activity with a superconducting magnetometer. *Science*, 175(4022), 664-666.
- Cohen, M. X. (2014). *Analyzing neural time series data: theory and practice*. MIT press.

- Colclough, G. L., Woolrich, M. W., Tewarie, P., Brookes, M. J., Quinn, A. J., & Smith, S. M. (2016). How reliable are MEG resting-state connectivity metrics? *NeuroImage*, 138, 284-293.
- Collins, D. L., Neelin, P., Peters, T. M., & Evans, A. C. (1994). Automatic 3D intersubject registration of MR volumetric data in standardized Talairach space. *Journal of computer assisted tomography*, 18(2), 192-205.
- Collura, T. F. (1993). History and evolution of electroencephalographic instruments and techniques. *Journal of Clinical Neurophysiology*, 10(4), 476-504.
- Colombo, M. A., Napolitani, M., Boly, M., Gosseries, O., Casarotto, S., Rosanova, M., Brichant, J.-F., Boveroux, P., Rex, S., & Laureys, S. (2019). The spectral exponent of the resting EEG indexes the presence of consciousness during unresponsiveness induced by propofol, xenon, and ketamine. *NeuroImage*, 189, 631-644.
- Corona, L., Tamilia, E., Perry, M. S., Madsen, J. R., Bolton, J., Stone, S. S., Stufflebeam, S. M., Pearl, P. L., & Papadelis, C. (2023). Non-invasive mapping of epileptogenic networks predicts surgical outcome. *Brain*, 146(5), 1916-1931.
- Cosandier-Rim   , D., Badier, J.-M., Chauvel, P., & Wendling, F. (2007). A physiologically plausible spatio-temporal model for EEG signals recorded with intracerebral electrodes in human partial epilepsy. *IEEE Transactions on Biomedical Engineering*, 54(3), 380-388.
- Cosandier-Rim   , D., Bartolomei, F., Merlet, I., Chauvel, P., & Wendling, F. (2012). Recording of fast activity at the onset of partial seizures: depth EEG vs. scalp EEG. *NeuroImage*, 59(4), 3474-3487.
- Cosandier-Rim   , D., Merlet, I., Badier, J.-M., Chauvel, P., & Wendling, F. (2008). The neuronal sources of EEG: modeling of simultaneous scalp and intracerebral recordings in epilepsy. *NeuroImage*, 42(1), 135-146.
- Crandall, P. H., Walter, R. D., & Rand, R. W. (1963). Clinical applications of studies on stereotactically implanted electrodes in temporal-lobe epilepsy. *Journal of Neurosurgery*, 20(10), 827-840.
- da Silva Castanheira, J., Wiesman, A. I., Hansen, J. Y., Misic, B., Baillet, S., Breitner, J., Poirier, J., Bellec, P., Bohbot, V., & Chakravarty, M. (2024). The neurophysiological brain-fingerprint of Parkinson's disease. *EBioMedicine*, 105.
- Dalal, S., Jerbi, K., Bertrand, O., Adam, C., Ducorps, A., Schwartz, D., Martinerie, J., & Lachaux, J.-P. (2013). Simultaneous MEG-intracranial EEG: new insights into the ability of MEG to capture oscillatory modulations in the neocortex and the hippocampus. *Epilepsy & Behavior*, 10.1016/j.yebeh.2013.1003.1012.
- Dalal, S. S., Baillet, S., Adam, C., Ducorps, A., Schwartz, D., Jerbi, K., Bertrand, O., Garnero, L., Martinerie, J., & Lachaux, J.-P. (2009). Simultaneous MEG and intracranial EEG recordings during attentive reading. *NeuroImage*, 45(4), 1289-1304.
- Dale, A. M., Fischl, B., & Sereno, M. I. (1999). Cortical surface-based analysis: I. Segmentation and surface reconstruction. *NeuroImage*, 9(2), 179-194.
- Dale, A. M., Liu, A. K., Fischl, B. R., Buckner, R. L., Belliveau, J. W., Lewine, J. D., & Halgren, E. (2000). Dynamic statistical parametric mapping: combining fMRI and MEG for high-resolution imaging of cortical activity. *Neuron*, 26(1), 55-67.
- Dale, A. M., & Sereno, M. I. (1993). Improved localization of cortical activity by combining EEG and MEG with MRI cortical surface reconstruction: a linear approach. *Journal of cognitive neuroscience*, 5(2), 162-176.

- Darvas, F., Pantazis, D., Kucukaltun-Yildirim, E., & Leahy, R. (2004). Mapping human brain function with MEG and EEG: methods and validation. *NeuroImage*, 23, S289-S299.
- Dash, D., Ferrari, P., Babajani-Feremi, A., Borna, A., Schwindt, P. D., & Wang, J. (2021). Magnetometers vs Gradiometers for Neural Speech Decoding. 2021 43rd Annual International Conference of the IEEE Engineering in Medicine & Biology Society (EMBC),
- De Munck, J. C., Van Dijk, B. W., & Spekreijse, H. (1988). Mathematical dipoles are adequate to describe realistic generators of human brain activity. *IEEE Transactions on Biomedical Engineering*, 35(11), 960-966.
- De Stefano, P., Carboni, M., Marquis, R., Spinelli, L., Seeck, M., & Vulliemoz, S. (2022). Increased delta power as a scalp marker of epileptic activity: a simultaneous scalp and intracranial electroencephalography study. *European journal of neurology*, 29(1), 26-35.
- Deligianni, F., Centeno, M., Carmichael, D. W., & Clayden, J. D. (2014). Relating resting-state fMRI and EEG whole-brain connectomes across frequency bands. *Frontiers in neuroscience*, 8, 258.
- DeSalvo, M. N., Douw, L., Tanaka, N., Reinsberger, C., & Stufflebeam, S. M. (2014). Altered structural connectome in temporal lobe epilepsy. *Radiology*, 270(3), 842-848.
- Donoghue, T., Haller, M., Peterson, E. J., Varma, P., Sebastian, P., Gao, R., Noto, T., Lara, A. H., Wallis, J. D., & Knight, R. T. (2020). Parameterizing neural power spectra into periodic and aperiodic components. *Nature neuroscience*, 23(12), 1655-1665.
- Donoghue, T., Schaworonkow, N., & Voytek, B. (2021). Methodological considerations for studying neural oscillations. *European journal of neuroscience*.
- Duan, W., Chen, X., Wang, Y.-J., Zhao, W., Yuan, H., & Lei, X. (2021). Reproducibility of power spectrum, functional connectivity and network construction in resting-state EEG. *Journal of Neuroscience Methods*, 348, 108985.
- Dubarry, A.-S., Badier, J.-M., Trébuchon-Da Fonseca, A., Gavaret, M., Carron, R., Bartolomei, F., Liégeois-Chauvel, C., Régis, J., Chauvel, P., & Alario, F.-X. (2014). Simultaneous recording of MEG, EEG and intracerebral EEG during visual stimulation: from feasibility to single-trial analysis. *NeuroImage*, 99, 548-558.
- Ebersole, J. S. (1997). Defining epileptogenic foci: past, present, future. *Journal of Clinical Neurophysiology*, 14(6), 470-483.
- Enatsu, R., & Mikuni, N. (2016). Invasive evaluations for epilepsy surgery: a review of the literature. *Neurologia medico-chirurgica*, 56(5), 221-227.
- Falco-Walter, J. (2020). Epilepsy—definition, classification, pathophysiology, and epidemiology. *Seminars in neurology*,
- Fender, D. (1987). Source localization of brain electrical activity. *Handbook of electroencephalography and clinical neurophysiology*, 355-403.
- Ferree, T. C., Eriksen, K. J., & Tucker, D. M. (2000). Regional head tissue conductivity estimation for improved EEG analysis. *IEEE Transactions on Biomedical Engineering*, 47(12), 1584-1592.
- Finger, H., Bönstrup, M., Cheng, B., Messé, A., Hilgetag, C., Thomalla, G., Gerloff, C., & König, P. (2016). Modeling of large-scale functional brain networks based on structural connectivity from DTI: comparison with EEG derived phase coupling networks and evaluation of alternative methods along the modeling path. *PLoS computational biology*, 12(8), e1005025.

- Fisher, R. S., Acevedo, C., Arzimanoglou, A., Bogacz, A., Cross, J. H., Elger, C. E., Engel Jr, J., Forsgren, L., French, J. A., & Glynn, M. (2014). ILAE official report: a practical clinical definition of epilepsy. *Epilepsia*, 55(4), 475-482.
- Fisher, R. S., Boas, W. V. E., Blume, W., Elger, C., Genton, P., Lee, P., & Engel Jr, J. (2005). Epileptic seizures and epilepsy: definitions proposed by the International League Against Epilepsy (ILAE) and the International Bureau for Epilepsy (IBE). *Epilepsia*, 46(4), 470-472.
- Fisher, R. S., Cross, J. H., D'souza, C., French, J. A., Haut, S. R., Higurashi, N., Hirsch, E., Jansen, F. E., Lagae, L., & Moshé, S. L. (2017). Instruction manual for the ILAE 2017 operational classification of seizure types. *Epilepsia*, 58(4), 531-542.
- Fonov, V. S., Evans, A. C., McKinstry, R. C., Almlí, C. R., & Collins, D. (2009). Unbiased nonlinear average age-appropriate brain templates from birth to adulthood. *NeuroImage*(47), S102.
- Fox, M. D., & Raichle, M. E. (2007). Spontaneous fluctuations in brain activity observed with functional magnetic resonance imaging. *Nature reviews neuroscience*, 8(9), 700-711.
- Frauscher, B., von Ellenrieder, N., Dubeau, F., & Gotman, J. (2015). Scalp spindles are associated with widespread intracranial activity with unexpectedly low synchrony. *NeuroImage*, 105, 1-12.
- Frauscher, B., Von Ellenrieder, N., Zelmann, R., Doležalová, I., Minotti, L., Olivier, A., Hall, J., Hoffmann, D., Nguyen, D. K., & Kahane, P. (2018). Atlas of the normal intracranial electroencephalogram: neurophysiological awake activity in different cortical areas. *Brain*, 141(4), 1130-1144.
- Friston, K., Harrison, L., Daunizeau, J., Kiebel, S., Phillips, C., Trujillo-Barreto, N., Henson, R., Flandin, G., & Mattout, J. (2008). Multiple sparse priors for the M/EEG inverse problem. *NeuroImage*, 39(3), 1104-1120.
- Friston, K. J., Frith, C. D., Liddle, P. F., & Frackowiak, R. S. (1993). Functional connectivity: the principal-component analysis of large (PET) data sets. *Journal of Cerebral Blood Flow & Metabolism*, 13(1), 5-14.
- Fuchs, M., Wagner, M., Köhler, T., & Wischmann, H.-A. (1999). Linear and nonlinear current density reconstructions. *Journal of Clinical Neurophysiology*, 16(3), 267-295.
- Fuchs, M., Wagner, M., Wischmann, H.-A., Köhler, T., Theißen, A., Drenckhahn, R., & Buchner, H. (1998). Improving source reconstructions by combining bioelectric and biomagnetic data. *Electroencephalography and clinical neurophysiology*, 107(2), 93-111.
- Garcés, P., Martín-Buro, M. C., & Maestú, F. (2016). Quantifying the test-retest reliability of magnetoencephalography resting-state functional connectivity. *Brain connectivity*, 6(6), 448-460.
- Gavaret, M., Dubarry, A.-S., Carron, R., Bartolomei, F., Trébuchon, A., & Bénar, C.-G. (2016). Simultaneous SEEG-MEG-EEG recordings overcome the SEEG limited spatial sampling. *Epilepsy research*, 128, 68-72.
- Giraud, A.-L., & Poeppel, D. (2012). Cortical oscillations and speech processing: emerging computational principles and operations. *Nature neuroscience*, 15(4), 511-517.
- Glasser, M. F., Smith, S. M., Marcus, D. S., Andersson, J. L., Auerbach, E. J., Behrens, T. E., Coalson, T. S., Harms, M. P., Jenkinson, M., & Moeller, S. (2016). The human connectome project's neuroimaging approach. *Nature neuroscience*, 19(9), 1175-1187.

- Gloor, P. (1985). Neuronal generators and the problem of localization in electroencephalography: application of volume conductor theory to electroencephalography. *Journal of Clinical Neurophysiology*, 2(4), 327-354.
- Goldenholz, D. M., Ahlfors, S. P., Hämäläinen, M. S., Sharon, D., Ishitobi, M., Vaina, L. M., & Stufflebeam, S. M. (2009). Mapping the signal-to-noise-ratios of cortical sources in magnetoencephalography and electroencephalography. *Human Brain Mapping*, 30(4), 1077-1086.
- Gorodnitsky, I. F., George, J. S., & Rao, B. D. (1995). Neuromagnetic source imaging with FOCUSS: a recursive weighted minimum norm algorithm. *Electroencephalography and clinical neurophysiology*, 95(4), 231-251.
- Gotman, J., & Pittau, F. (2011). Combining EEG and fMRI in the study of epileptic discharges. *Epilepsia*, 52, 38-42.
- Gramfort, A., Kowalski, M., & Hämäläinen, M. (2012). Mixed-norm estimates for the M/EEG inverse problem using accelerated gradient methods. *Physics in Medicine & Biology*, 57(7), 1937.
- Gramfort, A., Papadopoulos, T., Olivi, E., & Clerc, M. (2010). OpenMEEG: opensource software for quasistatic bioelectromagnetics. *Biomedical engineering online*, 9(1), 1-20.
- Gramfort, A., Papadopoulos, T., Olivi, E., & Clerc, M. (2011). Forward field computation with OpenMEEG. *Computational intelligence and neuroscience*, 2011(1), 923703.
- Granger, C. W. (1969). Investigating causal relations by econometric models and cross-spectral methods. *Econometrica: journal of the Econometric Society*, 424-438.
- Groppe, D. M., Bickel, S., Keller, C. J., Jain, S. K., Hwang, S. T., Harden, C., & Mehta, A. D. (2013). Dominant frequencies of resting human brain activity as measured by the electrocorticogram. *NeuroImage*, 79, 223-233.
- Grova, C., Aiguabella, M., Zelmann, R., Lina, J. M., Hall, J. A., & Kobayashi, E. (2016). Intracranial EEG potentials estimated from MEG sources: A new approach to correlate MEG and iEEG data in epilepsy. *Human brain mapping*, 37(5), 1661-1683.
- Grova, C., Daunizeau, J., Kobayashi, E., Bagshaw, A. P., Lina, J.-M., Dubeau, F., & Gotman, J. (2008). Concordance between distributed EEG source localization and simultaneous EEG-fMRI studies of epileptic spikes. *NeuroImage*, 39(2), 755-774.
- Grova, C., Daunizeau, J., Lina, J.-M., Bénar, C. G., Benali, H., & Gotman, J. (2006). Evaluation of EEG localization methods using realistic simulations of interictal spikes. *NeuroImage*, 29(3), 734-753.
- Guekht, A., Brodie, M., Secco, M., Li, S., Volkers, N., & Wiebe, S. (2021). The road to a World Health Organization global action plan on epilepsy and other neurological disorders. *Epilepsia*, 62(5), 1057-1063.
- Hämäläinen, M., Hari, R., Ilmoniemi, R. J., Knuutila, J., & Lounasmaa, O. V. (1993). Magnetoencephalography—theory, instrumentation, and applications to noninvasive studies of the working human brain. *Reviews of modern Physics*, 65(2), 413.
- Hämäläinen, M. S., & Ilmoniemi, R. J. (1994). Interpreting magnetic fields of the brain: minimum norm estimates. *Medical & biological engineering & computing*, 32, 35-42.
- Hamalainen, M. S., & Sarvas, J. (1989). Realistic conductivity geometry model of the human head for interpretation of neuromagnetic data. *IEEE Transactions on Biomedical Engineering*, 36(2), 165-171.

- Hamandi, K., Routley, B. C., Koelewijn, L., & Singh, K. D. (2016). Non-invasive brain mapping in epilepsy: applications from magnetoencephalography. *Journal of Neuroscience Methods*, 260, 283-291.
- Hara, K., Lin, F.-H., Camposano, S., Foxe, D., Grant, P., Bourgeois, B., Ahlfors, S., & Stufflebeam, S. (2007). Magnetoencephalographic mapping of interictal spike propagation: a technical and clinical report. *American journal of neuroradiology*, 28(8), 1486-1488.
- Hari, R. (1990). The neuromagnetic method in the study of the human auditory cortex. *Auditory evoked magnetic fields and potentials advances in audiology*, 6, 222/282.
- Hari, R., Baillet, S., Barnes, G., Burgess, R., Forss, N., Gross, J., Hämäläinen, M., Jensen, O., Kakigi, R., & Mauguière, F. (2018). IFCN-endorsed practical guidelines for clinical magnetoencephalography (MEG). *Clinical Neurophysiology*, 129(8), 1720-1747.
- Hassan, M., Merlet, I., Mheich, A., Kabbara, A., Biraben, A., Nica, A., & Wendling, F. (2017). Identification of interictal epileptic networks from dense-EEG. *Brain Topography*, 30, 60-76.
- Hauf, M., Jann, K., Schindler, K., Scheidegger, O., Meyer, K., Rummel, C., Mariani, L., König, T., & Wiest, R. (2012). Localizing seizure-onset zones in presurgical evaluation of drug-resistant epilepsy by electroencephalography/fMRI: effectiveness of alternative thresholding strategies. *American journal of neuroradiology*, 33(9), 1818-1824.
- Haufe, S., Nikulin, V. V., Müller, K.-R., & Nolte, G. (2013). A critical assessment of connectivity measures for EEG data: a simulation study. *NeuroImage*, 64, 120-133.
- He, B. J. (2014). Scale-free brain activity: past, present, and future. *Trends in cognitive sciences*, 18(9), 480-487.
- Hedrich, T. (2020). Combining high-density electrical source imaging and hemodynamic responses to epileptic discharges.
- Hedrich, T., Pellegrino, G., Kobayashi, E., Lina, J.-M., & Grova, C. (2017). Comparison of the spatial resolution of source imaging techniques in high-density EEG and MEG. *NeuroImage*, 157, 531-544.
- Heers, M., Chowdhury, R. A., Hedrich, T., Dubeau, F., Hall, J. A., Lina, J.-M., Grova, C., & Kobayashi, E. (2016). Localization accuracy of distributed inverse solutions for electric and magnetic source imaging of interictal epileptic discharges in patients with focal epilepsy. *Brain topography*, 29(1), 162-181.
- Heller, L., & van Hulsteyn, D. B. (1992). Brain stimulation using electromagnetic sources: theoretical aspects. *Biophysical journal*, 63(1), 129-138.
- Helmholtz, H. v. (1853). Ueber einige Gesetze der Vertheilung elektrischer Ströme in körperlichen Leitern, mit Anwendung auf die thierisch-elektrischen Versuche (Schluss.). *Annalen der Physik*, 165(7), 353-377.
- Henson, R. N., Flandin, G., Friston, K. J., & Mattout, J. (2010). A Parametric Empirical Bayesian framework for fMRI-constrained MEG/EEG source reconstruction. *Human Brain Mapping*, 31(10), 1512-1531.
- Hillebrand, A., & Barnes, G. R. (2011). Practical constraints on estimation of source extent with MEG beamformers. *NeuroImage*, 54(4), 2732-2740.
- Hillebrand, A., Barnes, G. R., Bosboom, J. L., Berendse, H. W., & Stam, C. J. (2012). Frequency-dependent functional connectivity within resting-state networks: an atlas-based MEG beamformer solution. *NeuroImage*, 59(4), 3909-3921.

- Hipp, J. F., Hawellek, D. J., Corbetta, M., Siegel, M., & Engel, A. K. (2012). Large-scale cortical correlation structure of spontaneous oscillatory activity. *Nature neuroscience*, 15(6), 884-890.
- Hipp, J. F., & Siegel, M. (2015). BOLD fMRI correlation reflects frequency-specific neuronal correlation. *Current Biology*, 25(10), 1368-1374.
- Hirano, Y., & Uhlhaas, P. J. (2021). Current findings and perspectives on aberrant neural oscillations in schizophrenia. *Psychiatry and clinical neurosciences*, 75(12), 358-368.
- Hnazaee, M. F., Wittevrongel, B., Khachatryan, E., Libert, A., Carrette, E., Dauwe, I., Meurs, A., Boon, P., Van Roost, D., & Van Hulle, M. M. (2020). Localization of deep brain activity with scalp and subdural EEG. *NeuroImage*, 223, 117344.
- Hoekema, R., Wieneke, G., Leijten, F., Van Veelen, C., Van Rijen, P., Huiskamp, G., Ansems, J., & Van Huffelen, A. (2003). Measurement of the conductivity of skull, temporarily removed during epilepsy surgery. *Brain Topography*, 16, 29-38.
- Hoshi, H., & Shigihara, Y. (2020). Age-and gender-specific characteristics of the resting-state brain activity: a magnetoencephalography study. *Aging (Albany NY)*, 12(21), 21613.
- Huang, M., Mosher, J. C., & Leahy, R. (1999). A sensor-weighted overlapping-sphere head model and exhaustive head model comparison for MEG. *Physics in Medicine & Biology*, 44(2), 423.
- Huang, Y., Hu, K., Green, A. L., Ma, X., Gillies, M. J., Wang, S., Fitzgerald, J. J., Pan, Y., Martin, S., & Huang, P. (2020). Dynamic changes in rhythmic and arrhythmic neural signatures in the subthalamic nucleus induced by anaesthesia and tracheal intubation. *British journal of anaesthesia*, 125(1), 67-76.
- Huang, Y., Sun, B., Debarros, J., Zhang, C., Zhan, S., Li, D., Zhang, C., Wang, T., Huang, P., & Lai, Y. (2021). Increased theta/alpha synchrony in the habenula-prefrontal network with negative emotional stimuli in human patients. *Elife*, 10.
- Hufnagel, A., Dümpelmann, M., Zentner, J., Schijns, O., & Elger, C. (2000). Clinical relevance of quantified intracranial interictal spike activity in presurgical evaluation of epilepsy. *Epilepsia*, 41(4), 467-478.
- Ikemoto, S., von Ellenrieder, N., & Gotman, J. (2022). Electroencephalography–functional magnetic resonance imaging of epileptiform discharges: Noninvasive investigation of the whole brain. *Epilepsia*, 63(11), 2725-2744.
- Ioannides, A., Liu, L., Kwapien, J., Drozd, S., & Streit, M. (2000). Coupling of regional activations in a human brain during an object and face affect recognition task. *Human Brain Mapping*, 11(2), 77-92.
- Jayakar, P., Gotman, J., Harvey, A. S., Palmini, A., Tassi, L., Schomer, D., Dubeau, F., Bartolomei, F., Yu, A., & Kršek, P. (2016). Diagnostic utility of invasive EEG for epilepsy surgery: indications, modalities, and techniques. *Epilepsia*, 57(11), 1735-1747.
- Jaynes, E. T. (1957). Information theory and statistical mechanics. *Physical review*, 106(4), 620.
- Jeffs, B., Leahy, R., & Singh, M. (1987). An evaluation of methods for neuromagnetic image reconstruction. *IEEE Transactions on Biomedical Engineering*(9), 713-723.
- Jensen, O., Spaak, E., & Zumer, J. M. (2019). Human brain oscillations: From physiological mechanisms to analysis and cognition. *Magnetoencephalography: From signals to dynamic cortical networks*, 471-517.
- Josephson, B. D. (1962). Possible new effects in superconductive tunnelling. *Physics letters*, 1(7), 251-253.

- Jurcak, V., Tsuzuki, D., & Dan, I. (2007). 10/20, 10/10, and 10/5 systems revisited: their validity as relative head-surface-based positioning systems. *NeuroImage*, 34(4), 1600-1611.
- Kaiboriboon, K., Nagarajan, S., Mantle, M., & Kirsch, H. E. (2010). Interictal MEG/MSI in intractable mesial temporal lobe epilepsy: spike yield and characterization. *Clinical Neurophysiology*, 121(3), 325-331.
- Kaipio, J., & Somersalo, E. (2006). *Statistical and computational inverse problems* (Vol. 160). Springer Science & Business Media.
- Kakisaka, Y., Alkawadri, R., Wang, Z. I., Enatsu, R., Mosher, J. C., Dubarry, A.-S., Alexopoulos, A. V., & Burgess, R. C. (2013). Sensitivity of scalp 10–20 EEG and magnetoencephalography. *Epileptic disorders*, 15, 27-31.
- Kakisaka, Y., Kubota, Y., Wang, Z. I., Piao, Z., Mosher, J. C., Gonzalez-Martinez, J., Jin, K., Alexopoulos, A. V., & Burgess, R. C. (2012). Use of simultaneous depth and MEG recording may provide complementary information regarding the epileptogenic region. *Epileptic Disorders*, 14, 298-303.
- Kaminski, M., & Liang, H. (2005). Causal influence: advances in neurosignal analysis. *Critical Reviews™ in Biomedical Engineering*, 33(4).
- Kandel, E. R., Koester, J., Mack, S., & Siegelbaum, S. (2021). *Principles of neural science* (Sixth edition ed.). McGraw Hill.
- Kane, N., Acharya, J., Beniczky, S., Caboclo, L., Finnigan, S., Kaplan, P. W., Shibasaki, H., Pressler, R., & van Putten, M. J. (2017). A revised glossary of terms most commonly used by clinical electroencephalographers and updated proposal for the report format of the EEG findings. Revision 2017. *Clinical neurophysiology practice*, 2, 170.
- Keitel, A., & Gross, J. (2016). Individual human brain areas can be identified from their characteristic spectral activation fingerprints. *PLoS biology*, 14(6), e1002498.
- Kim, J. A., & Davis, K. D. (2021). Magnetoencephalography: Physics, techniques, and applications in the basic and clinical neurosciences. *Journal of neurophysiology*, 125(3), 938-956.
- Kim, S., & Mountz, J. M. (2011). SPECT imaging of epilepsy: an overview and comparison with F-18 FDG PET. *International journal of molecular imaging*, 2011(1), 813028.
- Kobayashi, K., Yoshinaga, H., Ohtsuka, Y., & Gotman, J. (2005). Dipole modeling of epileptic spikes can be accurate or misleading. *Epilepsia*, 46(3), 397-408.
- Koessler, L., Benar, C., Maillard, L., Badier, J.-M., Vignal, J. P., Bartolomei, F., Chauvel, P., & Gavaret, M. (2010). Source localization of ictal epileptic activity investigated by high resolution EEG and validated by SEEG. *NeuroImage*, 51(2), 642-653.
- Koessler, L., Cecchin, T., Colnat-Coulbois, S., Vignal, J.-P., Jonas, J., Vespignani, H., Ramantani, G., & Maillard, L. G. (2015). Catching the invisible: mesial temporal source contribution to simultaneous EEG and SEEG recordings. *Brain topography*, 28, 5-20.
- Krings, T., Chiappa, K. H., Cuffin, B. N., Cochius, J. I., Connolly, S., & Cosgrove, G. R. (1999). Accuracy of EEG dipole source localization using implanted sources in the human brain. *Clinical Neurophysiology*, 110(1), 106-114.
- Krishnaswamy, P., Obregon-Henao, G., Ahveninen, J., Khan, S., Babadi, B., Iglesias, J. E., Hämäläinen, M. S., & Purdon, P. L. (2017). Sparsity enables estimation of both subcortical and cortical activity from MEG and EEG. *Proceedings of the National Academy of Sciences*, 114(48), E10465-E10474.
- Kural, M. A., Duez, L., Sejer Hansen, V., Larsson, P. G., Rampp, S., Schulz, R., Tankisi, H., Wennberg, R., Bibby, B. M., & Scherg, M. (2020). Criteria for defining interictal

- epileptiform discharges in EEG: a clinical validation study. *Neurology*, 94(20), e2139-e2147.
- Kybic, J., Clerc, M., Abboud, T., Faugeras, O., Keriven, R., & Papadopoulos, T. (2005). A common formalism for the integral formulations of the forward EEG problem. *IEEE transactions on medical imaging*, 24(1), 12-28.
- Labat, R. (1951). *Traité akkadien de diagnostics et pronostics médicaux*.
- Lachaux, J. P., Rodriguez, E., Martinerie, J., & Varela, F. J. (1999). Measuring phase synchrony in brain signals. *Human Brain Mapping*, 8(4), 194-208.
- Lagarde, S., Bénar, C.-G., Wendling, F., & Bartolomei, F. (2022). Interictal functional connectivity in focal refractory epilepsies investigated by intracranial EEG. *Brain connectivity*, 12(10), 850-869.
- Lai, Y., Van Drongelen, W., Ding, L., Hecox, K., Towle, V., Frim, D., & He, B. (2005). Estimation of in vivo human brain-to-skull conductivity ratio from simultaneous extra-and intracranial electrical potential recordings. *Clinical Neurophysiology*, 116(2), 456-465.
- Landman, B. A., & Warfield, S. K. (2019). *MICCAI 2012: Workshop on multi-atlas labeling*. éditeur non identifié.
- Lapalme, E., Lina, J.-M., & Mattout, J. (2006). Data-driven parceling and entropic inference in MEG. *NeuroImage*, 30(1), 160-171.
- Larson-Prior, L. J., Oostenveld, R., Della Penna, S., Michalareas, G., Prior, F., Babajani-Feremi, A., Schoffelen, J.-M., Marzetti, L., de Pasquale, F., & Di Pompeo, F. (2013). Adding dynamics to the Human Connectome Project with MEG. *NeuroImage*, 80, 190-201.
- Le Van Quyen, M., Foucher, J., Lachaux, J.-P., Rodriguez, E., Lutz, A., Martinerie, J., & Varela, F. J. (2001). Comparison of Hilbert transform and wavelet methods for the analysis of neuronal synchrony. *Journal of Neuroscience Methods*, 111(2), 83-98.
- Lecaignard, F., & Mattout, J. (2015). Forward models for EEG/MEG. *Brain Mapping*, 549-555.
- Lee, K., Khoo, H. M., Lina, J.-M., Dubeau, F., Gotman, J., & Grova, C. (2018). Disruption, emergence and lateralization of brain network hubs in mesial temporal lobe epilepsy. *NeuroImage: Clinical*, 20, 71-84.
- Leijten, F. S., Huiskamp, G.-J. M., Hilgersom, I., & Van Huffelen, A. C. (2003). High-resolution source imaging in mesiotemporal lobe epilepsy: a comparison between MEG and simultaneous EEG. *Journal of Clinical Neurophysiology*, 20(4), 227-238.
- Leopold, D. A., Murayama, Y., & Logothetis, N. K. (2003). Very slow activity fluctuations in monkey visual cortex: implications for functional brain imaging. *Cerebral Cortex*, 13(4), 422-433.
- Levira, F., Thurman, D. J., Sander, J. W., Hauser, W. A., Hesdorffer, D. C., Masanja, H., Odermatt, P., Logroscino, G., Newton, C. R., & Epilepsy, E. C. o. t. I. L. A. (2017). Premature mortality of epilepsy in low-and middle-income countries: a systematic review from the Mortality Task Force of the International League Against Epilepsy. *Epilepsia*, 58(1), 6-16.
- Li, C., & Van Buren, J. (1972). Micro-electrode recordings in the brain of man with particular reference to epilepsy and dyskinesia. *Neurophysiology Studied in Man. Amsterdam: Excerpta Medica*, 49-63.
- Limpiti, T., Van Veen, B. D., & Wakai, R. T. (2006). Cortical patch basis model for spatially extended neural activity. *IEEE Transactions on Biomedical Engineering*, 53(9), 1740-1754.

- Lin, F.-H., Witzel, T., Ahlfors, S. P., Stufflebeam, S. M., Belliveau, J. W., & Hämäläinen, M. S. (2006). Assessing and improving the spatial accuracy in MEG source localization by depth-weighted minimum-norm estimates. *NeuroImage*, 31(1), 160-171.
- Lina, J.-M., Chowdhury, R., Lemay, E., Kobayashi, E., & Grova, C. (2012). Wavelet-based localization of oscillatory sources from magnetoencephalography data. *IEEE Transactions on Biomedical Engineering*, 61(8), 2350-2364.
- Liu, A. K., Dale, A. M., & Belliveau, J. W. (2002). Monte Carlo simulation studies of EEG and MEG localization accuracy. *Human Brain Mapping*, 16(1), 47-62.
- Liu, Y., Su, H., & Li, C. (2024). Effect of Inverse Solutions, Connectivity Measures, and Node Sizes on EEG Source Network: A Simultaneous EEG Study. *IEEE Transactions on Neural Systems and Rehabilitation Engineering*.
- Lopes da Silva, F. (2004). Functional localization of brain sources using EEG and/or MEG data: volume conductor and source models. *Magnetic resonance imaging*, 22(10), 1533-1538.
- Lopes da Silva, F. (2013). EEG and MEG: relevance to neuroscience. *Neuron*, 80(5), 1112-1128.
- Lopes da Silva, F. (2023). EEG: origin and measurement. In *EEG-fMRI: physiological basis, technique, and applications* (pp. 23-48). Springer.
- Lopes da Silva, F., Van Rotterdam, A., Barts, P., Van Heusden, E., & Burr, W. (1976). Models of neuronal populations: the basic mechanisms of rhythmicity. *Progress in brain research*, 45, 281-308.
- López-Madróna, V. J., Medina Villalon, S., Badier, J. M., Trébuchon, A., Jayabal, V., Bartolomei, F., Carron, R., Barborica, A., Vulliémoz, S., & Alario, F. X. (2022). Magnetoencephalography can reveal deep brain network activities linked to memory processes. *Human brain mapping*, 43(15), 4733-4749.
- Lorente De Nó, R. (1947). Action potential of the motoneurons of the hypoglossus nucleus. *Journal of Cellular and Comparative Physiology*, 29(3), 207-287.
- Magiorkinis, E., Diamantis, A., Sidiropoulou, K., & Panteliadis, C. (2014). Highlights in the history of epilepsy: the last 200 years. *Epilepsy research and treatment*, 2014(1), 582039.
- Magiorkinis, E., Sidiropoulou, K., & Diamantis, A. (2010). Hallmarks in the history of epilepsy: epilepsy in antiquity. *Epilepsy & Behavior*, 17(1), 103-108.
- Mahjoory, K., Schoffelen, J.-M., Keitel, A., & Gross, J. (2020). The frequency gradient of human resting-state brain oscillations follows cortical hierarchies. *Elife*, 9, e53715.
- Malmivuo, J., & Plonsey, R. (1995). *Bioelectromagnetism: principles and applications of bioelectric and biomagnetic fields*. Oxford University Press, USA.
- Marc, R. E., Jones, B. W., Watt, C. B., Anderson, J. R., Sigulinsky, C., & Lauritzen, S. (2013). Retinal connectomics: towards complete, accurate networks. *Progress in retinal and eye research*, 37, 141-162.
- Marino, F., Halgren, E., Badier, J.-M., Gee, M., & Nenov, V. (1993). A finite difference model of electric field propagation in the human head: Implementation and validation. 1993 IEEE Annual Northeast Bioengineering Conference,
- Martínez-Cañada, P., Perez-Valero, E., Minguillon, J., Pelayo, F., López-Gordo, M. A., & Morillas, C. (2023). Combining aperiodic 1/f slopes and brain simulation: An EEG/MEG proxy marker of excitation/inhibition imbalance in Alzheimer's disease. *Alzheimer's & Dementia: Diagnosis, Assessment & Disease Monitoring*, 15(3), e12477.
- Matsubara, T., Tanaka, N., Peled, N., Sohrabpour, A., Sundaram, P., Okada, Y., Hämäläinen, M., Pearl, P. L., & Stufflebeam, S. (2024). Clinical utility of magnetoencephalography and its recent development. *Epilepsy & Seizure*, 16(1), 71-77.

- Mattout, J., Pélégriani-Issac, M., Garnero, L., & Benali, H. (2005). Multivariate source prelocalization (MSP): use of functionally informed basis functions for better conditioning the MEG inverse problem. *NeuroImage*, 26(2), 356-373.
- Medani, T., Garcia-Prieto, J., Tadel, F., Antonakakis, M., Erdbrügger, T., Höltershinken, M., Mead, W., Schrader, S., Joshi, A., & Engwer, C. (2023). Brainstorm-DUNEuro: An integrated and user-friendly Finite Element Method for modeling electromagnetic brain activity. *NeuroImage*, 267, 119851.
- Mellem, M. S., Wohltjen, S., Gotts, S. J., Ghuman, A. S., & Martin, A. (2017). Intrinsic frequency biases and profiles across human cortex. *Journal of neurophysiology*, 118(5), 2853-2864.
- Merlet, I., & Gotman, J. (1999). Reliability of dipole models of epileptic spikes. *Clinical Neurophysiology*, 110(6), 1013-1028.
- Meyer, S. S., Rossiter, H., Brookes, M. J., Woolrich, M. W., Bestmann, S., & Barnes, G. R. (2017). Using generative models to make probabilistic statements about hippocampal engagement in MEG. *NeuroImage*, 149, 468-482.
- Michel, C. M., Murray, M. M., Lantz, G., Gonzalez, S., Spinelli, L., & De Peralta, R. G. (2004). EEG source imaging. *Clinical Neurophysiology*, 115(10), 2195-2222.
- Mihaljević, B., Larrañaga, P., Benavides-Piccione, R., DeFelipe, J., & Bielza, C. (2020). Comparing basal dendrite branches in human and mouse hippocampal CA1 pyramidal neurons with Bayesian networks. *Scientific reports*, 10(1), 18592.
- Mikulan, E., Russo, S., Parmigiani, S., Sarasso, S., Zauli, F. M., Rubino, A., Avanzini, P., Cattani, A., Sorrentino, A., & Gibbs, S. (2020). Simultaneous human intracerebral stimulation and HD-EEG, ground-truth for source localization methods. *Scientific data*, 7(1), 127.
- Mikuni, N., Nagamine, T., Ikeda, A., Terada, K., Taki, W., Kimura, J., Kikuchi, H., & Shibasaki, H. (1997). Simultaneous recording of epileptiform discharges by MEG and subdural electrodes in temporal lobe epilepsy. *NeuroImage*, 5(4), 298-306.
- Miller, K. J., & Fine, A. L. (2022). Decision-making in stereotactic epilepsy surgery. *Epilepsia*, 63(11), 2782-2801.
- Miller, K. J., Sorensen, L. B., Ojemann, J. G., & Den Nijs, M. (2009). Power-law scaling in the brain surface electric potential. *PLoS computational biology*, 5(12), e1000609.
- Milligan, T. A. (2021). Epilepsy: a clinical overview. *The American Journal of Medicine*, 134(7), 840-847.
- Miskovic, V., MacDonald, K. J., Rhodes, L. J., & Cote, K. A. (2019). Changes in EEG multiscale entropy and power-law frequency scaling during the human sleep cycle. *Human Brain Mapping*, 40(2), 538-551.
- Mitchell, D. J., McNaughton, N., Flanagan, D., & Kirk, I. J. (2008). Frontal-midline theta from the perspective of hippocampal “theta”. *Progress in neurobiology*, 86(3), 156-185.
- Montez, T., Poil, S.-S., Jones, B. F., Manshanden, I., Verbunt, J. P., van Dijk, B. W., Brussaard, A. B., van Ooyen, A., Stam, C. J., & Scheltens, P. (2009). Altered temporal correlations in parietal alpha and prefrontal theta oscillations in early-stage Alzheimer disease. *Proceedings of the National Academy of Sciences*, 106(5), 1614-1619.
- Mormann, F., Lehnertz, K., David, P., & Elger, C. E. (2000). Mean phase coherence as a measure for phase synchronization and its application to the EEG of epilepsy patients. *Physica D: Nonlinear Phenomena*, 144(3-4), 358-369.
- Mosher, J. C., Baillet, S., & Leahy, R. M. (1999). EEG source localization and imaging using multiple signal classification approaches. *Journal of Clinical Neurophysiology*, 16(3), 225-238.

- Mosher, J. C., & Leahy, R. M. (1998). Recursive MUSIC: a framework for EEG and MEG source localization. *IEEE Transactions on Biomedical Engineering*, 45(11), 1342-1354.
- Mosher, J. C., Lewis, P. S., & Leahy, R. M. (1992). Multiple dipole modeling and localization from spatio-temporal MEG data. *IEEE Transactions on Biomedical Engineering*, 39(6), 541-557.
- Murakami, S., & Okada, Y. (2006). Contributions of principal neocortical neurons to magnetoencephalography and electroencephalography signals. *The Journal of physiology*, 575(3), 925-936.
- Nagy, P., Tóth, B., Winkler, I., & Boncz, Á. (2024). The effects of spatial leakage correction on the reliability of EEG-based functional connectivity networks. *Human Brain Mapping*, 45(8), e26747.
- Niso, G., Rogers, C., Moreau, J. T., Chen, L.-Y., Madjar, C., Das, S., Bock, E., Tadel, F., Evans, A. C., & Jolicoeur, P. (2016). OMEGA: the open MEG archive. *NeuroImage*, 124, 1182-1187.
- Niso, G., Tadel, F., Bock, E., Cousineau, M., Santos, A., & Baillet, S. (2019). Brainstorm pipeline analysis of resting-state data from the open MEG archive. *Frontiers in neuroscience*, 13, 284.
- Nolte, G., Bai, O., Wheaton, L., Mari, Z., Vorbach, S., & Hallett, M. (2004). Identifying true brain interaction from EEG data using the imaginary part of coherency. *Clinical Neurophysiology*, 115(10), 2292-2307.
- Nunez, P. L., & Silberstein, R. B. (2000). On the relationship of synaptic activity to macroscopic measurements: does co-registration of EEG with fMRI make sense? *Brain Topography*, 13, 79-96.
- Nunez, P. L., & Srinivasan, R. (2006). *Electric fields of the brain: the neurophysics of EEG*. Oxford University Press, USA.
- Nunez, P. L., Wingeier, B. M., & Silberstein, R. B. (2001). Spatial-temporal structures of human alpha rhythms: Theory, microcurrent sources, multiscale measurements, and global binding of local networks. *Human Brain Mapping*, 13(3), 125-164.
- Nuwer, M. R., Comi, G., Emerson, R., Fuglsang-Frederiksen, A., Guérit, J.-M., Hinrichs, H., Ikeda, A., Luccas, F. J. C., & Rappelsburger, P. (1998). IFCN standards for digital recording of clinical EEG. *Electroencephalography and clinical neurophysiology*, 106(3), 259-261.
- O'Brien, T., So, E. L., Mullan, B., Hauser, M., Brinkmann, B., Jack Jr, C., Cascino, G., Meyer, F., & Sharbrough, F. (1999). Subtraction SPECT co-registered to MRI improves postictal SPECT localization of seizure foci. *Neurology*, 52(1), 137-137.
- O'Reilly, C., & Elsabbagh, M. (2021). Intracranial recordings reveal ubiquitous in-phase and in-antiphase functional connectivity between homotopic brain regions in humans. *Journal of Neuroscience Research*, 99(3), 887-897.
- Oishi, M., Otsubo, H., Kameyama, S., Morota, N., Masuda, H., Kitayama, M., & Tanaka, R. (2002). Epileptic spikes: magnetoencephalography versus simultaneous electrocorticography. *Epilepsia*, 43(11), 1390-1395.
- Oostenveld, R., Fries, P., Maris, E., & Schoffelen, J.-M. (2011). FieldTrip: open source software for advanced analysis of MEG, EEG, and invasive electrophysiological data. *Computational intelligence and neuroscience*, 2011, 1-9.
- Ostlund, B. D., Alperin, B. R., Drew, T., & Karalunas, S. L. (2021). Behavioral and cognitive correlates of the aperiodic (1/f-like) exponent of the EEG power spectrum in adolescents with and without ADHD. *Developmental cognitive neuroscience*, 48, 100931.

- Oswal, A., Litvak, V., Brown, P., Woolrich, M., & Barnes, G. (2014). Optimising beamformer regions of interest analysis. *NeuroImage*, *102*, 945-954.
- Ouyang, G., Hildebrandt, A., Schmitz, F., & Herrmann, C. S. (2020). Decomposing alpha and 1/f brain activities reveals their differential associations with cognitive processing speed. *NeuroImage*, *205*, 116304.
- Pacia, S. V., & Ebersole, J. S. (1997). Intracranial EEG substrates of scalp ictal patterns from temporal lobe foci. *Epilepsia*, *38*(6), 642-654.
- Palva, J. M., Wang, S. H., Palva, S., Zhigalov, A., Monto, S., Brookes, M. J., Schoffelen, J.-M., & Jerbi, K. (2018). Ghost interactions in MEG/EEG source space: A note of caution on inter-areal coupling measures. *NeuroImage*, *173*, 632-643.
- Palva, S., & Palva, J. M. (2012). Discovering oscillatory interaction networks with M/EEG: challenges and breakthroughs. *Trends in cognitive sciences*, *16*(4), 219-230.
- Pani, S. M., Saba, L., & Fraschini, M. (2022). Clinical applications of EEG power spectra aperiodic component analysis: A mini-review. *Clinical Neurophysiology*, *143*, 1-13.
- Parkkonen, L., Fujiki, N., & Mäkelä, J. P. (2009). Sources of auditory brainstem responses revisited: contribution by magnetoencephalography. *Human brain mapping*, *30*(6), 1772-1782.
- Parvizi, J., & Kastner, S. (2018). Promises and limitations of human intracranial electroencephalography. *Nature neuroscience*, *21*(4), 474-483.
- Pascarella, A., Mikulan, E., Sciacchitano, F., Sarasso, S., Rubino, A., Sartori, I., Cardinale, F., Zauli, F., Avanzini, P., & Nobili, L. (2023). An in-vivo validation of ESI methods with focal sources. *NeuroImage*, 120219.
- Pascual-Marqui, R. D. (2002). Standardized low-resolution brain electromagnetic tomography (sLORETA): technical details. *Methods Find Exp Clin Pharmacol*, *24*(Suppl D), 5-12.
- Pascual-Marqui, R. D., Esslen, M., Kochi, K., & Lehmann, D. (2002). Functional imaging with low-resolution brain electromagnetic tomography (LORETA): a review. *Methods and findings in experimental and clinical pharmacology*, *24*(Suppl C), 91-95.
- Pascual-Marqui, R. D., Michel, C. M., & Lehmann, D. (1994). Low resolution electromagnetic tomography: a new method for localizing electrical activity in the brain. *International Journal of Psychophysiology*, *18*(1), 49-65.
- Pascual-Marqui, R. D., Pascual-Montano, A. D., Lehmann, D., Kochi, K., Esslen, M., Jancke, L., Anderer, P., Saletu, B., Tanaka, H., & Hirata, K. (2006). Exact low resolution brain electromagnetic tomography (eLORETA). *NeuroImage*, *31*(Suppl 1), S86.
- Pellegrino, G., Hedrich, T., Chowdhury, R., Hall, J. A., Lina, J. M., Dubeau, F., Kobayashi, E., & Grova, C. (2016). Source localization of the seizure onset zone from ictal EEG/MEG data. *Human brain mapping*, *37*(7), 2528-2546.
- Pellegrino, G., Hedrich, T., Chowdhury, R. A., Hall, J. A., Dubeau, F., Lina, J. M., Kobayashi, E., & Grova, C. (2018). Clinical yield of magnetoencephalography distributed source imaging in epilepsy: A comparison with equivalent current dipole method. *Human Brain Mapping*, *39*(1), 218-231.
- Pellegrino, G., Hedrich, T., Porras-Bettancourt, M., Lina, J. M., Aydin, Ü., Hall, J., Grova, C., & Kobayashi, E. (2020). Accuracy and spatial properties of distributed magnetic source imaging techniques in the investigation of focal epilepsy patients. *Human Brain Mapping*, *41*(11), 3019-3033.

- Pellegrino, G., Hedrich, T., Sziklas, V., Lina, J. M., Grova, C., & Kobayashi, E. (2021). How cerebral cortex protects itself from interictal spikes: The alpha/beta inhibition mechanism. *Human Brain Mapping*, 42(11), 3352-3365.
- Pellegrino, G., Schuler, A.-L., Arcara, G., Di Pino, G., Piccione, F., & Kobayashi, E. (2022). Resting state network connectivity is attenuated by fMRI acoustic noise. *NeuroImage*, 247, 118791.
- Pellegrino, G., Schuler, A. L., Arcara, G., Di Pino, G., Piccione, F., & Kobayashi, E. (2022). Resting state network connectivity is attenuated by fMRI acoustic noise. *NeuroImage* 247, 118791.
- Pellegrino, G., Xu, M., Alkuwaiti, A., Porras-Bettancourt, M., Abbas, G., Lina, J.-M., Grova, C., & Kobayashi, E. (2020). Effects of independent component analysis on magnetoencephalography source localization in pre-surgical frontal lobe epilepsy patients. *Frontiers in neurology*, 11, 479.
- Penfield, W., & Jasper, H. (1954). Epilepsy and the functional anatomy of the human brain.
- Pigorini, A., Avanzini, P., Barborica, A., Bénar, C.-G., David, O., Farisco, M., Keller, C. J., Manfredi, A., Mikulan, E., & Paulk, A. C. (2024). Simultaneous invasive and non-invasive recordings in humans: a novel Rosetta stone for deciphering brain activity. *Journal of Neuroscience Methods*, 110160.
- Pizzo, F., Roehri, N., Medina Villalon, S., Trébuchon, A., Chen, S., Lagarde, S., Carron, R., Gavaret, M., Giusiano, B., & McGonigal, A. (2019). Deep brain activities can be detected with magnetoencephalography. *Nature communications*, 10(1), 1-13.
- Plonsey, R., & Heppner, D. B. (1967). Considerations of quasi-stationarity in electrophysiological systems. *The Bulletin of mathematical biophysics*, 29, 657-664.
- Plummer, C., Vogrin, S. J., Woods, W. P., Murphy, M. A., Cook, M. J., & Liley, D. T. (2019). Interictal and ictal source localization for epilepsy surgery using high-density EEG with MEG: a prospective long-term study. *Brain*, 142(4), 932-951.
- Preti, M. G., Bolton, T. A., & Van De Ville, D. (2017). The dynamic functional connectome: State-of-the-art and perspectives. *NeuroImage*, 160, 41-54.
- Prichard, D., & Theiler, J. (1994). Generating surrogate data for time series with several simultaneously measured variables. *Physical review letters*, 73(7), 951.
- Pruis, G., Gilding, B. H., & Peters, M. (1993). A comparison of different numerical methods for solving the forward problem in EEG and MEG. *Physiological Measurement*, 14(4A), A1.
- Ramantani, G., Maillard, L., & Koessler, L. (2016). Correlation of invasive EEG and scalp EEG. *Seizure*, 41, 196-200.
- Rampp, S., Kaltenhäuser, M., Weigel, D., Buchfelder, M., Blümcke, I., Dörfler, A., & Stefan, H. (2010). MEG correlates of epileptic high gamma oscillations in invasive EEG. *Epilepsia*, 51(8), 1638-1642.
- Rampp, S., & Stefan, H. (2007). Magnetoencephalography in presurgical epilepsy diagnosis. *Expert review of medical devices*, 4(3), 335-347.
- Ramsay, I. S., Lynn, P. A., Schermitzler, B., & Sponheim, S. R. (2021). Individual alpha peak frequency is slower in schizophrenia and related to deficits in visual perception and cognition. *Scientific reports*, 11(1), 1-9.
- Reif, P. S., Strzelczyk, A., & Rosenow, F. (2016). The history of invasive EEG evaluation in epilepsy patients. *Seizure*, 41, 191-195.

- Rizkallah, J., Amoud, H., Fraschini, M., Wendling, F., & Hassan, M. (2020). Exploring the correlation between M/EEG source-space and fMRI networks at rest. *Brain Topography*, 33, 151-160.
- Rolando Grave de Peralta Menendez, A., Gonzalez, S., Lantz, G., Michel, C. M., & Landis, T. (2001). Noninvasive localization of electromagnetic epileptic activity. I. Method descriptions and simulations. *Brain Topography*, 14, 131-137.
- Rosenow, F., & Lüders, H. (2001). Presurgical evaluation of epilepsy. *Brain*, 124(9), 1683-1700.
- Rush, S., & Driscoll, D. A. (1968). Current distribution in the brain from surface electrodes. *Anesthesia & Analgesia*, 47(6), 717-723.
- Ryvlin, P., Cross, J. H., & Rheims, S. (2014). Epilepsy surgery in children and adults. *The Lancet Neurology*, 13(11), 1114-1126.
- Sadaghiani, S., Brookes, M. J., & Baillet, S. (2022). Connectomics of human electrophysiology. *NeuroImage*, 247, 118788.
- Salmelin, R. (2010). Multi-dipole modeling in MEG. *MEG: An introduction to methods*, 124-155.
- Salvatore, S. V., Lambert, P. M., Benz, A., Rensing, N. R., Wong, M., Zorumski, C. F., & Mennerick, S. (2024). Periodic and aperiodic changes to cortical EEG in response to pharmacological manipulation. *Journal of neurophysiology*, 131(3), 529-540.
- Santiuste, M., Nowak, R., Russi, A., Tarancon, T., Oliver, B., Ayats, E., Scheler, G., & Graetz, G. (2008). Simultaneous magnetoencephalography and intracranial EEG registration: technical and clinical aspects. *Journal of Clinical Neurophysiology*, 25(6), 331-339.
- Schäfer, C. B., Morgan, B. R., Ye, A. X., Taylor, M. J., & Doesburg, S. M. (2014). Oscillations, networks, and their development: MEG connectivity changes with age. *Human Brain Mapping*, 35(10), 5249-5261.
- Schaworonkow, N., & Voytek, B. (2021). Longitudinal changes in aperiodic and periodic activity in electrophysiological recordings in the first seven months of life. *Developmental cognitive neuroscience*, 47, 100895.
- Scheffer, I. E., Berkovic, S., Capovilla, G., Connolly, M. B., French, J., Guilhoto, L., Hirsch, E., Jain, S., Mathern, G. W., & Moshé, S. L. (2017). ILAE classification of the epilepsies: Position paper of the ILAE Commission for Classification and Terminology. *Epilepsia*, 58(4), 512-521.
- Scherg, M. (1984). Topographical analysis of auditory evoked potentials: derivation of components. *Evoked potentials*, 731.
- Scherg, M., & Von Cramon, D. (1986). Evoked dipole source potentials of the human auditory cortex. *Electroencephalography and Clinical Neurophysiology/Evoked Potentials Section*, 65(5), 344-360.
- Schnitzler, A., & Gross, J. (2005a). Functional connectivity analysis in magnetoencephalography. *International review of neurobiology*, 68, 173-195.
- Schnitzler, A., & Gross, J. (2005b). Normal and pathological oscillatory communication in the brain. *Nature reviews neuroscience*, 6(4), 285-296.
- Schoffelen, J. M., & Gross, J. (2009). Source connectivity analysis with MEG and EEG. *Human Brain Mapping*, 30(6), 1857-1865.
- Seeber, M., Cantonas, L.-M., Hoevels, M., Sesia, T., Visser-Vandewalle, V., & Michel, C. M. (2019). Subcortical electrophysiological activity is detectable with high-density EEG source imaging. *Nature communications*, 10(1), 753.
- Sekihara, K., Nagarajan, S. S., Poeppel, D., & Marantz, A. (2002). Performance of an MEG adaptive-beamformer technique in the presence of correlated neural activities: effects on

- signal intensity and time-course estimates. *IEEE Transactions on Biomedical Engineering*, 49(12), 1534-1546.
- Senoussi, M., Verbeke, P., Desender, K., De Loof, E., Talsma, D., & Verguts, T. (2022). Theta oscillations shift towards optimal frequency for cognitive control. *Nature Human Behaviour*, 1-14.
- Shafiei, G., Baillet, S., & Misic, B. (2022). Human electromagnetic and haemodynamic networks systematically converge in unimodal cortex and diverge in transmodal cortex. *PLoS biology*, 20(8), e3001735.
- Shi, H., Pattnaik, A. R., Aguila, C., Lucas, A., Sinha, N., Prager, B., Mojena, M., Gallagher, R., Parashos, A., & Bonilha, L. (2024). Utility of intracranial EEG networks depends on re-referencing and connectivity choice. *Brain Communications*, 6(3), fcae165.
- Shigeto, H., Morioka, T., Hisada, K., Nishio, S., Ishibashi, H., Kira, D.-i., Tobimatsu, S., & Kato, M. (2002). Feasibility and limitations of magnetoencephalographic detection of epileptic discharges: simultaneous recording of magnetic fields and electrocorticography. *Neurological research*, 24(6), 531-536.
- Shiraishi, H., Ahlfors, S. P., Stufflebeam, S. M., Takano, K., Okajima, M., Knake, S., Hatanaka, K., Kohsaka, S., Saitoh, S., & Dale, A. M. (2005). Application of magnetoencephalography in epilepsy patients with widespread spike or slow-wave activity. *Epilepsia*, 46(8), 1264-1272.
- Siems, M., & Siegel, M. (2020). Dissociated neuronal phase-and amplitude-coupling patterns in the human brain. *NeuroImage*, 209, 116538.
- Silver, A., & Zimmerman, J. (1965). Quantum transitions and loss in multiply connected superconductors. *Physical review letters*, 15(23), 888.
- Sohrabpour, A., Cai, Z., Ye, S., Brinkmann, B., Worrell, G., & He, B. (2020). Noninvasive electromagnetic source imaging of spatiotemporally distributed epileptogenic brain sources. *Nature communications*, 11(1), 1946.
- Sohrabpour, A., & He, B. (2021). Exploring the extent of source imaging: Recent advances in noninvasive electromagnetic brain imaging. *Current Opinion in Biomedical Engineering*, 18, 100277.
- Sohrabpour, A., Lu, Y., Kankirawatana, P., Blount, J., Kim, H., & He, B. (2015). Effect of EEG electrode number on epileptic source localization in pediatric patients. *Clinical Neurophysiology*, 126(3), 472-480.
- Sohrabpour, A., Lu, Y., Worrell, G., & He, B. (2016). Imaging brain source extent from EEG/MEG by means of an iteratively reweighted edge sparsity minimization (IRES) strategy. *NeuroImage*, 142, 27-42.
- Sporns, O. (2011). The human connectome: a complex network. *Annals of the new York Academy of Sciences*, 1224(1), 109-125.
- Sporns, O., Tononi, G., & Kötter, R. (2005). The human connectome: a structural description of the human brain. *PLoS computational biology*, 1(4), e42.
- Srinivasan, R., Winter, W. R., Ding, J., & Nunez, P. L. (2007). EEG and MEG coherence: measures of functional connectivity at distinct spatial scales of neocortical dynamics. *Journal of Neuroscience Methods*, 166(1), 41-52.
- Srinivasan, R., Winter, W. R., & Nunez, P. L. (2006). Source analysis of EEG oscillations using high-resolution EEG and MEG. *Progress in brain research*, 159, 29-42.

- Stam, C. J., Nolte, G., & Daffertshofer, A. (2007). Phase lag index: assessment of functional connectivity from multi channel EEG and MEG with diminished bias from common sources. *Human Brain Mapping*, 28(11), 1178-1193.
- Stam, C. J., & van Straaten, E. C. (2012). Go with the flow: use of a directed phase lag index (dPLI) to characterize patterns of phase relations in a large-scale model of brain dynamics. *NeuroImage*, 62(3), 1415-1428.
- Stephen, J., Aine, C., Ranken, D., Hudson, D., & Shih, J. J. (2003). Multidipole analysis of simulated epileptic spikes with real background activity. *Journal of Clinical Neurophysiology*, 20(1), 1-16.
- Stevens, C. F. (1979). The neuron. *Scientific American*, 241(3), 54-65.
- Sutter, R., & Kaplan, P. W. (2017). The history of continuous EEG monitoring. *Continuous EEG Monitoring: Principles and Practice*, 3-12.
- Tadel, F., Baillet, S., Mosher, J. C., Pantazis, D., & Leahy, R. M. (2011). Brainstorm: a user-friendly application for MEG/EEG analysis. *Computational intelligence and neuroscience*, 2011.
- Tadel, F., Bock, E., Niso, G., Mosher, J. C., Cousineau, M., Pantazis, D., Leahy, R. M., & Baillet, S. (2019). MEG/EEG group analysis with brainstorm. *Frontiers in neuroscience*, 13, 435877.
- Talairach, J., Bancaud, J., Bonis, A., Szikla, G., & Tournoux, P. (1962). Functional stereotaxic exploration of epilepsy. *Stereotactic and Functional Neurosurgery*, 22(3-5), 328-331.
- Tamilia, E., Matarrese, M. A., Ntolkeras, G., Grant, P. E., Madsen, J. R., Stufflebeam, S. M., Pearl, P. L., & Papadelis, C. (2021). Noninvasive mapping of ripple onset predicts outcome in epilepsy surgery. *Annals of neurology*, 89(5), 911-925.
- Tanaka, A., Akamatsu, N., Shouzaki, T., Toyota, T., Yamano, M., Nakagawa, M., & Tsuji, S. (2013). Clinical characteristics and treatment responses in new-onset epilepsy in the elderly. *Seizure*, 22(9), 772-775.
- Tao, J. X., Baldwin, M., Hawes-Ebersole, S., & Ebersole, J. S. (2007). Cortical substrates of scalp EEG epileptiform discharges. *Journal of Clinical Neurophysiology*, 24(2), 96-100.
- Taussig, D., Montavont, A., & Isnard, J. (2015). Invasive EEG explorations. *Neurophysiologie Clinique/Clinical Neurophysiology*, 45(1), 113-119.
- Taylor, M. J., Mills, T., & Pang, E. W. (2011). The development of face recognition; hippocampal and frontal lobe contributions determined with MEG. *Brain topography*, 24, 261-270.
- Taylor, P. N., Papasavvas, C. A., Owen, T. W., Schroeder, G. M., Hutchings, F. E., Chowdhury, F. A., Diehl, B., Duncan, J. S., McEvoy, A. W., & Miserocchi, A. (2022). Normative brain mapping of interictal intracranial EEG to localize epileptogenic tissue. *Brain*, 145(3), 939-949.
- Tierney, T. M., Levy, A., Barry, D. N., Meyer, S. S., Shigihara, Y., Everatt, M., Mellor, S., Lopez, J. D., Bestmann, S., & Holmes, N. (2021). Mouth magnetoencephalography: A unique perspective on the human hippocampus. *NeuroImage*, 225, 117443.
- Trujillo-Barreto, N. J., Aubert-Vázquez, E., & Valdés-Sosa, P. A. (2004). Bayesian model averaging in EEG/MEG imaging. *NeuroImage*, 21(4), 1300-1319.
- Uğurbil, K., Xu, J., Auerbach, E. J., Moeller, S., Vu, A. T., Duarte-Carvajalino, J. M., Lenglet, C., Wu, X., Schmitter, S., & Van de Moortele, P. F. (2013). Pushing spatial and temporal resolution for functional and diffusion MRI in the Human Connectome Project. *NeuroImage*, 80, 80-104.

- Unnwongse, K., Rampp, S., Wehner, T., Kowoll, A., Parpaley, Y., von Lehe, M., Lanfer, B., Rusiniak, M., Wolters, C., & Wellmer, J. (2023). Validating EEG source imaging using intracranial electrical stimulation. *Brain Communications*, 5(1), fcad023.
- Urbach, H., Kellner, E., Kremers, N., Blümcke, I., & Demerath, T. (2022). MRI of focal cortical dysplasia. *Neuroradiology*, 1-10.
- Uusitalo, M. A., & Ilmoniemi, R. J. (1997). Signal-space projection method for separating MEG or EEG into components. *Medical and biological engineering and computing*, 35(2), 135-140.
- Uutela, K., Hämäläinen, M., & Somersalo, E. (1999). Visualization of magnetoencephalographic data using minimum current estimates. *NeuroImage*, 10(2), 173-180.
- Vallarino, E., Hincapié, A. S., Jerbi, K., Leahy, R. M., Pascarella, A., Sorrentino, A., & Sommariva, S. (2023). Tuning Minimum-Norm regularization parameters for optimal MEG connectivity estimation. *NeuroImage*, 281, 120356.
- van Diessen, E., Diederer, S. J., Braun, K. P., Jansen, F. E., & Stam, C. J. (2013). Functional and structural brain networks in epilepsy: what have we learned? *Epilepsia*, 54(11), 1855-1865.
- Van Klink, N., Hillebrand, A., & Zijlmans, M. (2016). Identification of epileptic high frequency oscillations in the time domain by using MEG beamformer-based virtual sensors. *Clinical Neurophysiology*, 127(1), 197-208.
- Van Veen, B. D., Van Drongelen, W., Yuchtman, M., & Suzuki, A. (1997). Localization of brain electrical activity via linearly constrained minimum variance spatial filtering. *IEEE transactions on biomedical engineering*, 44(9), 867-880.
- Velmurugan, J., Badier, J.-M., Pizzo, F., Villalon, S. M., Papageorgakis, C., López-Madróna, V., Jegou, A., Carron, R., Bartolomei, F., & Bénar, C.-G. (2022). Virtual MEG sensors based on beamformer and independent component analysis can reconstruct epileptic activity as measured on simultaneous intracerebral recordings. *NeuroImage*, 264, 119681.
- Villalon, S. M., Paz, R., Roehri, N., Lagarde, S., Pizzo, F., Colombet, B., Bartolomei, F., Carron, R., & Bénar, C.-G. (2018). EpiTools, A software suite for presurgical brain mapping in epilepsy: Intracerebral EEG. *Journal of Neuroscience Methods*, 303, 7-15.
- Vinck, M., Oostenveld, R., Van Wingerden, M., Battaglia, F., & Pennartz, C. M. (2011). An improved index of phase-synchronization for electrophysiological data in the presence of volume-conduction, noise and sample-size bias. *NeuroImage*, 55(4), 1548-1565.
- von Ellenrieder, N., Beltrachini, L., & Muravchik, C. H. (2012). Electrode and brain modeling in stereo-EEG. *Clinical Neurophysiology*, 123(9), 1745-1754.
- von Ellenrieder, N., Beltrachini, L., Muravchik, C. H., & Gotman, J. (2014). Extent of cortical generators visible on the scalp: effect of a subdural grid. *NeuroImage*, 101, 787-795.
- von Ellenrieder, N., Khoo, H. M., Dubeau, F., & Gotman, J. (2021). What do intracerebral electrodes measure? *Clinical Neurophysiology*, 132(5), 1105-1115.
- von Ellenrieder, N., Pellegrino, G., Hedrich, T., Gotman, J., Lina, J.-M., Grova, C., & Kobayashi, E. (2016). Detection and magnetic source imaging of fast oscillations (40–160 Hz) recorded with magnetoencephalography in focal epilepsy patients. *Brain Topography*, 29(2), 218-231.
- von Helmholtz, H. L. F. (2004). Some laws concerning the distribution of electric currents in volume conductors with applications to experiments on animal electricity. *Proceedings of the IEEE*, 92(5), 868-870.

- Voytek, B., Canolty, R. T., Shestyuk, A., Crone, N. E., Parvizi, J., & Knight, R. T. (2010). Shifts in gamma phase–amplitude coupling frequency from theta to alpha over posterior cortex during visual tasks. *Frontiers in human neuroscience*, 4, 191.
- Voytek, B., Kramer, M. A., Case, J., Lepage, K. Q., Tempesta, Z. R., Knight, R. T., & Gazzaley, A. (2015). Age-related changes in 1/f neural electrophysiological noise. *Journal of Neuroscience*, 35(38), 13257-13265.
- Wagner, M., Fuchs, M., Wischmann, H., Drenckhahn, R., & K hler, T. (1996). Smooth reconstruction of cortical sources from EEG or MEG recordings. *NeuroImage*, 3(1), S168-S168.
- Wang, H. E., Bénar, C. G., Quilichini, P. P., Friston, K. J., Jirsa, V. K., & Bernard, C. (2014). A systematic framework for functional connectivity measures. *Frontiers in neuroscience*, 8, 405.
- Wang, X.-J. (2010). Neurophysiological and computational principles of cortical rhythms in cognition. *Physiological reviews*, 90(3), 1195-1268.
- Wax, M., & Anu, Y. (1996). Performance analysis of the minimum variance beamformer. *IEEE Transactions on Signal Processing*, 44(4), 928-937.
- Wen, H., & Liu, Z. (2016). Separating fractal and oscillatory components in the power spectrum of neurophysiological signal. *Brain Topography*, 29, 13-26.
- Wendel, K., Väisänen, O., Malmivuo, J., Gencer, N. G., Vanrumste, B., Durka, P., Magjarević, R., Supek, S., Pascu, M. L., & Fontenelle, H. (2009). EEG/MEG source imaging: methods, challenges, and open issues. *Computational intelligence and neuroscience*, 2009(1), 656092.
- Wendling, F. (2005). Neurocomputational models in the study of epileptic phenomena. *Journal of Clinical Neurophysiology*, 22(5), 285-287.
- Wendling, F., Bellanger, J.-J., Bartolomei, F., & Chauvel, P. (2000). Relevance of nonlinear lumped-parameter models in the analysis of depth-EEG epileptic signals. *Biological cybernetics*, 83(4), 367-378.
- Wennberg, R., Valiante, T., & Cheyne, D. (2011). EEG and MEG in mesial temporal lobe epilepsy: where do the spikes really come from? *Clinical Neurophysiology*, 122(7), 1295-1313.
- Whittingstall, K., Stroink, G., Gates, L., Connolly, J., & Finley, A. (2003). Effects of dipole position, orientation and noise on the accuracy of EEG source localization. *Biomedical engineering online*, 2(1), 1-5.
- Wiesman, A. I., da Silva Castanheira, J., & Baillet, S. (2022). Stability of spectral estimates in resting-state magnetoencephalography: Recommendations for minimal data duration with neuroanatomical specificity. *NeuroImage*, 247, 118823.
- Wilkinson, C. L., & Nelson, C. A. (2021). Increased aperiodic gamma power in young boys with Fragile X Syndrome is associated with better language ability. *Molecular autism*, 12(1), 1-15.
- Williams, N., Wang, S. H., Arnulfo, G., Nobili, L., Palva, S., & Palva, J. M. (2023). Modules in connectomes of phase-synchronization comprise anatomically contiguous, functionally related regions. *NeuroImage*, 272, 120036.
- Wilson, H. R., & Cowan, J. D. (1972). Excitatory and inhibitory interactions in localized populations of model neurons. *Biophysical journal*, 12(1), 1-24.
- Wipf, D. P., Owen, J. P., Attias, H. T., Sekihara, K., & Nagarajan, S. S. (2010). Robust Bayesian estimation of the location, orientation, and time course of multiple correlated neural sources using MEG. *NeuroImage*, 49(1), 641-655.

- Wirsich, J., Giraud, A.-L., & Sadaghiani, S. (2020). Concurrent EEG-and fMRI-derived functional connectomes exhibit linked dynamics. *NeuroImage*, 219, 116998.
- Wirsich, J., Iannotti, G. R., Ridley, B., Shamshiri, E. A., Sheybani, L., Grouiller, F., Bartolomei, F., Seeck, M., Lazeyras, F., & Ranjeva, J.-P. (2024). Altered correlation of concurrently recorded EEG-fMRI connectomes in temporal lobe epilepsy. *Network Neuroscience*, 8(2), 466-485.
- Wirsich, J., Jorge, J., Iannotti, G. R., Shamshiri, E. A., Grouiller, F., Abreu, R., Lazeyras, F., Giraud, A.-L., Gruetter, R., & Sadaghiani, S. (2021). The relationship between EEG and fMRI connectomes is reproducible across simultaneous EEG-fMRI studies from 1.5 T to 7T. *NeuroImage*, 231, 117864.
- Wirsich, J., Ridley, B., Besson, P., Jirsa, V., Bénar, C., Ranjeva, J.-P., & Guye, M. (2017). Complementary contributions of concurrent EEG and fMRI connectivity for predicting structural connectivity. *NeuroImage*, 161, 251-260.
- Xu, J., Mitra, S., Van Hoof, C., Yazicioglu, R. F., & Makinwa, K. A. (2017). Active electrodes for wearable EEG acquisition: Review and electronics design methodology. *IEEE reviews in biomedical engineering*, 10, 187-198.
- Zauli, F. M., Del Vecchio, M., Pigorini, A., Russo, S., Massimini, M., Sartori, I., Cardinale, F., d’Orio, P., & Mikulan, E. (2024). Localizing hidden Interictal Epileptiform Discharges with simultaneous intracerebral and scalp high-density EEG recordings. *Journal of Neuroscience Methods*, 110193.
- Zelmann, R., Frauscher, B., Aro, R. P., Gueziri, H.-E., & Collins, D. L. (2023). SEEGAtlas: A framework for the identification and classification of depth electrodes using clinical images. *Journal of Neural Engineering*, 20(3), 036021.
- Zhang, C., Yu, X., Yang, Y., & Xu, L. (2014). Phase synchronization and spectral coherence analysis of EEG activity during mental fatigue. *Clinical EEG and neuroscience*, 45(4), 249-256.
- Zhang, Y., Van Drongelen, W., & He, B. (2006). Estimation of in vivo brain-to-skull conductivity ratio in humans. *Applied physics letters*, 89(22), 223903.
- Zijlmans, M., Huiskamp, G. M., Leijten, F. S., Van Der Meij, W. M., Wieneke, G., & Van Huffelen, A. C. (2002). Modality-specific spike identification in simultaneous magnetoencephalography/electroencephalography: a methodological approach. *Journal of Clinical Neurophysiology*, 19(3), 183-191.